PROBING QUASAR SIGHT LINES IN THREE DIMENSIONS

Lise Bech Christensen

Astrophysikalisches Institut Potsdam

DISSERTATION ZUR ERLANGUNG DES NATURWISSENSCHAFTLICHEN GRADES DR. RER. NAT.;
EINGEREICHT AN DER MATHEMATISCH-NATURWISSENSCHAFTLICHEN
FAKULTÄT DER UNIVERSITÄT POTSDAM

June 2005

PROBING QUASAR SIGHT LINES IN THREE DIMENSIONS

by

Lise Bech Christensen

Astrophysikalisches Institut Potsdam

Abstract

This thesis explores the technique of integral field spectroscopy (IFS) to observe quasars at various redshifts, specifically to look for emission line objects close to the quasar sight lines. Observations with IFS allow simultaneous imaging and spectroscopy of a field in the sky. From the images objects can be identified right away. The spectra allow to determine the redshift and hence the distance of objects close to the quasar line of sight, thereby providing a three-dimensional view along the line of sight.

The first part of the thesis presents a search for galaxy counterparts to intervening strong hydrogen absorption lines seen in quasar (QSO) spectra. Observations with IFS, contrary to other techniques, do not require previous knowledge of the location of the objects for follow-up spectroscopy. Since the redshifts of the intervening damped Lyman-α (DLA) systems are known, the IFS data can be searched for emission lines at known wavelengths anywhere in the field surrounding the QSO. By looking for emission from galaxies selected from absorption lines in background quasar spectra, we avoid the selection biases involved in flux-limited surveys so that we can probe the faint end of the galaxy luminosity function. Here we analyse two samples separated according to their redshifts: A sample at low redshifts ($z < 1$) for which optical emission lines are searched for, and a high redshift sample ($z > 2$) where the Lyα emission is redshifted to optical wavelengths.

In the low redshift sample, we search for emission lines from known objects near the QSO sight line, and detect emission lines at the redshifts corresponding to those of the absorbers in six of eight systems investigated. Two of these objects have been confirmed recently by other authors using long-slit spectroscopy and photometric redshifts. We confirm the photometric redshift and identify four additional candidates to other systems. The offsets of the candidate emission lines to the QSOs probe the projected extension of the neutral gas disc. Using the spatial offsets as a proxy for the galaxy sizes, we estimate that the galaxies are consistent with having discs with an average scale length of 5 kpc, similar to local spiral galaxies.

In the particular case of the $z = 0.160$ sub-DLA towards PHL 1226, we find an offset of $1''$ between the continuum and the line emission regions. However, such large offsets are not expected in higher redshift systems where galaxies typically appear as point sources with the spatial resolution in our datasets. For the sub-DLA galaxy towards PHL 1226, we determine a solar abundance in the emission region using strong line diagnostics. We discuss the possible presence of a metallicity bias in DLA (and sub-DLA) systems in cases where metallicity gradients would be similar to those in local galaxies. Because of the larger cross sections of the galaxy outskirts, such gradients could explain the large scatter and low metallicities found in DLAs that probe random sight lines through galaxy discs.

In the high redshift sample that contains 21 DLAs and sub-DLAs, we find candidate Lyα emission lines from 8 systems, two of which are associated with sub-DLA systems. Line flux densities are similar to those of the few previously known systems. We find an average size of 20 kpc which is a few times larger than what is predicted by numerical simulations. Assuming that an exponential disc profile is a good representation of their morphologies, we derive an average disc

scale length of 5 kpc, which is similar to the scale length determined for the low redshift sample.

Because Lyα photons are resonantly scattered, converting the Lyα luminosities from the candidates into star-formation rates (SFR) will only provide a lower limit to the intrinsic SFR. Hence we estimate lower limits of 1–10 $M_{\odot}yr^{-1}$. We assume that the Schmidt-Kennicutt law, which relates the SFR per unit area to the surface density of gas, is valid for DLAs. This is used to argue that in order to achieve the measured SFRs, DLA galaxies must have radial sizes of $\sim$10 kpc in the neutral gas. Masses derived with a model of an exponential disc suggest that the average DLA galaxy at $z \approx 3$ has a gas disc mass similar to that of the Milky Way and other local disc galaxies which is consistent with predictions from numerical simulations. We argue that according to numerical simulations, DLA galaxy masses including stellar masses could be only 10% of the mass of a present day luminous L^* galaxy, where L^* is the characteristic luminosity in the Schechter luminosity function. To further determine the nature of the emission line candidates, it is crucial not only to obtain confirmation of the candidates by deeper spectroscopic measurements, but also to investigate rest-frame optical emission lines. This is necessary to constrain the dust effects for the derived SFRs.

The second part of this thesis investigates emission lines at the QSO redshifts. The low redshift sample contains three QSOs at $z < 1$, where the redshifted optical emission lines are covered by the observed wavelength range. Two radio-loud quasars are lobe-dominated and show extended [O II] emission line regions, while we detect no extended emission for the core-dominated quasar. Alignment of the extended emission nebulae with the radio jets, together with large velocities, suggest an interaction between the radio jets and the surrounding material.

Extended nebulae with narrow Lyα emission lines are found around a sample of high redshift ($2.7 < z < 4.5$) radio-quiet QSOs and one radio-loud, core-dominated QSO. The nebular emission lines are much more narrow than the nuclear Lyα emission line from the QSOs. IFS allows us to explore the velocity structure of the two brightest emission line nebulae and we find evidence for velocity gradients extending over a few arcseconds. Our results support theoretical predictions for the nebulae extensions and surface brightness.

1–2% of the QSO flux within a 20 Å narrow-band is re-emitted by the nebulae around the radio-quiet quasars. This is an order of magnitude smaller than what has been seen for lobe-dominated radio-loud QSOs investigated in the literature. We discuss these differences in the nebulae around radio-loud and radio-quiet QSOs. Analyses of correlations between the QSO ionising flux, radio flux densities, nebulae emission line flux, and nebulae sizes indicate that the ionising flux does not determine the nebular properties. More luminous nebulae are found to be larger, and we argue that interactions with the radio jets could be an additional factor which causes brighter emission in the surroundings. Alternatively, differences in the environments could affect the extended emission.

In conclusion, our use of IFS to search for faint emission lines, both from point sources and extended nebulae provides exciting new results within the scientific areas studied here.

Contents

CHAPTER 1

Introduction

A key question for our understanding of the Universe is how galaxies form and then evolve to galaxies with distinctly different morphologies and masses. Most information about high redshift galaxies comes from large surveys that use flux-limited samples which preferentially detect the brightest objects. Because such samples are biased towards brighter galaxies is it difficult to get a genuinely volume-limited sample at very large distances what would be essential for the understanding of galaxy evolution. To detect the fainter galaxies a different approach is required. For example such objects can be detected through absorption lines in spectra of background sources, typically bright quasars or quasi stellar objects (QSOs)[1] . Additional information can be derived from absorption lines from intervening galaxies. For example absorption line analyses give information on the distribution of neutral and ionised gas in the Universe. Strong absorption lines, either from metals or neutral hydrogen, also give an opportunity to study galaxies and their chemical composition. The strongest absorption systems, the damped Lyα lines (DLAs), are known to contain a large fraction of neutral hydrogen which provides the fuel from which stars are formed, and are believed to reside in either galaxies or proto-galaxies.

To understand galaxy formation it is crucial to discover the galaxies responsible for the main reservoir of the neutral gas in the Universe and to determine their properties such as star formation rates (SFRs) and sizes. Although this reservoir of neutral gas may diminish through consumption in star formation, the effect has been shown to be weak. Measuring SFRs in individual DLAs, coupled with the observed metallicity evolution allows a self-consistent test of the SFRs and histories. The global evolution of H I as derived from DLA statistics would then give an independent measurement of the star formation history of the Universe without the usual biases inherent in flux-limited samples. These tests will nevertheless be based on the assumption that the random sight lines probed by QSOs in existing surveys are not missing DLAs with special characteristics.

In order to understand the type of galaxies selected through absorption lines it is crucial to detect the absorbers themselves in emission. This chapter introduces various absorption line categories found in quasar spectra and their characteristics. The main focus will be on the strongest absorption lines about which the most detailed information has been gathered.

1.1 QSO absorption systems

Fig. 1.1 shows a typical quasar spectrum. In this specific case the QSO has a redshift of $z \approx 1.3$, and many absorption lines are seen. These absorption lines are traditionally divided into different

[1] Quasars constitute a sub-population of radio-loud objects and radio-quiet objects are termed quasi-stellar objects (QSOs) (Binney & Merrifield 1998), but here the concept QSO will be used for any background luminous active galactic nucleus (AGN).

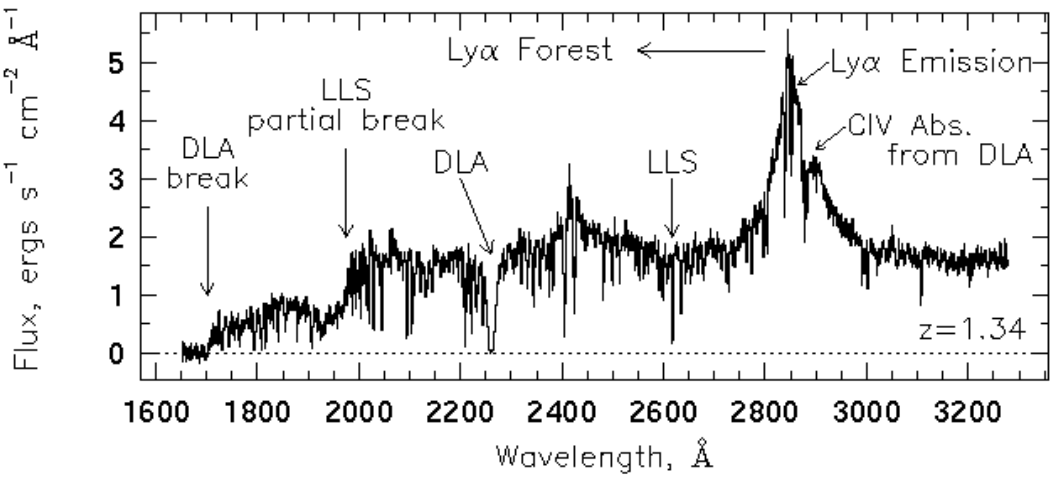

Fig. 1.1. Typical spectrum of a high redshift QSO, which illustrates the variety in equivalent widths and elements of various absorption lines. One damped Lyman-α (DLA) and one Lyman limit system (LLS) are present in this spectrum. The spectrum of PKS 0454+039 at $z = 1.34$ was obtained by HST/FOS (taken from Charlton et al. 2000).

categories according to the equivalent widths of the lines and the element by which they are caused. Blue-wards of the QSO Lyα emission line are several absorption lines of different equivalent widths characteristic for the Lyα-forest. Most of these lines are due to the absorption of photons by filaments or clouds of neutral hydrogen at redshifts lower than the QSO. Some of the lines are caused by metals associated with neutral clouds, which have been enriched by metal production from stars. For some Lyα absorption lines, notably those associated with higher H I column density clouds, several metal absorption lines can be identified. Other absorption systems are associated with the QSO, arising either in the QSO host galaxy, or in the immediate environment of the central part of the active galactic nucleus (AGN), as seen in broad absorption line quasar spectra.

In Fig. 1.1, three different types of Lyα absorption lines are indicated. The equivalent widths of the absorption lines are related to the column density, $N(\mathrm{H\,I})$, of the cloud. Below we summarise the main systems:

- Lyα forest having $N(\mathrm{H\,I}) < 10^{17}$ cm^{-2}. Most of the lines in the spectrum are of this type. Typical metallicities have been determined to be $\sim 10^{-3}$ based on the detection of C IV absorption lines associated with clouds with column densities as low as $N(\mathrm{H\,I}) \approx 5 \times 10^{14}$ cm^{-2} (Ellison et al. 1999).

- Lyman Limit systems (LLS) with $10^{17} < N(\mathrm{H\,I}) < 2 \times 10^{20}$ cm^{-2} are rarer than Lyα forest lines. At this column density the cloud becomes optically thick to radiation below 912 Å. This causes a characteristic break in the QSO spectrum at a wavelength corresponding to $912(1 + z)$ Å, hence explaining their name.

- Damped Lyα systems (DLA) with $N(\mathrm{H\,I}) > 2 \times 10^{20}$ cm^{-2} are even rarer systems and their absorption lines are very broad with characteristic damped wings. Similar column densities are present in galaxy discs. Several metal absorption lines are found associated with DLAs and detailed metallicity studies can be carried out.

Additionally, sub-Damped Lyα systems with $10^{19} < N(\mathrm{H\,I}) < 2 \times 10^{20}$ cm^{-2} have been introduced as separate class in the literature (Péroux et al. 2003a). Intermediate resolution

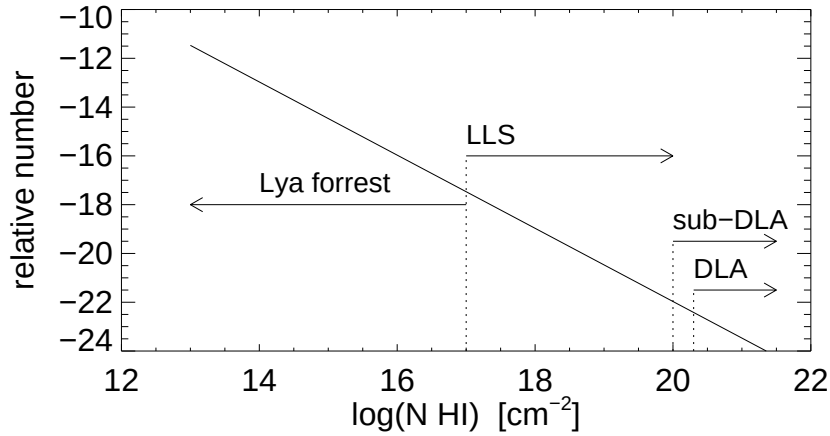

Fig. 1.2. Schematic representation of the column density distribution.

spectroscopy reveals that they also have damped wings, but they are not easily recognised in low-resolution spectra. Sub-DLAs are actually a sub-set of LLS with metallicities similar to those in DLA systems (Dessauges-Zavadsky et al. 2003), but ionisation corrections can be substantially larger than in DLAs (Prochaska & Herbert-Fort 2004).

To determine the column densities of the absorbers a measurement of the equivalent width, W, is needed. For the strongest absorbers in the DLA regime the relation between W measured in Å and $N(\mathrm{H\,I})$ is

$$N(\mathrm{H\,I}) = 10^{20}\left(\frac{W}{7.3}\right)^2 \mathrm{cm}^{-2} \tag{1.1}$$

LLS and DLAs were originally distinguished because in low-resolution spectra only DLA lines showed the characteristic broad wings (Wolfe et al. 1986). Through either line counts or more accurate profile fits, the number of systems of any given column density is determined. Investigations of many sight lines towards QSOs have shown that the column density distribution can be described by a power law

$$\frac{df(N)}{dN} \propto N^{-\beta}, \tag{1.2}$$

such that $f(N)$ gives the number of absorbers with a column density between N and $N + dN$. A fit of observations to Eq. (1.2) gives $\beta = 1.5$ as indicated in Fig. 1.2 (Tytler 1987; Lanzetta et al. 1991; Petitjean et al. 1993). Evidence has been given for a steepened power law at high column densities and high redshifts (Storrie-Lombardi & Wolfe 2000), but this effect could also explained by high $N(\mathrm{H\,I})$ systems which are overlooked due to dust extinction. Numerical simulations that predict column density distributions below the DLA limit, show that β =1.5 at all column densities (Vladilo & Peroux 2005).

The total neutral gas mass in the interstellar medium (ISM) can be estimated from

$$M_g \propto \int N f(N) dN \tag{1.3}$$

where the integral is to be taken over all column densities $[N_{\min}, N_{\max}]$. For $\beta = 1.5$ this integral is proportional to $\sqrt{N_{\max}}$ such that the total neutral gas mass is dominated by the highest column

density absorbers. The density of neutral matter in the Universe can then be calculated

$$\Omega_g \approx \Omega_{\rm DLA} = \frac{H_0}{c}\frac{m_{\rm H}\mu}{\rho_{\rm crit}}\sqrt{N_{\rm max}} \tag{1.4}$$

where $m_{\rm H}$ is the hydrogen atomic mass, μ is the mean molecular weight, and $\rho_{\rm crit} = 3H_0^2/8\pi G$ is the critical density. While most of the neutral matter resides in DLAs it has been shown that most of the atoms reside in the Lyα forest at high redshifts, and possibly in the warm intergalactic medium (IGM) in the local Universe.

When the column density distribution is evaluated as a function of redshift the evolution of the density in neutral gas can be studied. An upper limit of the DLA column density has to exist, otherwise $\Omega_{\rm DLA}$ would be infinite. Currently, the observed upper limit of log N(H I) = 22 cm^{-2} has been suggested to be due to dust obscuration biases such that the highest column density systems are missing from QSO surveys (Vladilo & Peroux 2005). Apart from the obscuration bias that prevents observations of DLAs with log $N(\mathrm{H\,I}) > 22$ cm^{-2}, rapid formation of molecular H_2 at very high H I column densities could act as a barrier. Observations have shown that at high redshifts there are relatively fewer very high column density DLAs, and at log $N(\mathrm{H\,I}) \approx 21.5$ the distribution steepens to a slope of –3 (Péroux et al. 2003b), which implies that Eq. (1.4) does not diverge for very large $N(\mathrm{H\,I})$ values. The lack of high column density systems is likely a statistical fluctuation, because another study has indicated that half of the $z > 3.5$ DLAs have log $N(\mathrm{H\,I}) > 21.5$ cm^{-2} (Prochaska & Herbert-Fort 2004). Furthermore, new observation have indicated an evolution of the number density dN/dz where more DLAs are found per unit redshift at $z > 2$ compared to the no evolution scenario. If the density is mostly constant at lower redshifts as argued in Rao (2005), this implies an increase of the average column density at low redshifts relative to high redshifts.

The redshift evolution of $\Omega_{\rm DLA}$ is still debated. Derivations of $\Omega_{\rm DLA} \approx 2 \times 10^{-3}$ have indicated that the density in neutral gas at high redshifts is similar to that from the mass tied in stars in the local Universe (Lanzetta et al. 1995b; Storrie-Lombardi & Wolfe 2000; Ellison et al. 2001; Péroux et al. 2003b; Bell et al. 2003)[2] . Earlier studies showed a decline in the total density in DLAs with cosmic time which was seen as evidence that DLAs at $z \approx 3$ turned their gas into stars seen at present. However, a survey for DLAs at $z < 1.6$ gave evidence for an almost constant $\Omega_{\rm DLA}$ from $z = 4$ to $z = 0$ (Rao & Turnshek 2000; Churchill 2001; Prochaska & Herbert-Fort 2004). More recent results from a much larger sample of DLAs have presented evidence for a decreasing density from $z = 4$ to $z = 2$ (Prochaska et al., 2005, in prep.). This decrease in $\Omega_{\rm DLA}$ supports that a conversion of gas into stars is taking place, and now appears consistent with 21 cm observations which indicate that the density in neutral gas is smaller at $z = 0$. Nevertheless, the low redshift DLAs still indicate a density similar to that at $z = 2$, but the value is slightly smaller than estimated previously (Rao 2005).

By integrating inferred SFRs in DLA systems, Wolfe et al. (2003b) showed that there is an agreement between the amount of matter converted into stars in DLAs and the density of the stellar mass in the local Universe. Combining relatively small SFRs with the information of a slow chemical evolution in the DLA population, these findings suggest a continuous formation of DLA clouds with cosmic time. A larger low-redshift sample is needed to determine $\Omega_{\rm DLA}$ with smaller error bars, though. Detections of DLA systems at $z < 1.6$ can be improved dramatically by targeting strong Mg II absorption systems (Rao & Turnshek 2000), and the large sample from the Sloan Digital Sky Survey (SDSS) QSO spectra (Nestor et al. 2004) should be investigated with UV spectroscopy.

[2] Compared to the density of baryonic matter $\Omega_b \approx 0.03$ this implies that ∼10% of the baryonic matter resides in DLAs.

1.2 DLA metallicities

Through analyses of metal absorption lines associated with DLA systems, important information regarding the chemical evolution of galaxies can be gained. Most of the information about the metallicity evolution in galaxies with cosmic time is derived from DLA systems. Exceptions include gravitationally lensed galaxies experiencing large flux magnifications (e.g. Pettini et al. 2002a; Lemoine-Busserolle et al. 2003), and large samples of Lyman break galaxies (LBGs) which have 20% solar to solar metallicities (Pettini et al. 2001; Shapley et al. 2003, 2004). This section describes the current knowledge of DLA metallicities.

1.2.1 Chemical composition

Although the IGM is largely ionised with a neutral fraction between 10^{-3} and 10^{-6}, the higher column density systems are self-shielded from the UV background due to the large optical depth to ionising photons. Because UV photons do not penetrate DLA clouds, the heavy elements inside the cloud are largely present in singly ionised form and ionisation corrections are negligible for most DLAs (Prochaska et al. 2002; Dessauges-Zavadsky et al. 2004). High ionisation species such as C IV and Si IV are frequently observed, while many more low-ionisation transition are found, typically Fe II, Si II, C II, Mg II, etc. If high signal-to-noise spectra can be obtained (i.e. if the background QSO is bright), several other weak transitions can be detected. A pioneering study of metal absorption lines associated with DLAs indicated an average metallicity of –1.1 dex at $z \sim 2$ with a significant scatter (Pettini et al. 1994).

The metal composition, studied though abundance ratios, can give important information on the material located inside the neutral clouds. For a given redshift, a wide range of metallicities indicate different formation histories of DLAs. Of great importance are the relative abundance patterns of specific elements created through different mechanisms in supernova (SN) explosions. The α-elements O, Ne, Mg, Si, S, Ar, Ca and Ti are mainly produced by Type II SN, while Fe group elements (Cr, Mn, Co, Fe, Ni, and perhaps Zn) are produced over longer timescales by less massive stars responsible for Type Ia SNe.

In the Galaxy, metal poor stars with [Fe/H] < -1 have α-elements which are over-abundant compared to Fe, with a typical value of [α/Fe] = +0.4 and for [Fe/H] $\gtrsim -1$ [α/Fe] decreases with increasing metallicity[3] . This is due to the yields of different SN types; Type II SNe produce 1/3 of the total amount of Fe, while Type Ia SNe produce 2/3 assuming a Salpeter initial mass function. On the other hand, only Type II SNe produce α-elements. The time delay between the different SNe types gives rise to the observed abundance ratios. For a young star-forming galaxy many Type II SNe enrich the medium, while it takes about 1 Gyr for SN Type Ia to form (depending on the initial conditions, like masses of the two stars and their separations). Thus in young galaxies, Type Ia SNe have not yet contributed to the Fe production, such that stars formed early have an α-element overabundance.

Abundance ratios in DLA systems have been compared to this characteristic chemical evolution of the Milky Way stars (Pettini et al. 1999; Nissen et al. 2004). These comparisons indicated that the α-element overabundance did not occur in DLAs, which suggested that DLAs have a somewhat lower high-mass SFR than the Galaxy. This would allow the Fe production to 'catch up' with the production of α-elements. In comparison, investigations of stellar metallicities in dwarf galaxies in the local group have shown that the metal poor stars do not have the same α-enrichment as star in the Galaxy, perhaps hinting that DLAs reside in dwarf galaxies. A more uniform analysis of a larger DLA sample did on the contrary show evidence for α-element enrichment at low metallicities

[3] The metallicity of a system is given in relation to solar value: [M/H] = log (M/H) – log $(M/H)_{\odot}$.

(Prochaska & Wolfe 2002; Prochaska 2003). These studies also find that the relative abundance ratios in DLAs are uniform when considering dust depletion effects.

Other investigations of DLAs have lead to important conclusions for galaxy and stellar evolutions. The discovery of very low nitrogen abundances in some DLAs compared to other systems, indicates that the enrichment of N in young galaxies is not dominated by production in massive stars (Centurión et al. 2003), whereas N is believed to be produced in intermediate mass stars between 4 and 8 solar masses (Henry et al. 2000; Pettini et al. 2002b). Thus, the investigations of DLA systems can provide insight to the enrichment processes and the stellar evolution that has taken place.

In a specifically metal-rich system with a metallicity of 0.5 solar, transitions from more than 25 elements have been detected (Prochaska et al. 2003b). Such observations offer the opportunity to make detailed models for the evolution of the neutral cloud in terms of relative contributions from SNe. In this particular study, no special abundance patterns were revealed which could have suggested contributions from population III stars.

One should bear in mind that QSO spectroscopy provides one single line of sight probing a small part of a larger intervening galaxy. The derived star formation history could depend very strongly upon the exact location of the neutral cloud, whether it were located in the bulge of a proto-galaxy, or in the outskirts of a larger galaxy. Therefore it is crucial to study the relation between the DLAs and their host galaxies, i.e. find the impact parameters, morphological types, kinematics, and rotation curves whenever possible. We will return to this discussion in Sect. 1.4.

Dust effects

Metallicities are not derived straightforwardly because dust will affect the measurements. A method to determine the dust content in DLA systems is to use abundance ratios which are both affected and unaffected by dust. Fe is easily depleted on dust grains, while this is not the case for Zn. These two elements are believed to be produced in the same manner in Type II and Ia SNe, such that the measurements of the Zn column density can be used as a trace element of Fe. [Zn/Fe] measurements are mostly larger than 0, which indicate that DLAs do indeed contain dust (Pettini et al. 1999).

A very dusty DLA cloud would obscure the background QSO to such an extent that it would not be detected in flux-limited optical surveys. It has been suggested that the observations of DLA systems are biased towards small amounts of dust contained in the clouds and thus chemically less evolved galaxies (Steidel et al. 1994b; Pei & Fall 1995; Steidel et al. 1997). This conclusion is supported by the models in Fall & Pei (1993) and numerical simulations by Cen et al. (2003). Despite this, an analysis of the colours of QSOs selected from radio surveys has shown that QSOs with DLAs in their sight line do not appear redder than a control sample. The interpretation is that the dust obscuration could be a minor effect accounting for at most 50% missing QSOs (Ellison et al. 2001), which is supported by investigations of a larger sample (Ellison 2005). A large uniformly selected number of QSOs in the SDSS Data Release 2 revealed no significant reddening for the sample that contained DLAs (Murphy & Liske 2004).

Hence, the current consensus is that although dust has to be present in DLAs as evidenced by the abundance ratios, the actual amount may not be sufficient to bias DLA surveys significantly. Nevertheless, no DLAs are observed above the limit [Zn/H] + log $N(\mathrm{H\,I}) < 21$, which could suggest that observations are biased against the most metal rich, dusty systems (Boisse et al. 1998). Similar results were found by comparing the observed QSO magnitude distribution with a self-consistent model that included dust extinction properties (Vladilo & Peroux 2005). Their models indicate that $\sim 90\%$ of the DLAs with approximately solar metallicity are missing from surveys, Hence, it seems possible that some of the high $N(\mathrm{H\,I})$ systems are missing in QSO surveys, while the number of missed DLAs of all column densities may be much smaller. If metal rich DLAs are missing, such a

bias would have a major impact on the study of global metallicities traced by DLAs and the density, $\Omega_{\rm DLA}$, because these quantities are dominated by the highest column density DLAs.

Extinction in DLAs

Using the information of dust presence one can estimate the DLA reddening. Bohlin et al. (1978) report a relation between $N(\mathrm{H\,I})$ and the reddening, $E(B-V)$, which can be used to estimate the extinction in DLA systems for a given extinction curve. Assuming that the dust properties are similar to the Milky Way and $R_V = A_V/E(B-V) = 3.1$, the column densities in DLAs suggest an average extinction $A_V < 0.15$ (Savaglio & Fall 2004). Such a small extinction is also supported by a detailed DLA abundance analysis (Prochaska & Wolfe 2002). Though the real dust properties in DLAs and the related extinction curve are not well known, there have been claims of detection of a 2175 Å feature characteristic for a Milky Way dust type (Junkkarinen et al. 2004), so that the assumptions mentioned above could be valid.

1.2.2 Chemical evolution

Previously, it has been difficult to determine whether there is a significant redshift evolution of metals contained in DLA systems (Pettini et al. 1997, 1999). Only few individual systems were observed with high resolution spectroscopy, but by different authors using different techniques. To find a metallicity evolution is difficult due to the large metallicity scatter at any given redshift. Some elements are easily depleted onto dust grains, biasing the metallicities towards lower values and therefore analyses of elements that are not depleted are necessary. A possible presence of a chemical evolution with redshift in a larger sample of Zn measurements in DLAs was found by Kulkarni & Fall (2002), and an expansion of the sample with other elements confirmed the existence of a chemical evolution (Prochaska et al. 2003a). The trend is weak, amounting to only –0.25±0.07 dex per unit redshift. Such a small metallicity increase with redshift can be reproduced by numerical models predictions (Pei & Fall 1995; Pei et al. 1999), while other models predict systematically larger metallicities at all redshifts for cold gas (Somerville et al. 2001).

When the analysis of DLA galaxies is seen in relation to galaxy evolution it must be emphasised that most metallicity studies analyse redshifts $z > 1.7$, which only account for the first 30% of the age of the Universe. The remaining 70% is poorly studied because of the fewer DLAs known at lower redshifts. At $0.1 < z < 1.5$ an analysis of the [Cr/Zn] abundance ratio has suggested that the chemical composition of DLAs (including DLA candidates), and hence also the dust reddening, is similar to that in high redshift DLAs (Khare et al. 2004). They find evidence for only a weak chemical evolution from $z = 0.4$ to $z = 3.9$, and extending this study with new lower redshift DLA systems at $z < 0.5$ gave results consistent with previous investigations (Kulkarni et al. 2005). All these studies agree that the metallicity slope does not intercept solar metallicity at zero redshift, which is found by observations of local disc galaxies. Generally, the DLA studies find [M/H] ≈ –0.7 at $z = 0$. However, the abundances for low redshift galaxies also show a significant scatter. For example Schulte-Ladbeck et al. (2005) showed that the very low redshift DLA galaxy SBS 1543+593 has ∼30% solar abundances similar to field galaxies.

1.2.3 Absorption line profiles

Observations of asymmetric metal line profiles in DLA systems have been interpreted as DLAs residing in massive rotating discs (Wolfe et al. 1986; Turnshek et al. 1989; Lu et al. 1997). On the other hand, numerical simulations have shown that these profiles could be reproduced by in-falling clouds in a hierarchical formation scenario (Haehnelt et al. 1998, 2000). The latter interpretation has some support by observations of absorption line profiles which show evidence for sub-systems

in lines with velocity widths >200 km s^{-1} (Ledoux et al. 1998). Also Prochaska & Wolfe (1997) showed that this single discs scenario is not supported by observations of the DLA metallicities and abundance patterns. These agreements do not give a definite proof that the hierarchical model is appropriate to describe the evolution of all galaxies in the Universe. Other observations have shown that neither a hierarchical formation scenario nor a monolithic model can explain galaxy evolution. A third scenario is proposed to explain the observations of galaxy metallicity, kinematics and optical colours (Lilly et al. 2003). The observations are interpreted in a 'downsizing' picture, where star formation occurs in progressively larger structures with increasing redshifts.

1.3 Lyα photon properties

Because much of this thesis concerns Lyα photons from high redshifts systems, this section explains the production and transfer effects of these photons.

In the absence of contributions from active galactic nuclei (AGN), the production of Lyα photons is dominated by stars more massive than 10 $M_\odot$ whose life time is of the order of 10 Myr, implying that Lyα emission comes only from the most recent star-forming events. The radiation at $\lambda < 912$ Å ionises the surrounding material, and most recombinations to the H I ground state will eventually create a Lyα photon plus several photons with longer wavelengths. Gould & Weinberg (1996) estimate that ∼60% of the ionising photons absorbed by a large column density cloud are re-radiated as Lyα photons, even including the fraction absorbed by dust. The power law spectral shape of an AGN implies that the Lyα emission can be very strong, with equivalent widths (EW) >200 Å (Charlot & Fall 1993). In pure star-forming galaxies the expected Lyα EW is smaller.

In a neutral medium, Lyα photons are easily absorbed due to their large cross section. A radiative transition from the 2P to the 1S state releases this photon again allowing yet another absorption after the photon has traveled some distance given by the mean free path. This effect does not change the wavelength of the initial photon. In a neutral cloud this process continues until the Lyα photon can escape to the highly ionised surrounding IGM. Therefore, resonance scattering increases the escape path of the photons by a large factor. Compared to UV photons just redwards of Lyα, the Lyα photons have an escape path ∼1000 times larger.

This idealised scenario is valid in the absence of dust. In the case that dust is present, Lyα photons are absorbed easily by the dust grains and raise the dust temperature, and the Lyα photons will be converted into longer wavelength photons. Because of their resonant nature, Lyα photons will not easily escape a dusty cloud, and when the dust content is ∼10% of the Galactic value, Lyα photons will be effectively absorbed (Charlot & Fall 1993). Oppositely, Gould & Weinberg (1996) find that the dust absorption plays a minor role. Analyses of absorption lines indicate a dust-to-gas ratio in DLAs of ∼1/30 solar (Prochaska & Wolfe 2002; Wolfe et al. 2003b), which suggests that high redshift proto-galaxies may not be very dusty. Where dust is absent, Lyα photons will be scattered through the halo from which the galaxy is forming. In such a case, the extent of the Lyα emission could probe the size of the galaxy neutral gas halo.

Most theoretical models for the escape of Lyα photons deal with static media. If the medium that produces Lyα photons is offset in velocity from the absorbing medium, a substantial fraction of Lyα photons can escape; this has been observed for local starburst galaxies (Kunth et al. 1998). Other explanations for Lyα photon transfer effects involve Lyα photons escaping along a direction where less star-formation has occurred and where less dust is present, resulting in a complex Lyα morphology. However, this simple explanation of kinematics is not supported by the analysis of Lyman Break galaxy spectra which show that weaker Lyα lines have larger velocity offsets with respect to absorption lines (Shapley et al. 2003). This is interpreted as due to absorption of the emission lines by dust.

To mention a few examples of Lyα emitting high redshift objects, Bunker et al. (2000) observed Lyα emission offset by $1''$ from the continuum emission from a gravitationally lensed galaxy at $z = 4$. However, this large offset is due to the arc geometry of the galaxy, while in the un-lensed case the offset would be $0''.1$, i.e. similar to a Lyα emitting LBG. An intrinsically chaotic nebula surrounding two LBGs and a sub-mm source was interpreted as a proto-cluster environment (Bower et al. 2004). The Lyα morphology around the sub-mm source showed a depression indicating that Lyα photons were absorbed. In radio-galaxies, Lyα emission extending more than 100 kpc has been reported (Villar-Martin et al. 1996; Villar-Martín et al. 2003). These observations show that in some environments Lyα photons do escape, likely made possible by intrinsic kinematics that can alleviate resonance scattering.

1.4 Galaxies associated with DLAs

To summarise, DLAs have column densities typical for galaxy discs and metallicities that suggest enrichment from stellar processes in galaxies. Line profiles do not constrain the properties of the galaxies in which DLAs reside. DLAs need not arise in discs only. Extended envelopes of neutral gas are common for (gas rich) galaxies and column densities in the DLA regime are found at large covering factors. This section explores the observations that have related galaxies to DLAs.

1.4.1 Surveys for DLA galaxies

Many observations have been undertaken for the purpose of finding the galaxy counterparts to DLAs. The conventional way to confirm a DLA galaxy is to first obtain deep observations of the field surrounding the QSO from which candidates close to the line of sight are selected. Follow-up spectroscopy of these candidates is necessary to obtain their redshift, and if one candidate has a redshift which is sufficiently close to the DLA redshift, this candidate will be considered as the galaxy responsible for the DLA line in the QSO spectrum. Such a galaxy is therefore called a DLA galaxy. This method is relatively time-consuming as the candidate galaxies can be very faint ($\gtrsim$25 mag) making spectroscopic confirmations a non-trivial task (e.g. Steidel et al. 1995; Lanzetta et al. 1995a). In the near-IR, dust obscuration in the DLA is less significant, so observations at these wavelengths are more likely to result in the detection of obscured DLA galaxies. Aragon-Salamanca et al. (1996) used ground-based near-IR images of 10 QSOs, but managed to detect only 2 galaxies closer than $1''.3$ to the QSOs. These results suggest that DLA galaxies are fainter than L^* galaxies, where L^* is the luminosity of a characteristic galaxy in the Schechter luminosity function. If DLA galaxies would trace a normal field population, the number of nearby objects in a snapshot survey in Colbert & Malkan (2002) would have been 2 to 3 with a luminosity of L^*. Thus their non-detection indicates that DLA galaxies are fainter than L^* galaxies, i.e. consistent with the conclusion of Aragon-Salamanca et al. (1996). Deeper near-IR studies with the HST/NICMOS have resulted in detections of fainter galaxies at small impact parameters (Warren et al. 2001) in agreement with these results.

Another approach used by Turnshek et al. (2001) and Rao et al. (2003) is to use a photometric redshift technique to confirm DLA galaxies at $z < 1$. They showed that this technique successfully recovers DLA galaxy redshifts with an uncertainty of $\Delta z = 0.07$. At higher redshifts this technique has not yet been implemented.

Because confirmations of DLAs at $z < 1.6$ require space-based observations, only a few systems are known at present time. At $z < 1$, 21 systems are confirmed (Rao et al. 2003; Chen & Lanzetta 2003; Lacy et al. 2003), while at higher redshifts ($z > 1$) $\sim$150 systems are confirmed (Curran et al. 2002). Recently, the SDSS QSO spectra allowed identification of additional $\sim$500 DLAs (Prochaska et al. 2005, in prep.). While the numbers of known low redshift DLAs are small,

the number of spectroscopically confirmed DLA galaxies is 11, or slightly more than half (Chen & Lanzetta 2003, and references therein). On the other hand, only 6 DLA galaxies at $z \gtrsim 2$ have been confirmed (Møller & Warren 1993; Møller et al. 1998; Fynbo et al. 1999; Djorgovski et al. 1996). Three of these DLAs are intervening systems ($z_{\rm abs} < z_{\rm em}$), and the other ones lie close to the QSO redshifts ($z_{\rm abs} \approx z_{\rm em}$). Another two systems might have been found from the detection of emission lines within the DLA absorption trough (Leibundgut & Robertson 1999; Ellison et al. 2002).

Due to the small number of detections, very little is known about the galaxies themselves and many attempts have been made to increase the sample. One investigation using Fabry-Perot images failed to detect Lyα emission line objects to a 3σ limit of 3×10^{-17} erg s^{-1} Å^{-1} (Lowenthal et al. 1995), but their observations were affected by a relative large seeing. Another study using the same technique was applied to a sample of 8 very strong Mg II absorption systems (of which 3 were later found to be DLA systems) in order to find [O II] emission lines from galaxies at $0.4 < z_{\rm abs} < 1.1$ (Yanny et al. 1990). They successfully found candidates with fluxes larger than 10^{-17} erg cm^{-2} s^{-1} at impact parameters of 6 to 276 kpc in all cases. Hence such technique would seem applicable to detect Lyα at $z > 2$.

1.4.2 Metallicities of DLA galaxies

In a few cases where DLA galaxies have been confirmed, emission lines from the galaxy can be used to obtain an independent measurement of the abundance which can be compared to the metallicities derived from the DLA lines. This has only been attempted for low redshift objects to date. The line of sight towards SBS 1543+593 which has a DLA line at $z = 0.0096$ intercepts a dwarf galaxy at an impact parameter of zero. The galaxy has an abundance of 12+log(O/H) = 8.2±0.2 in agreement with the metallicity derived from the absorption lines (Schulte-Ladbeck et al. 2005). DLA (absorption) metallicities compared to the metallicities derived from strong emission lines from the DLA hosts at $z < 1$ have indicated the presence of radial metallicity gradients (Ellison et al. 2005; Chen et al. 2005). These gradients are comparable to those in local disc galaxies where abundances derived from H II regions suggest a decreasing metallicity with increasing radius (Zaritsky et al. 1994). Fig. 1.3 shows metallicities for DLA and sub-DLA systems derived from absorption lines in comparison with abundances of H II regions in local galaxies. This figure demonstrates the clear distinction between metallicities in local galaxies and those in high redshift DLA systems. As discussed in Chapter 2, that treats the object denoted G4, radial metallicity gradients could explain this offset.

This type of investigation is lacking for high redshift systems, because only recently have optical emission lines been reported for two high redshift DLAs (Weatherley et al. 2005). Two emission lines in the spectrum of Q1215+333 were interpreted as Hβ and [O II] from a DLA galaxy at $z \approx 2$, and were used to derive a solar oxygen abundance (Elston et al. 1991). Later this observation could not be confirmed and is now regarded as spurious (Aragon-Salamanca et al. 1996).

Møller et al. (2004) found in their survey for DLA galaxies from about 20 systems, that the detection of Lyα emission from DLA galaxies preferentially occurs for high metallicity DLAs. This in apparently in contradiction with the commonly accepted fact that dust efficiently quenches Lyα photons (Charlot & Fall 1993). However, indications of a similar trend for escape of Lyα photons in dusty surroundings are found in sub-mm bright galaxies (Chapman et al. 2004). It is believed that these galaxies possess such vigorous star formation and hence SN activity that it could account for wind-blown channels which provide an escape path of Lyα photons. In comparison, DLA galaxies have SFRs two orders of magnitude lower, as described in Sect. 1.4.6 so further studies are needed to reach an understanding.

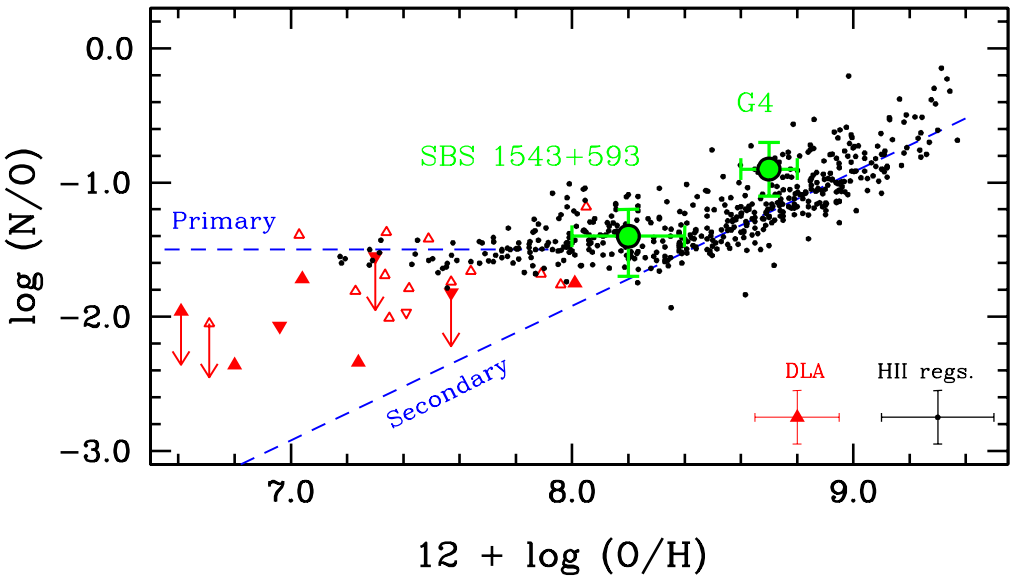

Fig. 1.3. Abundances of the galaxy responsible for the sub-DLA towards PHL 1226 (large filled circle named G4) and the DLA galaxy SBS 1543+593 compared to extragalactic H II regions (dots), DLA systems (triangles), and sub-DLA systems (inverted triangles). Typical errorbars are shown in the lower right corner. This figure, provided by Regina Schulte-Ladbeck, is an update of Fig. 10 in Schulte-Ladbeck et al. (2004), which uses data published in Pettini et al. (2002a). The dashed lines indicate the primary and secondary levels of N production in stars.

1.4.3 DLA cloud sizes

To avoid confusion, a clear distinction between the actual DLA cloud size and size of the galaxy it resides in must be made. To estimate the sizes of the neutral DLA clouds the density must be known. In a study of the C II* 1335 Å absorption line towards 30 QSOs, Wolfe et al. (2003a) find that some DLA clouds consist of cold gas ($T \approx 100$ K) with a typical density 10 cm^{-3}. Assuming a constant density the inferred linear size of a cloud is about 6 pc in diameter.

Another method to determine the sizes of DLA clouds uses QSO lenses separated by $< 1''$, such that transverse sizes smaller than 10 kpc can be probed. As an example, the DLA towards APM 08279+5255 has a projected size $> 200h^{-1}$ pc (Petitjean et al. 2000), while a lensed QSO with image separation of $0\farcs6$ suggests a DLA size larger than 5 kpc (Lopez et al. 2005). Because these sizes are 2–3 orders of magnitude larger than the size derived from the density, this indicates the presence of larger structures as would be expected for galaxy discs.

1.4.4 Morphologies of DLA galaxies

At low redshifts, DLA galaxies have been shown to have varied morphologies including low surface brightness galaxies, dwarves, and luminous L^* galaxies (Le Brun et al. 1997; Rao et al. 2003; Chen & Lanzetta 2003). This implies that DLAs do not arise in a specific Hubble type, which is supported by the large scatter of metallicities found. Arguments in favour of DLA galaxies being predominantly dwarf galaxies have been given based on their metallicities (Matteucci et al. 1997), but a direct imaging analysis of DLA galaxies at low redshifts indicated that there is no need to invoke a large population of dwarf galaxies (Chen et al. 2005).

A prediction of the radial sizes of the absorbing galaxies can be found when the galaxy luminosity function and number density distribution of DLAs is known. Local galaxies have been shown to follow the Holmberg relation

$$\frac{R}{R^*} = \left(\frac{L}{L^*}\right)^{\beta}, \tag{1.5}$$

where $\beta = 0.4$, and R describes the radial size. This relation states that brighter galaxies have larger sizes, and for DLA galaxies possibly larger neutral gas envelopes.

When combining this relation with the Schechter luminosity function, the number density distribution dN/dz, and a chosen cosmology one can derive the characteristic size of an L^* galaxy. Using these simple relations gives a typical absorber size of $R^* \sim 42$ kpc for a cosmology with $\Omega_m = 0.3$, $\Omega_\Lambda = 0.7$, and $H_0 = 70$ km s^{-1} Mpc^{-1} (See Appendix B.1 for further details). The main problems with this calculation lies in the uncertainty of the luminosity function which at $z > 2$ shows a steep faint end slope (Shapley et al. 2001), and may steepen with redshift (Sawicki & Thomson 2005), and whether the Holmberg relation holds for DLA galaxies. Unfortunately, the argument is reciprocal. To determine the size of the envelopes it is necessary to know the luminosity function, but to determine the luminosity function the absorbing galaxies need to be identified first.

For comparison with the theoretically expected absorber size, observations of DLA galaxy impact parameters can give a direct measurement of R^*. The projected angular sizes are necessarily lower limits due to projection effects. Having measured the impact parameter for 11 low redshift galaxies, Chen & Lanzetta (2003) derive scaling relations from Eq. (1.5) and find R^* = 24–30 kpc and $\beta = 0.26^{+0.24}_{-0.06}$. Using a K band analysis of the extension of strong Mg II absorption systems (which are typically in the LLS regime), Steidel (1995) and Steidel et al. (2002) suggest sizes of $\sim$50 kpc, and a slightly smaller $\beta = 0.15$. Both DLAs and LLS appear to have sizes that are slightly smaller than expected from the Holmberg relation with $\beta = 0.4$ implying that the galaxies may be sub-luminous.

Important clues on the structure of the halos where the Mg II absorbers could reside were given by an observed anti-correlation between $N(\mathrm{Mg\,II})$ and the impact parameter b (Churchill et al. 2000). Fig. 1.4 shows a schematic representation of the typical projected sizes for the different object classes in the adopted flat, lambda dominated cosmology. However, the simple model of a spherical halo being responsible for the Mg II absorption lines (and hence also LLS) suggested in Steidel et al. (1994a) is not supported by recent observations. Mg II clouds are now known to have a more patchy distribution and a covering factor less than 1 (Churchill et al. 2005). Because Mg II absorption strengths are correlated with $N(\mathrm{H\,I})$, the large Mg II galaxy sizes suggest that high column density clouds can be found at large impact parameters. Also lower column density lines in the Lyα forest and the distances to their parent galaxies have been shown to be anticorrelated (Chen et al. 1998, 2001). However, it still remains to be verified for galaxies responsible for DLAs.

1.4.5 Simulations of DLA galaxies

Because of the rarity of known DLA systems at $z < 1$ it is possible to turn to numerical simulations that predict observable properties such as column densities, luminosities, and impact parameters for DLA galaxies. Using semi-empirical simulations, Okoshi & Nagashima (2005) predict that typical DLA galaxies at $z < 1$ are low surface brightness galaxies with very small impact parameters (3 kpc) and have small SFRs (10^{-2} M$_\odot$ yr^{-1}). They state that this is in agreement with observations, but as mentioned above, observations of DLA galaxies at $z < 0.6$ showed that they are not necessarily faint dwarf galaxies and the impact parameters range from 0 to 34 kpc (Chen et al. 2005). Simulations of DLA galaxies at higher redshifts suggest similar impact parameters of $b \sim 3$ kpc

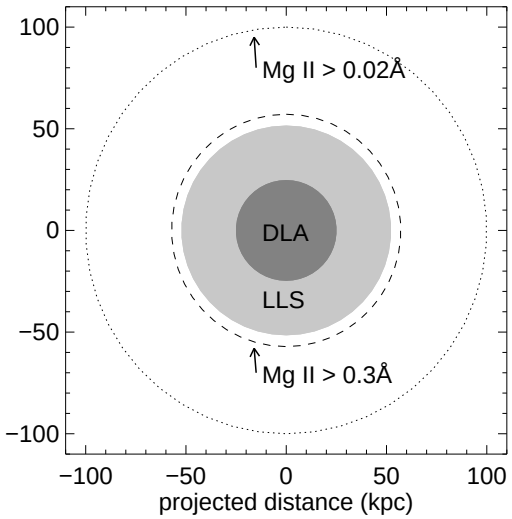

Fig. 1.4. Projected sizes of different object classes. The figure is adapted from Churchill et al. (2005) to the flat, lambda-dominated cosmology used here.

(Haehnelt et al. 2000; Hou et al. 2005). Hou et al. (2005) argue that their models assume single discs, what may conflict with observations of DLA impact parameters in a hierarchical merging scenario where multiple components are present. Thus, the results of the numerical simulations are still uncertain and are somehow in conflict with observations.

1.4.6 DLA galaxy star formation rates

Based on metallicity studies arguments for low SFRs in DLA galaxies have been claimed (e.g Pettini et al. 2002b). Investigations using long-slit observations to detect Hα emission from DLA galaxies only resulted in an upper limit of 20 $M_\odot$ yr^{-1} for the SFR in DLA galaxies (Bunker et al. 1995, 1999). A different conclusion was reached by analysing the absorption lines from the fine-structure transition C II* λ1335 which can be used as a proxy for the heating by star formation (Wolfe et al. 2003a,b). The idea behind this method is to balance the cooling rate measured from the absorption lines to the heating rate which, if created by the radiation from massive stars, should be proportional to the SFR. These studies found that the SFR could be similar to that in the Galaxy (Wolfe et al. 2004). However, the SFRs in individual DLA galaxies need to be confirmed, but this requires that they be detected in emission.

As mentioned, DLA systems dominate the contribution to the total neutral gas mass and provide the fuel for star formation throughout the Universe. In reality, it is molecular hydrogen that provides the fuel, but H_2 is distributed very patchily and are embedded in clouds of high $N(\mathrm{H\,I})$. If one extends the Schmidt-Kennicutt law, which states that the SFR is proportional to the gas surface density in a system, then it would naturally follow that DLA galaxies should dominate the formation of stars. Chapter 6 returns to this discussion of the SFR density traced by DLAs and their host galaxies.

1.5 Relation to high redshift galaxies

This section gives more details of observations of other high redshift galaxies, selected through different techniques and their relation to DLA galaxies. The purpose is to alleviate the difficulties

to identify the DLA galaxies by linking them to other types of objects.

1.5.1 Lyman break galaxies

The question of whether or not DLAs and LBGs sample the same population of galaxies has been a subject of much debate. Møller et al. (2002b) showed that the sizes, morphologies, colours, and velocities derived for 3 DLA galaxies are consistent with that of LBGs, but on average DLA galaxies are fainter. [O III] fluxes, velocity dispersions, and velocity offset from the Lyα lines for two DLA galaxies indicated similar results (Weatherley et al. 2005). Because DLA galaxies are selected on the basis of absorption properties rather than from their emission as LBGs, it is expected that their luminosities are on average smaller. In a study that compared the luminosity distribution of LBGs in the Hubble Deep Fields with the column density distribution in DLAs, Lanzetta et al. (2002) suggested that the similarity in their respective distributions could be explained if DLAs would arise in the low luminosity regions in LBGs.

An unanswered question is what fraction of DLA galaxies have Lyα emission. No high redshift DLA galaxy has been confirmed without spectroscopic observation of the Lyα emission line. We address this question in Chapter 5, where we find Lyα emission line candidates in $\sim$40% of the cases with a detection limit of 4×10^{-17} erg cm^{-2} s^{-1}. In comparison, the LBGs have an average flux of 7×10^{-17} erg cm^{-2} s^{-1} with strong Lyα emission from 25% of these, while 50% have Lyα in absorption (Shapley et al. 2003; Cooke et al. 2005). This indication of Lyα emission being absent in half of the sample is likely due to extinction (Steidel et al. 1996, 1999). Furthermore, in a star-forming galaxy an EW of 200 Å is expected, but smaller values ranging from 5–30 Å are observed for LBGs (Steidel et al. 1996), while DLA galaxies have slightly larger EWs of 60–80 Å (Warren & Møller 1996; Møller et al. 2002b).

Clustering properties

In order to discriminate between the two models for proto-galaxies, i.e. large discs vs. merging hierarchical clumps, it is necessary to estimate DLA galaxy masses. Through observations of their rotation curves the masses of DLA galaxies can be estimated, but this can only be done for a very limited number of systems at lower redshifts. Chen & Lanzetta (2003) have estimated masses of $> 10^{11}$ M$_\odot$ for a few $z < 1$ DLA galaxies based on their rotation curves. However, indirect methods to estimate masses of DLA systems and their environments exist. If DLA systems are formed in massive halos it is expected that a clustering of galaxies is present at their location. Then DLAs could be used as tracers of massive galaxies, whereas clustering would be weak in the case that DLA galaxies were smaller sub-units of galaxies yet to be formed.

LBGs are definitely such tracers of massive halos. They exhibit strong clustering properties showed by investigations of the two-point correlation functions (Adelberger et al. 2003). A similar investigation of the cross-correlation function of DLA systems would require a large number of DLAs detected in a small field. Instead, the LBG-DLA cross-correlation function can be studied. If DLAs form in over-dense regions, they would have a tendency to cluster around LBGs. Gawiser et al. (2001) studied this effect in one DLA field and found no evidence for clustering, which was supported by a study of four fields that indicated a lack of galaxies within a comoving radius of $5.7h^{-1}$ Mpc (Adelberger et al. 2003). Contrary to this, Bouché & Lowenthal (2004) used LBGs as tracers of large scale structure around the field of 3 DLAs using a two-point correlation function analysis which indicated that DLAs do indeed cluster around LBGs, with a correlation length of $(5\pm4.5)h^{-1}$ Mpc. This apparent contradiction in between observations could be due to small number statistics or perhaps cosmic variance and a larger study should be able to resolve this issue. Further indications of the DLA galaxy masses was given by the cross-correlation studies between

DLAs and galaxies in numerical simulations which indicated that the masses of DLA halos are smaller than for LBGs by a factor of $\gtrsim 5$ (Bouche et al. 2005).

It can also be argued that DLAs should not be present close to LBGs based on the fact that the ionising radiation from the massive galaxies would prevent the formation of DLA clouds (Steidel et al. 2001). This interpretation is supported by numerical simulations which show that DLAs are not found in the densest clusters because of the hostile environment (Cen et al. 2003).

1.5.2 Gamma-Ray burst selected DLA systems

Besides DLAs detected in QSO spectra, also spectra of Gamma-ray bursts (GRBs) afterglows have revealed DLA systems. The presence of a $z \approx 2$ DLA system in a GRB afterglow was noted by Jensen et al. (2001), while later more detailed studies of metallicities have been performed for other afterglows (Møller et al. 2002a; Vreeswijk et al. 2003; Savaglio et al. 2003; Hjorth et al. 2003a; Salamanca et al. 2002; Vreeswijk et al. 2004; Jakobsson et al. 2004). DLA systems which are selected on the basis of GRB afterglow observations are called GRB-DLAs, while the conventional DLAs in QSO spectra are called QSO-DLAs. There is a very clear intrinsic difference between QSO-DLAs and GRB-DLAs. While the QSO-DLAs are simply a chance projection of a neutral cloud in the line of sight to the QSO, GRBs occur very close to luminous regions in the host galaxies (Bloom et al. 2002), which we here assume to probe the galaxy disc. Combined with the knowledge that long-duration GRBs are related to Type Ic SNe (Hjorth et al. 2003b), i.e. from massive stars that do not move far away from their birth sites, GRB-DLAs will trace the disc metallicity at a very small impact parameter. The fact that the column densities in both metals and neutral hydrogen are larger on the average for the GRB-DLAs than for the QSO-DLAs suggests a different environment. Because the GRBs are located in galaxy discs, their sight lines only probe half of the column density in the discs on the average, which makes the discrepancy even larger.

Being associated with supernovae, GRBs are found in star-forming regions in typical starburst galaxies (Christensen et al. 2004). The large SFRs created in young starbursts can quickly enrich the surrounding medium and give rise to large metal column densities. Abundance patterns suggest that metals are on average more depleted in GRB-DLAs than in QSO-DLAs (Savaglio & Fall 2004). Compared to this, DLA metallicities suggest that some star formation has taken place, but not enough to obtain solar metallicity levels as found for the LBGs. This discrepancy could indicate that the largest column densities found in starburst galaxies are lacking from the DLA surveys. Hence QSO-DLAs could trace different regions of the host galaxies than GRB-DLAs. If the sight line towards the QSO passes through the outskirts of a large galaxy, metallicity estimates based solely on that region may not be representative for the whole galaxy.

1.6 Goals and outline of this work

This thesis explores the emission lines from DLA galaxies. At high redshift protogalaxies had little time to evolve, i.e. the cosmic time-span only corresponds to a small fraction of the age of the Universe. In order to investigate the evolution one needs to study a larger cosmic time interval, and therefore, it is interesting to compare the high redshift observations with those at redshifts less than one.

We use integral field spectroscopy targeted towards QSOs with known intervening DLAs. We will focus on observations of DLAs, but sub-DLAs in the same QSO spectra are included as well. Additionally, the three-dimensional observations provided by the integral field data also allow an investigation of the QSO surroundings with the same data set used in the DLA studies.

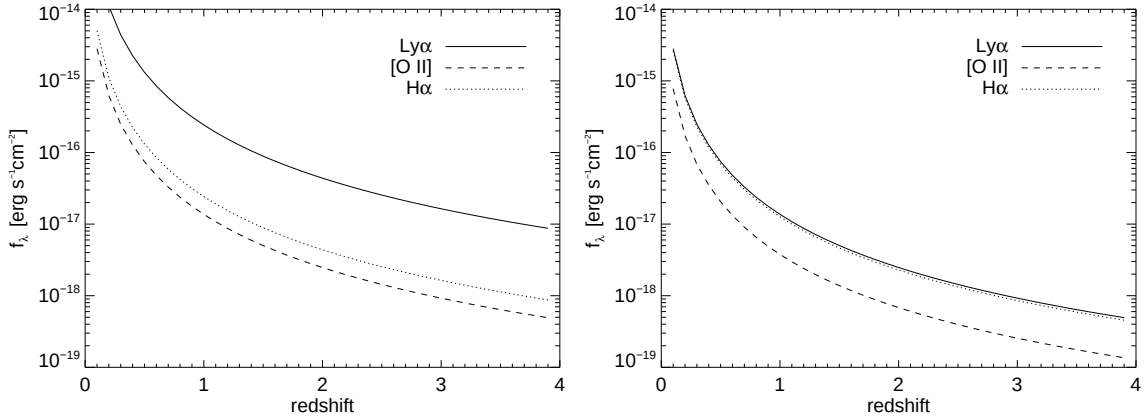

Fig. 1.5. Expected line fluxes for an object with a SFR = 1 $M_\odot yr^{-1}$ as a function of redshift. The left panel includes no extinction and the right panel includes an extinction of $A_V = 0.15$ assuming an extinction curve similar to the Large Magellanic cloud (see Savaglio & Fall 2004).

1.6.1 Emission line survey

Our survey for DLA galaxies and other absorbers is divided in two parts: One for the high redshift systems at $z > 2$ and one at $z < 1$. A more practical line of reasoning is which emission lines are most appropriately searched for. For pure star forming regions (i.e. H II regions), Lyα is expected to be 10 times brighter than Hα emission and only weakly depending on the temperature. However, any dust present in the DLA galaxy can effectively quench the Lyα photons present due to the longer escape path. Thus, Lyα may not be the brightest emission line in the spectrum. At $z > 1.7$, Lyα is redwards of the atmospheric cut-off and can be observed with ground-based telescopes, while optical emission lines will lie in the near-IR. Hα is expected to be bright, but more importantly, extinction usually does not play a major role. Another bright line present in H II regions is the forbidden transition [O II] λ3727, which in the absence of extinction and for solar metallicities is about 3 times fainter than Hα for a given SFR.

Fig. 1.5 illustrates the expected line flux from an object with a SFR = 1 $M_\odot$ yr^{-1} as a function of redshift in a flat cosmology with $H_0 = 70$ km s^{-1} Mpc^{-1}, $\Omega_m = 0.3$, and $\Omega_\Lambda = 0.7$. In the left panel, predicted line fluxes from Lyα, [O II], and Hα are indicated assuming zero extinction, while in the right hand panel, the same line fluxes are shown but now with an intrinsic extinction of $A_V = 0.15$. The Lyα emission line is now fainter than the [O II] line, but we have ignored resonance scattering, which implies that the observed Lyα emission line should be even fainter. When $A_V = 1$, Lyα becomes fainter than the other two lines and is difficult to observe even at $z > 2$ with the current largest telescopes. Considering these indications, a search for Lyα at high redshifts becomes difficult if dust is present. Similarly, a search for [O II] will only be sensitive to objects which have large SFRs, such as galaxies which have experienced a recent burst of star formation. However, also the [O II] line is extincted where dust is present. Basically, not much is currently known about the expected line fluxes from DLA galaxies, so our purpose is to probe for as faint emission lines as possible to detect with an integral field spectrograph.

1.6.2 Structure of this thesis

Chapters 2–8 can be read separately as they describe independent investigations. The main part of this thesis concerns the detection of faint galaxies which cause absorption lines in background QSO spectra. Starting from the lowest redshifts and approaching the QSOs, Chapter 2 describes

the emission line abundance and kinematics of a low redshift absorber towards PHL 1226. It is suggested that metallicity gradients in DLA galaxies could potentially bias metallicities derived from absorption lines. Chapter 3 describes the use of integral field spectroscopy (IFS) to search for emission lines from DLA galaxies at $z < 1$. It is demonstrated that IFS is capable of detecting emission lines from a few previously known absorbing galaxies, and a few more candidate detections are presented as well. Moving to higher redshifts, the detection of Lyα emission from the DLA galaxy towards Q2233+131 is described in Chapter 4. Extended emission is reported here, but higher spectral resolution data obtained later do not confirm this. Building on the knowledge to detect faint emission lines, Chapter 5 presents a small survey for Lyα emission from DLA galaxies at $z > 2$. It is shown that IFS is able to detect candidate emission line objects at the expected redshifts for a large fraction of the DLAs. Based on these candidate emission lines combined with information on DLA galaxies in the literature, Chapter 6 investigates the nature of DLAs and their parent galaxies.

Moving progressively closer to the quasar redshifts themselves, Chapters 7 and 8 describe the extended emission line nebulae surrounding QSOs. These investigations are relevant for the study of the QSO environments, their host galaxies, and the differences between radio-loud and radio-quiet quasars. We find that extended emission line nebulae appear to be common around both radio-loud and quiet quasars, although their properties are somewhat different. We discuss these finding in terms of differences in the material nearby the quasar host galaxies, and interactions with radio jets.

Chapter 9 presents the conclusions and future perspectives for the use of integral field spectroscopy for the questions that are left unanswered in this thesis.

References

Adelberger, K. L., Steidel, C. C., Shapley, A. E., & Pettini, M. 2003, ApJ, 584, 45
Aragon-Salamanca, A., Ellis, R. S., & O'Brien, K. S. 1996, MNRAS, 281, 945
Bell, E. F., McIntosh, D. H., Katz, N., & Weinberg, M. D. 2003, ApJS, 149, 289
Binney, J. & Merrifield, M. 1998, Galactic astronomy (Princeton University Press, QB857 .B522 1998)
Bloom, J. S., Kulkarni, S. R., & Djorgovski, S. G. 2002, AJ, 123, 1111
Bohlin, R. C., Savage, B. D., & Drake, J. F. 1978, ApJ, 224, 132
Boisse, P., Le Brun, V., Bergeron, J., & Deharveng, J. 1998, A&A, 333, 841
Bouché, N. & Lowenthal, J. D. 2004, ApJ, 609, 513
Bouche, N., Gardner, J. P., Weinberg, D. H., et al. 2005, ApJ in press (astro-ph/0504172)
Bower, R. G., Morris, S. L., Bacon, R., et al. 2004, MNRAS, 351, 63
Bunker, A. J., Moustakas, L. A., & Davis, M. 2000, ApJ, 531, 95
Bunker, A. J., Warren, S. J., Clements, D. L., Williger, G. M., & Hewett, P. C. 1999, MNRAS, 309, 875
Bunker, A. J., Warren, S. J., Hewett, P. C., & Clements, D. L. 1995, MNRAS, 273, 513
Cen, R., Ostriker, J. P., Prochaska, J. X., & Wolfe, A. M. 2003, ApJ, 598, 741
Centurión, M., Molaro, P., Vladilo, G., et al. 2003, A&A, 403, 55
Chapman, S. C., Smail, I., Windhorst, R., Muxlow, T., & Ivison, R. J. 2004, ApJ, 611, 732
Charlot, S. & Fall, S. M. 1993, ApJ, 415, 580
Charlton, J., Churchill, C., & Murdin, P. 2000, Encyclopedia of Astronomy and Astrophysics
Chen, H., Lanzetta, K. M., Webb, J. K., & Barcons, X. 1998, ApJ, 498, 77
—. 2001, ApJ, 559, 654
Chen, H.-W., Kennicutt, R. C., & Rauch, M. 2005, ApJ, 620, 703
Chen, H.-W. & Lanzetta, K. M. 2003, ApJ, 597, 706

Christensen, L., Hjorth, J., & Gorosabel, J. 2004, A&A, 425, 913
Churchill, C. W. 2001, ApJ, 560, 92
Churchill, C. W., Kacprzak, G. G., & Steidel, C. C. 2005, In Probing Galaxies through Quasar Absorption Lines (astro-ph/0504392)
Churchill, C. W., Mellon, R. R., Charlton, J. C., et al. 2000, ApJ, 543, 577
Colbert, J. W. & Malkan, M. A. 2002, ApJ, 566, 51
Cooke, J., Wolfe, A. M., Prochaska, J. X., & Gawiser, E. 2005, ApJ, 621, 596
Curran, S. J., Webb, J. K., Murphy, M. T., et al. 2002, Publications of the Astronomical Society of Australia, 19, 455
Dessauges-Zavadsky, M., Calura, F., Prochaska, J. X., D'Odorico, S., & Matteucci, F. 2004, A&A, 416, 79
Dessauges-Zavadsky, M., Péroux, C., Kim, T.-S., D'Odorico, S., & McMahon, R. G. 2003, MNRAS, 345, 447
Djorgovski, S. G., Pahre, M. A., Bechtold, J., & Elston, R. 1996, Nature, 382, 234
Ellison, S. L. 2005, In Probing Galaxies through Quasar Absorption Lines (astro-ph/0505111)
Ellison, S. L., Kewley, L. J., & Mallén-Ornelas, G. 2005, MNRAS, 357, 354
Ellison, S. L., Lewis, G. F., Pettini, M., Chaffee, F. H., & Irwin, M. J. 1999, ApJ, 520, 456
Ellison, S. L., Yan, L., Hook, I. M., et al. 2001, A&A, 379, 393
—. 2002, A&A, 383, 91
Elston, R., Bechtold, J., Lowenthal, J., & Rieke, M. 1991, ApJL, 373, L39
Fall, S. M. & Pei, Y. C. 1993, ApJ, 402, 479
Fynbo, J. U., Møller, P., & Warren, S. J. 1999, MNRAS, 305, 849
Gawiser, E., Wolfe, A. M., Prochaska, J. X., et al. 2001, ApJ, 562, 628
Gould, A. & Weinberg, D. H. 1996, ApJ, 468, 462
Haehnelt, M. G., Steinmetz, M., & Rauch, M. 1998, ApJ, 495, 647
—. 2000, ApJ, 534, 594
Henry, R. B. C., Edmunds, M. G., & Köppen, J. 2000, ApJ, 541, 660
Hjorth, J., Møller, P., Gorosabel, J., et al. 2003a, ApJ, 597, 699
Hjorth, J., Sollerman, J., Møller, P., et al. 2003b, Nature, 423, 847
Hou, J. L., Shu, C. G., Shen, S. Y., et al. 2005, ApJ, 624, 561
Jakobsson, P., Hjorth, J., Fynbo, J. U., et al. 2004, A&A, 427, 785
Jensen, B. L., Fynbo, J. U., Gorosabel, J., et al. 2001, A&A, 370, 909
Junkkarinen, V. T., Cohen, R. D., Beaver, E. A., et al. 2004, ApJ, 614, 658
Khare, P., Kulkarni, V. P., Lauroesch, J. T., et al. 2004, ApJ, 616, 86
Kulkarni, V. P. & Fall, S. M. 2002, ApJ, 580, 732
Kulkarni, V. P., Fall, S. M., Lauroesch, J., et al. 2005, ApJ, 618, 68
Kunth, D., Mas-Hesse, J. M., Terlevich, E., et al. 1998, A&A, 334, 11
Lacy, M., Becker, R. H., Storrie-Lombardi, L. J., et al. 2003, AJ, 126, 2230
Lanzetta, K. M., Bowen, D. V., Tytler, D., & Webb, J. K. 1995a, ApJ, 442, 538
Lanzetta, K. M., McMahon, R. G., Wolfe, A. M., et al. 1991, ApJS, 77, 1
Lanzetta, K. M., Wolfe, A. M., & Turnshek, D. A. 1995b, ApJ, 440, 435
Lanzetta, K. M., Yahata, N., Pascarelle, S., Chen, H., & Fernández-Soto, A. 2002, ApJ, 570, 492
Le Brun, V., Bergeron, J., Boisse, P., & Deharveng, J. M. 1997, A&A, 321, 733
Ledoux, C., Petitjean, P., Bergeron, J., Wampler, E. J., & Srianand, R. 1998, A&A, 337, 51
Leibundgut, B. & Robertson, J. G. 1999, MNRAS, 303, 711
Lemoine-Busserolle, M., Contini, T., Pelló, R., et al. 2003, A&A, 397, 839
Lilly, S. J., Carollo, C. M., & Stockton, A. N. 2003, ApJ, 597, 730
Lopez, S., Reimers, D., Gregg, M. D., et al. 2005, ApJ, 626, 767
Lowenthal, J. D., Hogan, C. J., Green, R. F., et al. 1995, ApJ, 451, 484

Lu, L., Sargent, W. L. W., & Barlow, T. A. 1997, ApJ, 484, 131
Matteucci, F., Molaro, P., & Vladilo, G. 1997, A&A, 321, 45
Møller, P., Fynbo, J. P., & Fall, S. M. 2004, A&A, 422, L33
Møller, P., Fynbo, J. P. U., Hjorth, J., et al. 2002a, A&A, 396, L21
Møller, P. & Warren, S. J. 1993, A&A, 270, 43
Møller, P., Warren, S. J., Fall, S. M., Fynbo, J. U., & Jakobsen, P. 2002b, ApJ, 574, 51
Møller, P., Warren, S. J., & Fynbo, J. U. 1998, A&A, 330, 19
Murphy, M. T. & Liske, J. 2004, MNRAS, 354, L31
Nestor, D. B., Turnshek, D. A., & Rao, S. M. 2004, ApJ accepted (astro-ph/0410493)
Nissen, P. E., Chen, Y. Q., Asplund, M., & Pettini, M. 2004, A&A, 415, 993
Okoshi, K. & Nagashima, M. 2005, ApJ, 623, 99
Péroux, C., Dessauges-Zavadsky, M., D'Odorico, S., Kim, T., & McMahon, R. G. 2003a, MNRAS, 345, 480
Péroux, C., McMahon, R. G., Storrie-Lombardi, L. J., & Irwin, M. J. 2003b, MNRAS, 346, 1103
Pei, Y. C. & Fall, S. M. 1995, ApJ, 454, 69
Pei, Y. C., Fall, S. M., & Hauser, M. G. 1999, ApJ, 522, 604
Petitjean, P., Aracil, B., Srianand, R., & Ibata, R. 2000, A&A, 359, 457
Petitjean, P., Webb, J. K., Rauch, M., Carswell, R. F., & Lanzetta, K. 1993, MNRAS, 262, 499
Pettini, M., Ellison, S. L., Bergeron, J., & Petitjean, P. 2002a, A&A, 391, 21
Pettini, M., Ellison, S. L., Steidel, C. C., & Bowen, D. V. 1999, ApJ, 510, 576
Pettini, M., Rix, S. A., Steidel, C. C., et al. 2002b, ApJ, 569, 742
Pettini, M., Shapley, A. E., Steidel, C. C., et al. 2001, ApJ, 554, 981
Pettini, M., Smith, L. J., Hunstead, R. W., & King, D. L. 1994, ApJ, 426, 79
Pettini, M., Smith, L. J., King, D. L., & Hunstead, R. W. 1997, ApJ, 486, 665
Prochaska, J. X. 2003, ApJ, 582, 49
Prochaska, J. X., Gawiser, E., Wolfe, A. M., Castro, S., & Djorgovski, S. G. 2003a, ApJL, 595, L9
Prochaska, J. X. & Herbert-Fort, S. 2004, PASP, 116, 622
Prochaska, J. X., Howk, J. C., O'Meara, J. M., et al. 2002, ApJ, 571, 693
Prochaska, J. X., Howk, J. C., & Wolfe, A. M. 2003b, Nature, 423, 57
Prochaska, J. X. & Wolfe, A. M. 1997, ApJ, 487, 73
—. 2002, ApJ, 566, 68
Rao, S. M. 2005, in Probing Galaxies through Quasar Absorption Lines, ed. P. R. Williams, C. Shu, & B. Ménard, IAU Colloquium 199
Rao, S. M., Nestor, D. B., Turnshek, D. A., et al. 2003, ApJ, 595, 94
Rao, S. M. & Turnshek, D. A. 2000, ApJS, 130, 1
Salamanca, I., Vreeswijk, P. M., Kaper, L., et al. 2002, in Lighthouses of the Universe: The Most Luminous Celestial Objects and Their Use for Cosmology Proceedings of the MPA/ESO/, p. 197, 197
Savaglio, S. & Fall, S. M. 2004, ApJ, 614, 293
Savaglio, S., Fall, S. M., & Fiore, F. 2003, ApJ, 585, 638
Sawicki, M. & Thomson, D. 2005, Apj, in press.
Schulte-Ladbeck, R. E., König, B., Miller, C. J., et al. 2005, ApJ, 625, L75
Schulte-Ladbeck, R. E., Rao, S. M., Drozdovsky, I. O., et al. 2004, ApJ, 600, 613
Shapley, A. E., Erb, D. K., Pettini, M., Steidel, C. C., & Adelberger, K. L. 2004, ApJ, 612, 108
Shapley, A. E., Steidel, C. C., Adelberger, K. L., et al. 2001, ApJ, 562, 95
Shapley, A. E., Steidel, C. C., Pettini, M., & Adelberger, K. L. 2003, ApJ, 588, 65
Somerville, R. S., Primack, J. R., & Faber, S. M. 2001, MNRAS, 320, 504
Steidel, C. C. 1995, in QSO Absorption Lines, ESO Astrophysics Symposia, ed. G. Meylan (Springer-Verlag Berlin Heidelberg New York.), 139

Steidel, C. C., Adelberger, K. L., Giavalisco, M., Dickinson, M., & Pettini, M. 1999, ApJ, 519, 1
Steidel, C. C., Dickinson, M., Meyer, D. M., Adelberger, K. L., & Sembach, K. R. 1997, ApJ, 480, 568
Steidel, C. C., Dickinson, M., & Persson, S. E. 1994a, ApJL, 437, L75
Steidel, C. C., Giavalisco, M., Pettini, M., Dickinson, M., & Adelberger, K. L. 1996, ApJL, 462, L17
Steidel, C. C., Kollmeier, J. A., Shapley, A. E., et al. 2002, ApJ, 570, 526
Steidel, C. C., Pettini, M., & Adelberger, K. L. 2001, ApJ, 546, 665
Steidel, C. C., Pettini, M., Dickinson, M., & Persson, S. E. 1994b, AJ, 108, 2046
Steidel, C. C., Pettini, M., & Hamilton, D. 1995, AJ, 110, 2519
Storrie-Lombardi, L. J. & Wolfe, A. M. 2000, ApJ, 543, 552
Turnshek, D. A., Rao, S. M., Nestor, D., et al. 2001, ApJ, 553, 288
Turnshek, D. A., Wolfe, A. M., Lanzetta, K. M., et al. 1989, ApJ, 344, 567
Tytler, D. 1987, ApJ, 321, 49
Villar-Martin, M., Binette, L., & Fosbury, R. A. E. 1996, A&A, 312, 751
Villar-Martín, M., Vernet, J., di Serego Alighieri, S., et al. 2003, MNRAS, 346, 273
Vladilo, G. & Peroux, C. 2005, A&A, submitted (astro-ph/0502137)
Vreeswijk, P. M., Ellison, S. L., Ledoux, C., et al. 2004, A&A, 419, 927
Vreeswijk, P. M., Møller, P., & Fynbo, J. U. 2003, A&A, 409, L5
Warren, S. J. & Møller, P. 1996, A&A, 311, 25
Warren, S. J., Møller, P., Fall, S. M., & Jakobsen, P. 2001, MNRAS, 326, 759
Weatherley, S. J., Warren, S. J., Møller, P., et al. 2005, MNRAS, 358, 985
Wolfe, A. M., Gawiser, E., & Prochaska, J. X. 2003a, ApJ, 593, 235
Wolfe, A. M., Howk, J. C., Gawiser, E., Prochaska, J. X., & Lopez, S. 2004, ApJ, 615, 625
Wolfe, A. M., Prochaska, J. X., & Gawiser, E. 2003b, ApJ, 593, 215
Wolfe, A. M., Turnshek, D. A., Smith, H. E., & Cohen, R. D. 1986, ApJS, 61, 249
Yanny, B., York, D. G., & Williams, T. B. 1990, ApJ, 351, 377
Zaritsky, D., Kennicutt, R. C., & Huchra, J. P. 1994, ApJ, 420, 87

CHAPTER 2

Abundances and kinematics of a candidate sub-damped Lymanα galaxy toward PHL 1226

L. CHRISTENSEN[1], R. E. SCHULTE-LADBECK[2], S. F. SÁNCHEZ[1], K. JAHNKE[1], T. BECKER[1], A. KELZ[1], M. M. ROTH[1], L. WISOTZKI[1,3]

Astrophysikalisches Institut Potsdam, An der Sternwarte 16, 14482 Potsdam, Germany
Department of Physics & Astronomy, University of Pittsburgh, 3941 O'Hara Street, Pittsburgh, PA, USA
Institut für Physik, Universität Potsdam, Am Neuen Palais 10, 14469 Potsdam, Germany

Abstract

The spectrum of the quasar PHL 1226 is known to have a strong Mg II and sub-damped Lymanα (sub-DLA) absorption line system with $N(\mathrm{H\,I}) = (5 \pm 2) \times 10^{19}$ cm^{-2} at $z = 0.1602$. Using integral field spectra from the Potsdam Multi Aperture Spectrophotometer (PMAS) we investigate a galaxy at an impact parameter of $6\farcs4$ which is most probably responsible for the absorption lines. A fainter galaxy at a similar redshift and a slightly larger distance from the QSO is known to exist, but we assume that the absorption is caused by the more nearby galaxy. From optical Balmer lines we estimate an intrinsic reddening consistent with 0, and a moderate star formation rate of 0.5 M$_\odot$yr^{-1} is inferred from the Hα luminosity. Using nebular emission line ratios we find a solar oxygen abundance $12 + \log(\mathrm{O/H}) = 8.7 \pm 0.1$ and a solar nitrogen to oxygen abundance ratio $\log(\mathrm{N/O}) = -1.0 \pm 0.2$. This abundance is larger than those of all known sub-DLA systems derived from analyses of metal absorption lines in quasar spectra. On the other hand, the properties are compatible with the most metal rich galaxies responsible for strong Mg II absorption systems. These two categories can be reconciled if we assume an abundance gradient similar to local galaxies. Under that assumption we predict abundances $12 + \log(\mathrm{O/H}) = 7.1$ and $\log(\mathrm{N/O}) = -1.9$ for the sub-DLA cloud, which is similar to high redshift DLA and sub-DLA systems. We find evidence for a rotational velocity of $\sim$200 km s^{-1} over a length of $\sim$7 kpc. From the geometry and kinematics of the galaxy we estimate that the absorbing cloud does not belong to a rotating disk, but could originate in a rotating halo.

2.1 Introduction

Metal absorption line systems in QSO spectra are frequently used to derive abundances of intervening neutral gas clouds of high column density. A classic definition divides strong QSO

† This chapter is published in *Astronomy & Astrophysics*, 2005, 429, 477

hydrogen absorption systems into different regimes: Lyman limit systems (LLS) with column densities of neutral hydrogen in the range $10^{17} < N(\mathrm{H\,I}) < 2 \times 10^{20}$ cm^{-2}, and damped Lyα systems (DLAs) having $N(\mathrm{H\,I}) > 2 \times 10^{20}$ cm^{-2} (Wolfe et al. 1986). Sub-DLA systems with $10^{19} < N(\mathrm{H\,I}) < 2 \times 10^{20}$ cm^{-2} also show broad absorption line wings characteristic for DLAs and contain a large fraction of the neutral hydrogen at high redshifts (Péroux et al. 2003). Strong hydrogen absorption lines in QSO spectra are believed to arise in gas-rich (proto)-galaxies, but any relation between absorption line systems and the galaxies responsible for these is not well understood. Deep imaging studies of the fields around QSOs which exhibit strong Lyα absorption lines have revealed several absorbing galaxy candidates close to the line of sight (e.g. Le Brun et al. 1997). Follow-up spectroscopy is necessary to confirm the candidates as the corresponding absorbing galaxies.

To date only few (13) low-redshift DLAs and sub-DLA galaxies have been identified (Turnshek et al. 2001; Rao et al. 2003; Chen & Lanzetta 2003; Lacy et al. 2003, and references therein), while at high redshift even fewer confirmations exist (Møller & Warren 1993; Djorgovski et al. 1996; Fynbo et al. 1999; Møller et al. 2002; Christensen et al. 2004; Møller et al. 2004). Considering the difficulties of confirming the absorbing galaxies, alternative approaches have been carried out to determine which types of galaxies produce DLA systems. Through measurements of relative abundances of various elements, it has been suggested that DLA galaxies are likely dwarf galaxies (Pettini et al. 1999; Prochaska et al. 2003; Dessauges-Zavadsky et al. 2003; Nissen et al. 2004). Sub-DLAs show the same spread in metallicity as the DLA systems indicating a similar nature of the two samples (Péroux et al. 2003). Although metallicities of DLA and sub-DLA systems can be easily derived from the QSO spectra, the metallicity of the parent galaxy has only been determined for one DLA galaxy previously (Schulte-Ladbeck et al. 2004).

Studies have shown that Mg II absorption systems arise in halos of a wide range of galaxy types (Bergeron & Boisse 1991; Steidel et al. 1994) and are typically associated with LLS. Mg II systems have been suggested to be related to rotating disks (Charlton & Churchill 1998), while Steidel et al. (2002) found that Mg II systems cannot be explained by simple disk models and suggested that the absorption occurs in rotating halos.

The quasar PHL 1226 (Q0151+045 at $z = 0.404$) has a strong Mg II absorption system at $z = 0.1602$ (Bergeron et al. 1988, hereafter B88). A column density of $N(\mathrm{H\,I}) = (5 \pm 2) \times 10^{19}$ cm^{-2} was measured in a UV HST spectrum classifying the object as sub-DLA (Rao 2004, private communication). A bright $V = 19.2 \pm 0.3$ galaxy at a projected angular separation of $6\farcs4$ to the west of the QSO was identified as being responsible for the absorption system by B88, who named this galaxy G4. For a flat cosmological model with $\Omega_\Lambda = 0.7$ and $H_0 = 70$ km s^{-1} Mpc^{-1}, which we use throughout the paper, an impact parameter of $6\farcs4$ corresponds to 17.6 kpc. An additional fainter galaxy, G3 ($V = 20.5$) at a similar redshift, was found at an impact parameter $10\farcs9$ to the north of the QSO. Either galaxy could be responsible for the absorption system considering the scaling-law between Mg II halo sizes and galaxy luminosities (Bergeron & Boisse 1991; Le Brun et al. 1993; Guillemin & Bergeron 1997). Optical spectroscopy of G3 and G4 is presented in Ellison et al. (2005).

In this paper we present a study of the galaxy G4 using integral field spectroscopy with the Potsdam Multi Aperture Spectrophotometer (PMAS; Roth et al. 2000). We describe the data reduction in Sect. 2.2. Spectra and synthetic narrow-band emission line images are presented in Sect. 2.3 From the spectra we derive the intrinsic reddening, oxygen and nitrogen abundances, and star formation rate in Sect. 2.4. We analyse the kinematics of the galaxy itself in Sect. 2.5. A discussion is presented in Sect. 2.6, and the conclusions in Sect. 2.7.

date (UT)	exposure time (s)	airmass	seeing	$\sigma_{\rm star}$(%)	S/N
Sep. 5 2002 02:48	1800	1.19	$1''$	0.5	5.9
Sep. 5 2002 03:20	1800	1.19	$1''$	0.5	5.7
Sep. 8 2002 00:03	1800	1.57	$1\farcs3$–$1\farcs5$	10	3.9
Sep. 8 2002 00:36	1800	1.14	$1\farcs3$–$1\farcs5$	9	4.2

Table 2.1. Log of the observations. $\sigma_{\rm star}$ denotes the standard deviation of flux in images of the guide star during each integration. Column 6 lists the signal to noise ratio of a one-dimensional spectrum within a $1''$ radius of the QSO.

2.2 Observations and data reduction

PMAS is an Integral Field Instrument developed at the Astrophysikalisches Institut Potsdam. It is currently installed at the Calar Alto Observatory 3.5m Telescope in Spain and has been available as a common user instrument since July 1, 2002. Observations using integral field units have the advantage of combining imaging and spectroscopy information in one dataset. In 2002, we started a project to use PMAS for the study of sub-DLA and DLA galaxies. The great advantage of using integral field spectroscopy for the investigation of the very few currently known sub-DLA and DLA galaxies is that they allow us to obtain data on the galaxies' positions, velocity fields and star-forming properties all in one data cube. Such data are critical to derive the nature of the galaxies causing absorption systems in QSOs. It is our goal to use this new instrument to identify galaxies responsible for low- as well as high-redshift QSO absorbers, and to study their properties.

During the pilot observing run for this project, we observed two QSO fields. Observations for the DLA galaxy toward Q2233+131 revealed an extended Lyman-α emission nebula surrounding the galaxy responsible for the DLA; the analysis was presented in Christensen et al. (2004). A second object observed in the pilot study was PHL 1226 (Q0151+045). The $8''\times8''$ PMAS field was targeted at the galaxy G4 because it is closer to the QSO than G3, and thus the more likely absorbing galaxy. An additional criterion was technical – G4 is more than a magnitude brighter than G3 which is farther than $8''$ away from PHL 1226; its observation would have required another set-up and a large amount of observing time. Here, we report in detail on the results which can be obtained from the PMAS data of G4.

We obtained 4×1800s exposures of G4 divided over two nights on Sep. 5 and 8, 2002, using a grating with 300 lines mm^{-1} which resulted in a spectral resolution of 6.6 Å FWHM. The chosen grating angle allowed to cover the wavelength range 4575–7880 Å. The first night was photometric with a seeing of $1''$, while the seeing was varying during the second night and the conditions were not photometric. A log of the observations is presented in Table 2.1.

The PMAS instrument has two cameras; one for the spectrograph, and an additional camera used for acquisition and guiding (A&G camera) which is equipped with a 1k$\times$1k SITe CCD. Using data from the A&G camera, one can estimate the variations and the evolution of the sky quality during the night. Photometry of the guide star images taken during the spectral integrations, show variations with a standard deviation presented in column 5 of Table 2.1.

The spectrograph is coupled by 256 fibers to a 16×16 element micro-lens array. During the observations each lens covered $0\farcs5\times0\farcs5$ on the sky. The detector is a 2k$\times$4k SITe ST002A CCD which was read out in a 2×2 binned mode.

Data reduction was performed with IDL based routines written specifically for PMAS data (Becker 2002). After bias subtraction the spectra were extracted using information of the location of the 256 spectra on the CCD obtained from a calibration frame obtained with an exposure of a continuum emission lamp immediately before or after each target exposure. In the extraction a Gaussian line profile was used to increase the signal-to-noise ratio of the extracted spectra.

Wavelength calibration was done using calibration spectra of Hg-Ne emission line lamps also obtained following the science exposures. The accuracy of the wavelength calibration was checked using sky emission lines, showing a standard deviation of 0.3 Å. Corrections for varying fiber-to-fiber transmissions as a function of wavelength uses flat field spectra obtained from the twilight sky.

Cosmic rays were removed from the spectra using the L.A. Cosmic routine within IRAF (van Dokkum 2001). Each of the 4 exposures were corrected for an average extinction value appropriate for Calar Alto before combining them. The effect of differential atmospheric extinction was corrected using the theoretical approach described in Filippenko (1982). We checked whether the data cube was appropriately corrected for the differential atmospheric refraction by cross-correlating each monochromatic image with the broad-band image shown in Fig. 2.1. This showed that the relative shift with wavelength was smaller than $0\farcs08$, which was negligible for the further analysis. Subtraction of the sky background was done by creating an average sky spectrum by selecting spaxels (spatial elements) located between the QSO and the galaxy, uncontaminated by flux from any of these two. This sky spectrum was subtracted from all 256 spectra.

The method for combining the individual exposures was as follows. Firstly, monochromatic images were made from the data cube at some selected wavelength. Then we found a scale factor between the images, by calculating the total flux in the images. Because the spectra taken on Sep. 8 were of poorer quality than the first ones, the individual data cubes were scaled to the ones from Sep 5., and the final combination took the varying seeing into account by applying a weighting scheme, where the weights were given from the signal to noise ratio of each spectrum. The signal-to-noise ratio was found from a 1D spectrum created by co-adding spectra within $1''$ radial aperture centered on the galaxy. These S/N ratios are listed in column 6 in Table 2.1. Finally, flux calibration was done the standard way by comparing the spectra obtained of the spectrophotometric standard, BD+28°4211 observed on Sep. 5 with table values. After the data reduction the spectra are contained in a data cube of dimensions $16 \times 16 \times 1008$ pixels.

Further analysis of the reduced data cube was done using the Euro3D Visualization Tool (Sánchez 2004), while one-dimensional spectra were analysed using both IRAF and our own software (Sánchez et al., 2004, in prep.). Fig. 2.1 presents a composed broad-band image, with dimensions $8''\times8''$. To the east (left), the QSO is seen at the edge of the field. The absorbing galaxy G4, identified by B88, is the principal source in the field at the position $(-6.5, -1.5)$ in agreement with the impact parameter of $6\farcs4$.

2.3 Galaxy and QSO spectra

In the dust maps of Schlegel et al. (1998) a Galactic reddening of $E(B-V)$ = 0.051 is found in the direction toward PHL 1226. The reduced spectra were de-reddened using this value before deriving other quantities. From the reduced data cube, one can create spectra from chosen spaxels or monochromatic- and narrow-band images in any wavelength region. A spectrum of the QSO created by co-adding 20 spaxels is shown in Fig. 2.2.

One sees that strong telluric absorption lines are present around 7600 Å which coincidentally corresponds to Hα at the redshift of the absorber. When line fluxes are derived, this feature will skew the results towards lower values if not corrected for. Thus, to correct for this effect, a model for the telluric absorption line was created. The QSO spectrum was smoothed using a Gaussian function with $\sigma = 10$ Å, normalised to 1 at 7580 Å and outside the region around 7600 Å the value was set to 1. Following, all spectra were divided by this model to correct for the absorption as demonstrated in in Fig. 2.4, which brought out the presence of the [N II] (6548 Å) line in the spectrum of G4 as explained in detail in Sect. 2.3.2.

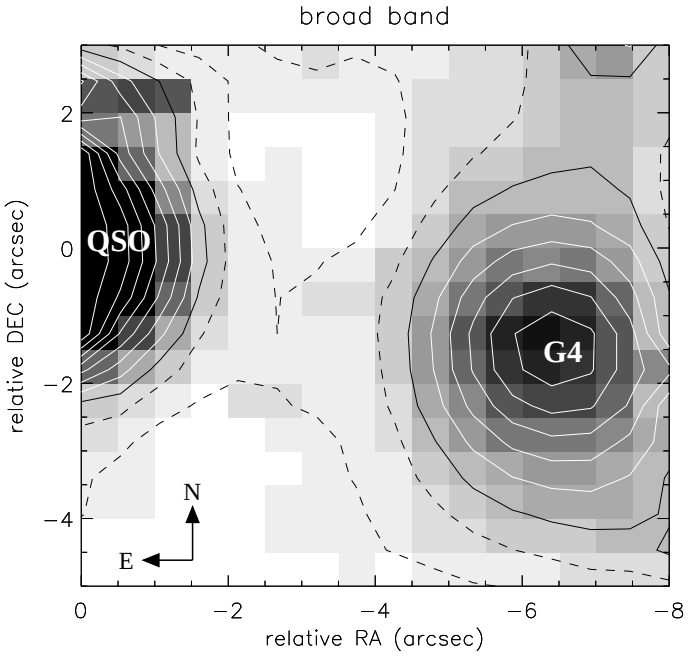

Fig. 2.1. Broad band image in the wavelength range $4500 < \lambda < 8000$ Å of the QSO at the position (0,0) and the galaxy G4 at $(-6.5, -1.5)$ as indicated. Each spaxel represents a spectrum and the field of view is $8'' \times 8''$. North is up and east is left. Coordinates are relative to the QSO position.

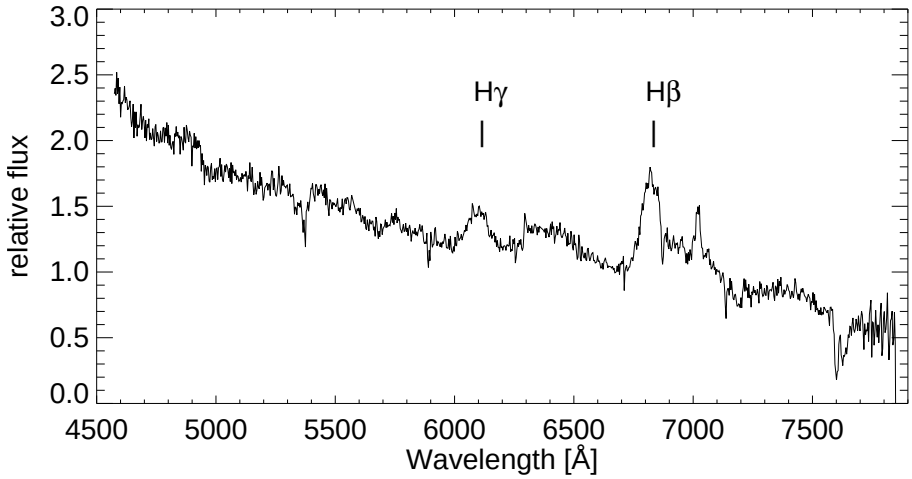

Fig. 2.2. Spectrum of PHL 1226 created by co-adding 20 spaxels. The flux levels are relative since the QSO is located at the edge of the field of view. Broad emission lines from Hγ and Hβ at $z = 0.404$ can be seen at 6100 Å and 6820 Å, respectively.

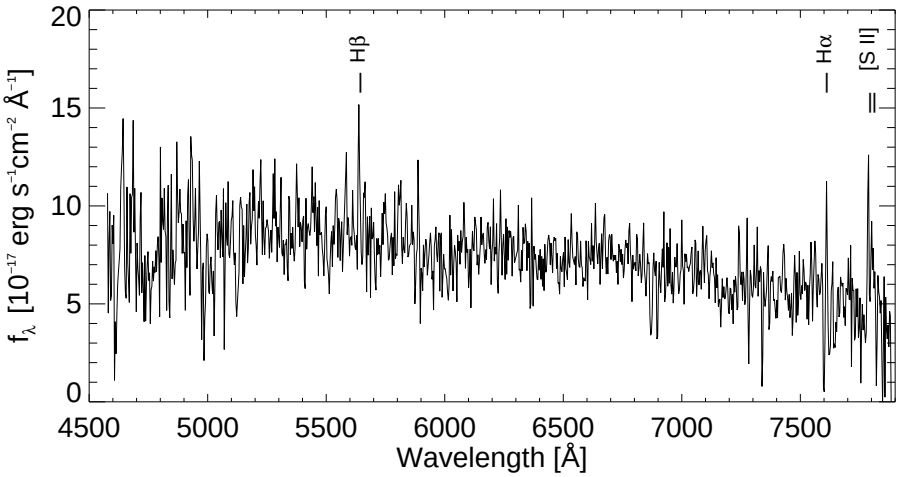

Fig. 2.3. Spectrum of the galaxy created by co-addition of 112 spaxels. Any emission line present in the galaxy has been smeared out because many spaxels do not contribute to the line emission as shown in Sect. 2.3.1. The seemingly strong [S II] lines are partly caused by errors in sky subtraction.

Co-adding all spaxels (112 in an area of $4'' \times 7''$) corresponding roughly to the size of the galaxy in this dataset results in the spectrum presented in Fig. 2.3. This spectrum gives the total continuum flux from the galaxy with S/N = 6 and does not show strong emission lines, specifically not before the correction for telluric absorption is applied. One must note that co-adding 112 spaxels dilutes any emission line signal coming from a potentially smaller region. Additionally, residuals from the background subtraction can artificially enhance emission lines. This appears to be the case for the sulfur lines in Fig. 2.3, because they lie close to strong sky lines. In order to increase the signal to noise ratio of the emission line spectrum, and be less affected by sky subtraction residuals, a localization of the emission line region needs to be done.

To check the spectrophotometry, we convolved the galaxy spectrum with a transmission curve of the Bessell V band filter. We find $V = 19.08 \pm 0.05$, corresponding to an absolute magnitude M_V = –20.3 for the galaxy in agreement with the photometry in B88.

2.3.1 Emission line images

Emission line images are created by selecting appropriate narrow-band filters from the data cube. These narrow-band images are created in a wavelength range of $\pm$10Å around the emission wavelength as shown in Fig. 2.5. The continuum emission is subtracted using narrow-band images in wavelengths adjacent to the emission lines. Compared to the broad band image in the lower right panel, one sees that most of the emission lines originate $\sim 1''$ to the south of the G4 centre. Furthermore, the strongest emission is located in a region within a $2'' \times 2''$ aperture. No other strong emission line regions are found in the field.

2.3.2 High surface brightness region

To create a spectrum with a higher signal to noise ratio relevant for deriving properties from the emission lines, we selected spaxels from Fig. 2.5 where the surface brightness of the emission lines is strongest, i.e. within a $1''$ radial aperture (corresponding to $\sim$15 spaxels) centered on $(-6.5, -2.5)$. Several lines can be identified in the spectrum shown in Fig. 2.6. Observed line

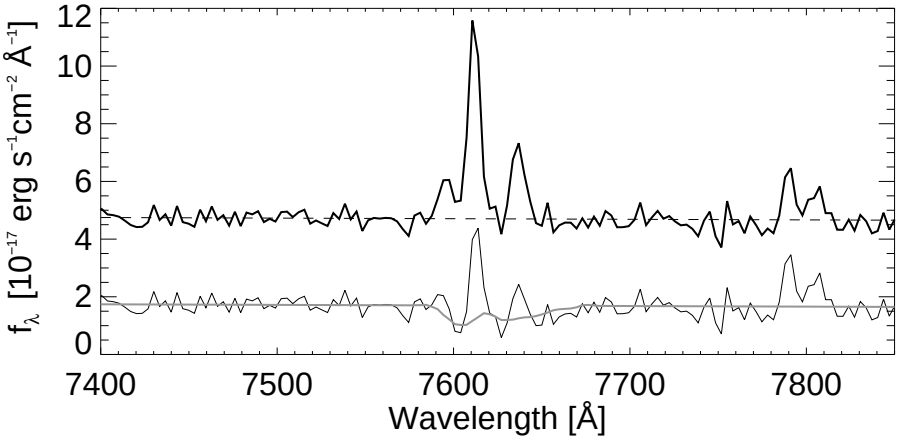

Fig. 2.4. Zoom in of the spectrum in Fig. 2.6 in the region around [N II], Hα, and [S II]. This plot shows the effect of correcting for the telluric absorption feature around 7600 Å. The lower spectrum (thin line) is the uncorrected spectrum, and the gray line is the model of the telluric feature created from the QSO spectrum. The upper spectrum (thick line) has been corrected for the absorption feature and offset by $+3\times10^{-17}$ erg cm^{-2} s^{-1} Å^{-1} for clarity.

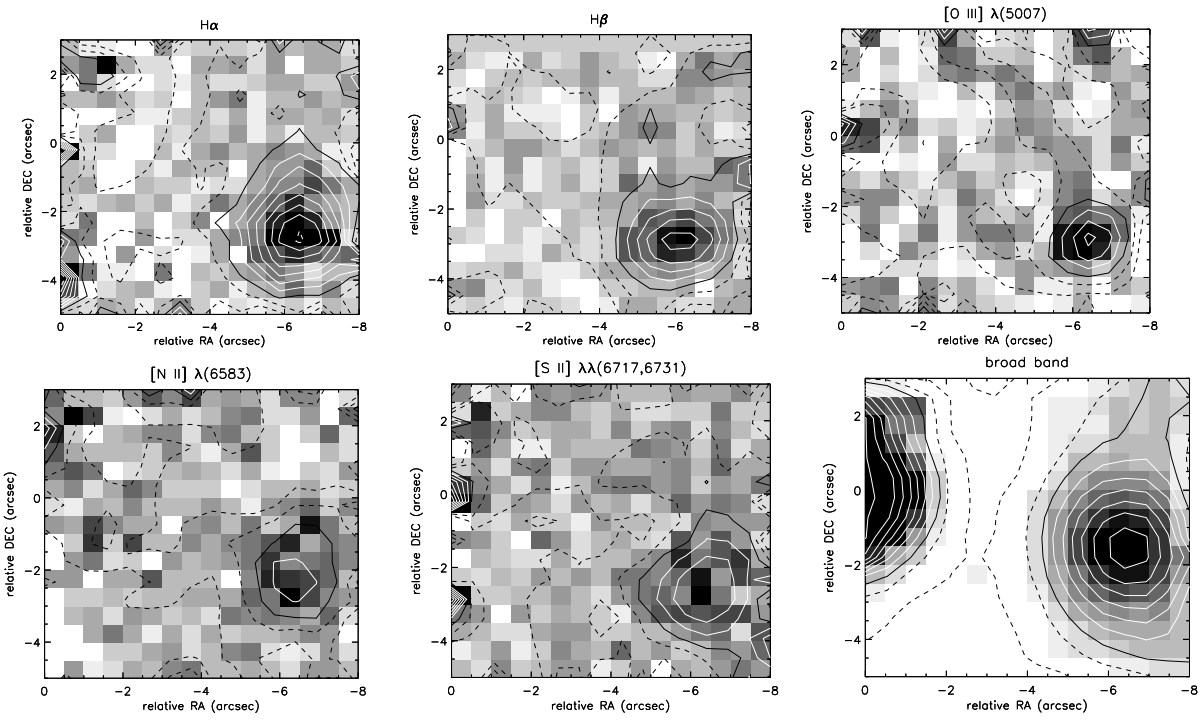

Fig. 2.5. Emission line images of various emission lines where the continuum has been subtracted using images using adjacent wavelengths. For comparison a broad band image is included in the lower right hand panel. Smoothed contours of 2, 4, 6,...σ levels are overlayed. The solid black line represent the 4σ level.

fluxes and equivalent widths (EW) are listed in Table 2.2. All emission line fluxes refer to the spectrum which has been corrected for the telluric absorption feature.

The median redshift of the emission lines is $z_{\rm em} = 0.1595 \pm 0.0006$ in agreement with $z = 0.1592 \pm 0.0020$ found by B88. The observed FWHM of emission lines are 7.2 ± 0.5Å

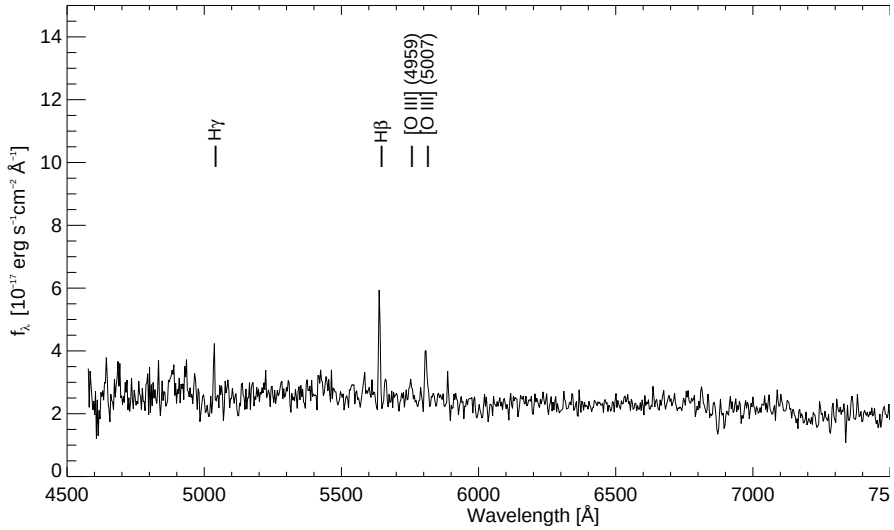

Fig. 2.6. Spectrum of the galaxy created by co-adding 15 spaxels that appeared to be associated with the bright line emission region. Emission lines listed in Table 2.2 are indicated.

and 6.1 ± 1.1Å for Hα and Hβ, respectively, which implies that the lines are consistent with being unresolved given the spectral resolution. Line fluxes of the faint lines have been derived assuming a similar width as for the brighter lines. The velocity difference between the absorption system and the median emission redshift is 180 km s^{-1}. In Sect. 2.5 we will return to further analysis of the kinematics involved in this system along with the implications.

To check if the correction for telluric absorption is appropriate we measure the line ratio [N II]λ6583/[N II]λ6548 which should theoretically be 3.0 (Wiese et al. 1966), while the derived ratio is 3.58 ± 0.76. Thus, we conclude that the correction does not introduce large errors of the derived line fluxes. Before application of the correction the line ratio is $\sim$2, however, it is uncertain as the continuum level is wrongly placed because of the telluric absorption.

Although unaffected by the correction for telluric absorption, the [O III]λ5007/[O III]λ4959 line ratio should be 2.87, while we measure the ratio 2.31$\pm$0.85. Line ratios of the emission lines [O III]λ5007 vs. Hβ and [N II]λ6583 vs. Hα classify this object as an H II galaxy according to the classification scheme of Veilleux & Osterbrock (1987).

Using long slit spectroscopy B88 find a Hβ line flux of 2.2×10^{-16} erg cm^{-2} s^{-1}, which is slightly below our measured line flux given in Table 2.2. Their long slit spectrum was obtained with a $1\farcs5$ slit, i.e. smaller than our $1''$ radial aperture for creating the spectrum. Therefore, our finding of a larger line flux can be explained by small slit-losses in their spectrum.

2.4 Derived properties

Using the strong emission lines observed in the galaxy spectrum we derive the dust reddening, abundances from the nebular emission lines in Table 2.2, and its star formation rate.

2.4.1 Dust reddening

From the observed Balmer decrement the dust content can be estimated. In the Case B Balmer recombination scenario the ratio of the emission lines is $I(\mathrm{H}\alpha)/I(\mathrm{H}\beta) = 2.85$, depending

line ($\lambda_{\rm air}$)	λ^a (Å)	redshift	line flux $\times 10^{-16}$ erg cm^{-2} s^{-1}	EW (Å)
Hγ (4340.49)	5037.29	0.1602	1.53±0.48	3.8
Hβ (4861.36)	5639.60	0.1598	2.97±0.37	8.9
[O III] (4958.91)	5754.00	0.1600	0.70±0.23	2.8
[O III] (5006.84)	5808.78	0.1598	1.62±0.28	6.6
[N II] (6548.05)	7594.64	0.1595	0.83±0.17	7.6
Hα (6562.85)	7611.88	0.1595	8.98±0.28	43.8
[N II] (6583.45)	7635.31	0.1595	2.97±0.17	16.2
[S II] (6716.44)	7788.96	0.1594	3.04±0.60	17.1
[S II] (6730.82)	7804.33	0.1592	1.95±0.50	15.5

Table 2.2. List of emission lines in the galaxy spectrum and the corresponding redshifts. Line fluxes are derived after a correction for Galactic extinction and telluric absorption was applied. Fluxes and EWs are the observed ones. ^{a} Heliocentric vacuum values.

slightly on the temperature and density (Brocklehurst 1971), while the observed flux ratio is $F(\mathrm{H}\alpha)/F(\mathrm{H}\beta) = 3.02\pm0.39$ which is consistent with no reddening.

Using the Milky Way extinction curve in Fitzpatrick (1999), we find the reddening $E(B-V) = 0.05\pm0.09$ or equivalently $A_V = 0.16\pm0.28$ for a Galactic value of $R_V = 3.1$. Similarly, the theoretical ratio of $I(\mathrm{H}\gamma)/I(\mathrm{H}\beta)$ is 0.46 in the case B scenario, while we measure $F(\mathrm{H}\gamma)/F(\mathrm{H}\beta) = 0.52 \pm 0.17$. This corresponds to $E(B-V)$ = 0.25±0.88 which is in agreement with the reddening derived from the Hα/Hβ line ratio.

Because the internal extinction in this system is consistent with 0, we do not correct the derived emission line fluxes for this effect. With integral field data one can in principle create dust maps by dividing the Hα-image with the Hβ-image, but in this case, the signal to noise ratio is not high enough to derive a reliable extinction map.

2.4.2 Chemical abundances

Using the line fluxes of strong emission lines we derive abundances of oxygen and nitrogen using various calibrations and diagnostics from the literature.

Oxygen

To determine the oxygen abundance of the galaxy we make use of the relation $O3N2 \equiv \log([\mathrm{O\,III}]\lambda5007/\mathrm{H}\beta)/([\mathrm{N\,II}]\lambda6583/\mathrm{H}\alpha)$ recently calibrated in Pettini & Pagel (2004). Our data cover all the strong lines involved in the $O3N2$ calibration which for G4 yields $12 + \log(\mathrm{O/H}) = 8.66 \pm 0.10$, while an additional error of 0.14 dex is due to the scatter in the calibration itself. The abundance corresponds to the solar oxygen abundance 8.66±0.05 in Asplund et al. (2004). This solar oxygen abundance is lower than found in models previously[1] , driving the derived oxygen abundance for G4 relative to solar towards higher values than reported in the literature for other Mg II galaxies. Taking instead the solar oxygen abundance 8.74±0.08 obtained by Holweger (2001), G4 has sub-solar metallicity ($0.8Z_\odot$), but still consistent with solar within 1σ errors.

The $O3N2$ ratio benefits from the fact that the involved lines are not separated by long wavelength ranges, and thus the quantity is largely unaffected by dust obscuration. At any rate, the small intrinsic reddening inferred for G4 implies that the $O3N2$ ratio is affected little.

For comparison we also calculate oxygen abundances using line diagnostics calibrated by other authors. For example, the oxygen abundance can be estimated from the ratio $N2 \equiv \log([\mathrm{N\,II}]/\mathrm{H}\alpha)$ using the calibration in Denicoló et al. (2002). These two strong emission lines are present

[1] The larger solar O abundance in Holweger (2001) compared to that derived in Asplund et al. (2004) is due to an ignored contribution from a Ni blend, but also a difference between their adopted 1D and 3D models.

Diagnostic	$12 + \log$(O/H)
$O3N2$ (1)	8.66 ± 0.10
$N2$ (1)	8.65 ± 0.03
$N2$ (2)	8.77 ± 0.06
R_{23} (3)	9.02 ± 0.13

Table 2.3. Oxygen abundance determinations. Diagnostics have been taken from following papers: (1) Pettini & Pagel (2004), (2) Denicoló et al. (2002), (3) Kobulnicky et al. (1999)

in the G4 spectrum, and the calibration gives $12 + \log(\text{O/H}) = 8.77 \pm 0.06$. Applying instead the slightly different calibration of the $N2$ ratio in Pettini & Pagel (2004), we find $12 + \log(\text{O/H}) = 8.65 \pm 0.03$ in agreement with the $O3N2$ diagnostic. The intrinsic 1σ scatter of this latter $N2$ calibration causes an additional uncertainty of 0.18 dex.

As another line of inquiry, we combine our data of G4 with those available in the literature. Oxygen abundances have frequently been determined using the $R_{23} \equiv ([\text{O II}]\lambda3727 + [\text{O III}]\lambda4959 + [\text{O III}]\lambda5007)/\text{H}\beta$ intensity ratio (Pagel et al. 1979). Although the spectrum of G4 does not cover the wavelength of [O II], we can estimate roughly the value if it had been covered. If the flux reported in B88 ($[\text{O II}] = 4.1 \times 10^{-16}$ erg cm^{-2} s^{-1}) is not corrected for Galactic extinction, the un-absorbed value will be $f_{\rm obs} = 4.1 \times 10^{0.4 E_{B-V} R(5963\text{Å})}$, where $E(B-V)$ is the Galactic extinction, and $R(5945\text{Å}) = 4.125$ is the value of the extinction curve at the wavelength of [O II] at $z = 0.1595$. Furthermore, we correct the slit-loss present in their spectra by applying a scale factor between their Hβ line flux and ours. We estimate the [O II] line flux $F([\text{O II}]) = (6.7 \pm 0.4) \times 10^{-16}$ erg cm^{-2} s^{-1}. Ellison et al. (2005) find an [O II] flux twice this value, but also their Hβ and [O III] fluxes are twice the ones we measure.

Using the scaled B88 [O II] line flux we find $\log R_{23} = 0.48 \pm 0.18$, which according to the calibrations in Kobulnicky et al. (1999) gives $12 + \log(\text{O/H}) = 9.02 \pm 0.13$. This value agrees within the errors with the R_{23}-based $12 + \log(\text{O/H}) = 8.9 \pm 0.2$ in Ellison et al. (2005) which justifies our assumption of applying a scaling factor of the [O II] flux.

All the derived abundances using the various diagnostics are summarised in Table 2.3. Kobulnicky et al. (1999) report that the calibration is very uncertain for line fluxes with lower signal to noise ratio than 8:1. Given such uncertainties of the latter abundance determination, combined with the fact that the $O3N2$ calibration involves emission lines detected in the data, and not a scaled [O II] flux derived from B88, we rely on the oxygen abundance derived from the $O3N2$ ratio. Thus, we find that the galaxy has a solar oxygen abundance.

Nitrogen

Having derived a solar oxygen abundance for G4, this information can be used to estimate the electron temperature which in turn is used to determine the N abundance. Because oxygen is the main coolant of a gaseous nebula, one expects to see a correlation between the oxygen abundance and the electron temperature of an H II region. From a sample of extragalactic H II regions with a large range of O abundances van Zee et al. (1998b) derive T_e. In their 39 regions with 8.56<12+log(O/H)<8.76, similar to the value of G4 within errors, we find an average $T_e = 7000 \pm 900$ K. This temperature estimate is in agreement within 1σ errors with the relation between R_{23} and the [N II] temperature in Thurston et al. (1996), which yields $t_{[\text{N II}]} = 7600 \pm 1000$ K. The uncertainty both reflects the calibration scatter (500 K) and the uncertainties of line fluxes (900 K).

Abundances of ionized nitrogen can then be derived using the relation between temperature and nitrogen to oxygen ratio (Pagel et al. 1992). Disregarding ionization corrections, the nitrogen abundance can be derived assuming (N/O) = (N^+/O^+), which is a valid approximation since the

Diagnostic	log(N/O)
(1)	-0.98 ± 0.23
(2)	-0.90 ± 0.22
(3)	-0.98 ± 0.13
(4)	-0.90 ± 0.08

Table 2.4. Nitrogen abundance determinations using different diagnostics from following papers: (1) van Zee et al. (1998b); Pagel et al. (1992), (2) Thurston et al. (1996); Pagel et al. (1992), (3) Shaw & Dufour (1995), (4) Kewley & Dopita (2002).

ionization potentials for O^+ and N^+ are similar. Furthermore, as shown by the models in Thurston et al. (1996), this approximation is accurate within 5%. For the emission lines from G4 we find $\log(\mathrm{N/O}) = -0.98 \pm 0.23$ using the average T_e, i.e. sub-solar, but consistent within 1σ with the solar value $\log(\mathrm{N/O})_\odot = -0.81$ (Holweger 2001). A similar result is obtained from the [N II] temperature which gives $\log(\mathrm{N/O}) = -0.90 \pm 0.22$. A linear relation between the O and N abundance at high oxygen abundances is observed in extragalactic H II regions (van Zee et al. 1998a), thus a solar N/O abundance is expected for G4.

Ionic abundances can also be derived using software for analysis of emission line nebulae within the IRAF/STSDAS environment (Shaw & Dufour 1995). As inputs we use the [N II] temperature estimated above and a low density environment ($n = 10$ cm^{-3}) which is preferred from the observed [S II] $\lambda\lambda$6717,6731 line ratio. These values give $\log$ (N/O) $= -0.98 \pm 0.13$ where the error mostly depends on the uncertainty of the temperature. Choosing instead a density of 100 cm^{-3} only increases $\log$ (N/O) by 0.01 dex.

As a consistency check, we investigated whether the derived oxygen abundance is in agreement with calibrations to derive the (N/O) abundance ratio. Using the polynomial relations between the oxygen abundance and $\log(N^+/O^+)$ in Kewley & Dopita (2002) yields $\log$ (N/O) $= -0.90 \pm 0.08$ inferred from the oxygen abundance derived from the $O3N2$ diagnostics. The error includes the uncertainty of the chosen ionization parameter. However, as shown in Kewley & Dopita (2002) this diagnostic is relatively independent of the ionization parameter for metallicities larger than half solar, which is the case here. The derived abundance ratios using the various estimators are summarised in Table 2.4. From these values we conclude that the galaxy has $\log(\mathrm{N/O}) = -1.0 \pm 0.2$.

2.4.3 Star formation rate

The derived line fluxes of emission lines can be used to derive an overall star formation rate (SFR) of the galaxy. A redshift of $z = 0.1595$ corresponds to a luminosity distance of 2.35×10^{27} cm (760 Mpc) for the given cosmological model. Thus, the Hα line flux corresponds to a luminosity $L(\mathrm{H}\alpha) = (6.25 \pm 0.20) \times 10^{40}$ erg s^{-1}. Using the relation

$$\mathrm{SFR} = 7.9 \times 10^{-42} L(\mathrm{H}\alpha) \quad (\mathrm{erg\ s^{-1}}) \tag{2.1}$$

in Kennicutt (1998) to convert the flux to a SFR we find SFR = 0.49 ± 0.15 M$_\odot$yr^{-1}. The uncertainty includes the one from the line flux and a larger additional uncertainty from the intrinsic scatter of the calibration of the conversion factor of $\sim$30%.

The Hα based SFR relies only on the data set of G4 presented here, while an alternative measure of the SFR can be estimated from the scaled [O II] line flux. At $z = 0.1595$ the luminosity is $L([\mathrm{O\,II}]) = (4.67 \pm 0.28) \times 10^{40}$ erg s^{-1}, which, using the conversion in Kennicutt (1998), yields SFR = 0.43 ± 0.12 M$_\odot$yr^{-1}. This value is furthermore in agreement with the calibration in Kewley et al. (2004), which yields SFR = 0.45 ± 0.17 M$_\odot$yr^{-1}. The agreement between the SFR of the

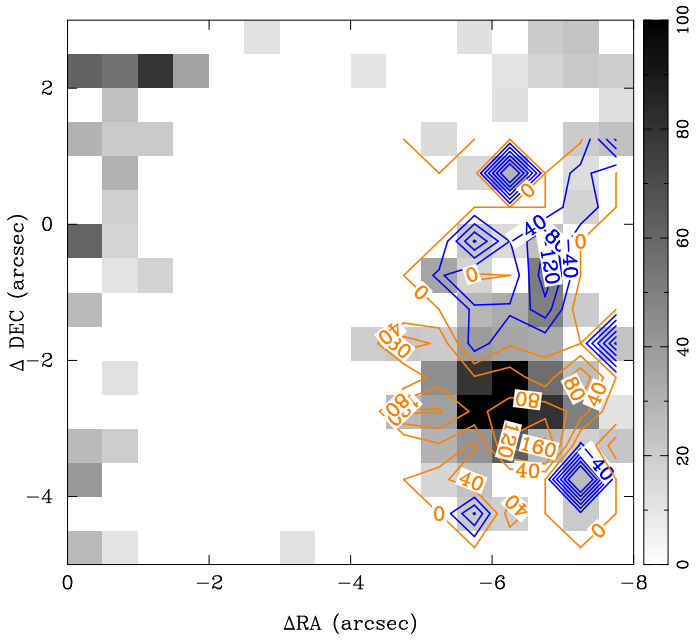

Fig. 2.7. The gray scale image shows the intensity of the Hα emission line. Relative velocities in km s^{-1} inferred from Hα emission lines are shown as contours. Orange contours are positive velocities, and blue contours are negative. Only regions showing Hα emission have been included for clarity. In comparison, the relative velocity difference of absorption in the sub-DLA cloud is +180 km s^{-1} towards the QSO sight-line.

galaxy derived from different calibrations gives credibility to the inferred small internal reddening in the galaxy.

2.5 Kinematics

From the redshift difference between the sub-DLA cloud and the galaxy found from the one-dimensional spectrum of G4, we find that the relative velocity difference is 180 km s^{-1}. Considering that the galaxy seems to be a fairly luminous galaxy, such a velocity difference over a distance of 17.6 kpc could be consistent with rotation of a massive disk, but the orientation of the galaxy with the major axis oriented roughly north-south, while the sub-DLA cloud lies to the north-east, does not support this hypothesis. We analyse here only radial velocities but note that the proper motion of the cloud could be significant.

By fitting the strongest Hα emission lines with Gaussians we examine the dynamics of the galaxy G4. Because each individual spectrum is rather noisy, the fitting could only be done satisfactorily in the region around the strongest emission. In Fig. 2.7, velocity offsets relative to the systemic $z = 0.1595$ are shown as contours overlayed an image of the Hα emission intensity. Uncertainties of the centroids of the Gaussian fits to the strongest lines are of the order of one tenth of the spectral resolution, i.e. 0.6 Å corresponding to errors of 25 km s^{-1}. We find evidence for a systematic velocity of ~ -120 to $+160$ km s^{-1} with the rotation axis oriented roughly east-west. The point of zero-level velocity is located roughly 0.″5 to the south of the centre of the G4 continuum emission.

In this representation the absorbing cloud towards the QSO (at coordinates 0,0) has a velocity offset of +180 km s^{-1} with respect to zero velocity of the Hα emission. We conclude that it is unlikely that the absorbing cloud is participating in a disk rotation.

In the integral field data we measure a velocity of 160 km s^{-1} relative to the zero velocity contour of Hα at a distance of $\sim$2″ corresponding to 5.5 kpc. However, if one takes the centre of the galaxy as the true reference point, the velocity difference is $\sim$200 km s^{-1} over a distance of 2.″5 (6.9 kpc) as indicated in Fig. 2.7. Assuming that the galaxy is viewed edge-on, the dynamical mass is $M_{\rm dyn} = v_c^2 r/G = (6 \pm 2) \times 10^{10}$ M$_\odot$, where the error is due to the uncertainty of the velocity. Because the inclination axis is not known, this value is a lower limit, while another uncertainty is due to the fact that we probably do not reach asymptotic values for the rotation curve. In any case, the estimate shows that the galaxy is a fairly massive one.

2.6 Discussion

Having derived various properties of the sub-DLA galaxy, we proceed by comparing them to those of other sub-DLA and DLA galaxies in the literature. We emphasize once again that there is another galaxy, G3, at the same redshift as G4 but having a larger impact parameter. G3 might contribute to the absorption seen in PHL 1226. No galaxy in Fig. 3 of B88, however, is closer to the QSO than G4, and we discuss in section 6.3 that our data allow us to exclude an emission-line galaxy with a smaller impact parameter than G4 between G4 and the QSO. As is common practice in the literature on DLA galaxies, we proceed with the assumption that the absorbing cloud belongs to the galaxy with the smallest impact parameter.

2.6.1 Relationship with DLAs, sub-DLAs and Mg II systems

The derived oxygen abundance of the galaxy G4 is larger than abundances derived for high redshift sub-DLAs (Dessauges-Zavadsky et al. 2003; Péroux et al. 2003). Furthermore, compared to the nearby DLA absorber SBS 1543+594 (Schulte-Ladbeck et al. 2004), this galaxy has a higher abundance, but that goes in hand with its higher luminosity. In fact we calculate $M_B = -20.0$ using the spectrum in Fig. 2.3 shifted to the rest frame and convolved with the Bessell B band transmission function. G4 exhibits values which are entirely consistent with the local luminosity-metallicity relation (Kobulnicky & Koo 2000; Pilyugin et al. 2004).

On the other hand, G4 has an oxygen abundance compatible with the upper end of abundances derived for the Mg II selected galaxies ($-0.6 < [\mathrm{O/H}] < -0.1$ derived in Guillemin & Bergeron 1997). For comparison, high resolution spectra of strong Mg II absorption systems towards a couple of QSOs at $z \sim 1$ have indicated metallicities ranging from 0.1 to 1 times solar (Ding et al. 2003a,b). This could indicate a general agreement between metallicities derived using absorption lines and emission line diagnostics.

The kinematic investigation showed that the absorber is clearly not associated with a disk, but it could be part of a rotating halo as suggested for other Mg II absorbers (Steidel et al. 2002). The galaxy G4 and its sub-DLA system could thus be similar to the $z = 0.16377$ sub-DLA towards Q0850+4400 (Lanzetta et al. 1997). They showed that the absorption arises at large galactocentric distance (17 kpc) and does not participate in a general disk rotation.

Alternatively, Bond et al. (2001) suggested that a substantial fraction of very strong Mg II systems arise in superwinds from galaxies. Along similar lines, expanding superbubbles were suggested to be the explanation for metal absorption line mirror symmetries seen in the strong Mg II absorber towards Q1331+17 (Ellison et al. 2003). A superwind from the galaxy G4 is unlikely at present time given the relatively small SFR. However, as it is comparable to an L^* galaxy, a previous starburst could have expelled neutral gas clouds enriched by metals.

2.6.2 Abundance gradient effect

Metallicity studies of DLAs and sub-DLAs are trying to explain the question of what is the nature of the parent galaxy. Only in very few currently known cases, where the parent galaxy has been clearly identified, can such an investigation be carried out. Abundances derived from metal absorption lines associated with the DLAs can be compared to abundances based on emission line diagnostics for H II regions in the galaxy. The DLA galaxy SBS 1543+594 is one example, where the impact parameter is small – in fact, the sight line to the QSO goes through the disk of the dwarf galaxy. In such a case, the inferred metallicity of the DLA cloud and the galaxy is expected to be similar. However, in the case of the G4/sub-DLA system towards PHL 1226 where the impact parameter is larger and the sub-DLA cloud possibly does not belong to the disk of the galaxy, one would expect to find lower (O/H) and (N/O) abundances of the sub-DLA cloud due to abundance gradients.

Analysing abundances in extragalactic H II regions Vila-Costas & Edmunds (1992) and Zaritsky et al. (1994) found a large scatter in the abundance gradients for individual galaxies of a given Hubble type. They also found a tendency for more shallow gradients, expressed in dex/kpc, for early and late type spirals compared to intermediate type spirals. Locally, three face-on disk galaxies were found to have strong abundance gradients along the major axes in the outer regions of their disks (Ferguson et al. 1998, hereafter F98). Fewer studies have analysed the metallicity gradient along the minor axes of galaxies, but smaller metallicities have been found for extraplanar H II regions compared to the core of an edge-on galaxy (Tüllmann et al. 2003). The study of H II regions in face-on galaxies can therefore also be biased by projection effects.

The data presented here do not allow us to estimate the Hubble type of G4, making it difficult to predict an appropriate abundance gradient. If one takes the measured metallicity gradient from F98 with an average in $\log$(O/H) of -0.09 dex kpc^{-1}, the abundance of the sub-DLA cloud at 17.6 kpc is expected to be $\sim$1.6 dex lower than what we find for the G4 disk. Similarly, the average gradient in $\log$(N/O) is -0.05 dex kpc^{-1} which implies an abundance ratio smaller by 0.9 dex. Thus one could expect 12+$\log$(O/H) = 7.1 and $\log$(N/O) = -1.9 for the sub-DLA abundances. We assume that the gradients are straight lines which may not be the case (Zaritsky et al. 1994). If a low abundance of the PHL 1226 sub-DLA cloud should be confirmed by future space based spectroscopy, these values would place the sub-DLA system toward PHL 1226 among the metallicities for the currently measured high redshift DLA and sub-DLA systems measured by several authors (Pettini et al. 2002b; Lopez et al. 2002; Lopez & Ellison 2003; Centurión et al. 2003).

These approximate cloud metallicities are crude estimates since the impact parameter is a lower limit due to the unknown inclination angle, and the individual abundance gradients in F98 vary within a factor of 2. Furthermore, the lowest metallicities observed by F98 reach 12+$\log$(O/H) = 7.95, thus we are extrapolating their metallicity gradient.

2.6.3 Sub-DLA cloud properties

Other properties of G4 such as Hβ luminosity, EW of Hβ, absolute magnitude, and oxygen abundance are compatible with those of emission line field galaxies at redshifts $0.26 < z < 0.82$ (Kobulnicky et al. 2003). This apparently seems to be in contradiction with the spectroscopic analyses suggesting that sub-DLAs/DLAs are chemically less evolved than star forming galaxies at similar redshifts. Specifically, sub-DLAs/DLAs have sub-solar metallicity and element abundances suggesting low SFRs (Pettini et al. 2002a; Prochaska et al. 2003; Péroux et al. 2003; Dessauges-Zavadsky et al. 2003). On the other hand we can not, with the currently available data set, exclude the possibility that a galaxy less luminous than G4 closer to the line of sight towards PHL 1226 is responsible for the sub-DLA. In the integral field data presented here we find no evidence for line emission closer to the line of sight than $5''$ to the west of the QSO. With the presented single pointing towards the QSO we can not say anything about the other directions.

As argued, either galaxy G4 or G3 could be responsible for the sub-DLA cloud. If the cloud were associated with G3, it too has to be associated with a halo because of the orientation of the galaxy which suggests an elongation in the east-west direction (i.e. perpendicular to the direction toward PHL 1226). Assuming that the sub-DLA cloud indeed belongs to the galaxy G4, we find a velocity difference of 180 km s^{-1} from the sub-DLA cloud redshift to the Hα velocity at the centre of G4, for which we estimate the galaxy mass $(6 \pm 2) \times 10^{10}$ M$_\odot$. In this case, the escape velocity at a distance of 17.6 kpc is 200$\pm$30 km s^{-1} implying that the cloud could be gravitationally bound.

Yet another possibility for the location of the sub-DLA cloud is gravitational interaction between systems. Indeed the galaxies G4 and G3 have a distance of 12.″6 from each other corresponding to 35 kpc, so it could be an interacting system, but with the currently available observations we can not test this scenario.

2.7 Conclusions

Using integral field spectroscopy with PMAS we have observed the absorber G4, previously identified by Bergeron et al. (1988), toward the QSO PHL 1226 at an impact parameter of 6.″4. This galaxy is most probably responsible for a strong Mg II and sub-DLA absorption system at $z = 0.1602$ in the QSO spectrum. At the same redshift another galaxy, G3, is present. We cannot determine whether the PHL 1226 absorber belongs to galaxy G4 or G3, but concentrate on G4. Their impact parameters of 6.″4 and 10.″9 correspond to 18 and 29 kpc, respectively, implying that either could be responsible for the absorption given the scaling-law of Mg II absorbers.

A strong emission line region is shown to be limited to an area of approximately 1″ in radius within the galaxy. In the spectra we find emission lines from [O III], [N II], [S II] as well as Balmer lines Hγ, Hβ and Hα at the redshift 0.1595$\pm$0.0006. We do not find regions of emission at the same redshift closer to the QSO line of sight.

From the Balmer line ratios we find evidence of an intrinsic reddening of $E(B-V)$ = 0.05$\pm$0.16, i.e. consistent with 0. From the measured Hα line flux we derive a SFR = 0.5 M$_\odot$ yr^{-1}.

Using the $O3N2$ line ratio diagnostics from Pettini & Pagel (2004) we derive a solar oxygen abundance $12+\log$(O/H) $= 8.7 \pm 0.1$. Also a solar value of the abundance ratio $\log$(N/O)=–1.0$\pm$0.2 is found implying a metallicity comparable to the upper-end of metallicities for the currently known sample of Mg II galaxies.

A kinematic analysis of the Hα emission line showed that the galaxy has rotational velocities of –120 to +160 km s^{-1} relative to the systemic redshift with the rotational axis oriented roughly east-west. The sub-DLA cloud, on the other hand, has a velocity difference of 180 km s^{-1} relative to the galaxy and an impact parameter of 17.6 kpc above the disk assuming that the disk is seen edge on. With such geometry and kinematics, the sub-DLA cloud is likely part of a rotating halo and possibly gravitationally bound. From relative velocity measurements we derive a kinematic mass of 6$\times$10^{10} M$_\odot$, which corresponds to a fairly massive galaxy. The absolute magnitude is $M_V = -20.3$ and $M_B = -20.0$ which is consistent with the mass-luminosity relation for spiral galaxies (Forbes 1992).

With future UV space-based spectroscopy it will be possible to compare the metallicity of the sub-DLA cloud towards PHL 1226 with abundances derived for the galaxy, which is necessary in order to understand the relation between the absorption lines in QSO spectra and the galaxies responsible for them. If there is a difference in metallicity in line with the metallicity gradients observed in local disk galaxies, we expect that the properties of the sub-DLA cloud will be similar to those of high redshift DLA and sub-DLA systems. This is an intriguing prospect which could suggest that the specific sight line through the galaxy responsible for the DLA or sub-DLA cloud has important consequences on the derived properties of the cloud.

Acknowledgments. L. Christensen acknowledges support by the German Verbundforschung associated with the ULTROS project, grant no. 05AE2BAA/4. R. Schulte-Ladbeck is thankful for funding from HST archival grant no. 10282. S. F. Sánchez acknowledges the support from the Euro3D Research Training Network, grant no. HPRN-CT2002-00305. K. Jahnke and L. Wisotzki acknowledge a DFG travel grant under Wi 1389/12-1.

References

Asplund, M., Grevesse, N., Sauval, A. J., Allende Prieto, C., & D. Kiselman, D. 2004, A&A, 417, 751
Becker, T. 2002, PhD thesis, Astrophysikalisches Institut Potsdam, Germany
Bergeron, J. & Boisse, P. 1991, A&A, 243, 344
Bergeron, J., Boulade, O., Kunth, D., et al. 1988, A&A, 191, 1, (B88)
Bond, N. A., Churchill, C. W., Charlton, J. C., & Vogt, S. S. 2001, ApJ, 562, 641
Brocklehurst, M. 1971, MNRAS, 153, 471
Centurión, M., Molaro, P., Vladilo, G., et al. 2003, A&A, 403, 55
Charlton, J. C. & Churchill, C. W. 1998, ApJ, 499, 181
Chen, H.-W. & Lanzetta, K. M. 2003, ApJ, 597, 706
Christensen, L., Sánchez, S. F., Jahnke, K., et al. 2004, A&A, 417, 487
Denicoló, G., Terlevich, R., & Terlevich, E. 2002, MNRAS, 330, 69
Dessauges-Zavadsky, M., Péroux, C., Kim, T.-S., D'Odorico, S., & McMahon, R. G. 2003, MNRAS, 345, 447
Ding, J., Charlton, J. C., Bond, N. A., Zonak, S. G., & Churchill, C. W. 2003a, ApJ, 587, 551
Ding, J., Charlton, J. C., Churchill, C. W., & Palma, C. 2003b, ApJ, 590, 746
Djorgovski, S. G., Pahre, M. A., Bechtold, J., & Elston, R. 1996, Nature, 382, 234
Ellison, S. L., Kewley, L. J., & Mallén-Ornelas, G. 2005, MNRAS, 357, 354
Ellison, S. L., Mallén-Ornelas, G., & Sawicki, M. 2003, ApJ, 589, 709
Ferguson, A. M. N., Gallagher, J. S., & Wyse, R. F. G. 1998, AJ, 116, 673
Filippenko, A. V. 1982, PASP, 94, 715
Fitzpatrick, E. L. 1999, PASP, 111, 63
Forbes, D. A. 1992, A&AS, 92, 583
Fynbo, J. U., Møller, P., & Warren, S. J. 1999, MNRAS, 305, 849
Guillemin, P. & Bergeron, J. 1997, A&A, 328, 499
Holweger, H. 2001, in AIP Conf. Proc. 598, ed.R. F. Wimmer-Schweingruber, 23
Kennicutt, R. C. 1998, ARA&A, 36, 189
Kewley, L. J. & Dopita, M. A. 2002, ApJS, 142, 35
Kewley, L. J., Geller, M. J., & Jansen, R. A. 2004, AJ, 127, 2002
Kobulnicky, H. A., Kennicutt, R. C., & Pizagno, J. L. 1999, ApJ, 514, 544
Kobulnicky, H. A. & Koo, D. C. 2000, ApJ, 545, 712
Kobulnicky, H. A., Willmer, C. N. A., Phillips, A. C., et al. 2003, ApJ, 599, 1006
Lacy, M., Becker, R. H., Storrie-Lombardi, L. J., et al. 2003, AJ, 126, 2230
Lanzetta, K. M., Wolfe, A. M., Altan, H., et al. 1997, AJ, 114, 1337
Le Brun, V., Bergeron, J., Boisse, P., & Christian, C. 1993, A&A, 279, 33
Le Brun, V., Bergeron, J., Boisse, P., & Deharveng, J. M. 1997, A&A, 321, 733
Lopez, S. & Ellison, S. L. 2003, A&A, 403, 573
Lopez, S., Reimers, D., D'Odorico, S., & Prochaska, J. X. 2002, A&A, 385, 778
Møller, P., Fynbo, J. P., & Fall, S. M. 2004, A&A, 422, L33
Møller, P. & Warren, S. J. 1993, A&A, 270, 43

Møller, P., Warren, S. J., Fall, S. M., Fynbo, J. U., & Jakobsen, P. 2002, ApJ, 574, 51
Nissen, P. E., Chen, Y. Q., Asplund, M., & Pettini, M. 2004, A&A, 415, 993
Péroux, C., Dessauges-Zavadsky, M., D'Odorico, S., Kim, T., & McMahon, R. G. 2003, MNRAS, 345, 480
Pagel, B. E. J., Edmunds, M. G., Blackwell, D. E., Chun, M. S., & Smith, G. 1979, MNRAS, 189, 95
Pagel, B. E. J., Simonson, E. A., Terlevich, R. J., & Edmunds, M. G. 1992, MNRAS, 255, 325
Pettini, M., Ellison, S. L., Bergeron, J., & Petitjean, P. 2002a, A&A, 391, 21
Pettini, M., Ellison, S. L., Steidel, C. C., & Bowen, D. V. 1999, ApJ, 510, 576
Pettini, M. & Pagel, B. E. J. 2004, MNRAS, 348, L59
Pettini, M., Rix, S. A., Steidel, C. C., et al. 2002b, ApJ, 569, 742
Pilyugin, L. S., Vílchez, J. M., & Contini, T. 2004, A&A, 425, 849
Prochaska, J. X., Gawiser, E., Wolfe, A. M., Castro, S., & Djorgovski, S. G. 2003, ApJL, 595, L9
Rao, S. M., Nestor, D. B., Turnshek, D. A., et al. 2003, ApJ, 595, 94
Roth, M. M., Bauer, S., Dionies, F., et al. 2000, in Proc. SPIE, Vol. 4008, 277–288
Sánchez, S. F. 2004, AN, 325, 167
Schlegel, D. J., Finkbeiner, D. P., & Davis, M. 1998, ApJ, 500, 525
Schulte-Ladbeck, R. E., Rao, S. M., Drozdovsky, I. O., et al. 2004, ApJ, 600, 613
Shaw, R. A. & Dufour, R. J. 1995, PASP, 107, 896
Steidel, C. C., Kollmeier, J. A., Shapley, A. E., et al. 2002, ApJ, 570, 526
Steidel, C. C., Pettini, M., Dickinson, M., & Persson, S. E. 1994, AJ, 108, 2046
Thurston, T. R., Edmunds, M. G., & Henry, R. B. C. 1996, MNRAS, 283, 990
Tüllmann, R., Rosa, M. R., Elwert, T., et al. 2003, A&A, 412, 69
Turnshek, D. A., Rao, S. M., Nestor, D., et al. 2001, ApJ, 553, 288
van Dokkum, P. G. 2001, PASP, 113, 1420
van Zee, L., Salzer, J. J., & Haynes, M. P. 1998a, ApJL, 497, L1
van Zee, L., Salzer, J. J., Haynes, M. P., O'Donoghue, A. A., & Balonek, T. J. 1998b, AJ, 116, 2805
Veilleux, S. & Osterbrock, D. E. 1987, ApJS, 63, 295
Vila-Costas, M. B. & Edmunds, M. G. 1992, MNRAS, 259, 121
Wiese, W. L., Smith, M. W., & Glennon, B. M. 1966, Atomic transition probabilities. Vol.: Hydrogen through Neon. A critical data compilation (NSRDS-NBS 4, Washington, D.C.: US Department of Commerce, National Buereau of Standards, 1966)
Wolfe, A. M., Turnshek, D. A., Smith, H. E., & Cohen, R. D. 1986, ApJS, 61, 249
Zaritsky, D., Kennicutt, R. C., & Huchra, J. P. 1994, ApJ, 420, 87

CHAPTER 3

Integral-field spectroscopic observations of damped Lyman-α galaxies at z$<$1

L. CHRISTENSEN[1], S. F. SÁNCHEZ[1,2], K. EXTER[3], K. JAHNKE[1], L. WISOTZKI[1,4], M. M. ROTH[1]

[1] Astrophysikalisches Institut Potsdam, An der Sternwarte 16, 14482 Potsdam, Germany

[2] Centro Astronomico Hispano Aleman de Calar Alto, Spain

[3] Instituto de Astrofísica de Canarias, La Laguna, Tenerife

[4] Potsdam University, Am Neuen Palais 10, 14469 Potsdam, Germany

Abstract

Using integral field spectroscopy we investigate galaxy counterparts to damped Lyman-α (DLA) systems at $z < 1$. The sample consists of seven QSOs with eight known DLA systems, out of which one has a spectroscopically confirmed galaxy at the DLA redshift, and another with a photometric redshift consistent with the DLA redshift. The data allow us to confirm the emission lines from the two DLA galaxies and one Lyman limit galaxy also reported in the literature. Additionally, four more candidate emission lines from DLA galaxies are detected. Apart from one object only one emission line is detected per object at the 3σ levels. Nevertheless, the emission line fluxes and detection significances are similar to the previously known objects. We find a strong anticorrelation between the column densities in the DLAs and the projected distances between the QSO and the galaxy sight lines. If interpreted as caused by exponential disks, the scale length of an average DLA galaxy disk traced by the neutral hydrogen is $\sim$5 kpc.

3.1 Introduction

Damped Lyman-α systems (DLAs) have column densities of neutral hydrogen larger than 2×10^{20} cm^{-2}. DLA systems contain a large fraction of neutral gas throughout the Universe (Lanzetta et al. 1995b; Storrie-Lombardi & Wolfe 2000) with a close to constant density down to below $z = 1.65$ (Rao & Turnshek 2000) and no strong evolution with redshift has been detected. Although more than 500 DLA systems are currently known mainly from the Sloan Digital Sky Survey (Prochaska, 2005, in prep.) most are high redshift objects. DLA lines at $z < 1.7$ need confirmation from space-based UV spectroscopy, which implies that relatively few DLAs are known. Although

[†] A version of this chapter will be submitted to *Astronomy & Astrophysics*

only few DLAs are known at these redshifts the interval corresponds to 70% of the age of the Universe.

Much information regarding the DLA evolution has been derived from absorption line studies. Metallicities of DLAs show a weak increase with increasing cosmic time and a large scatter between individual systems (Kulkarni & Fall 2002; Prochaska et al. 2003). Metallicities reach an average sub-solar level at the lowest redshifts (Kulkarni et al. 2005).

The DLA column density is similar to column densities in galaxy disks. Combined with kinematic analyses of associated metal absorption lines DLAs were believed to arise when the sight line to a QSO intercepts the disk of a (proto-) galaxy (Wolfe et al. 1986). The kinematics derived from metal absorption line profiles were interpreted as being caused by rotating massive disks (Prochaska & Wolfe 1997), but also merging sub-galaxy sized clumps of gas could explain the observations (Haehnelt et al. 1998).

Investigations of DLAs at $z < 1.5$ have found that galaxies harboring the clouds that cause DLA lines have a wide range of galaxy morphologies consisting of L^* galaxies, dwarfs and low-surface-brightness galaxies (Le Brun et al. 1997; Rao et al. 2003; Lacy et al. 2003) but otherwise the properties of the galaxies are representative for the field population as a whole (Chen et al. 2005, hereafter C05). Because of the larger cross section for galaxy outskirts, DLAs could preferentially probe the less metal enriched environments in the case where a significant radial metallicity gradient is present (Christensen et al. 2005; Ellison et al. 2005; Chen et al. 2005).

Traditionally, deep imaging surveys have been carried out to find candidate DLA galaxies near the sight line of the QSO (Steidel et al. 1994; Le Brun et al. 1997). However, the DLA galaxy is not necessarily the brightest nearby galaxy, and follow-up spectroscopy is needed for many faint galaxies to confirm the galaxy redshifts. Curiously, even though extensive deep campaigns have been carried out, some DLA galaxies have still not been detected spectroscopically (Steidel et al. 1995; Turnshek et al. 2001).

Integral field spectroscopy (IFS) makes it possible to obtain imaging and follow-up spectroscopy simultaneously. In this paper we present an investigation using IFS of DLA systems at $z < 1$ in a sample of seven QSOs with eight known DLA systems. Out of these eight DLA systems, three have previously confirmed DLA galaxies, two by spectroscopic observations and one by its photometric redshift. Throughout the paper we use a flat cosmology with H_0 = 70 km s^{-1} Mpc^{-1}, $\Omega_m = 0.3$, and Ω_Λ = 0.7.

3.2 Sample selection

At redshifts $z < 1$, 21 DLAs have been confirmed through space-based UV spectroscopy of QSOs (Rao & Turnshek 2000; Curran et al. 2002; Lacy et al. 2003). Imaging studies of 11 of these QSOs is presented in Chen & Lanzetta (2003), and follow-up long slit spectra of 6 DLA galaxies in C05. Several new $z < 1.7$ candidate DLAs have recently been found because of their strong Mg II and Fe II absorption lines in QSO spectra from the Sloan Digital Sky Survey (Nestor et al. 2004), but a measurement of their $N(\mathrm{H\,I})$ needs space based UV spectroscopy because the success rate of confirming DLAs using this technique is below 50% (Rao & Turnshek 2000; Rao 2005).

All of the confirmed DLAs can be observed from the northern hemisphere, and we selected QSOs brighter than $R = 19$ for our studies. This criterion was included to ensure that the signal from the QSO was sufficient to determine accurately the spatial location of the candidates with respect to the QSO, but more importantly to be able to study the wavelength dependent variations of the PSF which is important when the QSO emission has to be subtracted. Furthermore, targets were selected preferentially when expected emission lines did not coincide with strong sky emission

(1) Coordinate name	(2) Alt. name	(3) $z_{\rm em}$	(4) $z_{\rm abs}$	(5) $\log N({\rm H\,I})$ (cm^{-2})	(6) [M/H]	(7) References
Q0454+039	PKS 0454+039	1.345	0.8596	20.76±0.02	[Zn/H]=–1.01±0.12	(2,3,10)
Q0738+313	OI 363	0.630	0.2212	20.90±0.08	[Zn/H]<–0.7	(4,9)
			0.0912	21.18±0.06	[Zn/H]<–1.14	(4,9)
Q0809+4822	3C 196	0.871	0.4368	20.8±0.2		(5,6)
Q0952+179	PKS 0952+17	1.478	0.239	21.32±0.05	[Zn/H]<–1.02	(3,7,9)
Q1209+107		2.193	0.6295	20.3±0.1		(3)
Q1622+239	3C 336	0.927	0.656	20.4±0.1	[Fe/H]=–1.2	(3,8)
Q1629+120	PKS 1629+120	1.795	0.532	20.7±0.1		(7)

Table 3.1. List of the observed objects with redshifts, column densities, and metallicities taken from the literature. References for the DLAs: (1) Snijders et al. (1982), (2) Steidel et al. (1995), (3) Rao & Turnshek (2000), (4) Rao & Turnshek (1998), (5) Cohen et al. (1996), (6) Boisse et al. (1998), (7) Rao et al. (2003), (8) Steidel et al. (1997), (9) Kulkarni et al. (2005), (10) Pettini et al. (2000).

lines. Only classical DLAs were targeted, but we also examine other strong lines that may be present within the spectral range of the observations.

Seven of the targets were observed because much time was lost due to bad weather. We preferred to increase the integration times for individual objects to obtain similar detection levels in all fields rather than observe the complete sample. Properties of the observed DLAs are listed in Table. 3.1.

3.3 Observations and data reduction

Our programme was carried out with two different integral field units with two telescopes. Most observations were done with the Potsdam Multi Aperture Spectrophotometer (PMAS) mounted on the 3.5m telescope at Calar Alto (Roth et al. 2000, 2005). Other observations were obtained with INTEGRAL mounted on the WHT at La Palma. A log of the observations is given in Table 3.2. Maximum exposure times of 1800s were used because of the large number of pixels affected by cosmic ray hits. Furthermore, because of varying conditions such as atmospheric transmission and seeing, the total exposure time for each object had to be adjusted, or sometimes the exposure had to be repeated under better conditions.

The PMAS data were obtained using two gratings; one with 300 gr mm^{-1} and one with 600 gr mm^{-1} with a resolution of 3.2 and 1.6 Å pixel^{-1}, respectively, and with spectral resolution of twice these values. PMAS has 16×16 (256) fibres coupled to a lens-array, that during the observations covered a total field of view of $8''\times8''$. No significant amount of flux is lost between fibres. Each fibre provides a spectrum that samples one region of the sky, and which are later called 'spaxels' (spatial element pixels). PMAS has an acquisition camera which can be used to monitor the photometric conditions which are given in columns 7 and 8 in Table 3.2.

For the INTEGRAL observations we used the SB2 fibre bundle which has 219 fibres (Arribas et al. 1998), which provides a non-contiguous sampling of a $12''\times16''$ field of view, and each fibre covers a diameter of $0\farcs9$ on the sky. We used a 600 gr mm^{-1} grating giving 2.9 Å pixel^{-1} and a resolution of 6 Å. The INTEGRAL data were obtained in non-photometric conditions.

The basics of the data reductions for the two data sets were the same, but the programs were different. PMAS data reduction uses IDL routines specifically developed for PMAS data (Becker 2002), while the INTEGRAL data reduction was done with specifically developed IRAF tasks (see Garcia-Lorenzo et al. 2005). After bias subtraction the individual spectra were located on the CCD by tracing spectra of continuum lamps. The science spectra were extracted using appropriate

widths. Wavelength calibrations were done using exposures of emission line lamps taken before or after the science integrations. The wavelength calibration was checked by comparison with strong sky emission lines which indicated that the accuracy was approximately one tenth of the spectral resolution. Flat fielding of the data was done by dividing by a flat field frame which is created by extracting spectra of a twilight sky exposure. After extracting the individual flat field spectra, a median flat field spectrum was made, and the individual spectra were divided by a smoothed version of the median flat field spectrum. This process corrected the science spectra for fibre throughput differences and wavelength dependent transmissions as well. For flux calibrations, we used observations of spectrophotometric standard for each night at each applied grating position, but not always obtained close in time.

Background subtraction was different in the two data sets. PMAS, in the standard configuration, does not have sky-fibres and background subtraction was done by selecting spaxels that are not contaminated by flux from any sources. Because the position of the DLA galaxy was intrinsically unknown, several different, independent sky subtractions had to be analysed. INTEGRAL has 30 sky fibres located in a ring surrounding the science fibres. An average of selected sky-fibres was subtracted from the extracted, flat-fielded, and wavelength calibrated data set. An atmospheric extinction correction was applied to each exposure assuming an average extinction curve for the observatory site, before the individual exposures were combined.

Reduced individual data cubes were investigated through two different approaches. The first one compensated for the differential atmospheric refraction (DAR) by applying a correction to each monochromatic slice given by an analytical expression (Filippenko 1982). Spatial offsets between individual cubes were determined at a fixed wavelength from the centroid of the QSO. This fixed wavelength was chosen close to the expected emission lines from the DLA galaxies. The data cubes were co-added taking both the absolute shifts and the wavelength dependent shifts into account. The other approach was to correct accurately for the DAR using empirically determined shifts for the QSO centroid as a function of wavelength. To determine these shifts, a 2-dimensional Gaussian PSF was fit to each monochromatic image and a smooth polynomial was fit to the centroid as a function of wavelength. Using these shifts the individual data cubes were combined using the DRIZZLE package (Fruchter & Hook 2002) while retaining the original pixel sizes.

The first method did not correct accurately for the DAR, and we found that a residual shift of the QSO centroid was present. We estimated that $\sim$10% of the original shifts were still present after the theoretical shifts were applied, and this could be significant for observations at high airmasses. On the other hand, the second method achieved a constant position of the QSO centroid. Even though the latter procedure produced better centering, we used the first version here, because we are only analysing small wavelength regions at a time. Subtraction of the QSO emission as explained in Sect. 3.4 gave similar results for the two cases.

Further inspection of the reduced data cubes was done with the Euro3D visualisation tool (Sánchez 2004), while analyses of one-dimensional spectra were done with routines in both IDL and IRAF. For references to the QSOs and the corresponding DLA absorption systems, Fig. 3.1 presents the calibrated spectra of the individual QSOs. First, a QSO spectrum was created by co-adding spaxels within typically twice the seeing *FWHM*. A second QSO spectrum was created by co-adding all spectra in the data cube that have emission from the QSO. This second spectrum had a significantly lower signal-to-noise ratio than the first, so we scaled the first spectrum to the second with a smooth polynomial function of the ratio between the two spectra. This procedure created a less noisy spectrum, but also avoided effects of the DAR residuals that shifts the spatial location of the QSO with wavelength. The spectra presented in Fig. 3.1 have not been corrected for galactic reddening.

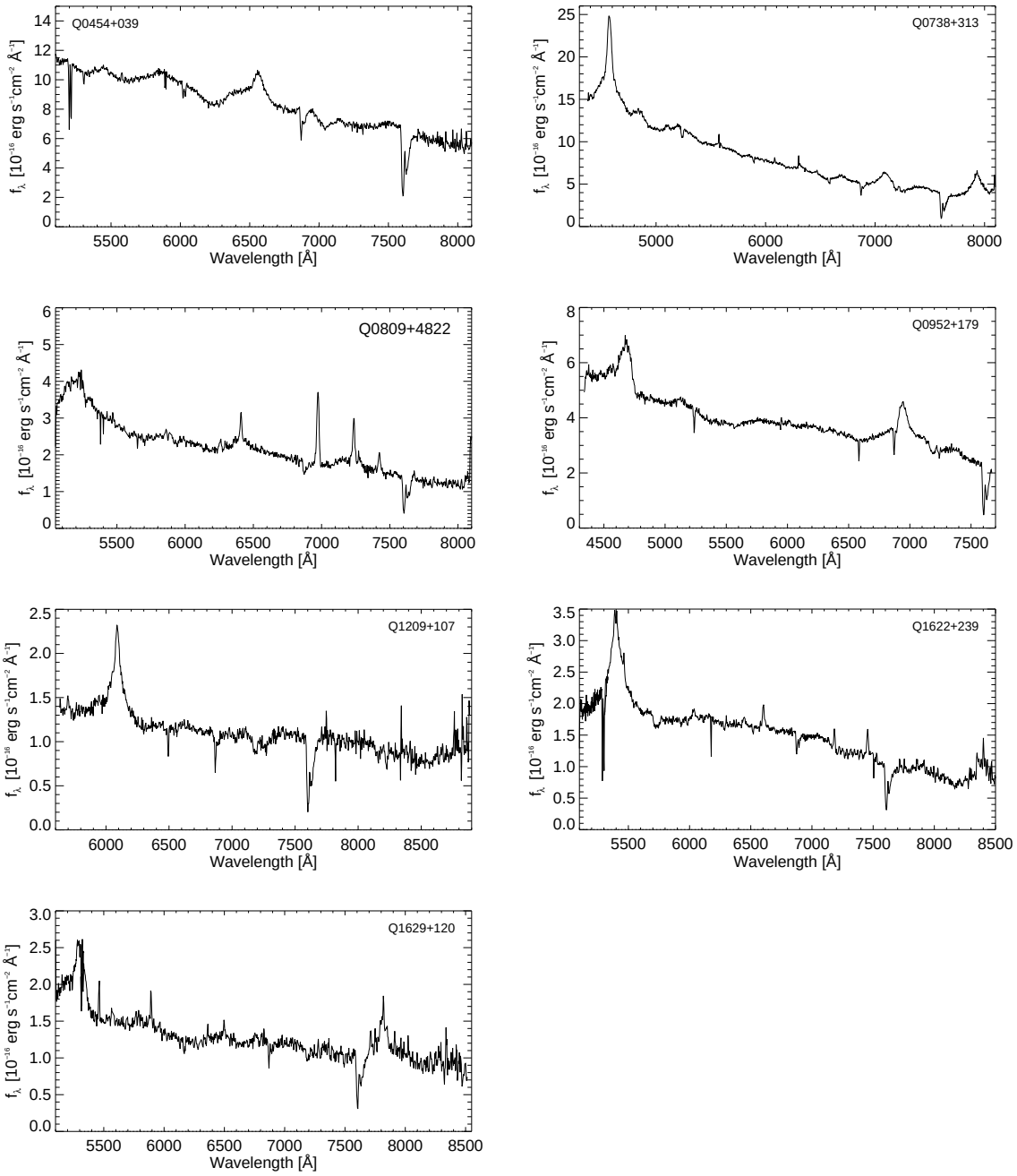

Fig. 3.1. Spectra of the QSOs not corrected for Galactic extinction and telluric absorption lines which are strong at $\lambda \approx 6900$ Å and $\lambda \approx 7600$ Å. At $\lambda > 8000$ Å residuals from sky subtractions are prominent. When more than one observation of a QSO has been done, the one-dimensional spectra from PMAS and INTEGRAL were combined to show the complete spectral range.

(1) QSO	(2) date	(3) Instrument	(4) exp.time (s)	(5) grating (mm^{-1})	(6) $\Delta\lambda$ (Å)	(7) seeing ($''$)	(8) conditions
Q0454+039	2004-01-16	INTEGRAL	7×1800	600	5000 – 8100		
Q0738+313	2004-01-16	INTEGRAL	4×1800	600	5000 – 8100		
	2003-04-27	PMAS	2×1800	300	4380 – 7680	0.8	stable
	2003-04-30	PMAS	2×1800	300	4380 – 7680	1.2	stable
Q0809+4822	2004-01-16	INTEGRAL	8×1800	600	5000 – 8100		
Q0952+179	2003-04-30	PMAS	3×1800	300	4300 – 7670	1.0 – 1.5	stable
Q1209+107	2003-05-03	PMAS	3×1800	300	5630 – 8880	0.7	stable
	2003-06-21	PMAS	4×1800	600	6860 – 8330		
Q1622+239	2003-04-27	PMAS	6×1800	300	5300 – 8510	1.0	stable
	2003-06-19	PMAS	4×1800	600	5100 – 6650	2.0	non phot
	2003-06-20	PMAS	8×1800	600	5100 – 6650	0.8	stable
Q1629+120	2003-04-30	PMAS	6×1800	300	5310 – 8520	1.5	non phot
	2003-06-18	PMAS	4×1800	600	5100 – 6650	1.5 – 2.0	stable
	2003-06-18	PMAS	4×1800	600	6450 – 7950		
	2003-06-22	PMAS	2×1800	600	5100 – 6650	2.0	non phot
	2003-06-22	PMAS	2×1800	600	6450 – 7950		

Table 3.2. Log of the observations. Seeing conditions for the PMAS data set were measured with the acquisition and guiding camera, and the stability of the relative photometry of guide stars are indicated in column (8). The INTEGRAL data were obtained in a single non-photometric night with deteriorating seeing conditions.

3.4 Search for DLA optical counterparts

From the data cubes we created narrow-band images centered on the wavelength for the expected emission lines at the DLA redshifts. Mostly, these images were dominated by emission from the QSO, so the QSO emission needed to be subtracted first.

Two different methods were investigated. The first used a two-dimensional Gaussian fitting of each monochromatic slice in the data cube. Assuming that the centroid and the spatial *FWHM* varied smoothly with wavelength, the fits could be used to create a model of the QSO emission in the data cube. Subtracting this model created a residual data cube that could be investigated for emission lines (see Sánchez et al. 2004).

A simpler method, applicable over wavelength ranges of $\sim$500 Å, was to subtract a scaled version of the one-dimensional QSO spectrum from each spaxel in the data cube. The scaling factor to be applied was estimated close to the expected wavelength of the emission lines. The reason for the imperfect QSO emission subtraction over longer wavelength ranges is due to the simplified application of the correction for theoretically predicted DAR, and the residual shifts of the QSO centroids present in the final data cubes.

We found that using the second method provided smaller residuals in the spectra, and the following results will use this latter method. When two emission lines from one object is expected to be present within the wavelength range, we created residual data cubes in both cases, where the scaling factor for the QSO subtraction was estimated close to the wavelengths of interest.

To label an emission line object detected in the residual data cube as a good candidate, we require that it be detected in a narrow-band image with a signal larger than 3σ above the background noise, and also the corresponding one-dimensional spectrum should have an emission line detected with a signal larger than 3σ above the background noise. To facilitate visualisation and detection of faint objects, the data cubes were interpolated to pixel sizes of $0\farcs2$ on the side using a Delaunay interpolation routine. A simpler nearest neighbor routine is not appropriate for the spacing between

the spaxels in the INTEGRAL data. Only the representation of the images are interpolated, the original spaxels were retained for creating the associated spectra.

Fig. 3.2 shows interpolated narrow-band images created from the data cubes. The left panels show narrow-band images of the QSO offset by ∼20 Å from the emission line wavelength, and overlayed by contours of an image centered on the emission after the QSO emission has been subtracted. The middle panels show the reverse as in the left panels, and the right panels show the extracted spectra of candidate emission line objects located in the images.

3.5 Notes on individual objects

In this section we describe the IFS data of the QSOs and the detected emission lines. Properties of the emission line candidates detected in each field are presented in Table 3.3. For each DLA system we describe previous imaging campaigns. Where the magnitudes derived from the IFS data differ from the literature values, this could be caused by an intrinsic QSO variability or by non-photometric conditions. With the available data, we could not estimate which is the case and we chose not to correct the flux levels of the calibrations.

Q0454+039

This QSO with $z_{\rm em} = 1.345$ has a DLA line at $z_{\rm abs} = 0.8596$. The only identified absorption lines in the QSO spectrum in Fig. 3.1 from the DLA system are the Mg II doublet at 2800 Å.

The galaxy labeled 'G1' in Steidel et al. (1995) is visible in our spectrum located 4″ east and 1″ north of the QSO. We confirm the redshift $z = 0.072$ from the detection of Hα and [O III] λ5007 lines. Other emission lines are too faint to be identified or close to strong sky lines.

In a narrow-band image centered on the [O II] emission line at $z = 0.8596$ (middle panel in Fig. 3.2) we find an object ∼1″ north of the QSO with a candidate emission line. Steidel et al. (1995) finds an object ∼2″ north of the QSO, which they suggest to be the DLA galaxy. In this case, an accurate location of the centroid of the emission line object in the INTEGRAL data cube is not possible due to undersampling of the seeing by the large fibre sizes. Therefore the positional uncertainty could be of the order of 1″, and we tentatively confirm that this object is indeed the DLA galaxy based on the rough positional agreement combined with an emission line at the expected wavelength. Other strong emission lines from this object fall outside the spectral window in the data cube.

The spectral resolution is too low to resolve the [O II] doublet. Assuming that the emission line is indeed [O II] the emission line luminosity is 2.7×10^{41} erg cm^{-2} s^{-1}, which corresponds to a star formation rate (SFR) of 4±2 M$_\odot$ yr^{-1} according to the conversion in Kennicutt (1998).

Q0738+313

Two DLA systems are found in the spectrum of this QSO with $z_{\rm em} = 0.630$ at $z_{\rm abs} = 0.2212$ and $z_{\rm abs} = 0.0912$ (Rao & Turnshek 2000).

The strong Mg II system at $z = 0.22$ was initially detected by Boisse et al. (1992) and later the two DLAs towards this QSO were detected based on UV spectroscopy (Rao & Turnshek 1998). An image of the QSO showed many galaxies nearby and the closest candidate, also found in Le Brun et al. (1993) is named 'G1'. Follow-up spectroscopy of this galaxy showed that the galaxy has a similar redshift as the $z = 0.2212$ DLA (Cohen 2001), and deep imaging though 7 bands indicated an elliptical or S0 morphology for the galaxy (Turnshek et al. 2001). No emission lines are reported from G1. We clearly detect the continuum emission from this galaxy in the INTEGRAL data cube but find no emission lines either. The signal-to-noise ratio in the combined spectrum is too low to identify absorption lines or the 4000 Å break which confirmed the $z = 0.2212$ redshift.

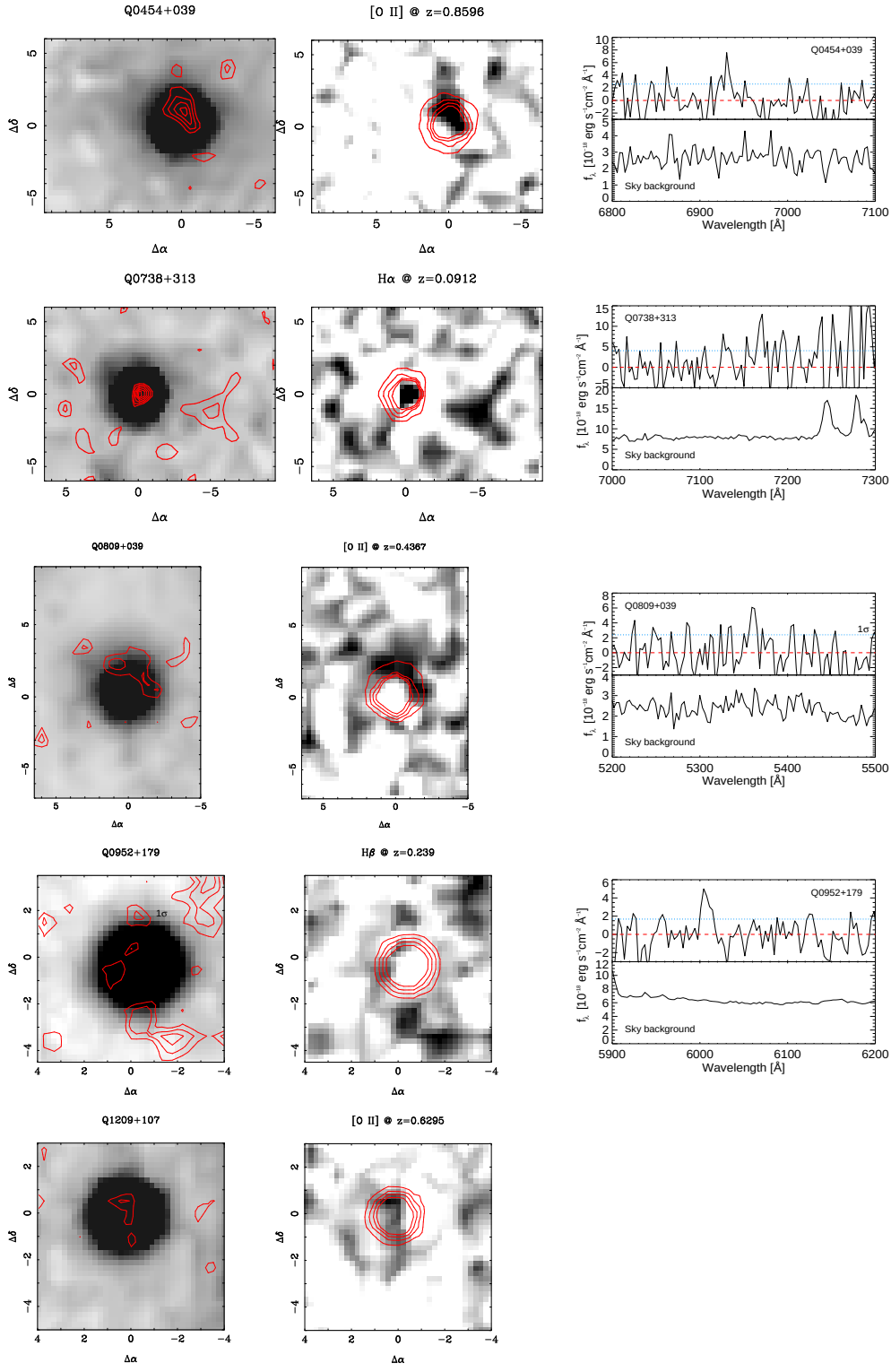

Fig. 3.2. Left panels: narrow-band images of the QSOs with overlayed contours of narrow-band images centered on wavelengths of the emission lines at the DLA redshifts. The middle panels show the reverse. All images have orientation north up and east left. Right hand panels: Spectra of candidates created from co-adding spaxels associated with candidate objects found in the narrow-band images. Only for Q1209+107 were no candidates found.

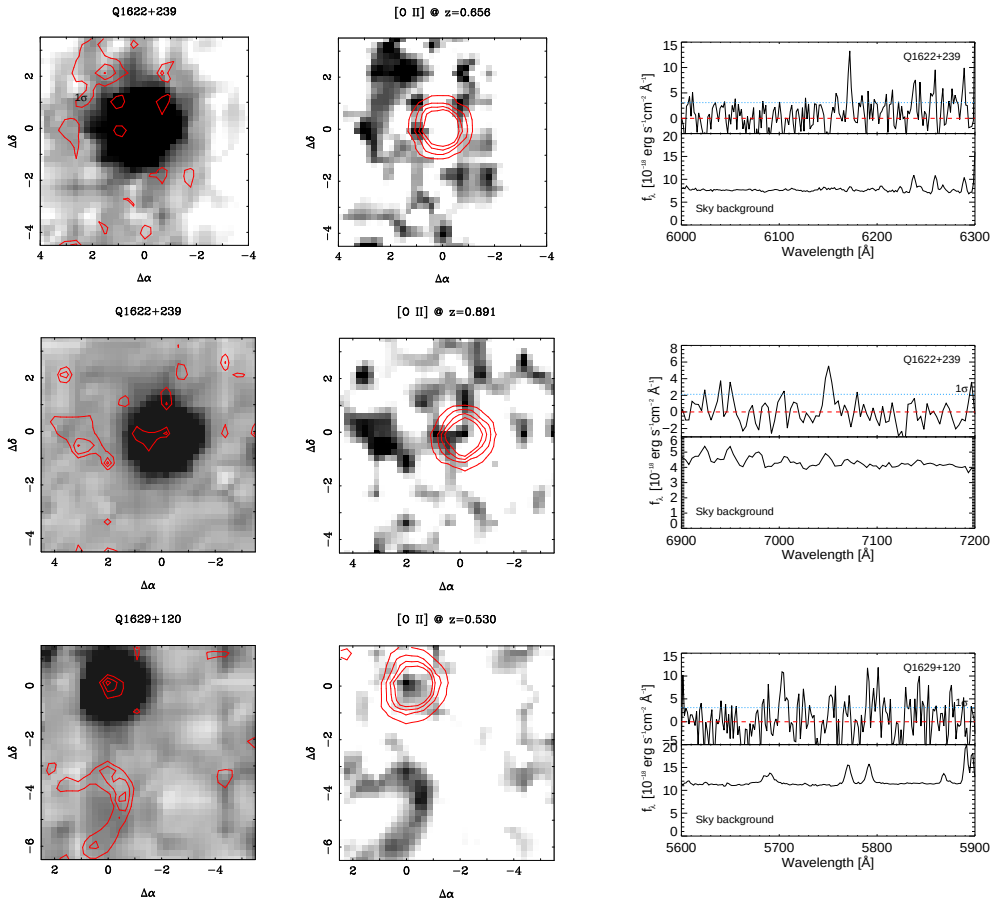

Fig. 3.2. Plots of the candidates – continued.

Cohen (2001) suggested that the $z = 0.0912$ DLA system was associated with a galaxy at $z = 0.106$ that could be associated with a group containing the DLA galaxy. However, the projected distance of 80 Mpc is larger than a typical cluster size. Turnshek et al. (2001) suggested instead that the $z = 0.0912$ DLA galaxy is associated with a faint fuzz and a 'jet' feature close to the QSO seen in a deep K band image; a fuzz that can also be found in an earlier r band image (Le Brun et al. 1993). X-ray data showed extended emission and Siemiginowska et al. (2003) suggested that the fuzz could be associated with the QSO, but they did not exclude the DLA galaxy interpretation. That the feature is not at the quasar redshift is supported by the narrow-band imaging study in Hutchings (1992), which indicated no associated structure in [O II] at the quasar redshift. Q0738+313 is a core-dominated quasar with an X-ray jet to the south (Siemiginowska et al. 2003), so the jet feature is not likely an optical counterpart at the quasar redshift.

Fig. 3.3 shows a comparison between the K band image from Turnshek et al. (2001) and narrow-band images created from the INTEGRAL data cubes. To facilitate a comparison, the QSO emission is retained in the narrow-band images, and only Fig. 3.2 shows a narrow-band image after QSO subtraction. The middle panels in Fig. 3.3 show images centered on Hα and [O III] at $z = 0.09$, and the right hand panels are corresponding off-band images. We clearly find structures similar to those observed by Turnshek et al. (2001). The associated one-dimensional spectrum has a low signal-to-noise ratio as shown in the left panel in Fig. 3.2. Because of the larger field of view of INTEGRAL, the brightest emission feature is not covered by the deeper PMAS data. Nevertheless, the PMAS data also confirm the presence of the structure extending towards the west in an Hα narrow-band image.

We therefore interpret the data as evidence for a spectroscopic confirmation of the DLA galaxy. We estimate the impact parameter for the brightest emission from Fig. 3.2 to be $5\farcs2$ or 8.8 kpc at the DLA redshift. Interpreting the detected emission line extracted from the INTEGRAL data as Hα emission at $z = 0.092$ the line flux correspond to SFR = 0.02 $M_\odot$ yr^{-1}.

Q0809+4822

This is a radio-loud QSO at $z_{\rm em} = 0.871$ with a DLA at $z_{\rm abs} = 0.4368$ where extended line emission is present at the QSO redshift (Crawford & Fabian 1989). Extended [O II] and [Ne III] emission line regions at $z = 0.871$ are detected in the INTEGRAL data cube, and we find that the location of the strongest emission is spatially coincident with the radio lobes[1] . The northern part of the extended emission confuses the detection of emission from the DLA galaxy because at the redshift of the DLA, Hβ coincides with [O II] at the QSO redshift, and the [O II] emission from the DLA also falls a the same wavelengths as the broad Mg II emission line from the QSO. Nevertheless, emission lines from a nearby galaxy identified by Boisse & Boulade (1990) at an impact parameter of $1\farcs5$ to the north was confirmed in C05, who determined $z_{\rm em} = 0.4374$.

An object is found $2''$ north of the QSO in a narrow-band image that includes [O II] emission at $z = 0.4378$ (see Fig. 3.2). The line flux and redshift is consistent with that reported in C05. Hβ emission which is reported to be strong in C05, is also found to be strong in these spaxels. It is possible that this object is contaminated by [O II] at the QSO redshift ($z = 0.871$) which falls close to the expected wavelength for Hβ at the DLA redshift. Because of this possibility we do not treat the line any further. Even if the Hβ line is contaminated, there is no doubt that the DLA galaxy has been detected. Table 3.3 reports the properties from the [O II] emission line.

[1] Further analysis will be presented in Chapter 7

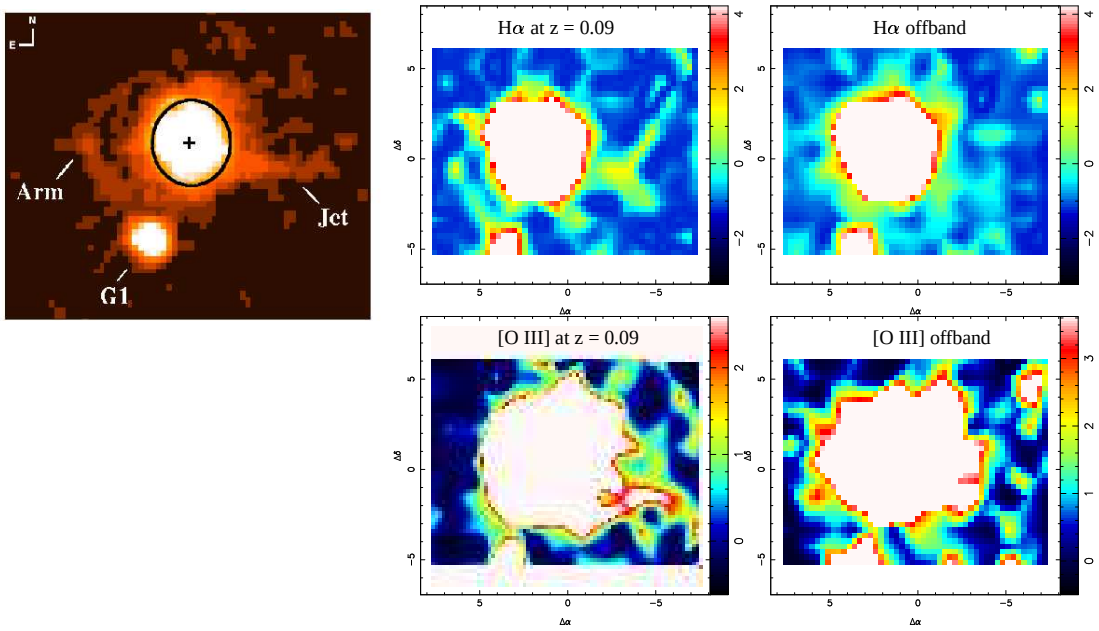

Fig. 3.3. Comparison of the K band image from Turnshek et al. (2001) (left) with a narrow-band image created from the data cube that includes Hα at $z = 0.0912$ (middle, top) and [O III] λ5007 (middle, bottom). In the left panel, the 'jet' feature extends $\sim$7$''$from the QSO center, which is similar to the extension in the middle panels. Image scalings have been chosen to enhance the jet feature in the data cubes. The images in the right column are off-band images created from wavelength regions next to those shown in the middle panels.

Q0952+179

This QSO with $z_{\rm em} = 1.478$ has a DLA line at $z_{\rm abs} = 0.239$. Multiband imaging of the field of Q0952+179 has shown 9 objects that could belong to the same host galaxy near the QSO sight line (Nestor et al. 2002; Rao et al. 2003). The closest part of these objects has a projected distance of less than 7 kpc to the QSO, i.e. less than 2$''$, and is assumed to be the DLA galaxy, but no spectroscopic confirmation exists.

Subtracting the QSO emission from the data cube reveals an object to the south-east roughly spatially coincident with the object labeled '2' in Rao et al. (2003). Extracting the spectra from this region, we find an emission line candidate. If interpreted as Hβ it has a redshift of $z = 0.235$ which is blue-wards of the DLA redshift by 600 km s^{-1}. No [O III] emission line is detected, but this can be in agreement with the expected emission line strength for star forming galaxies, where the [O III]/Hβ emission line ratio lies between 0.6 and 10 (Veilleux & Osterbrock 1987). No [O II] emission line is detected either for this object at this redshift, but the signal-to-noise ratio in the data cube decreases at the blue end of the spectral range. We derive a 2σ upper limit for the associated [O II] flux of 1×10^{-16} erg cm^{-2} s^{-1} based on simulations of artificial emission lines.

Alternatively, the line could be [O II] at $z = 0.615$. For this redshift the data do not cover other bright emission lines. While the line could be [O III] λ5007 at $z = 0.202$, the one-dimensional spectrum showed no corresponding Hβ or [O II] emission lines.

We can use the Hβ emission line to estimate the SFR. Assuming the ratio Hα/Hβ = 2.85 appropriate for case B recombination and a conversion from Hα to a SFR (Kennicutt 1998) gives SFR > 0.24 M$_\odot$ yr^{-1}. Extracting spectra in the region of the object denoted '1' about 3$''$ to the east of the QSO in Rao et al. (2003) revealed no emission lines, and the other objects detected near to the QSO sight line are outside the 8$''\times$8$''$ field of view.

Q1209+107

This QSO with $z_{\rm em} = 2.193$ has a DLA line at $z_{\rm abs} = 0.6295$. An object seen 1.″3 from the QSO (Arnaud et al. 1988), was later well resolved in a WFPC image which showed a galaxy with a magnitude m_{F702W} = 21.6 at an impact parameter of 1.″6 east of the QSO (Le Brun et al. 1997). Because this object is the primary candidate for the DLA galaxy we examined the spaxels around its position.

The [O II] line at the DLA redshift falls at the same wavelength as the broad C III] emission line from the QSO and the Hβ emission line lies close to strong skylines. A spectrum of spaxels co-added at the position of the galaxy shows no emission lines at the DLA redshift with a 3σ upper limit of 5×10^{-17} erg cm^{-2} s^{-1} for Hβ and 4×10^{-17} erg cm^{-2} s^{-1} for [O II]. Emission lines at other redshifts are not apparent in the co-added spectrum either, and no other candidates for the DLA galaxy were found in the IFS data either.

Cristiani (1987) find emission at $z = 0.3922$ from a galaxy at a distance of 7″ from the QSO. This galaxy is believed to be responsible for a strong Mg II system, but it lies outside the field of the data cube. We looked for emission line objects at this redshift from a potentially fainter object closer to the QSO sight line, but no emission line object was found.

Q1622+239

This QSO at $z_{\rm em} = 0.927$ has a DLA line at $z_{\rm abs} = 0.656$ and another strong absorption line at $z = 0.8908$.

A detailed investigation of the field surrounding the QSO is described in (Steidel & Dickinson 1992) who identify 3 Mg II selected galaxies, and suggests that the DLA at $z = 0.656$ could be related to a galaxy at an impact parameter of 14.″2. However, they do not rule out that a group of galaxies is present at that redshift and that the true DLA absorber lies closer to the QSO sight line. Using higher spatial resolution imaging with the HST/WFPC2 Steidel et al. (1997) find that the large over-density of galaxies in the field is mainly due to the presence of a cluster at the QSO redshift. They find no evidence for a closer galaxy candidate at the DLA redshift. In a narrow-band image centered on Hα at the DLA redshift no emission was found at a limit of 3.7×10^{-17} erg cm^{-2} s^{-1} within $30h^{-1}$ kpc from the QSO (Bouché et al. 2001), where $h^{-1} = H_0/100$ km s^{-1} Mpc^{-1}.

First the $z = 0.656$ DLA system is investigated. In the low resolution spectra which covers the largest spectral range, the region around the redshifted [O II] line is affected by a CCD defect, and potential emission lines could be contaminated by residuals from the QSO spectral subtraction. On the other hand, Hβ lies close to strong sky lines and the residuals from the sky subtraction are large. In any case, we find no candidate emission lines that satisfy the criteria for DLA galaxy candidate selection. Given the problems that were present in the low resolution data sets, the QSO was observed at higher spectral resolution. In the higher resolution data set, taken during the night with the best seeing, we find an [O II] emission line candidate offset by 2.″1 to the north-east. After applying a correction for galactic extinction using the reddening in Schlegel et al. (1998), the associated emission line flux is $(5.3\pm1.7)\times10^{-17}$ erg cm^{-2} s^{-1}, which corresponds to SFR = 1.4±0.5 M$_\odot$ yr^{-1}. We note that this value appears to be inconsistent with the Hα narrow-band study indicating a 3σ upper limit of 0.15 M$_\odot$ yr^{-1} kpc^{-2} (Bouché et al. 2001).

There are other reasons to suspect that the emission line may be a spurious detection. While the candidate emission line object does appear in two independent data cube combinations using the exposures from May 20, when analysing the higher resolution data taken on the night with poorer conditions this object was not detected. Furthermore, no object is present in a very deep WFPC2 image to a 3σ limiting magnitude of $m \approx 26$ within a 1″ radial aperture, which implies that the [O II] emission line has a very large equivalent width ($EW_{\rm rest} \gtrsim 180$ Å). Other studies of [O II]

emission lines from local star-forming galaxies have found only few [O II] EWs larger than 100 Å (Gallagher et al. 1989).

We can not check if the line is [O II] at $z = 0.656$ because only this line is covered. We examined for other emission lines to test if the line were either Hα, Hβ, or [O III], but no other lines were seen at the expected wavelengths. It could also potentially be Lyα at $z = 4.08$. Given the number density of Lyα emitters ($\sim 10^{-4}$ Mpc^{-3} per log luminosity in Hu et al. 2004), there is only a small probability (10^{-7}) that the detected line is Lyα within the small field and wavelength interval in the narrow-band image.

The strong absorption line at $z = 0.8908$ has the column density $8 \times 10^{17} < N(\mathrm{H\,I}) < 2.5 \times 10^{19}$ cm^{-2} (Steidel et al. 1997). The absorbing galaxy at $z = 0.892$ was detected $\sim 3''$ east of the QSO (Steidel et al. 1997, ; galaxy ID Number 3). Although formally not satisfying the DLA criterion, we note that the $z = 0.8908$ galaxy is detected in the lowest resolution IFS data cube. An emission line object with a flux of 5×10^{-17} erg cm^{-2} s^{-1} is found $2\farcs8$ east of the QSO and interpreting the line as [O II] the redshift is $z = 0.8913 \pm 0.0005$ consistent with that reported in Steidel et al. (1997). No other strong emission lines from this object at this redshift is within the wavelength range in the data cube.

In conclusion we suggest the detection of an [O II] emission line from the $z = 0.656$ DLA galaxy, but its properties appear different from galaxies selected in flux limited surveys. Therefore, this needs confirmation by deeper data.

Q1629+120

This QSO at $z_{\rm em} = 1.795$ has a DLA line at $z_{\rm abs} = 0.532$. In an imaging study a DLA galaxy candidate was found at an impact parameter of $3\farcs2$ corresponding to 20.2 kpc for the adopted cosmology, and a photometric redshift estimate indicated that the galaxy is the DLA counterpart (Rao et al. 2003).

Co-adding the spaxels around the position of the DLA galaxy candidate shown in Fig. 3.2 reveals an emission line that can be interpreted as [O II] emission at the DLA redshift. As listed in Table 3.3 the emission line has $z_{\rm em} = 0.5304$ corresponding to a velocity offset of 280 km s^{-1}. The position of this object in the data cube is offset by $1''$ compared to that reported in Rao et al. (2003). However, combining the positional uncertainties in the IFS data with a possible offset in emission lines with respect to the continuum emission, we consider this line as evidence for the DLA spectroscopic confirmation.

3.6 Impact parameters

This section analyses the properties of both candidate and confirmed emission line objects described in the previous section. Table 3.3 lists the properties of the emission lines from Fig. 3.2 where we have included the Lyman limit system at $z = 0.891$ towards Q1622+239 as well. Line fluxes listed in Table 3.3 are detected with a signal-to-noise ratio less than 3 in most cases. We also calculate the significance of the detection by dividing the line flux by $\sqrt{n_p} \times s/n$, where n_p is the number of pixels that show excess emission and s/n is the signal-to-noise level in the background. This quantity is listed in Column 8.

If DLAs belong to neutral gas disks in galaxies and these galaxies have a very simple structure which can be approximated by exponential disks as for local galaxies, it is expected that there is an anticorrelation between the impact parameter and the column density. A combined imaging and spectroscopic study of galaxies causing Lyα absorption lines below the DLA regime indicated exactly such a relation (Lanzetta et al. 1995a). This anticorrelation improves when including a parameter for the galaxy luminosities (Chen et al. 1998, 2001).

(1) QSO	(2) ΔRA ($''$)	(3) ΔDEC ($''$)	(4) b (kpc)	(5) z	(6) f_λ (erg cm^{-2} s^{-1})	(7) Δ V (km s^{-1})	(8) σ	(9) *FWHM* (km s^{-1})
Q0454+039	0.2	0.8	6.3	0.8591	(7.4±3.2)×10^{-17}	–80	11	540±250
Q0738+313	–5.0	–1.3	8.8	0.0920	(11.5±8.0)×10^{-17}	220	8	230±200
Q0809+039†	1.0	2.0	12.7	0.4378	(9.0±3.4)×10^{-17}	220	8	810±180
Q0952+179	0.0	2.2	8.2	0.2354	(6.5±2.3)×10^{-17}	–640	15	520±220
Q1622+239	1.3	1.7	14.9	0.6560	(4.5±1.5)×10^{-17}	0	8	50±140
†	2.8	0	21.8	0.8913	(6.1±2.4)×10^{-17}	80	12	330±130
Q1629+120†	–0.1	–2.2	14.0	0.5304	(6.9±3.1)×10^{-17}	320	7	280±130

Table 3.3. Properties of the emission lines from DLA galaxies. Objects indicated by '†' are previously confirmed, the others are candidates. Column 2, 3, and 4 list the offsets of the emission line object in RA, DEC, and projected distance in kpc at the DLA (emission line) redshifts in Col. 5, respectively. Columns 6 and 7 list the integrated emission line flux where no correction of Galactic extinction has been applied and the velocity offset from the DLA redshift. Column 8 lists the integrated significance of the emission lines and Column 9 the line width of the emission lines after correcting for the instrumental resolution.

Fig. 3.4 shows the column density of the DLAs as a function of the impact parameter of the emission object estimated in the IFS data cubes. The plot includes two Lyman limit systems/sub-DLAs; the $z = 0.8913$ galaxy towards Q1622+239 and the sub-DLA galaxy at $z = 0.16$ towards PHL 1226 taken from a related IFS study (Christensen et al. 2005). In that paper we analysed emission lines from a galaxy at an impact parameter of 17.6 kpc which was known previously (labeled G4 in Bergeron et al. 1988), and which gives rise to a sub-DLA with $N(\mathrm{H\,I}) = (5 \pm 2) \times 10^{19}$ cm^{-2} (Rao 2004, private communication). A clear trend of an anticorrelation is present and a fit to an exponential profile, $N(b) = N_0 \exp(-b/h)$ with a scale length h, gives log$N_0 = 21.8 \pm 0.1$ cm^{-2} and $h = 4.8 \pm 0.2$ kpc. Such a scale length is similar to H I measurements for local disk galaxies (e.g. Thomas et al. 2004). Errors for this relation are derived assuming zero uncertainty of the impact parameters and a minimum uncertainty of 0.1 in log$N(\mathrm{H\,I})$. The presence of an anticorrelation is supported by a Pearson test which gives a correlation coefficient of –0.90, where a value of –1 indicates a perfect anticorrelation. A generalised Kendall's tau test rejects the null hypothesis that a correlation is not present with a probability of 99%.

Such a tight correlation is probably caused by the small number of galaxies involved, and including the galaxies in the sample by C05 would indeed increase the scatter in the correlation. For a tight correlation to be present DLA galaxies should belong to a single population of galaxies in contradiction with observations (Le Brun et al. 1997). Furthermore, the correlation is sensitive to the column density of the two Lyman limit systems included. As shown by simulations of the $N(\mathrm{H\,I})$ versus impact parameter the scatter can be very large (C05). However, we point out that we have only included those DLA galaxies detected with emission lines. The $z = 0.2212$ DLA galaxy at an impact parameter of 20 kpc and log $N(\mathrm{H\,I})$ = 20.9 cm^{-2} (Cohen 2001; Turnshek et al. 2001) does not agree with the indicated relation. Since this galaxy is confirmed by absorption lines in its spectrum the galaxy type could be different from the others.

3.7 Conclusions and discussion

Using integral field spectroscopy we have carried out an investigation of $z < 1$ DLA systems to look for emission lines from the galaxies that cause DLA absorption lines in spectra of background

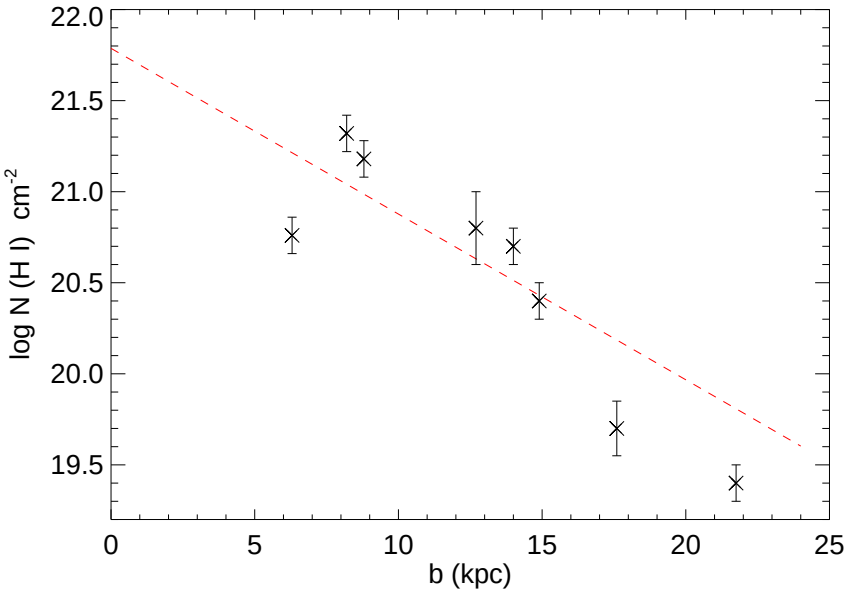

Fig. 3.4. Column density of the DLAs as a function of the impact parameters estimated from emission line objects in the IFS data cubes. An exponential profile fit to all the data points is shown by the dashed line. This profile has a central column density of log $N(\mathrm{H\,I})$ = 21.8±0.1 cm^{-2} and a scale length of 4.8±0.2 kpc.

QSOs. Our sample includes seven DLAs and involves a third of the currently known DLA systems at these redshifts.

Apart from the reconfirmation of the emission lines from the DLA galaxy towards Q0809+4822 we detect candidate emission lines from 4 new objects. Additionally, we detect an emission line from the DLA galaxy towards PKS 1629+120 and confirm the photometric redshift in Rao et al. (2003). New detections of emission lines from DLA galaxies are found for the $z = 0.0912$ DLA toward Q0738+313, the $z = 0.8596$ DLA towards Q0453+039, the $z = 0.239$ DLA towards Q0952+179, while a candidate for the $z = 0.656$ towards Q1622+239 is questioned due to its inferred large [O II] equivalent width. All these candidate emission lines are, like the previously confirmed lines in this IFS study, detected at 3σ levels above the background noise.

The seven objects detected in the data cubes, including one sub-DLA towards PHL 1226 (Christensen et al. 2005), show a significant anticorrelation between the impact parameter and the column density of the DLA clouds. This can be explained if DLA galaxies constitute a population of galaxies with an average scale length of ∼5 kpc which is similar to that of spiral galaxies. We also explained that this simple relation accounts for those DLA galaxies detected by their emission lines in the IFS data. One other DLA galaxy which does not have detected emission lines falls outside this relation.

Our re-confirmations of emission lines from previously known galaxies make us conclude that IFS is a useful technique for the identification of emission lines from galaxies associated with DLA lines in QSO spectra. For future investigations, when the candidate DLA galaxies are unknown, IFS can be used as a first step to detect emission lines. A similar study as presented here performed on an 8m class telescope would obtain higher signal and more than one emission line which is necessary to determine the redshift uniquely. As shown in Chen et al. (2005), high signal-to-noise ratio slit spectroscopy data allow determination of abundances and rotation curves for the DLA galaxies. In the case that an emission line region is not spatially coincident with the continuum emission or that the emission line regions are extended, IFS is suitable to locate the emission lines. Slit spectroscopy

on the other hand provides higher through-puts than IFS and is a useful alternative to obtain higher signal data for a detailed study, when the slit location and orientation can be determined in advance.

Acknowledgments. L. Christensen acknowledges support by the German Verbundforschung associated with the ULTROS project, grant no. 05AE2BAA/4. S.F. Sánchez acknowledges the support from the Euro3D Research Training Network, grant no. HPRN-CT2002-00305.

References

Arnaud, J., Hammer, F., Jones, J., & Le Fevre, O. 1988, A&A, 206, L5
Arribas, S., Carter, D., Cavaller, L., et al. 1998, in Proc. SPIE Vol. 3355, p. 821-827, Optical Astronomical Instrumentation, Sandro D'Odorico; Ed., 821–827
Becker, T. 2002, PhD thesis, Astrophysikalisches Institut Potsdam, Germany
Bergeron, J., Boulade, O., Kunth, D., et al. 1988, A&A, 191, 1, (B88)
Boisse, P. & Boulade, O. 1990, A&A, 236, 291
Boisse, P., Boulade, O., Kunth, D., Tytler, D., & Vigroux, L. 1992, A&A, 262, 401
Boisse, P., Le Brun, V., Bergeron, J., & Deharveng, J. 1998, A&A, 333, 841
Bouché, N., Lowenthal, J. D., Charlton, J. C., et al. 2001, ApJ, 550, 585
Chen, H., Lanzetta, K. M., Webb, J. K., & Barcons, X. 1998, ApJ, 498, 77
—. 2001, ApJ, 559, 654
Chen, H.-W., Kennicutt, R. C., & Rauch, M. 2005, ApJ, 620, 703
Chen, H.-W. & Lanzetta, K. M. 2003, ApJ, 597, 706
Christensen, L., Schulte-Ladbeck, R. E., Sánchez, S. F., et al. 2005, A&A, 429, 477
Cohen, J. G. 2001, AJ, 121, 1275
Cohen, R. D., Beaver, E. A., Diplas, A., et al. 1996, ApJ, 456, 132
Crawford, C. S. & Fabian, A. C. 1989, MNRAS, 239, 219
Cristiani, S. 1987, A&A, 175, L1
Curran, S. J., Webb, J. K., Murphy, M. T., et al. 2002, Publications of the Astronomical Society of Australia, 19, 455
Ellison, S. L., Kewley, L. J., & Mallén-Ornelas, G. 2005, MNRAS, 357, 354
Filippenko, A. V. 1982, PASP, 94, 715
Fruchter, A. S. & Hook, R. N. 2002, PASP, 114, 144
Gallagher, J. S., Hunter, D. A., & Bushouse, H. 1989, AJ, 97, 700
Garcia-Lorenzo, B., Sánchez, S. F., Mediavilla, E., Gonzales-Serano, J. I., & Christensen, L. 2005, ApJ, 621, 146
Haehnelt, M. G., Steinmetz, M., & Rauch, M. 1998, ApJ, 495, 647
Hu, E. M., Cowie, L. L., Capak, P., et al. 2004, AJ, 127, 563
Hutchings, J. B. 1992, AJ, 104, 1311
Kennicutt, R. C. 1998, ARA&A, 36, 189
Kulkarni, V. P. & Fall, S. M. 2002, ApJ, 580, 732
Kulkarni, V. P., Fall, S. M., Lauroesch, J., et al. 2005, ApJ, 618, 68
Lacy, M., Becker, R. H., Storrie-Lombardi, L. J., et al. 2003, AJ, 126, 2230
Lanzetta, K. M., Bowen, D. V., Tytler, D., & Webb, J. K. 1995a, ApJ, 442, 538
Lanzetta, K. M., Wolfe, A. M., & Turnshek, D. A. 1995b, ApJ, 440, 435
Le Brun, V., Bergeron, J., Boisse, P., & Christian, C. 1993, A&A, 279, 33
Le Brun, V., Bergeron, J., Boisse, P., & Deharveng, J. M. 1997, A&A, 321, 733
Nestor, D. B., Rao, S. M., Turnshek, D. A., et al. 2002, in Astronomical Society of the Pacific Conference Series, 34

Nestor, D. B., Turnshek, D. A., & Rao, S. M. 2004, ApJ accepted (astro-ph/0410493)
Pettini, M., Ellison, S. L., Steidel, C. C., Shapley, A. E., & Bowen, D. V. 2000, ApJ, 532, 65
Prochaska, J. X., Gawiser, E., Wolfe, A. M., Castro, S., & Djorgovski, S. G. 2003, ApJL, 595, L9
Prochaska, J. X. & Wolfe, A. M. 1997, ApJ, 487, 73
Rao, S. M. 2005, in Probing Galaxies through Quasar Absorption Lines, ed. P. R. Williams, C. Shu, & B. Ménard, IAU Colloquium 199
Rao, S. M., Nestor, D. B., Turnshek, D. A., et al. 2003, ApJ, 595, 94
Rao, S. M. & Turnshek, D. A. 1998, ApJL, 500, L115
—. 2000, ApJS, 130, 1
Roth, M. M., Bauer, S., Dionies, F., et al. 2000, in Proc. SPIE, Vol. 4008, 277–288
Roth, M. M., Becker, T., Bauer, S.-M., et al. 2005, PASP, accepted
Sánchez, S. F. 2004, AN, 325, 167
Sánchez, S. F., Garcia-Lorenzo, B., Mediavilla, E., González-Serrano, J. I., & Christensen, L. 2004, ApJ, 615, 156
Schlegel, D. J., Finkbeiner, D. P., & Davis, M. 1998, ApJ, 500, 525
Siemiginowska, A., Stanghellini, C., Brunetti, G., et al. 2003, ApJ, 595, 643
Snijders, M. A. J., Boksenberg, A., Penston, M. V., & Sargent, W. L. W. 1982, MNRAS, 201, 801
Steidel, C. C., Bowen, D. V., Blades, J. C., & Dickenson, M. 1995, ApJL, 440, L45
Steidel, C. C. & Dickinson, M. 1992, ApJ, 394, 81
Steidel, C. C., Dickinson, M., Meyer, D. M., Adelberger, K. L., & Sembach, K. R. 1997, ApJ, 480, 568
Steidel, C. C., Pettini, M., Dickinson, M., & Persson, S. E. 1994, AJ, 108, 2046
Storrie-Lombardi, L. J. & Wolfe, A. M. 2000, ApJ, 543, 552
Thomas, H. C., Alexander, P., Clemens, M. S., et al. 2004, MNRAS, 351, 362
Turnshek, D. A., Rao, S. M., Nestor, D., et al. 2001, ApJ, 553, 288
Veilleux, S. & Osterbrock, D. E. 1987, ApJS, 63, 295
Wolfe, A. M., Turnshek, D. A., Smith, H. E., & Cohen, R. D. 1986, ApJS, 61, 249

CHAPTER 4

Integral Field Spectroscopy of Extended Lyα Emission from the DLA Galaxy in Q2233+131

L. CHRISTENSEN[1], S. F. SÁNCHEZ[1], K. JAHNKE[1], T. BECKER[1], L. WISOTZKI[1,2], A. KELZ[1], L. Č. POPOVIĆ[1,3], M. M. ROTH[1]

[1] Astrophysikalisches Institut Potsdam, An der Sternwarte 16, 14482 Potsdam, Germany

[2] Potsdam University, Am Neuen Palais 10, 14469 Potsdam, Germany

[3] Astronomical Observatory, Volgina 7, 11160 Belgrade 74, Serbia

Abstract

This paper presents observations of an extended Lyman-α emission nebula surrounding the galaxy responsible for the Damped Lyman-α Absorption (DLA) line in the spectrum of the quasar Q2233+131. With the Potsdam Multi Aperture Spectrophotometer (PMAS) we measure the properties of the extended Lyα emission in an area of $3''\times5''$ having a total line flux of $(2.8 \pm 0.3) \times 10^{-16}$ erg cm^{-2} s^{-1}, which at redshift $z = 3.15$ corresponds to a luminosity of $(2.4^{+0.3}_{-0.2})\times10^{43}$ erg s^{-1} and a size of 23$\times$38 kpc. The location of the emission is spatially coincident with the previously detected DLA galaxy, but extends significantly beyond its limb. We argue that the Lyα emission is likely to be caused by an outflow from the DLA galaxy, presumably powered by star formation. In the case of negligible dust extinction, the Lyα luminosity indicates a star-formation rate of 19 ± 10 M$_\odot$ yr^{-1} consistent with that derived from the UV continuum flux from the parent galaxy. The wind velocity indicated by the integral field spectra is of the order of several hundred km s^{-1}. We find no indication of emission originating in a rotating disk.

4.1 Introduction

High redshift quasars (QSOs) show multiple absorption lines bluewards of the redshifted 1216 Å Lymanα (Lyα) wavelength. Known as the Lymanα forest, this is caused by absorption in neutral hydrogen clouds along the line of sight towards the QSO. Clouds having column densities larger than 2×10^{20}cm^{-2} give rise to line profiles with broad wings characteristic of damped Lyα lines. To date approximately 150 Damped Lyα Absorbers (DLAs) with redshifts of $0.1 < z < 4.6$ have been confirmed (Curran et al. 2002). It has been found that DLAs contain a significant fraction of total gas mass compared to the mass of the stars in present day galaxies (Wolfe et al. 1995;

† This chapter is published in *Astronomy & Astrophysics*, 2004, 417, 487

Storrie-Lombardi et al. 1996; Storrie-Lombardi & Wolfe 2000), and it is questioned whether there is a significant evolution with redshift (Rao & Turnshek 2000). Spectroscopic observations have shown that the DLAs have metallicities of 0.01–1 times solar with a mild increase with decreasing redshift (Prochaska et al. 2003), suggesting that DLAs are star-forming objects. Nevertheless, the relation between DLAs and galaxies is not well understood. At higher redshifts, the DLA galaxies have been suggested to be thick disks or the progenitors of present day spirals galaxies (Wolfe et al. 1986), while others suggest that the counterparts could be dwarfs (Hunstead et al. 1990), or galaxy building blocks in a hierarchical merging scenario (Haehnelt et al. 1998).

Many investigations have been performed in order to establish what the galaxy counterparts to the DLAs resemble most (e.g. Le Brun et al. 1997; Warren et al. 2001; Colbert & Malkan 2002). Typically, deep broad-band or narrow-band imaging of the fields containing the DLAs has been carried out, and objects near the line of sight of the QSOs are detected after subtraction of the QSO point spread function. These candidate DLA galaxies are typically faint. Successive follow-up spectroscopy of the candidates is required to reveal whether or not they have the same redshift as the DLA line. Only in 4 cases DLA galaxies have been confirmed this way for the high redshift ($z \gtrsim 1.9$) DLA galaxies (Møller & Warren 1993; Djorgovski et al. 1996; Fynbo et al. 1999; Møller et al. 2002). In two additional cases Lyα emission lines have been detected in the troughs of the DLA lines in the QSO spectra (Leibundgut & Robertson 1999; Ellison et al. 2002).

We here present a study of the Q2233+131 at $z = 3.295$, which has a DLA line at $z = 3.153$ (Sargent et al. 1989). The metallicity of the DLA is [Fe/H] = –1.4 (Lu et al. 1997), and the column density of H I is below the classical limit of a DLA line, having $N_{\rm H\,I} = 1\times10^{20}$ cm^{-2}, thus formally characterizing this as a Lyman-Limit system. In accordance with previous papers on this object we will continue to denote it a DLA absorber. A candidate galaxy responsible for the absorption was found at an impact parameter of $2\farcs3$ using the Lyman break technique, suggesting a redshift larger than 3 (Steidel et al. 1995). This object was confirmed as the absorbing galaxy having the same redshift as the DLA line (Djorgovski et al. 1996, hereafter D96). These authors measured a Lyα line flux of $(6.4\pm1.2)\times10^{-17}$ erg cm^{-2} s^{-1} in a Keck long-slit spectrum and found the magnitudes of the Lyman break galaxy of $R = 24.8 \pm 0.1$ and $V = 25.1 \pm 0.2$. Warren et al. (2001) found $H = 25.34 \pm 0.17$ for the galaxy using near-IR photometry with the HST/NICMOS, and Møller et al. (2002) found $V_{50} = 25.75 \pm 0.12$ with STIS images.

With integral field spectroscopy the conventional two step approach for confirming a DLA galaxy can be avoided. A previous attempt to use this technique only yielded an upper limit for the line emission from the DLA galaxy in BR 1202–0725 (Petitjean et al. 1996), while the spectral range of the observations of the DLA system in APM 08279+5255 did not cover the appropriate wavelengths for the redshifted Lyα emission (Ledoux et al. 1998b). We show here that with the Potsdam Multi Aperture Spectrophotometer (PMAS) instrument we not only detect Lyα emission from the DLA galaxy at $z = 3.15$, but we find that the object causing the Lyα emission is extended, and the line flux is larger than reported previously in the literature.

In Sect. 4.2 of this paper we will describe the spectroscopic observations, and the procedures for reducing the data. We analyse the spectra of the QSO and the extended emission from the DLA in Sects. 4.3 and 4.4, respectively, addressing the nature of the extended emission. The relation between the Lyα emission and the location of the DLA galaxy seen in high spatial resolution Hubble Space Telescope (HST) images is described in Sect. 4.5. Similarities with other Lyα emitting objects are described in Sect. 4.6, which leads to possible interpretations for the origin of the extended Lyα nebula in Sect. 4.7. The ionised gas mass in the nebula is estimated in Sect. 4.8. In Sect. 4.9 we present our conclusions.

Throughout the paper we assume a flat Universe with $H_0 = 70$ km s^{-1} Mpc^{-1}, $\Omega_m = 0.3$, and $\Omega_\Lambda = 0.7$. The redshift $z = 3.15$ then corresponds to a luminosity distance of 8.3×10^{28} cm (27.0 Gpc), $1''$ corresponds to a linear size of 7.6 kpc, and the look-back time is 11.5 Gyr.

4.2 Observations and data reduction

The PMAS integral field instrument uses two cameras: A cryogenic acquisition and guiding camera (A&G camera) that can be used for imaging in addition to the integral field spectrograph (IFS) (Roth et al. 2000). The A&G camera has a SITe TK1024 chip with 1k×1k pixels with a scale of $0\farcs2$ per pixel giving a field of view of $3\farcm4 \times 3\farcm4$. The PMAS spectrograph is equipped with 256 fibers coupled to a 16×16 lens array, that we used with a spatial sampling of $0\farcs5 \times 0\farcs5$ per fiber on the sky, resulting in a field of view of $8'' \times 8''$. The spectrograph camera has a SITe ST002A 2k×4k CCD and its 256 spectra have a FWHM of ∼2 pixels when using a 2×2 binned read-out mode. The spectra are aligned on the CCD with 7 pixels between adjacent spectra making cross-contamination negligible.

PMAS is mounted on the 3.5m telescope at Calar Alto. We observed Q2233+131 on Sep. 2 2002 for a total of 7200 s (4×1800 s) at an airmass between 1.094 and 1.15 and a seeing between $1\farcs0$ and $1\farcs3$ measured by the A&G camera. Using a 300 gr/mm grating yielded a spectral resolution of 6 Å while the grating was set to cover the wavelength range of 3930–7250 Å. Calibration images were obtained following the science exposures and consisted of spectra of emission line lamps (HgNe), and spectra of a continuum lamp needed to locate the 256 individual spectra on the CCD. Observations of the spectrophotometric standard stars BD +28° 4211 and Hz4 were obtained during the night for flux calibration.

Reduction of the data was done in IDL with P3D_online, a software package written specifically for reducing PMAS data (Becker 2002). After bias subtraction the 256 spectra were extracted from the two-dimensional frames. Wavelength calibration was performed using the emission line lamp spectra. For the flat fielding the average transmission of each fiber was determined using exposures of the sky at twilight. Cosmic ray hits were removed from each of the 4 files using the L.A.Cosmic routine within IRAF (van Dokkum 2001), and the rejected pixels were inspected by eye checking that no pixels close to the Lyα emission line were affected. The data cubes were corrected for the effect of differential atmospheric refraction using the formula of Filippenko (1982). Given the small airmass of Q2233+131 during the observation the effect is small, but not negligible at long wavelength intervals. At the wavelength of the DLA line the effect can be ignored, since this was the reference wavelength for estimating the relative offsets before combining the 4 frames. This method ensures that the position of the DLA galaxy relative to the centroid of the QSO at other wavelengths is not shifted. In the end the four files were co-added, resulting in a data cube of dimensions 16×16×1024 pixels.

For subtraction of the sky background, an average background spectrum was created by co-adding several spectra at the edge of the field of view, uncontaminated by the QSO flux, and subtracted from all 256 individual spectra. All further data calibration was done using IRAF. For the standard star observations we coadded all spectra within a radial aperture of $3''$, and compared the one-dimensional standard star spectrum with table values to create a sensitivity function taking into account the atmospheric extinction typical for Calar Alto (Hopp & Fernandez 2002). Finally, the spectra were flux calibrated using this sensitivity function.

Further analysis and inspection of the data was performed with the "Euro3D Visualization Tool", which is a very efficient tool made for visualizing integral field data (Sánchez 2004).

4.3 The QSO spectrum

We constructed narrow-band images by selecting appropriate wavelength intervals in the combined 3D data cube, resulting in images with 16×16 spatial pixels ("spaxels"). In Fig. 4.1 such an image of Q2233+131 is shown in the wavelength range 5200–5300 Å. For creating a one-dimensional

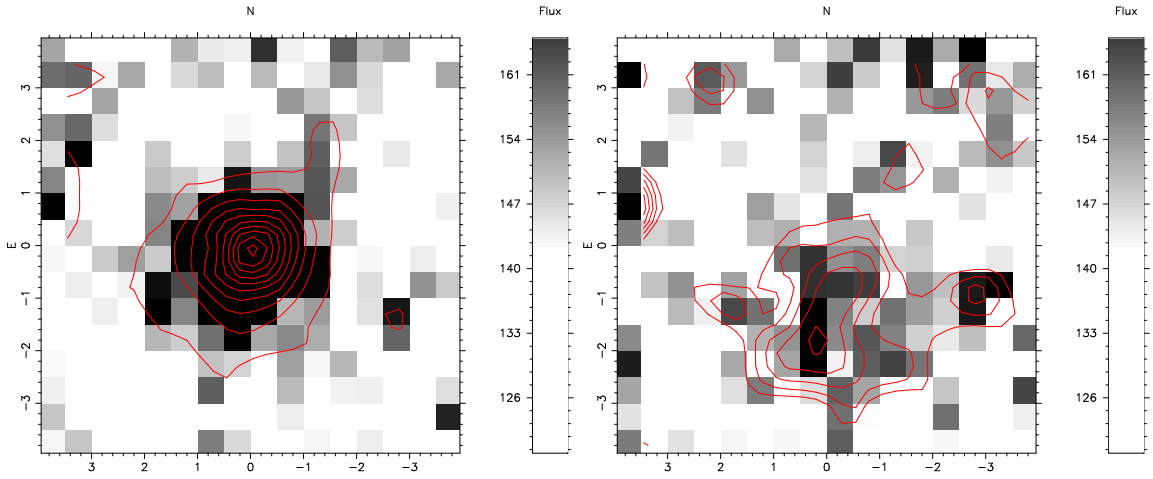

Fig. 4.1. Left hand panel: Image of Q2233+131 in the wavelength range 5200–5300 Å. This image shows the 16×16 spatial pixel ("spaxel") field of view of PMAS corresponding to $8''\times8''$. The QSO is centered in the field at (0,0). Right hand panel: Co added narrow-band image of the Q2233+131, with a field of view of $8''\times8''$, north is up and east is left. Selecting the wavelength range 5040–5055 Å an extended object of roughly $5''\times3''$ appears, which is the extended Lyα emission from the DLA galaxy. The selected wavelengths correspond to the DLA absorption trough in the QSO spectrum. The centroid of the QSO is at (0,0) while the position of the DLA galaxy found from the broad band observations in D96 and in the space-based images is at ($-0\farcs9$,$-2\farcs2$). Apparently, the extended source overlaps with the position of the QSO, but this is caused by the fact that some QSO emission is present at the longest selected wavelengths ($\lambda > 5050$Å), as emission from the red wing of the DLA line has been included. Contours of 5–8σ levels above the background have been overplotted for guiding the eye. The contours correspond to the combined emission from the Lyα nebula and the QSO. The high signal at the left edge of the field at (3.5,1) is caused by a bad fiber.

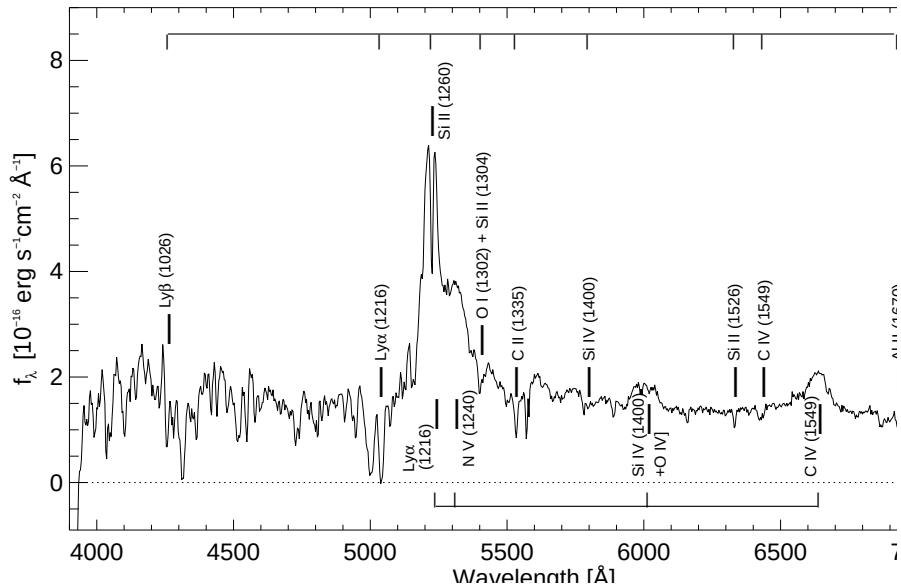

Fig. 4.2. Spectrum of Q2233+131. All spaxels within a radial aperture of $2''$ have been coadded and then scaled to the total flux of the QSO, measured within a $3''$ radial aperture. The bright line at 5200 Å is Lyα emission from the QSO. This and other emission lines from the QSO are labeled under the spectrum. The DLA line at 5050 Å and the corresponding metal absorption lines belonging to this system are labeled above the spectrum. Redshifts of all lines are given in Table 4.1.

Ion	$\lambda_{\rm lab}$ [Å]	$z_{\rm em}$	$z_{\rm abs}$
Lyα	1215.67	3.2949	
N V	1238.82, 1242.80	3.2840	
Si IV + O IV] (blends)	1400	3.2881	
C IV	1548.20, 1550.78	3.2838	
Lyα	1215.67		3.1476
Si II	1260.42		3.1468
O I	1302.16		3.1479
C II	1334.53		3.1476
Si IV	1400		3.1490
Si II	1526.71		3.1485
C IV	1548.20, 1550.78		3.1477
Al II	1670.789		3.1478
Lyα(DLA galaxy)	1215.67	3.1538	

Table 4.1. List of emission lines from the Q2233+131 itself and the absorption lines, related to the $z = 3.15$ DLA system detected in the QSO spectrum. A standard air-to-vacuum correction has been applied to the observed lines before deriving the redshifts. The uncertainties of the measured redshifts are typically $\pm$0.0005.

object spectrum one can select spaxels in this image, each of which represents a single spectrum, and co-add the selected spectra.

For comparison with later spectra we created a combined spectrum of Q2233+131 by co-adding all spectra within a radial aperture of 2″ ($\sim$45 spaxels) in Fig. 4.1. An overall aperture correction of 2% was applied, and the resulting spectrum is shown in Fig. 4.2.

We detect many absorption features from metal lines in the spectrum of the QSO associated with the $z = 3.15$ DLA system, some of which were already recognized in D96. The redshifts of these lines, listed in Table 4.1, matches the redshift of the DLA line. We derive a mean systemic redshift $z = 3.1475 \pm 0.0005$ from the all metal lines in the DLA apart from the Si IV and O IV 1400 Å blend which has a larger offset than the low ionization species. A detailed analysis of the metallicity and column densities is outside the scope of this paper, as higher spectral resolution would be necessary for this purpose. For the same reason the Lyβ absorption line is blended with the Lymanα forest. The dip seen in the tip on the Lyα emission from the QSO is probably caused by Si II 1260 Å at the redshift of the DLA system.

In addition to the absorption lines we find broad emission lines from Lyα, N V 1240, Si IV + O IV 1400 Å and C IV 1549 Å from the QSO. Including these four lines we find the redshift $z = 3.2877 \pm 0.0052$ for the QSO.

4.4 The spectrum of the DLA galaxy

In Fig. 4.1 we show another narrow-band image, this time selected from the wavelength interval 5040–5055 Å, corresponding to the absorption trough in the QSO spectrum. An extended object is visible to the south and south-west of the location of the QSO. The size of this object is roughly $5'' \times 3''$, however, some of the extended object emission is due to the presence of emission in the red wing of the DLA line from the QSO. We note that the very high signal which appears at the left edge of the field with coordinates (3.5,1) is due to a bad flat-field effect of one single fiber, which has a lower overall transmission.

We have added 35 spaxels which are apparently associated with the emission line object. A part of the spectrum around the emission line is shown in the upper panel in Fig. 4.3 where one clearly sees an emission line at $\sim$5050 Å. This wavelength corresponds to Lyα at the redshift of the DLA

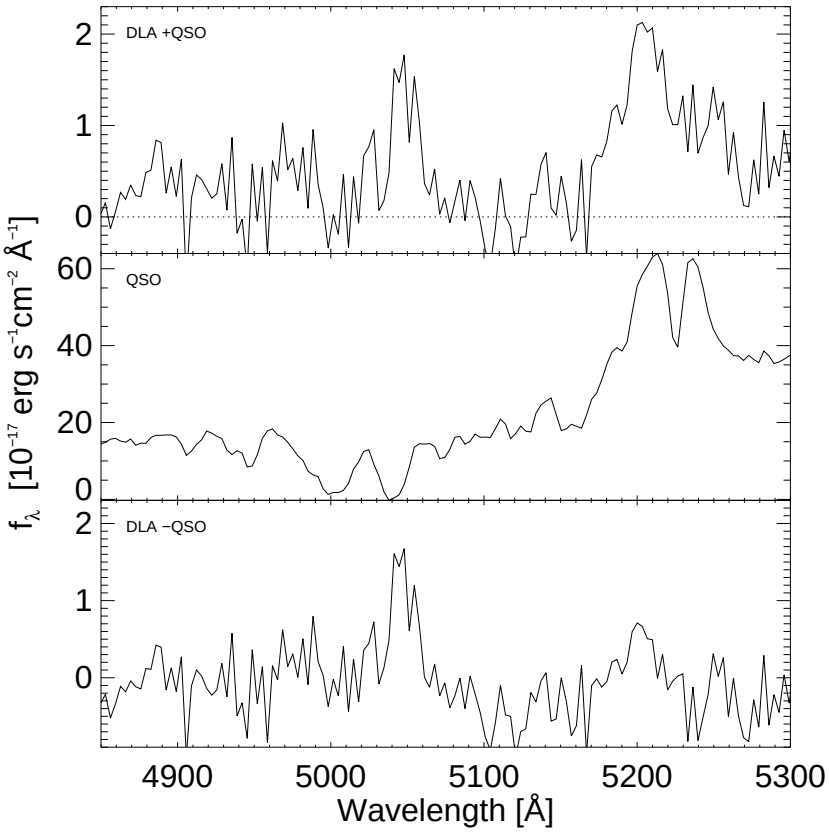

Fig. 4.3. Spectrum of the extended emission associated with the DLA galaxy at $z = 3.15$ in Q2233+131. The spectrum has been obtained by co-adding $\sim$35 spectra which appear to be associated with the DLA galaxy in the image in Fig. 4.1. The few spaxels which are overlapping the position of the QSO have not been coadded, since these are contaminated by flux from the wing of the QSO and not associated with the Lyα emission object. An emission line at 5050 Å corresponds to Lyα at the redshift of the DLA line in the QSO. The broad emission feature at $\sim$5200 Å is due to residual Lyα emission from the QSO at a radial distance of $2''$ from the centre of the QSO. For comparison we have plotted the total QSO spectrum in the middle panel with the same wavelength range. Note the scale on the y-axis differs by a factor of $\sim$30 between the two plots. In the lower panel we have plotted the DLA spectrum where a scaled QSO spectrum has been subtracted.

line at $z = 3.1538 \pm 0.0005$, in agreement within 1σ with the redshift published in D96. A second line is present at ∼5200 Å which is caused by the Lyα emission from the QSO at a distance of 2″. For comparison the same section of the QSO spectrum is shown in the middle panel in Fig. 4.3. There appears to be another broad absorption line at 5000 Å, but a high resolution spectrum of the QSO has shown that this feature is caused by a blend of 5–6 individual absorption lines (Bechtold 1994). The lower panel shows the spectrum of the DLA where a scaled spectrum of the QSO has been subtracted. In fact, the Lyα emission line at 5050 Å is effected very little by this subtraction.

The spectra were analysed with the ONEDSPEC package in IRAF. We measured a full width half maximum (FWHM) of the Lyα emission line of 20 ± 2Å. The resolution in the combined spectra is 7.9 Å, measured from the FWHM of the 5577 Å night sky line in the combined spectra. This yields an internal FWHM of 18.4 ± 3.3 Å of the Lyα line, corresponding to a rest frame velocity of 1090 ± 190 km s^{-1}. We see no emission line from N V λ1240 or C IV λ1549 from the DLA galaxy down to a 3σ detection limit of $1{\times}10^{-17}$ erg cm^{-2} s^{-1} in agreement with D96, albeit their detection limit was 10 times fainter.

The redshift difference between the DLA galaxy's Lyα emission component and the DLA absorption components in the QSO spectrum is $\Delta z = 0.0063 \pm 0.0007$ corresponding to a velocity of 450±50 km s^{-1}. This is larger than the 209 km s^{-1} reported in D96. Here we have used information from all the detected absorption lines in calculating the systemic redshift of the DLA. If we instead used the redshift reported in D96 for the absorption minimum of the DLA line itself, we would find a velocity difference of 270±40 km s^{-1}, which is within 2σ of their value. Since the interstellar absorption lines have been shown to be blue-shifted by > -100 km s^{-1} with respect to the stars in Lyman Break Galaxies (Shapley et al. 2003), the latter value (∼300 km s^{-1}) is probably a better estimate.

The line flux measured by fitting the observed line with a Gaussian profile is $(2.4 \pm 0.3) \times 10^{-16}$ erg cm^{-2} s^{-1}; a simple summation of the flux values for each pixel from the emission line gives the same result within the errors. From the dust maps of Schlegel et al. (1998) a Galactic reddening of $E(B-V) = 0.068$ in the direction towards Q2233+131 is found. Correcting for this effect increases the line flux to $(2.8 \pm 0.3) \times 10^{-16}$ erg cm^{-2} s^{-1} and the total luminosity of the source is $2.4^{+0.3}_{-0.2} \times 10^{43}$ erg s^{-1} in the adopted cosmology. With the noise in each spectral element around 5000 Å of $3.2{\times}10^{-18}$ erg cm^{-2} s^{-1} Å^{-1} and the line flux being measured over 20 pixels, the significance of the detection of the Lyα line is 15σ. The size of the object is 23×38 kpc above a 3σ detection threshold of 1×10^{-17} erg cm^{-2} s^{-1} Å^{-1}.

A measurement of the equivalent width (EW) of the emission line is hampered by the fact that the continuum emission is extremely faint. From the observed ground-based V and R band magnitudes in D96 together with magnitudes from HST images (derived in Section 4.5), we estimate the flux from the underlying continuum at ∼5050 Å to be $(1.1 \pm 0.4) \times 10^{-19}$ erg cm^{-2} s^{-1} Å^{-1} assuming a power-law spectral energy distribution, $f_\nu \propto \nu^\beta$ in the continuum. With this line and continuum flux we derive the rest frame EW=190^{+150}_{-70} Å. The large error is mainly caused by the uncertainty for the continuum flux. Furthermore, the measured EW must be taken as a lower limit because the effect of dust extinction affects the Lyα flux more than the UV continuum emission.

4.4.1 Velocity structure

With integral field spectra one can in principle determine the velocity structure of the Lyα nebula. Specifically, it would be interesting to search for signs of rotation. A detailed analysis of the velocity structure is not possible with the present dataset, since in several of the individual spectra the emission line is only detected on a $\sim 2\sigma$ level, which makes any analysis of any velocity structure unreliable. Instead we summed up the ∼15 spectra in the left-most (eastern) part and the ∼15 in the right-most (western) part, respectively. A sketch of the division is shown in

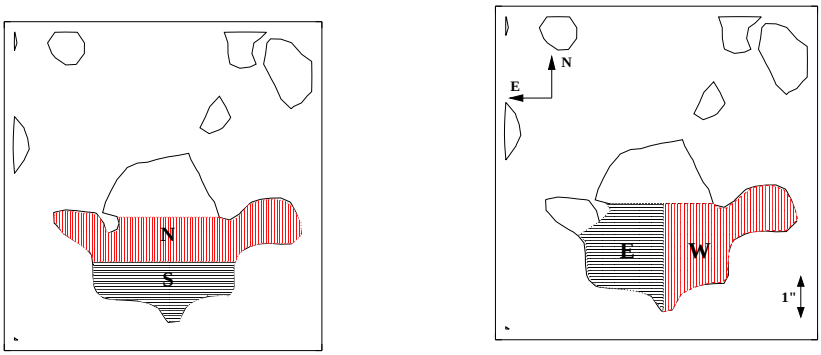

Fig. 4.4. The images show the lowest (5σ) contour level taken from Fig. 4.1. The chosen division between a north and a south region is indicated in the left panel, and the division between an east and a west region to the right. In both cases the emission spatially coincident with the QSO has not been included.

region	centroid (Å)	$f_{\rm line}$ (erg cm^{-2} s^{-1})	FWHM (km s^{-1})	EW (Å)
total	5048.3	2.4×10^{-16}	1090±190	190^{+150}_{-70}
east	5049.6	1.0×10^{-16}	770±150	
west	5052.1	1.3×10^{-16}	1120±200	
south	5048.8	0.7×10^{-16}	650±150	
north	5053.4	1.3×10^{-16}	890±150	

Table 4.2. Properties of the Lyα emission from different parts of the extended nebula derived from fitting a single Gaussian profile to the observed spectrum. The 1σ errors of the estimations of the Gaussian centroids are 0.5 Å. Note that there is an overlap of the selected spectra belonging to the various regions such that some spectra belonging to the east part also belong to the north (see Fig. 4.4). The EW is not meaningful to calculate for the different regions, as the continuum emission is restricted to the total emission. Line fluxes listed in column 3 have not been corrected for Galactic extinction.

Fig. 4.4. The Lyα emission for each region is still detectable, and the line flux of each is $\sim1\times10^{-16}$ erg cm^{-2} s^{-1} Å^{-1}. We fitted Gaussians to the emission line in these two regions, and find that the peak of the emission is shifted by +2.5 Å from the east to the west part, which corresponds to a rest-frame velocity difference of $\sim$150 km s^{-1}. This is small compared to the rotational velocity of present day large spiral galaxies. Repeating this exercise by splitting the extended object into a southern and a northern part as shown in Fig. 4.4, the emission line is shifted by 5 Å corresponding to a difference of $\sim$300 km s^{-1}, where the northern part has the largest redshift. This velocity is comparable to that expected for spiral galaxies, but the geometry is unusual for a disk, and as shown in Sect. 4.4.2 the apparent shift of the emission line can be caused by a combination of more than one emission region. In Table 4.2 we summarize the properties for the different parts of the extended Lyα nebula, and in Fig. 4.5 we show the Lyα line for the different regions. The 1σ errors for the centroids of the Gaussian profiles are 0.5 Å estimated from simulations of artificial spectra having faint emission lines at known wavelengths. From these simulated spectra we also estimate that the 1σ error for the EWs is $\sim$2 Å. All regions are seen to have a large FWHM indicating velocities of 700–1100 km s^{-1}, i.e. they are well resolved by our spectra.

Previously, the existence of a disk in this system has been suggested from studies of the metal absorption line profiles (Lu et al. 1997). This interpretation is not supported by Ledoux et al.

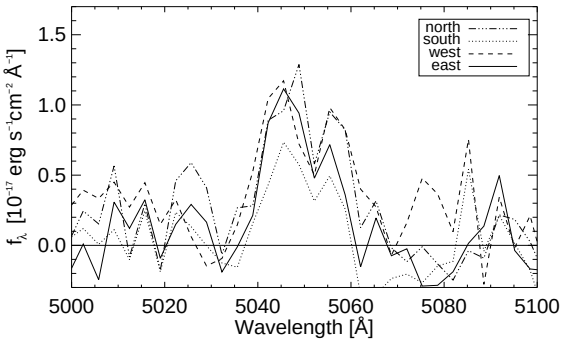

Fig. 4.5. Spectra of the four different regions of the emission line object. The north, south, east, and west regions correspond to those listed in Table 4.2. All regions are seen to have the same double peaked profile of the Lyα line.

(1998a), who concluded that the profiles could be caused by several interacting components, an interpretation which is motivated by cold dark matter simulations of hierarchical clustering of proto-galaxies (Haehnelt et al. 1998). Under the assumption of a rotating disk, the enclosed mass calculated from $M_{\rm dyn} = v_c^2 r/G$ is $\sim 10^{10}$ M$_\odot$. As will be discussed below, the Lyα emission is unlikely to originate in a rotating disk, and the mass calculated here is probably overestimated.

4.4.2 The double peaked Lyα line

In Fig. 4.2 the Lyα emission line appears to have a double peaked profile. As this feature is not apparent in D96, we double checked carefully for its integrity. Although the dip near the line centre is of the order of the noise level, it appears in all spectra and therefore is almost certainly real. In Fig. 4.5 all the four separate spectra described above have the same double peaked profile. The feature is not caused by the subtraction of the sky background, nor is it due to imperfections in the CCD in the region around the emission line.

The difference between our measured emission redshift and the one reported in D96 may indicate that our wavelength calibration has an error of $\sim$1 Å. This would not have an effect on the reported velocity difference since the error would be systematic in all our spectra and not affect the differences in the estimated Gaussian maxima. Furthermore, as mentioned, the spectra are contaminated by the QSO, but a subtraction of a scaled QSO spectrum from the four individual spectra does not change the Lyα line profile.

Anyhow, we caution the reader that other features appear to be systematic in the spectra, e.g. a slightly smaller systematic depression is present in all the spectra around 5020 Å that could be due to an error in the background estimation. Keeping this in mind, we note that a similar double peaked feature was observed for the Lyα line of the DLA galaxy in Q2059–360. However, for this object the line profile changed with slit position (Leibundgut & Robertson 1999).

The values for the centroids of the Gaussian fits listed in Table 4.2 can thus be affected by unequal contributions from two separate emission components. We re-analysed the profiles by simultaneously fitting two Gaussians resulting in centroids of the two peaks listed in column 1 and 2 in Table 4.3. For these two-Gaussian fits the widths of the two individual components are barely resolved with this spectral resolution. The location of the first peak is shifted by 1.1 Å from east to west, corresponding to 65 km s^{-1}, while the second component is shifted by –1Å. Since the uncertainties for the estimate of the Gaussian centroids are 0.5 Å, the shifts are consistent with 0 within 1σ errors. The shifts for the north-south regions are likewise small (< 2.5Å corresponding to < 150 km s^{-1}). For all regions the splitting between the two Gaussians are 10 – 12.5 Å

region	centroid 1 Å	centroid 2 Å	abs. centroid Å
east	5045.9	5056.3	5051.1
west	5044.8	5057.3	5051.0
south	5046.3	5056.3	5050.7
north	5046.5	5058.8	5052.2

Table 4.3. The location of the two peaks from fitting simultaneously two Gaussians to the spectra in Fig. 4.5. The centroids for the fits between the 4 regions vary with < 2.5 Å indicating small velocity differences. For all regions the splitting between the two Gaussians are 10–12 Å corresponding to velocities of $600-750$ km s^{-1}. The third column lists the centroid for the absorption line for the fits consisting of an emission line and an absorption line.

corresponding to velocities of 600 – 750 km s^{-1}. Very likely, the velocity structure across the extended Lyα nebula is complex, and single Gaussian fits for such extended areas as analysed here is over-simplistic.

Additionally, we have fit the profiles by a combination of a single Gaussian emission line and a Gaussian absorption line creating the dip seen in the spectra. The centroids for the absorption line for these fits are listed in Table 4.3 in column 3. The χ^2s from these fits were slightly smaller than for the two emission component fits, indicating that the presence of an absorption line is preferred.

4.4.3 Artificial slit spectra

With integral field data we can reproduce the observations expected from slit spectroscopy. In Fig 4.6 we show a cut of the PMAS spectra around the DLA line in the QSO, where we have indicated the emission from the extended Lyα nebula by small circles. In comparison we have in the upper right hand panel created an artificial long slit spectrum with a width of $1''$, and the corresponding one-dimensional spectrum is shown in the lower panel. These plots can directly be compared to the ones presented in D96. We derive a line flux of $(6.5 \pm 1.0) \times 10^{-17}$ erg cm^{-2} s^{-1} Å^{-1} for the Lyα line, confirming the flux reported in D96, and a FWHM of 6.5 ± 1.0 Å, corrected for the instrumental resolution, corresponding to a velocity of 390 ± 60 km s^{-1}. This FWHM is similar to the the value in D96. With these simple exercises we have shown that it is possible to reproduce the previously published results derived from long-slit spectroscopy.

One sees furthermore in Fig. 4.6, that the Lyα emission indicated by the small circles do not overlap spatially with the location of the QSO. This implies that the contours in Fig. 4.1 at a distance less than $1''$ from the QSO only show emission from the QSO itself and not Lyα emission from the DLA galaxy. Therefore we consider that selecting the emission region from the DLA galaxy as indicated in Fig. 4.4 is the real extension of the Lyα nebula associated with the DLA galaxy.

4.5 HST deep imaging

For comparison of the extended emission with high spatial resolution and deeper optical data previously unpublished HST/WFPC2 images of Q2233+131 were retrieved from the HST archive. Previously, a high spatial resolution image from HST/STIS was presented by Møller et al. (2002) and we also retrieved the STIS images from the archive for comparison. The WFPC2 planetary camera images were obtained through the F702W filter with a total integration time of 10800 s and the images were combined using the drizzle package in IRAF (Fruchter & Hook 2002). The resulting pixel scale in the drizzled image is $0\farcs023$.

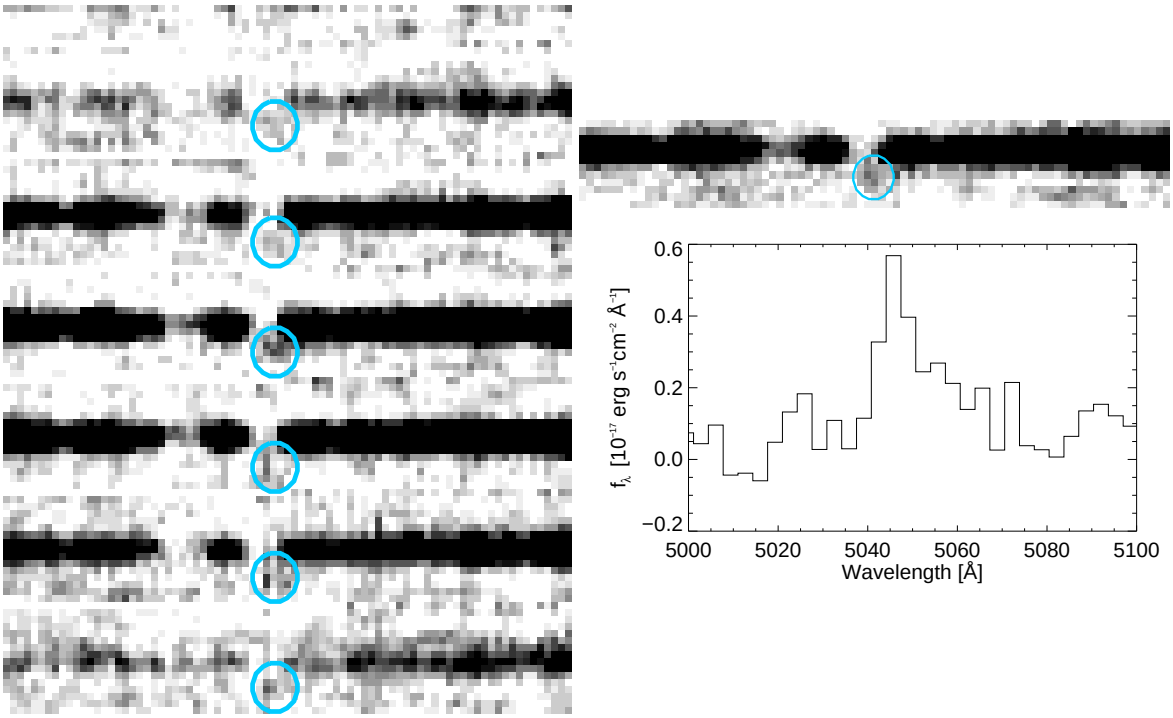

Fig. 4.6. The left hand panel shows a section of the PMAS spectra consisting of spectra from 100 fibers around the region of the DLA. The spectra are oriented with a horizontal dispersion direction. Here are shown 6 groups of spectra where the emission from the extended nebula is visible within the small circles. Each group can be considered as representing a 0.″5 wide two-dimensional long slit spectrum. In comparison we have in the upper right hand panel shown an artificial long-slit spectrum one would have obtained with a 1.″0 slit placed in the north-south orientation as indicated in Fig 4.7. The lower right hand panel shows the corresponding one-dimensional spectrum from extracting the Lyα emission spectrum. This is directly comparable to that in D96, in the sense that it exhibits the same red-winged profile, the same line flux, and the same line width. Note that the emission within the small circles do not overlap spatially with the QSO emission.

An $8'' \times 8''$ section of the WFPC2 image is shown in Fig. 4.7. The DLA galaxy is visible towards the south and the contours of the extended Lyα nebula detected by PMAS has been overplotted. The exact positioning of the contours was checked from the knowledge of the location of the QSO in the PMAS images from Fig. 4.1. The Lyα nebula is clearly extended, but it is difficult to measure the extension of it in the direction towards the QSO since it is contaminated by the flux from the red wing of the DLA line. Avoiding this contamination requires an exact knowledge of the point spread function behavior with wavelength such that the flux contribution from the QSO can be subtracted. However as argued from Fig. 4.6, there is no spatial overlap between the QSO and the Lyα nebula so the contours to the north is caused by QSO emission only. In the other direction towards the south there is a clear cutoff in the contours. We therefore conclude that the Lyα nebula is more elongated in the east–west direction than in the north–south direction yielding the extension of the Lyα nebula of $3'' \times 5''$. Considering that the observed extension of the nebula is a convolution of the true emission and the seeing during the observations, it could originate in smaller clouds in a more complex environment.

In the WFPC2 image a faint and small galaxy is visible at the position indicated in D96 and Møller et al. (2002), and which is identical to the Lyman Break Galaxy (LBG) detected by Steidel et al. (1995). The impact parameter measured in the image is $2\farcs37$ corresponding to 18 kpc in the adopted cosmology, the position angle is 159.1°, and the size of the galaxy along the major axis is $0\farcs5$, which at $z = 3.15$ corresponds to 3.8 kpc.

In Fig. 4.7, the size of the Lyα nebula appears much larger than the size of the DLA galaxy in the WFPC2 image. To quantify this we investigated whether some low surface brightness emission is lost in the WFPC2 image due to different sensitivities. In the WFPC2 image the 3σ limiting magnitude is 26.8 mag arcsec^{-2}, corresponding to a flux limit of 6×10^{-17} erg cm^{-2} s^{-1} arcsec^{-2}, while the PMAS observations of the Lyα object detect emission of $4{\times}10^{-17}$ erg cm^{-2} s^{-1} arcsec^{-2}, implying that the detection limit of the PMAS spectra are roughly the same as for the WFPC2 images. Therefore, if the continuum emission were as extended as the Lyα line emission it would have been detected in the HST images.

The optical magnitude of the LBG corresponds to an L^* galaxy (D96). In Fig. 4.7 the DLA galaxy is seen to be composed of two components separated by $0\farcs25$ corresponding to $\sim$2 kpc at the redshift of the DLA galaxy, and the two components are aligned almost orthogonal to the long axis of the extended emission. A galactic outflow will naturally occur along the minor axis of the galaxy as described in Heckman et al. (1990), which would explain the orientation of the elongated Lyα nebula with respect to the LBG orientation. The irregular morphology of the galaxy was also found by Møller et al. (2002) in their HST/STIS data. They noted that the morphology of the DLA galaxy was not unusual compared to field galaxies at the same redshift.

Using aperture photometry in IRAF we find the magnitude of the DLA galaxy $m_{\rm F702W} = 24.80 \pm 0.1$ using the planetary camera zero point from the WFPC2 Instrument Handbook. This corresponds to a continuum flux of $\sim 3{\times}10^{-19}$ erg cm^{-2} s^{-1} Å^{-1} at $\lambda = 1690$ Å in the rest frame of the DLA galaxy. This is below our detection limit in the PMAS spectra and explains the non-detection of underlying continuum emission from the DLA galaxy. Dust obscuration would make the intrinsic luminosity only larger. The derived flux from the WFPC2 image, confirming that the UV continuum is consistent with being flat, is in agreement with the hypothesis in D96 that the galaxy is very young, and in a star-bursting phase. Using the same aperture for the STIS data we derive $m(V_{50}) = 25.65 \pm 0.1$ in agreement within 1σ of the value reported in Møller et al. (2002).

4.6 Lyα emission from high redshift objects

We now compare the properties of other DLA galaxies with those for the Q2233+131 DLA galaxy.

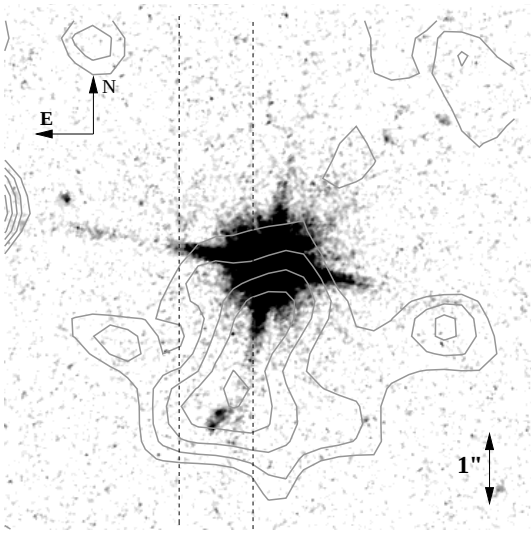

Fig. 4.7. A negative $8'' \times 8''$ WFPC2 image of the Q2233+131. North is up and east is left. The identified absorbing galaxy is seen towards the south of the QSO and the contours of the object in Fig. 4.1 are overlaid. Note again, that the emission is a sum of the Lyα emission from the nebula and some emission from the QSO. The levels of the contours correspond to 5–8σ above the median background, with steps of 0.75σ. There is a peak in the Lyα emission close to the location of the DLA galaxy. Indicated by the vertical dashed lines are the position of the artificial slit from which the spectrum in Fig. 4.6 was created

.

The EW of the observed Lyα line is relatively large compared to that of other high redshift galaxies (Shapley et al. 2003). However, one must note that using a $1''$ long slit spectrum one would have obtained a 4 times smaller flux, and therefore decreased the inferred EW by the same amount. Values of Lyα EWs for high redshift Lyα emitters are > 14 Å, while some may have EWs which are two orders of magnitude larger (Kudritzki et al. 2000). For the Lyα emission from the DLA galaxies in PKS 0528–250 and Q2206–1958 the measured EWs are 63 Å and 83 Å, respectively, which is typical for LBGs at the same redshifts (Møller et al. 2002).

We found that the line width for the Q2233+131 DLA galaxy suggest larger velocities: 1000 km s^{-1} compared to $\sim$700 km s^{-1} observed for other DLA galaxies. An explanation for this may be that we have co-added the spectra over a large area. Velocity differences of 300 km s^{-1} have been found from one end to the other of the extended emission, and with the artificial slit spectra created from the integral field spectra we indeed find a smaller value.

Leibundgut & Robertson (1999) found evidence for an extended Lyα emission nebula associated with the DLA in Q2059–360 using long-slit spectroscopy, with the slit placed at several positions offset from the QSO. They found a velocity difference between the Lyα emission line and the DLA absorption of +490 km s^{-1}, and that the Lyα emission line could be described by two components separated by 5 Å. However, they could not exclude that the Lyα emission was affected by the QSO, which has a very small redshift difference from the Lyα emission line. Nevertheless, these observations are remarkably similar to those presented here of the Q2233+131 DLA, except for the fact that the QSO in our case is well separated in redshift space by $\Delta z = 0.15$.

The properties derived for the Q2233+131 Lyα nebula are also similar to the DLA galaxy detected in Q0151+048A which is described in Fynbo et al. (1999) and Fynbo et al. (2000). They concluded that some of the extended Lyα emission could be caused by photoionization by the QSO, which has the same redshift as the DLA. This is not the case here. The proper distance between the QSO and the DLA is 120 Mpc in the adopted cosmology. Using the relation between the QSO absolute magnitude and the distance to the DLA given in Warren & Møller (1996), we find that the

ionizing flux can be at most 10^{-21} erg cm^{-2} s^{-1} arcsec^{-2}, which is 4 orders of magnitude below the observed value.

Warren & Møller (1996) found evidence that the DLA galaxy termed S1 in Q0528–250 has an extension of $1''$ after correcting for atmospheric seeing suggesting that Lyα emission is more extended than the region emitting continuum radiation.

Previously a couple of LBGs at $z = 3.1$ have been associated with surrounding Lyα emission nebulae in Steidel et al. (2000), who termed these "Lyα blobs". The properties of the extended nebula presented here are less extreme, but not very different from the Lyα blobs. The total luminosity of the Lyα emission from the DLA nebula is a factor 10 less than from the Lyα blobs, and the line width of the DLA emission is a factor of 2 smaller (Ohyama et al. 2003). The inferred size of the DLA emission is smaller than for the Lyα blobs, which have sizes of $\sim 15''$, i.e. a factor of 3 larger than the DLA's emission, but much of the emission is diffuse, and substructure in the blobs is clearly visible.

It is likely that the observed extension of the DLA galaxy's Lyα emission becomes larger as one goes to fainter fluxes, and since the surface brightness decreases with redshift as $(1+z)^4$, it is difficult to detect faint extended objects especially with a 4m class telescope.

4.7 Origin of the extended emission

We address now the question whether the Lyα emission is induced by a superwind from the DLA galaxy and caused by star formation, or if it originates in a rotating disk.

For the assumption of a rotating disk the relation $v_c = v(\mathrm{FWHM})/(2\sin i)$ gives $v_c = (545 \pm 65)/\sin i$. Such a large value makes the interpretation of a rotating disk questionable. A more likely explanation is resonance scattering of Lyα photons that can also produce a large FWHM of the emission line. The resonant nature of the Lyα photon neither increases nor decreases the total flux emitted by the source, only the escape direction, but when the dust-to-gas ratio of the environment exceeds 10% of the Galactic value, the extinction will be significant due to the increased escape path from the resonance scattering of the Lyα photons. While in dust free star-forming galaxies the expected Lyα EW is 100–200 Å (Charlot & Fall 1993), the fact that the measured EW is similar to this value suggests that the most probable source of ionization is massive star formation, and that dust extinction plays a small role.

The red wing of the line profile observed by D96 is marginally detected in our lower resolution data. We can reproduce the line profile in the artificial slit spectrum in Fig. 4.6, but it is much weaker when co-adding several spaxels as in Fig. 4.2 indicating the presence of some velocity structure.

4.7.1 Lyα emission indicative of star formation

In star-forming galaxies, it is mainly the OB stars that produce Lyman continuum photons. These photons will be absorbed by the surrounding neutral hydrogen and re-emitted as line photons. Kennicutt (1998) gives the relation between the Hα luminosity (L) of a galaxy and its star-formation rate (SFR). Assuming case B recombination (Osterbrock 1989) and that the expected ratio of Lyα to Hα flux is $F(\mathrm{Ly}\alpha)/F(\mathrm{H}\alpha) \approx 10$, implies that

$$\mathrm{SFR}\ (\mathrm{M}_\odot\ \mathrm{yr}^{-1}) = L(\mathrm{Ly}\alpha)/1.26 \times 10^{42}\ \mathrm{erg\ s}^{-1}$$

The conversion factor depends strongly on the adopted initial mass function, and we adopt an uncertainty of 50%. The relation between the SFR and the luminosity also depends on the escape fraction of the Lyα photons, which is very uncertain as the extinction is unknown.

Assuming that the Lyα emission is caused by star formation we find SFR $= 19 \pm 10$ M$_\odot$ yr^{-1}, not corrected for the unknown escape fraction. This is a typical value compared to the SFRs found for LBGs having strong Lyα emission (Shapley et al. 2003). It is also consistent with the observed continuum, as can be shown using the conversion from the continuum flux at 1500Å in the rest frame of a galaxy and the SFR, for which Madau et al. (1998) gives the relation SFR(M$_\odot$ yr^{-1}) $= 1.3 \times 10^{-28} L_\nu$ (erg s^{-1} Hz^{-1}). We take into account an uncertainty for the conversion factor of $\sim$30%. The observed R band corresponds to 1500 Å in the rest frame of the DLA system. Correcting the R band magnitude for Galactic extinction and applying an offset converting Vega magnitudes to AB magnitudes (Fukugita et al. 1995) cancels each other out, i.e. $R_{AB} = 24.8 \pm 1$. Using the relation above this magnitude corresponds to a SFR$= 12 \pm 5$ M$_\odot$ yr^{-1}, which is consistent with the SFR derived from the Lyα flux.

Given the uncertainties regarding the conversions from fluxes to SFRs, we find that the Lyα emission around the DLA galaxy could be caused by massive stars. In principle a significant amount of dust would imply that the true Lyα flux is higher than derived from the UV flux. On the other hand, the consistency between the two measurements indicates that dust extinction plays no major role in this particular case. A low dust content could imply a larger escape fraction of the Lyα photons. Another explanation of the large Lyα luminosity could be the complex dynamics involved in this system (Dawson et al. 2002), and not directly related to the dust content as argued for nearby galaxies (Kunth et al. 2003).

4.7.2 Origin of the double peaked emission line

Several authors have analysed the transfer of Lyα photons in neutral clouds (Adams 1972; Urbaniak & Wolfe 1981; Zheng & Miralda-Escudé 2002). Even in the case of a static cloud, the emission profile of Lyα would have a double peak, whereas an outflow would blend the two components of the line. The wavelength difference between the two components is $\Delta\lambda = \sqrt{\frac{2kT}{m_H c^2}}\lambda_0$, where k is the Boltzmann constant, T is the temperature, m_H is the Hydrogen mass, c is the speed of light, and λ_0 is the rest frame wavelength of Lyα. Assuming a temperature of 10^4 K, the corresponding splitting of the line is 0.2 Å at $z = 3.15$, which is much smaller than the observed splitting. On the other hand, given the observed splitting, a temperature of 3×10^7 K is required, which is two orders of magnitude higher than temperatures in superwind outflows at distances far away from the central starburst (Heckman et al. 1990). We therefore argue that the observed double peak is not caused by a static neutral cloud, but has a more complex origin.

In the case of an outflow, the double peaked emission line can be explained. A galactic wind, powered by star formation and supernova explosions, expands outwards and interacts with the surrounding material, shock heats and accelerates this, producing emission line filaments. The preferred direction of expansion is where the pressure gradient is largest, i.e. along the rotation axis of the galaxy usually aligned with the minor axis. The wind creates a large shell of swept up material, and observations towards such an object would intersect the shell in the front and the rear end giving rise to a double peaked emission line profile. Such double peaked profiles of optical emission lines have been observed for nearby starburst galaxies which exhibit these large scale outflows typically termed superwinds (Heckman et al. 1990). Additionally, a double peaked Lyα emission line profile was found from the starburst galaxy T1214–277 by Mas-Hesse et al. (2003), who concluded that the feature is caused by emission in an outflow. The inferred velocity separation between the two peaks from the DLA galaxy emission are similar to the highest ones measured for the nearby galaxies in Heckman et al. (1990) and similar to the Lyα emission line splitting from T1214–277 (Mas-Hesse et al. 2003).

4.7.3 The emitter and the absorber

In the case of a superwind outflow, the DLA cloud is affected by its impact, or could event be created by a such. Taniguchi & Shioya (2001) found that a superwind can create Lyman limit systems with $N_H > 10^{19}$ cm^{-2} along filaments. Followed by gravitational collapse along such filaments DLA clouds can be created. Several authors have pointed out that there could be a relation between superwinds from galaxies and the metal absorption systems seen in quasar spectra (e.g. Heckman et al. 1990; Nulsen et al. 1998), thus explaining the early chemical enrichment of neutral gas clouds seen at the highest redshifts. However, Bond et al. (2001) conclude the opposite, on the basis of Mg II absorption profiles, that superwinds are not causing the majority of DLA systems.

The velocity difference between the emitter and the absorber could be caused by the impact of a superwind from the galaxy which would accelerate a pre-existing low temperature clouds in the surrounding environment. Depending on the initial distance from the starburst, column density of the neutral gas cloud, and the luminosity of the starburst, it can be shown that the expected acceleration is of the order of a few times 100 km s^{-1} (Heckman et al. 1990). This would be consistent with the velocity difference of $\sim$300 km s^{-1} between the Lyα emission and the DLA absorption measured here.

4.8 Mass estimate

When the Lyα luminosity is known, the mass contained in the extended nebula can be evaluated following the method described in Morse et al. (1998). The luminosity is given by

$$L_{\mathrm{Ly}\alpha} = j_{\mathrm{Ly}\alpha} V f \quad [\mathrm{erg\ s^{-1}}] \tag{4.1}$$

where $j_{\mathrm{Ly}\alpha}$ is the volume emissivity, V is the volume, and f is the volume filling factor. For gas with a temperature of $T = 10^4$ K assuming case B recombination, Osterbrock (1989) gives

$$j_{\mathrm{Ly}\alpha} = 3.56 \times 10^{-24} n_p n_e \quad [\mathrm{erg\ cm^{-3} s^{-1}}] \tag{4.2}$$

where n_p and n_e are the number densities of protons and electrons respectively. The total mass of ions in the nebula assuming negligible metal content is

$$M_{\mathrm{ion}} = (n_p m_p + n_{He} m_{He}) V f \tag{4.3}$$

Using the approximations $n_p = 0.9 n_e$ and $n_{He} = 0.1 n_p$, this reduces to

$$\begin{aligned} M_{\mathrm{ion}} &= 1.26 n_e m_p V f \\ &\approx 1.06 \times 10^{-57} n_e V f \quad [M_\odot] \end{aligned} \tag{4.4}$$

Combining the Equations 4.2 and 4.4 gives

$$M_{\mathrm{ion}} \approx 5.91 \times 10^{-46} (L_{\mathrm{Ly}\alpha} V f)^{1/2} \tag{4.5}$$

For calculating the volume of the Lyα nebula, we make an approximation by a cylinder with a radius of 10 kpc and a height of 40 kpc. With the calculated luminosity given above we find $M_{\mathrm{ion}} = 5.7 \times 10^{10} (f)^{1/2} M_\odot$. Assuming $f = 10^{-5}$ taken as a rough guess, along with the arguments in McCarthy et al. (1990), we find $M_{\mathrm{ion}} = 1.8 \times 10^8 M_\odot$.

Due to the unknown dust content in the cloud the unextincted Lyα luminosity could be much higher than derived, and consequently also the mass. On the other hand, a smaller filling factor

would decrease the derived mass, i.e. these two unknown factors may even compensate each other to some extent.

4.9 Conclusions

Using integral field spectra obtained with PMAS, we have presented evidence that the DLA galaxy previously known to be responsible for the DLA system in Q2233+131 has an extended envelope of Lyα emission. From the spectra we constructed an artificial narrow-band image which showed that the extension of the emission is $3''\times5''$ corresponding to 23×38 kpc. This cloud has a line flux of $(2.8 \pm 0.3) \times 10^{-16}$ erg cm^{-2} s^{-1} corrected for Galactic extinction, corresponding to a luminosity of $(2.4^{+0.3}_{-0.2}) \times 10^{43}$ erg s^{-1} at $z = 3.1538$. We derive the rest frame EW= 190^{+150}_{-70} Å.

The source of the ionization is likely star formation within the DLA galaxy. The measurement of the Lyα luminosity is generally considered as a very uncertain method for estimating the SFR given the unknown dust obscuration and escape fractions. With this in mind we find a SFR = 19±10 M$_\odot$ yr^{-1} from the Lyα luminosity, a result which is consistent with the SFR = 12±5 M$_\odot$ yr^{-1} derived from the UV continuum flux from the observed ground based R band magnitude. The agreement between the two suggests that dust extinction plays only a small role.

A velocity offset of ∼270±40 km s^{-1} between the emission and the absorption component in the DLA galaxy does not support the hypothesis that the absorbing cloud resides in a rotating disk. We investigated the velocity structure of the extended Lyα emission further by constructing 4 composite spectra. By fitting Gaussian profiles to spectra from the eastern and western region we found an offset of 2.5 Å, which corresponds to a velocity difference of 150 km s^{-1}. The splitting of the spectra into a northern and a southern region gave a velocity difference of 300 km s^{-1}. These results combined with the extended nature of the Lyα nebula is not consistent with the properties of a disk similar to that in large spiral galaxies.

The object's characteristics (luminosity, FWHM, and spatial extension) are similar to that for some LBGs for which extended Lyα emission has been detected. These high redshift Lyα emitters are thought to be created by an outflowing wind. Recombination of ionised hydrogen creates Lyα photons that are resonantly scattered in the environment, which results in the observed extended envelope. We therefore consider the interpretation of an outflow from the galaxy a more likely interpretation. Furthermore, a galactic outflow can create emission lines with double peaked profiles in agreement with the observations.

We argued that the DLA cloud is not a part of a rotating disk surrounding the DLA galaxy. The relation between the extended Lyα emission and the DLA cloud in the line of sight towards the QSO is somewhat speculative. The wind responsible for the extended emission can create neutral clouds with high column densities located along filamentary structures. Gravitational collapse in these filaments can create DLA clouds. Another explanation could be a previously existing neutral gas cloud which has been accelerated by the superwind giving rise to a velocity separation of 300 km s^{-1}. A third explanation is that the DLA cloud could be an otherwise unrelated infalling cloud. This third explanation is questionable, given the fact that the measured metallicity in the DLA cloud suggests some processing of stellar material.

We have demonstrated the advantages of using integral field spectroscopy for investigating DLA systems in the terms of confirming the galaxies responsible for the DLA absorption. First of all, one can avoid the conventional two step procedure for detecting candidate DLA galaxies near the line of sight towards the QSOs, which later have to be followed up spectroscopically. With integral field spectra one can create artificial narrow-band images suited to any wavelengths required. Secondly,

a non-extended line emitting region could be missed by placing the slit in a less favorable angle, while in the case of an extended emission the line fluxes would inevitably be underestimated.

We will undertake further investigation of the Q2233+131 DLA system with PMAS in order to investigate the velocity structure of the Lyα nebula. Specifically, the system should be observed with a higher spectral resolution which should allow to determine the presence of P Cygni profiles expected for the case of superwind outflows but also in order to investigate the double peaked profile in detail.

Acknowledgments. L. Christensen acknowledges support by the German Verbundforschung associated with the ULTROS project, grant no. 05AE2BAA/4. S.F. Sánchez acknowledges the support from the Euro3D Research Training Network, grant no. HPRN-CT2002-00305. K. Jahnke and L. Wisotzki acknowledge a DFG travel grant under Wi 1369/12-1. L. Č. Popović acknowledges support by Alexander von Humboldt Foundation through the program for foreign scholars and the Ministry of Science, Technologies and Development of Serbia through the project "Astrophysical Spectroscopy of Extragalactic Objects". We thank Palle Møller for his comments and suggestions on an earlier version of this paper.

References

Adams, T. F. 1972, ApJ, 174, 439
Bechtold, J. 1994, ApJS, 91, 1
Becker, T. 2002, PhD thesis, Astrophysikalisches Institut Potsdam, Germany
Bond, N. A., Churchill, C. W., Charlton, J. C., & Vogt, S. S. 2001, ApJ, 562, 641
Charlot, S. & Fall, S. M. 1993, ApJ, 415, 580
Colbert, J. W. & Malkan, M. A. 2002, ApJ, 566, 51
Curran, S. J., Webb, J. K., Murphy, M. T., et al. 2002, Publications of the Astronomical Society of Australia, 19, 455
Dawson, S., Spinrad, H., Stern, D., et al. 2002, ApJ, 570, 92
Djorgovski, S. G., Pahre, M. A., Bechtold, J., & Elston, R. 1996, Nature, 382, 234
Ellison, S. L., Yan, L., Hook, I. M., et al. 2002, A&A, 383, 91
Filippenko, A. V. 1982, PASP, 94, 715
Fruchter, A. S. & Hook, R. N. 2002, PASP, 114, 144
Fukugita, M., Shimasaku, K., & Ichikawa, T. 1995, PASP, 107, 945
Fynbo, J. U., Burud, I., & Møller, P. 2000, A&A, 358, 88
Fynbo, J. U., Møller, P., & Warren, S. J. 1999, MNRAS, 305, 849
Haehnelt, M. G., Steinmetz, M., & Rauch, M. 1998, ApJ, 495, 647
Heckman, T. M., Armus, L., & Miley, G. K. 1990, ApJS, 74, 833
Hopp, U. & Fernandez, M. 2002, Calar Alto Newsletter No.4, http://www.caha.es/newsletter/news02a/hopp/paper.pdf
Hunstead, R. W., Fletcher, A. B., & Pettini, M. 1990, ApJ, 356, 23
Kennicutt, R. C. 1998, ARA&A, 36, 189
Kudritzki, R.-P., Méndez, R. H., Feldmeier, J. J., et al. 2000, ApJ, 536, 19
Kunth, D., Leitherer, C., Mas-Hesse, J. M., Östlin, G., & Petrosian, A. 2003, ApJ, 597, 263
Le Brun, V., Bergeron, J., Boisse, P., & Deharveng, J. M. 1997, A&A, 321, 733
Ledoux, C., Petitjean, P., Bergeron, J., Wampler, E. J., & Srianand, R. 1998a, A&A, 337, 51
Ledoux, C., Theodore, B., Petitjean, P., et al. 1998b, A&A, 339, L77
Leibundgut, B. & Robertson, J. G. 1999, MNRAS, 303, 711
Lu, L., Sargent, W. L. W., & Barlow, T. A. 1997, ApJ, 484, 131

Madau, P., Pozzetti, L., & Dickinson, M. 1998, ApJ, 498, 106
Mas-Hesse, J. M., Kunth, D., Tenario-Tagle, G., et al. 2003, ApJ, 598, 858
McCarthy, P. J., Spinrad, H., Dickinson, M., et al. 1990, ApJ, 365, 487
Møller, P. & Warren, S. J. 1993, A&A, 270, 43
Møller, P., Warren, S. J., Fall, S. M., Fynbo, J. U., & Jakobsen, P. 2002, ApJ, 574, 51
Morse, J. A., Cecil, G., Wilson, A. S., & Tsvetanov, Z. I. 1998, ApJ, 505, 159
Nulsen, P. E. J., Barcons, X., & Fabian, A. C. 1998, MNRAS, 301, 168
Ohyama, Y., Taniguchi, Y., Kawabata, K. S., et al. 2003, ApJL, 591, L9
Osterbrock, D. E. 1989, Astrophysics of gaseous nebulae and active galactic nuclei (Mill Valley, CA, University Science Books)
Petitjean, P., Pecontal, E., Valls-Gabaud, D., & Charlot, S. 1996, Nature, 380, 411
Prochaska, J. X., Gawiser, E., Wolfe, A. M., Castro, S., & Djorgovski, S. G. 2003, ApJL, 595, L9
Rao, S. M. & Turnshek, D. A. 2000, ApJS, 130, 1
Roth, M. M., Bauer, S., Dionies, F., et al. 2000, in Proc. SPIE, Vol. 4008, 277–288
Sánchez, S. F. 2004, AN, 325, 167
Sargent, W. L. W., Steidel, C. C., & Boksenberg, A. 1989, ApJS, 69, 703
Schlegel, D. J., Finkbeiner, D. P., & Davis, M. 1998, ApJ, 500, 525
Shapley, A. E., Steidel, C. C., Pettini, M., & Adelberger, K. L. 2003, ApJ, 588, 65
Steidel, C. C., Adelberger, K. L., Shapley, A. E., et al. 2000, ApJ, 532, 170
Steidel, C. C., Pettini, M., & Hamilton, D. 1995, AJ, 110, 2519
Storrie-Lombardi, L. J., McMahon, R. G., & Irwin, M. J. 1996, MNRAS, 283, L79
Storrie-Lombardi, L. J. & Wolfe, A. M. 2000, ApJ, 543, 552
Taniguchi, Y. & Shioya, Y. 2001, ApJ, 547, 146
Urbaniak, J. J. & Wolfe, A. M. 1981, ApJ, 244, 406
van Dokkum, P. G. 2001, PASP, 113, 1420
Warren, S. J. & Møller, P. 1996, A&A, 311, 25
Warren, S. J., Møller, P., Fall, S. M., & Jakobsen, P. 2001, MNRAS, 326, 759
Wolfe, A. M., Lanzetta, K. M., Foltz, C. B., & Chaffee, F. H. 1995, ApJ, 454, 698
Wolfe, A. M., Turnshek, D. A., Smith, H. E., & Cohen, R. D. 1986, ApJS, 61, 249
Zheng, Z. & Miralda-Escudé, J. 2002, ApJ, 578, 33

4.10 Notes on the DLA towards Q2233+131

After publication of this present chapter in A&A, more studies of this object have been carried out. These give more information on the properties of emission lines from this sub-DLA galaxy.

Revisiting the Lyα emission nebula

Further studies of the Lyα emission line from the DLA galaxy towards Q2233+131 with higher spectral resolution could not confirm the extension of the Lyα emission nebula.

The results in this chapter were derived from an early version of the data reduction. Chapter 5 uses a more advanced data reduction procedure which improves the signal-to-noise ratio for the extracted spectra. Using the improved reduction procedure on the data set in this Chapter indicates a smaller extension for the nebula and no signal at the position $(2, -1)$ in Fig. 4.1. The signal at $(-3, -1)$ is still present, but the spaxels associated with it would not pass the tests invoked in Chapter 5 for being a good candidate. Furthermore, the double peak emission line profile has a much smaller significance in a higher signal-to-noise spectrum, and is consistent with the noise level.

Concerning the apparent wavelength shift, those are also present in the re-reduction of the data sets, but higher resolution data give opposite results. However, a wavelength shift is consistent with zero within the uncertainties. We interpret the shift presented in this chapter as caused by residuals from the QSO emission because of the spatial overlap (due to seeing effects) of the QSO and Lyα emission object. Very close to the QSO, i.e. to the north, the residuals are stronger while to the south the emission is clearly separated from the QSO emission.

Star formation rates

The star formation rate inferred from the UV flux and Lyα emission line for this object is in qualitative agreement with a SFR = 28 $M_\odot$ yr^{-1} derived from the detection of the [O III] line (Weatherley et al. 2005). Because this line is much less affected by dust extinction the agreement indicate further that dust can only have a minor effect.

CHAPTER 5

An integral-field spectroscopic survey for high redshift Damped Lyman-α galaxies

L. CHRISTENSEN[1], S. F. SÁNCHEZ[1,2], K. JAHNKE[1], L. WISOTZKI[1,3], M. M. ROTH[1]

[1] Astrophysikalisches Institut Potsdam, An der Sternwarte 16, 14482 Potsdam, Germany

[2] Centro Astronomico Hispano Aleman de Calar Alto, Spain

[3] Potsdam University, Am Neuen Palais 10, 14469 Potsdam, Germany

Abstract

We present integral field spectroscopic observations of candidate Lyα emission lines from galaxy counterparts to damped Lyman-α systems (DLAs) towards high redshift QSOs. Candidates are identified from their Lyα emission at a wavelength close to the DLA line where the background QSO emission is absorbed. We have observed 14 DLAs and 8 sub-DLAs towards 9 QSOs including two previously confirmed emission line objects. Besides these two confirmed objects, we find 8 candidates corresponding to a detection frequency of $\sim$40%. Lyα emission candidates are found associated with both high and low metallicity DLAs. In comparison with the few previously confirmed Lyα emitting DLA galaxies the candidates have comparable line fluxes and line widths. Velocity offsets are somewhat larger and the impact parameters appear to be larger on the average suggesting H I cross sections larger than 10 kpc. Using the impact parameters as a measure of neutral gas disc sizes suggest that the average candidate DLA galaxy has an exponential scale length of $\sim$5 kpc. This is consistent with high redshift DLAs residing in gas discs with similar sizes as spiral galaxies neutral discs in the local Universe (not necessarily implying that DLA galaxies at high redshifts are luminous L^* galaxies). We also suggest that there may be an anticorrelation between the DLA galaxy luminosities and the column density of the DLA.

5.1 Introduction

Galaxy counterparts to Damped Lyman-α systems (DLAs) seen in QSO spectra were suggested to be (proto)-disc galaxies with line of sight clouds of neutral gas with column densities $N(\mathrm{H\,I}) > 2 \times 10^{20}$ cm^{-2} (Wolfe et al. 1986). Analyses of absorption line profiles indicated that rotational components with velocities of $\sim$200 km $^{-1}$ could be involved in these systems in accordance

[†] This paper will be submitted to *Astronomy & Astrophysics*. A few major results based on this Chapter is published in the IAUC 199 conference proceedings (Christensen et al. 2005).

with the large disc scenario (Prochaska & Wolfe 1997; Ledoux et al. 1998a). On the other hand, numerical simulations showed that merging proto-galactic clumps in a hierarchical formation scenario could give rise to the observed line profiles too (Haehnelt et al. 1998).

A large fraction of the neutral hydrogen present at $z > 2$ is contained in these high column density DLA systems (Lanzetta et al. 1995; Storrie-Lombardi & Wolfe 2000; Péroux et al. 2001). In addition to the classical DLAs, clouds with column densities $10^{19} < N(\mathrm{H\,I}) < 2\times 10^{20}$ cm^{-2} also show some degree of damping wings characteristic for DLA systems. Such sub-DLA systems are also suggested to contain a significant fraction of the neutral matter in the Universe (Péroux et al. 2003), and metallicity studies have shown that properties of the sub-DLA systems are similar to those of DLA systems (Dessauges-Zavadsky et al. 2003). The main difference between DLAs and sub-DLAs is that the latter systems have significant ionisation corrections (Prochaska & Herbert-Fort 2004).

How DLAs are associated with galaxies has been a subject of much study. Originally, either space-based or ground-based deep images were obtained to identify objects near the line of sight to the QSOs (Steidel et al. 1995; Le Brun et al. 1997; Warren et al. 2001). To confirm nearby objects as galaxies that are responsible for the DLA lines in the QSO spectra, follow-up spectra are needed to confirm the galaxy redshifts. At $z < 1$ confirmations of 14 systems exist to date (Rao et al. 2003; Chen & Lanzetta 2003; Lacy et al. 2003; Chen et al. 2005, and references therein), while at $z \gtrsim 2$ only 6 DLA galaxies are confirmed through spectroscopic observations of Lyα emission from the DLA galaxies (Møller & Warren 1993; Djorgovski et al. 1996; Møller et al. 1998; Leibundgut & Robertson 1999; Møller et al. 2002, 2004).

Integral field spectroscopy (IFS) is an alternative which provides images and spectra at each point on the sky simultaneously. This technique can be used to look for emission line objects at wavelengths previously known but at an unknown spatial location. This paper presents a small survey aimed to detect Lyα emission from DLA galaxies. At the Lyα wavelength corresponding to the redshift of the DLA system, the QSO emission has been absorbed, facilitating the location of emission line objects very near to the QSO sight line. Previously, IFS searches for emission from DLA galaxies towards two QSOs resulted in upper limits for their fluxes (Petitjean et al. 1996; Ledoux et al. 1998b), while an IFS study of a previously known sub-DLA galaxy is presented in Christensen et al. (2004). Similarly, a Fabry-Perot imaging study of several QSO fields did not result in detections of emission from DLA galaxies (Lowenthal et al. 1995).

This paper is organised as follows. Section 5.2 describes the sample of QSOs included in the survey, which were known previously to have DLAs and sub-DLAs in their spectra. Section 5.3 describes the data reduction and analysis. In Section 5.4 the method of detecting emission line candidates is described. Section 5.5 presents the results and comments to each object observed. Properties of the Lyα emission candidates detected in the small survey in relation to previously known objects are presented in Section 5.6. Section 5.7 summarises our findings. Throughout the paper we use a flat cosmology with $H_0 = 70$ km s^{-1} Mpc^{-1}, $\Omega_m = 0.3$, and $\Omega_\Lambda = 0.7$.

5.2 Sample selection

To study the applicability of IFS to identify DLA galaxies we first selected systems, where Lyα emission was detected previously. Two of these systems could be observed during our runs; Q2233+131 and PHL 1222 originally identified by Steidel et al. (1995), Djorgovski et al. (1996) and Møller et al. (1998), respectively. Both objects are reported to have extended Lyα emission (Fynbo et al. 1999; Christensen et al. 2004). Additionally, we selected a number of other DLA systems without previous detections of associated Lyα emission to search for more DLA galaxies. The selected systems were chosen based upon following criteria

1. $N(\mathrm{H\,I}) > 2 \times 10^{20}$ cm^{-2}
2. DLA redshift ($2 < z < 4$)
3. Bright QSO ($R < 19$)
4. Northern hemisphere object
5. Preferably multiple DLAs[1]

The third criterion was included to ensure that the signal from the QSO was sufficient to determine accurately the spatial location of the candidates with respect to the QSO in the data cubes, and to be able to determine the PSF variations as a function of wavelength, which is necessary for the subtraction of the QSO emission. From the list of DLA systems compiled by S. Curran[2] we found 66 QSOs matching these criteria in 2003. More recently, detections of DLAs in the Sloan Digital Sky Survey QSO spectra has greatly increased the number of known DLAs (Prochaska & Herbert-Fort 2004).

A systematic survey of all 66 objects would require a large amount of time with present instruments, so we selected a few systems based on their observability at the allocated observing runs. Furthermore, we avoided DLAs where their redshifted Lyα wavelength lie close to sky emission lines. Because of the selection effect that enter the sample and the small number of DLAs involved in the survey, a proper statistical investigation is not the aim of this paper. This would require a cleaner sample selection and as shown in this paper that should be feasible with IFS on an 8m class telescope with reasonable time requirements. Instead the present study focuses on a few systems to analyse the applicability of IFUs for this kind of investigation.

We have observed 9 QSOs with a total number of 14 DLA systems and 8 sub-DLA systems listed in Table 5.2. This table includes two previously known Lyα emitting DLA galaxies, although the criteria listed above were not satisfied. E.g. the absorption system towards Q2233+131 has $N(\mathrm{H\,I}) = 1 \times 10^{20}$ cm^{-2} classifying it as a sub-DLA. Another example is Q0953+4749, which has $V = 19.5$, i.e. fainter that the limit, however this was included because of the three DLAs present in its spectrum (Bunker et al. 2003).

5.3 Observations and data reduction

Using the Potsdam Multi Aperture Spectrophotometer (PMAS) mounted on the 3.5m telescope at Calar Alto we have observed the objects during several runs from 2002–2004 as listed in Table 5.2. The PMAS integral field unit (IFU) was used in standard configuration where 256 fibres are coupled to a the 16×16 element lens array. During the observations each fibre covered $0\farcs5 \times 0\farcs5$ on the sky. Each fibre gives a spatial pixel element (spaxel) represented by a single spectrum. The 256 spectra were recorded on a 2k×4k CCD which was read out in a 2×2 binned mode. With a separation of 7 pixels between individual spectra, the fibre to fibre cross-talk is negligible. A detailed overview of the PMAS instrument and capabilities is given in Roth et al. (2005).

A maximum exposure time of 1800s was used because of the large number of pixels affected by cosmic ray hits. Furthermore, because of varying conditions such as the atmospheric transmission and seeing the total exposure time for each object was adjusted, or sometimes repeated under better conditions. The photometric properties during observations are monitored with the PMAS

[1] In retrospect, this criterion could be ill chosen, because extinction in foreground DLAs could affect emission from background DLA galaxies in the case that the galaxies lie in the same line of sight. Hence, upper limits on detections can be biased.

[2] `http://www.phys.unsw.edu.au/~sjc/dla/`

Table 5.1.

Coordinate name	Alt. name	$z_{\rm em}$	$z_{\rm abs}$	$\log N(\mathrm{H\,I})$	Metallicity	Ref
Q0151+048A	PHL 1222	1.93	1.934	20.36±0.10		(1)
Q0953+4749	PC 0953+4749	4.457	3.404	21.15±0.15	[Fe/H]=>–2.718, [α/H]=–1.82±0.28	(2,3)
			3.891	21.20±0.10	[Fe/H]=>–1.712, [α/H]=–1.50±0.15	
			4.244	20.90±0.15	[Fe/H]=–2.50±0.17, [Si/H]=–2.23±0.15	
Q1347+112		2.679	2.471	20.3		(4,5,6)
			2.05	20.3*		(7)
Q1425+606	SBS 1425+606	3.163	2.827	20.30±0.04	[Fe/H]=–1.33±0.04, [Si/H]>–1.03	(8,9,10,21)
Q1451+1223	B1451+123	3.246	2.469	20.39±0.10	[Fe/H]=–2.46±0.11, [Si/H]=–2.13±0.14	(11,3)
			3.171	19.70±0.15	[Fe/H]=–1.87±0.16, [Si/H]=–1.61±0.15	
			2.254	19.9*	[Fe/H]=–1.47±0.17, [Si/H]>–0.40	(6,12,19)
Q1759+7539	GB2 1759+756	3.05	2.625	20.76±0.10	[Fe/H]=–1.18±0.01 , [Si/H]–0.79±0.01	(13,18,20)
			2.91	19.8	[Fe/H]=–1.65	(18)
Q1802+5616	PSS J1802+5616	4.158	3.391	20.30±0.10	[Fe/H]=–1.54±0.11, [α/H]=–1.43±0.15	(3)
			3.554	20.50±0.10	[Fe/H]=–1.93±0.12, [Fe+0.4/H]=–1.52±0.22	
			3.762	20.55±0.15	[Fe/H]=–1.82±0.26, [α/H]=–1.55±0.19	
			3.811	20.35±0.20	[Fe/H]=–2.19±0.23, [Si/H]=–2.04±0.22	
Q2155+1358	PSS J2155+1358	4.256	3.316	20.55±0.15	[Fe/H]>–1.65,[Si/H]=–1.26±0.17	(3)
			3.142	19.94±0.10	[Fe/H]=–2.21±0.21, [Si/H]=–1.85±0.15	(14,19)
			3.565	19.37±0.15	[Fe/H]<–2.40, [Si/H]=–1.27±0.14	(14)
			4.212	19.61±0.15	[Fe/H]=–2.18±0.25, [Si/H]=–1.92±0.11	(14)
Q2233+131		3.295	3.153	20.0	[Fe/H]=–1.4, [Si/H]=–1.04	(15,16,17)
			2.551	20.0		(12,16)

List of the observed DLA and sub-DLA systems with column densities and metallicities taken from the literature. * denotes a system where the reported $N(\mathrm{H\,I})$ needs to be confirmed through high resolution spectroscopy. References: (1) Møller et al. (1998), (2) Schneider et al. (1991), (3) Prochaska et al. (2003), (4) Smith et al. (1986), (5) Wolfe et al. (1986), (6) Turnshek et al. (1989), (7) Wolfe et al. (1995), (8) Chaffee et al. (1994), (9) Stepanian et al. (1996), (10) Prochaska et al. (2002a), (11) Bechtold (1994), (12) Lanzetta et al. (1991), (13) Prochaska et al. (2001), (14) Péroux et al. (2003), (15) Steidel et al. (1995), (16) Lu et al. (1997), (17) Lu et al. (1993), (18) Outram et al. (1999), (19) Dessauges-Zavadsky et al. (2003), (20) Prochaska et al. (2002b), (21) Lu et al. (1996).

QSO	date	exp.time (s)	grating	λ coverage (Å)	seeing	conditions
Q0151+048A	2003-08-27	5×1800	V600	3500–5080	0.8 – 1.2	stable
Q0953+4749	2004-04-16	4×1800	V300	3630–6980	0.9	stable
	2004-04-21	5×1800	V300	3630–6980	1.0	non phot.
Q1347+112	2004-04-20	7×1800	V300	3630–6980	0.6	non-phot.
Q1425+606	2004-04-19	6×1800	V300	3630–6750	1.0	stable
Q1451+1223	2004-04-17	7×1800	V300	3630–6980	0.8	non-phot.
Q1759+7539	2004-04-21	7×1800	V300	3630–6980	1.0 – 1.5	non phot.
Q1802+5616	2003-06-18	2×1800	V600	5100–6650	1.0	non-phot.
	2003-06-20	3×1800	V600		1.0	non phot.
	2003-06-21	4×1800	V600		1.8	non phot.
	2003-06-22	6×1800	V600		0.9	stable
Q2155+1358	2003-08-26	7×1800	V600	4015–5610	0.7	stable
	2003-08-27	4×1800	V600		0.8	non phot.
Q2233+131	2002-09-03†	4×1800	V300			
	2003-08-24	6×1800	V600	4000–5600	0.6	stable
	2003-08-25	4×1800	V600		0.7	non phot.

Table 5.2. Log of the observations. The last two columns show the average seeing during the integrations and the photometric conditions derived from the A&G camera images. † Results form these observations are published in Christensen et al. (2004).

acquisition and guiding camera (A&G camera) which is equipped with a 1k×1k CCD. Seeing values listed in Table 5.2 refer to the seeing measured in the A&G camera images. Determining actual spectrophotometric conditions requires monitoring of the extinction coefficients which can not be determined from the A&G camera images. In Table 5.2 'stable' simply means that the photometry of the guiding star was constant within 1% during the observations.

The data were obtained using 2 gratings; one with 300 lines mm^{-1} and one with 600 lines mm^{-1} with spectral resolutions of 6.4 and 3.2 Å pixel^{-1}, respectively. Observations of spectrophotometric standard stars were carried out at the beginning and end of each night at the grating position used for the observations to give a specific wavelength range.

Data reduction was done by first subtracting an average bias frame. Before extracting the 256 spectra most cosmic ray hits were removed by the routine described in Pych (2004). A high threshold was chosen such that not all cosmic rays were removed, because a low threshold would also remove bright sky emission lines from some spectra. Remaining cosmic rays were removed from the extracted spectra using the program L.A. Cosmic (van Dokkum 2001).

The locations of the spectra on the CCD were found from exposures of a continuum lamp taken either before or after science exposures. The spectral extraction was done in two different ways; a simple method, that added all flux between each spectrum on the CCD (i.e. 7 pixels), and another method that took into account the profile of the spectrum on the CCD. This second method assumed that the spectral profiles are represented by Gaussian functions (Gaussian extraction) with widths that were allowed to vary with wavelength. The second method was shown to increase the signal-to-noise ratio by $>$10% for faint objects and therefore unless otherwise noted, the results from the 'Gaussian extraction' data cubes will be reported.

After extraction, the spectra were wavelength corrected using an exposure of emission line lamps taken just before or after the observations. Comparisons with sky emission lines indicated an accuracy of the wavelength calibration of about 10% of the spectral resolution. After this, the spectra were corrected for wavelength dependent throughput variations by dividing with a normalised flat field spectrum obtained from twilight sky observations. These sky spectra were extracted in a similar way as the science observations, and a normalised flat field spectrum was created by dividing each

of the 256 spectra with a smoothed average spectrum.

Before combining individual frames the extracted spectra were arranged into data cubes. Secondly, each data cube was corrected for extinction using an average extinction curve for Calar Alto (Hopp & Fernandez 2002). The combination took into account a correction for the differential atmospheric refraction using a theoretical prediction (Filippenko 1982). Relative spatial shifts between individual data cubes were determined from a two-dimensional Gaussian fit to the QSO PSF at a wavelength close to the strong absorption lines.

Subtraction of the sky background was an iterative process because the locations of the objects of interest were not known beforehand. PMAS, in the configuration used, does not have separate sky fibres. Instead, we selected 10–20 fibres uncontaminated by the QSO emission and the average spectrum was subtracted from all 256 spectra. Several different spaxel selections were examined visually before an appropriate sky spectrum was found.

Flux calibration was done the standard way from observations of spectrophotometric standard stars. A one-dimensional spectrum of the standard star was constructed by co-adding flux from all 256 spaxels. This was used to create a sensitivity function that could be applied to each of the 256 spectra in the science exposures. For non-photometric nights the flux calibrated spectra were compared with QSO spectra from the literature to estimate photometric errors. However, no correction factor was applied to our spectra, because any variability of the QSOs would make such scaling uncertain. In cases of discrepancy we note in Sect. 5.5.5 that there is difference, which could be caused by either non-photometric conditions or intrinsic variability.

For reference we present spectra of the target QSOs in Fig. 5.1. Where present, metal absorption lines corresponding to the strongest DLAs are indicated, but a detailed analysis of metal absorption lines requires higher resolution spectroscopy as presented elsewhere (e.g. Prochaska et al. 2003; Péroux et al. 2003; Dessauges-Zavadsky et al. 2003). DLA redshifts derived from the metal absorption lines were consistent with those reported in the literature within the accuracy of the wavelength calibration of the data cubes.

5.4 Search for DLA optical counterparts

The observations allowed to cover the wavelengths of Lyα for most of the strong absorption systems listed in Table 5.2. Only the highest redshift sub-DLA system towards Q2155+1358 was not covered, i.e. the total number of systems included in this analysis is 21 DLA and sub-DLA systems.

5.4.1 Method

For this project we are only interested in small wavelength regions corresponding to Lyα at the DLA redshifts, and thus the investigation could be carried out using customised narrow-band filters (e.g. Fynbo et al. 1999, 2000). IFS, on the other hand, has the advantage that narrow-band images can be created with widths adjustable to the widths of the emission lines and typically narrow-band filters have larger transmission *FWHM*. Hence, IFS allows to detect emission line objects with a higher signal-to-noise ratio than possible with narrow-band filters. A disadvantage is the relatively small field of view of current IFUs, but it is adequate given the predicted small DLA galaxy sizes. It is possible to estimate the expected DLA galaxy sizes. Using a Schechter luminosity function and a power-law relation between the disc luminosity and gas radius given by the Holmberg relation $R \propto L^{\beta}$, one can calculate the expected impact parameter. Combining $\beta = 0.26$ in Chen et al. (2005) with the luminosity function in Poli et al. (2003) found for $z = 3$ galaxies one finds $R^{*} \approx 30$ kpc. If DLA galaxies are similar to an L^{*} galaxy this implies that DLA galaxies are expected to lie closer than $\sim 4''$ to the QSO sight line. Thus, the current small field of view IFUs are suited to use for the search for Lyα emission from DLA galaxies.

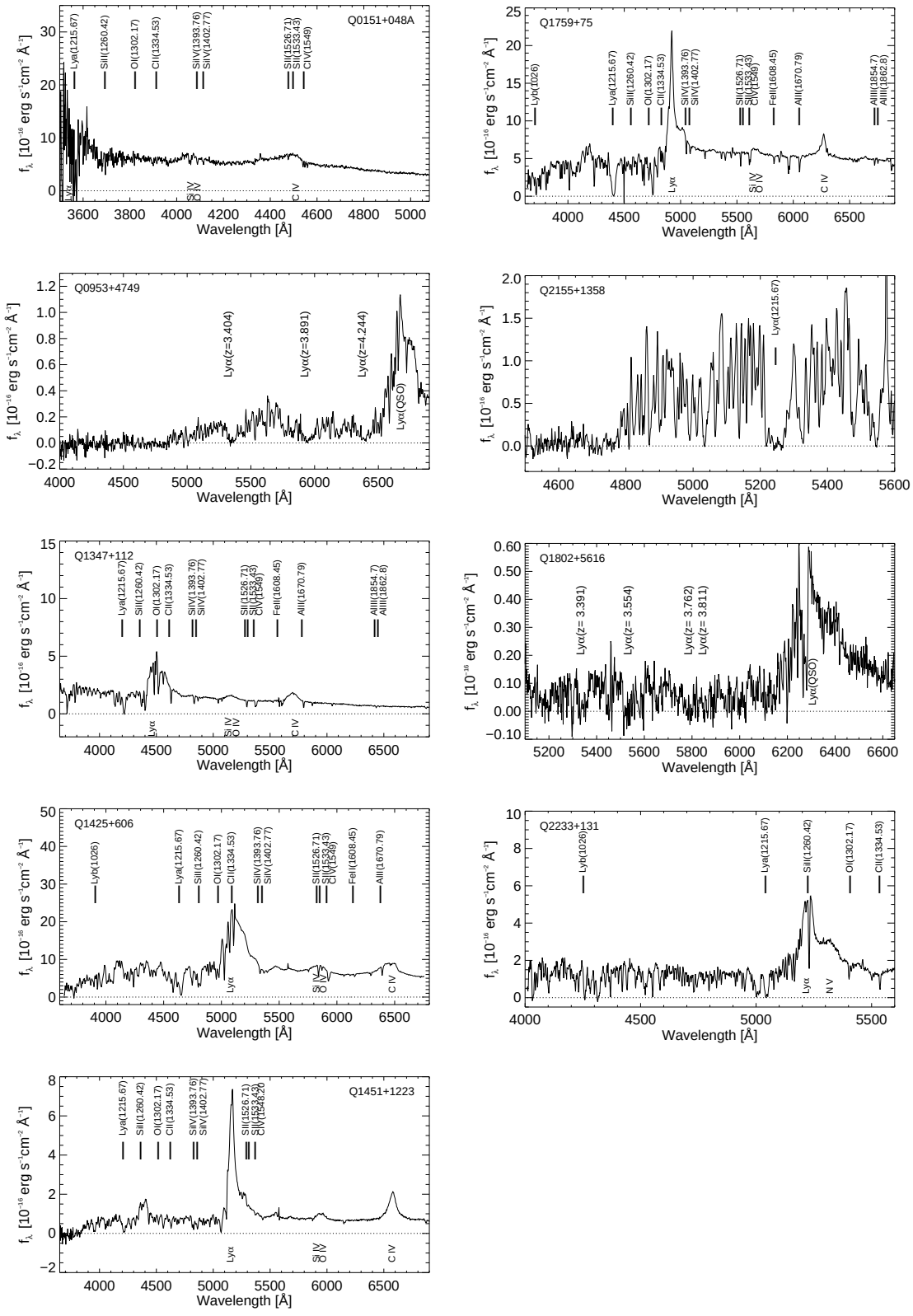

Fig. 5.1. QSO spectra extracted within 3″ radial apertures where no correction for Galactic reddening is applied. Metal absorption lines associated with the DLA systems are indicated. For those QSOs with multiple DLA lines, only the DLA lines and their redshifts are indicated.

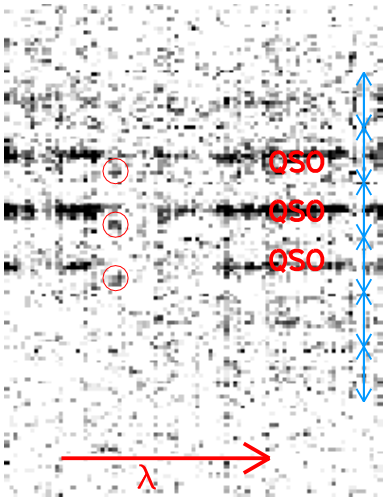

Fig. 5.2. Row-stacked spectrum of the region around the $z = 3.391$ DLA in Q1802+5616. Because of the faintness of the QSO, identifying visually the DLA (absorption) line is difficult in this representation. The brightest emission comes from the QSO itself while a candidate Lyα emission object is present with a negative velocity offset from the DLA line. The blue vertical arrows each indicate a cross dispersion direction with sizes of 16 pixels. I.e. each of these sections correspond to a long-slit spectrum offset from each other by $0\farcs5$.

Lyα emission from DLA galaxies are offset from the QSO- DLA line by $\gtrsim 200$ km s^{-1} (Møller et al. 2002), whereas Lyα emission from high redshift galaxies can have larger offsets (Shapley et al. 2003). We therefore chose to investigate narrow-band images at velocities ranging from approximately –1000 to +1000 km s^{-1} from the DLA line.

First, the reduced data-cubes were stacked in a two-dimensional frame called a row-stacked spectrum. We inspected visually the region around the DLA lines for emission line objects. When the spatial offset from the QSO is larger than the seeing, or alternatively when the QSO is very faint which was the case for Q1802+5616 (Fig. 5.2), emission line objects can be identified directly because of the ordering of the spectra in the row-stacked spectrum. In the case of PMAS spectra, an emission line object will appear with a separation of 16 spectra as demonstrated in Fig. 5.2. Only this one case allowed an immediate visual detection.

Further inspections of the data cubes was done using the Euro3D visualisation tool (Sánchez 2004). Where no objects could be detected visually further sampling of the data cubes was necessary to increase the signal to detect candidate emission line objects.

From the final reduced, sky-subtracted data cubes, narrow-band images were created with an initial width of 10–15 Å depending on the spectral resolution of the observations. Images were created offset by –10 to +10 Å from the DLA line to allow for possible velocity shifts of the Lyα emission line, which corresponds to velocity offsets of $\sim$1000 km s^{-1} at the observed wavelengths. Images were inspected visually for objects brighter than the background. If detected, spectra in these regions were co-added and inspected for emission lines at the wavelength chosen in the narrow-band image. This step was necessary to discriminate between emission lines and individual noisy spectra. Due to lower transmission of a few fibres, after flat fielding the spectra have larger than average noise levels, and in a very narrow-band image these spectra can appear bright. If an emission line was seen, a second pass narrow-band image was created using information of the emission line width to increase the signal of the detection. A second pass one-dimensional spectrum was created after inspection for more bright spaxels surrounding the emission line candidate. This process was iterated until no improvement of the signal in either narrow-band images or spectra was found.

Everything was done interactively, but as explained in Sect. 5.5.3, a visual identification of faint emission lines was found to be more effective than an automatic routine.

5.4.2 Candidate selection

To allow a better visual detection of emission line objects, the narrow-band images were interpolated to smaller pixel sizes. These interpolated narrow-band images of the candidates are shown in Fig. 5.3. In all panels the images are 8″ on a side, with pixel scales 0.″2 pixel^{-1} and the orientation is north up and east left. The left panels show interpolated images of the QSO at wavelengths near to the DLA wavelength. Contours correspond to an image centered on the visually detected emission feature close to the DLA redshifts. The noise level was determined statistically by analysing the pixel intensity distribution in a many narrow-band images constructed from the final data cube and offset by –50 Å to +50 Å from the DLA line. Only pixels uncontaminated by the QSO emission was analysed. In the middle panels the plots are reversed, such that the image shows the emission line object and the contours correspond to the QSO narrow-band image. In these panels the innermost contour corresponds to the effective seeing *FWHM*.

To enhance the visibility of the candidates, when these are offset in velocity from the DLA line, the QSO emission was subtracted from the data cubes before creating the images. This subtraction of the QSO emission was done using a simple approach. A scale factor between the one-dimensional QSO spectrum and each spectrum in the data cube was determined close to the DLA line. Applying this scale factor, the QSO emission was then subtracted, thus retaining objects with different spectral characteristics in the data cube.

Spectra of the candidates are shown in the right hand column. These one-dimensional spectra are created by co-adding spaxels from the original spaxels, i.e. not from the interpolated images. Typically, between 4 and 10 bright spaxels were identified and co-added to create the one-dimensional spectrum. The dotted line in Fig. 5.3 corresponds to the 1σ RMS level determined from a statistical analysis of the pixel values in the data cube. This level was found to be identical to the noise level measured directly in the shown one-dimensional spectrum. In the lower sub-panels are shown the corresponding noise spectrum in the data cubes before sky subtraction was done. This was obtained by co-adding the same number of spaxels as in the upper sub-panels and calculating the standard deviation. Note that in many cases the signal of the candidate is similar to the statistical sky background noise.

Properties of the candidate objects corresponding to those with spectra in Fig. 5.3 are listed in Table 5.3. Offsets in RA, DEC from the QSO and the corresponding projected distance at the DLA redshift are listed in columns 2, 3, and 4. Emission lines were fit using `ngaussfit` in IRAF. After fitting a Gaussian function to the emission lines, central wavelengths are converted to vacuum wavelengths, and the redshifts listed in column 5 are derived. Fluxes in column 6 are derived from the Gaussian fits, and errors in the peak flux, line width, and continuum placement are propagated for calculation of the flux uncertainties. Column 7 gives the velocity difference between the DLA redshift from Table 5.2 and those for the candidate Lyα emission lines. The flux measurements and the associated errors indicate that most of the candidates are detected with a signal-to-noise ratio of $\lesssim$3. We integrate the signal-to-noise estimate over the emission line, $\sigma = f/(\sqrt{N} \times s/n)$, where f is the line flux, and N is the number of pixels the emission line covers and s/n is the RMS noise in adjacent wavelength intervals. This quantity is listed in column 8. Column 9 gives the observed emission line *FWHM* after correcting for the instrumental resolution which was measured from sky emission lines in the reduced data cubes. Finally column 10 gives the significance of the candidate detection explained in detail in Section 5.5.1.

The properties listed in Table 5.3 are the measured values, i.e. fluxes have not been corrected for Galactic extinction. Columns 3 and 4 in Table 5.4 list the values of Galactic reddening towards

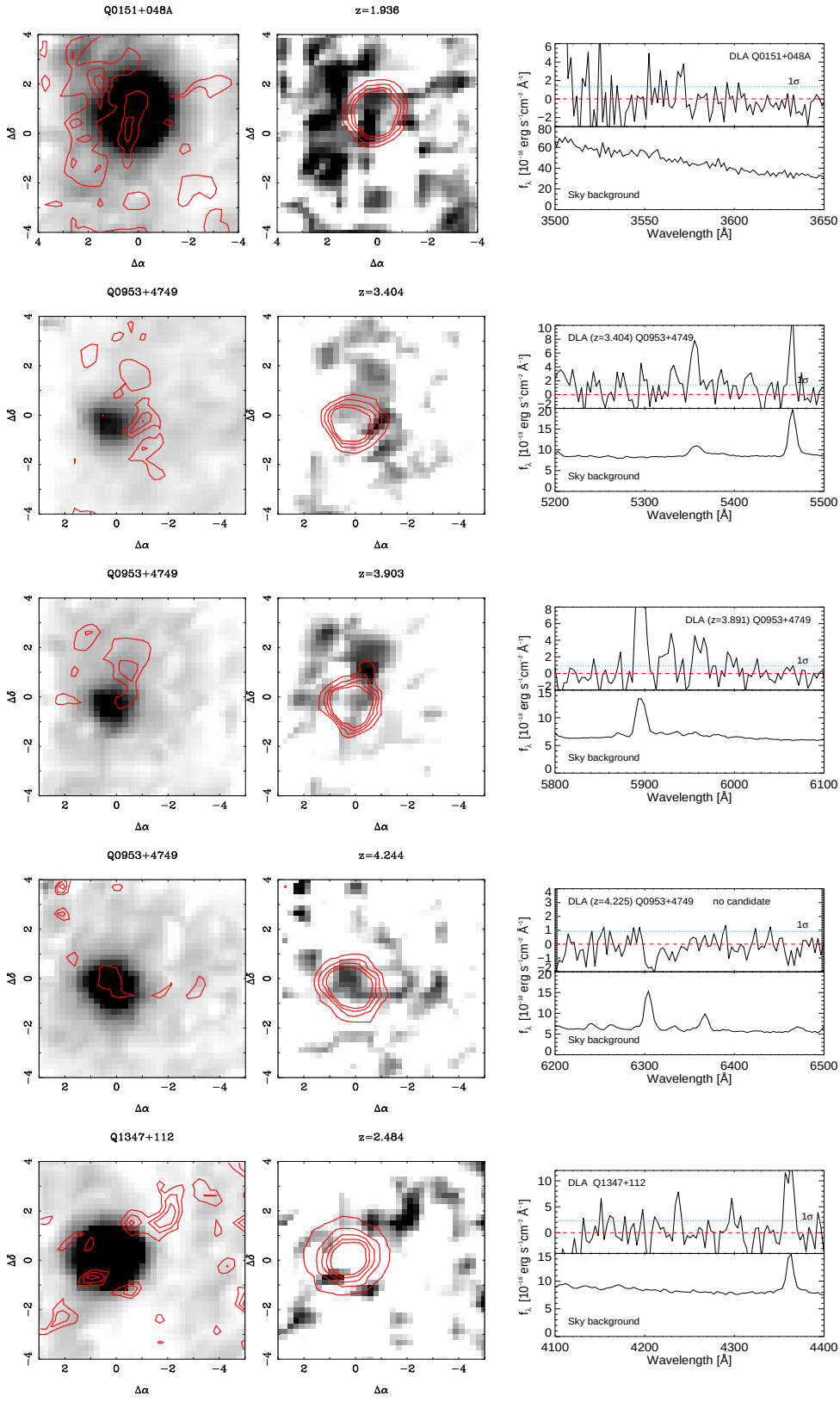

Fig. 5.3. *Left panels*: narrow-band images of the QSOs with overlayed contours of narrow-band images centered on the DLA wavelengths. Contour levels correspond to 2,3,4σ levels above the background noise. *Middle panels*: the reverse, where the contours are arbitrary apart from the central one that shows the QSO seeing *FWHM*. *Right hand panels*: Candidate spectra created from co-adding spaxels associated with the emission line candidates. The spectra in the lower panel show the RMS noise from background sky spectra.

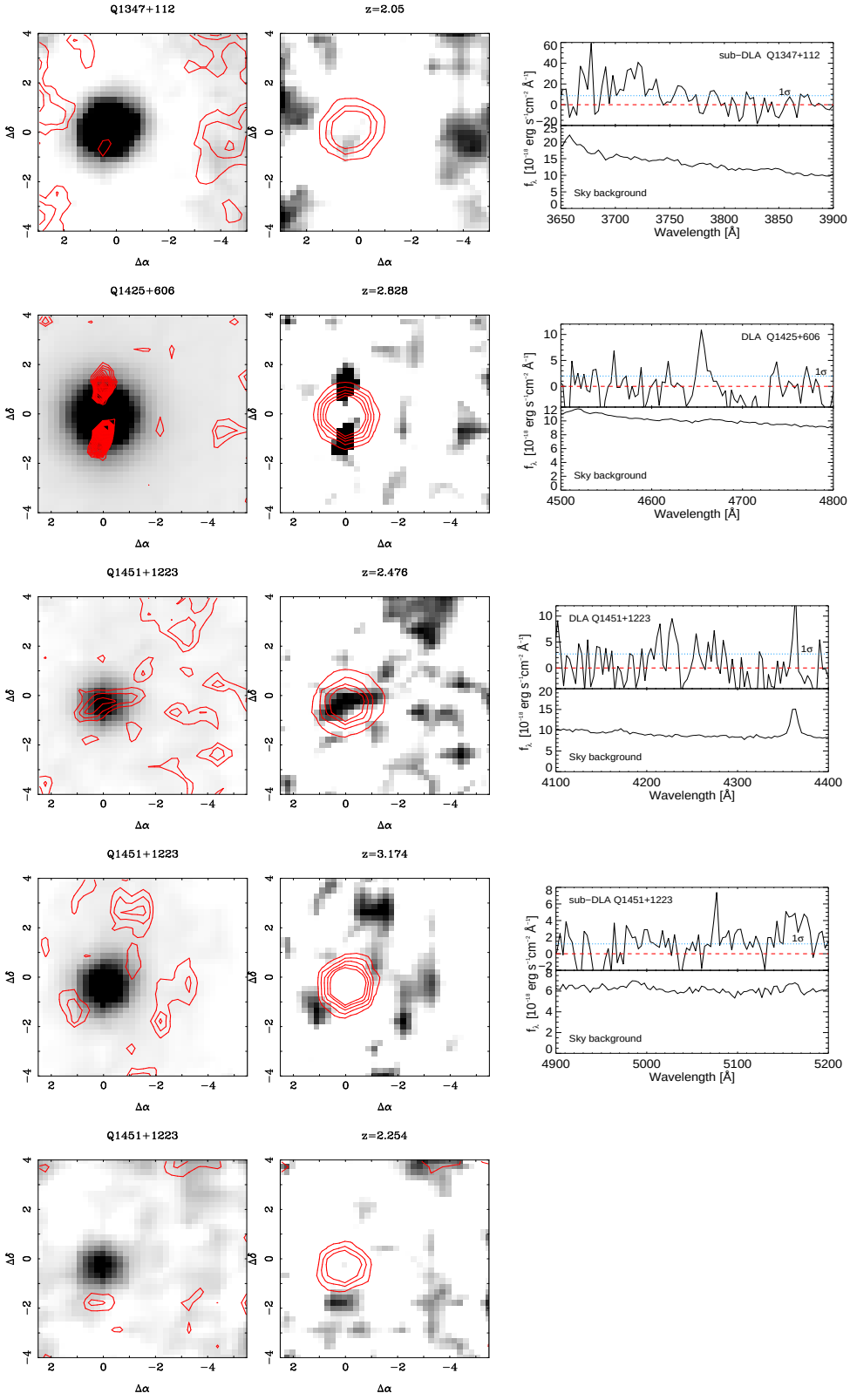

Fig. 5.3. Plots of candidates– continued.

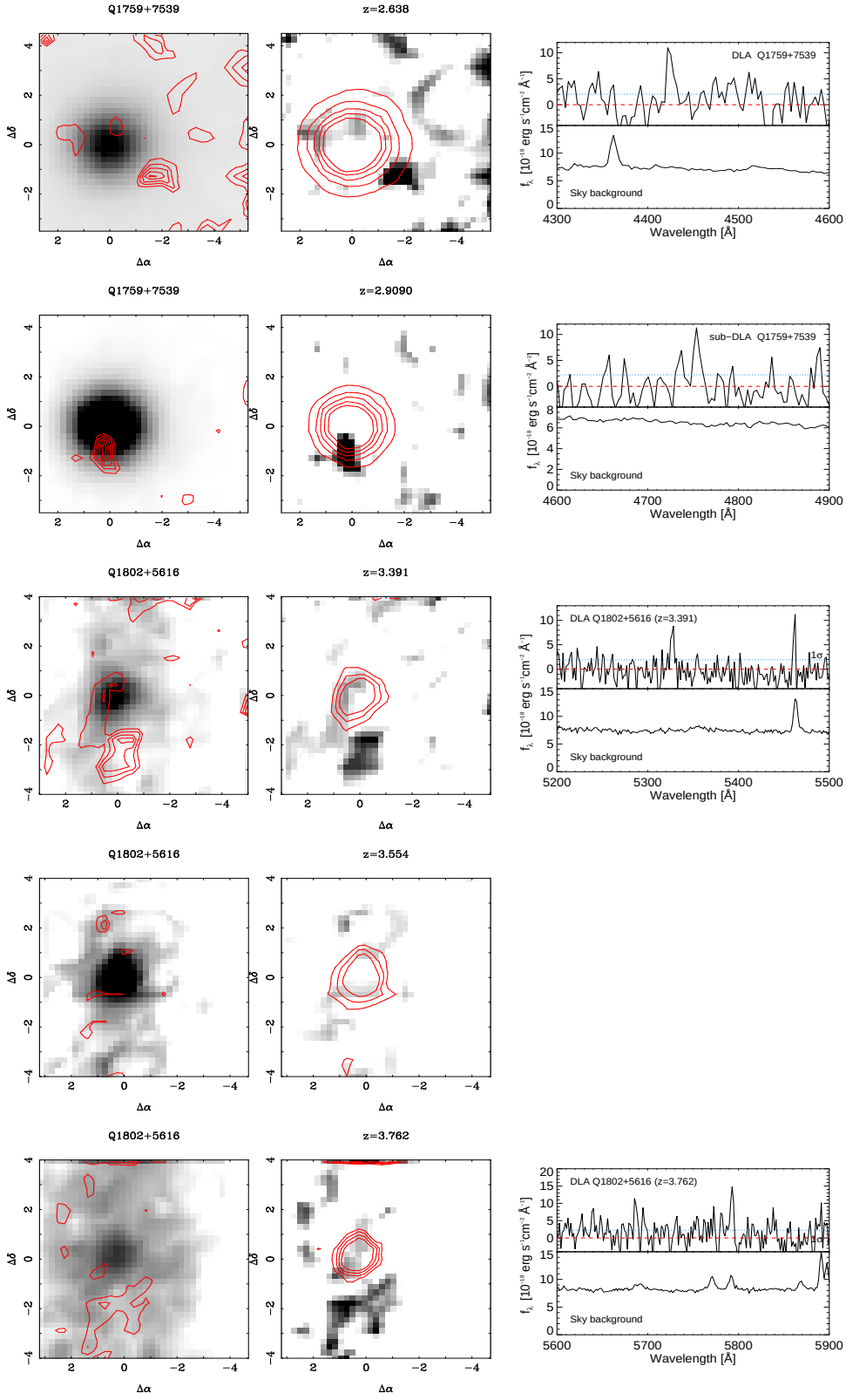

Fig. 5.3. Plots of candidates– continued.

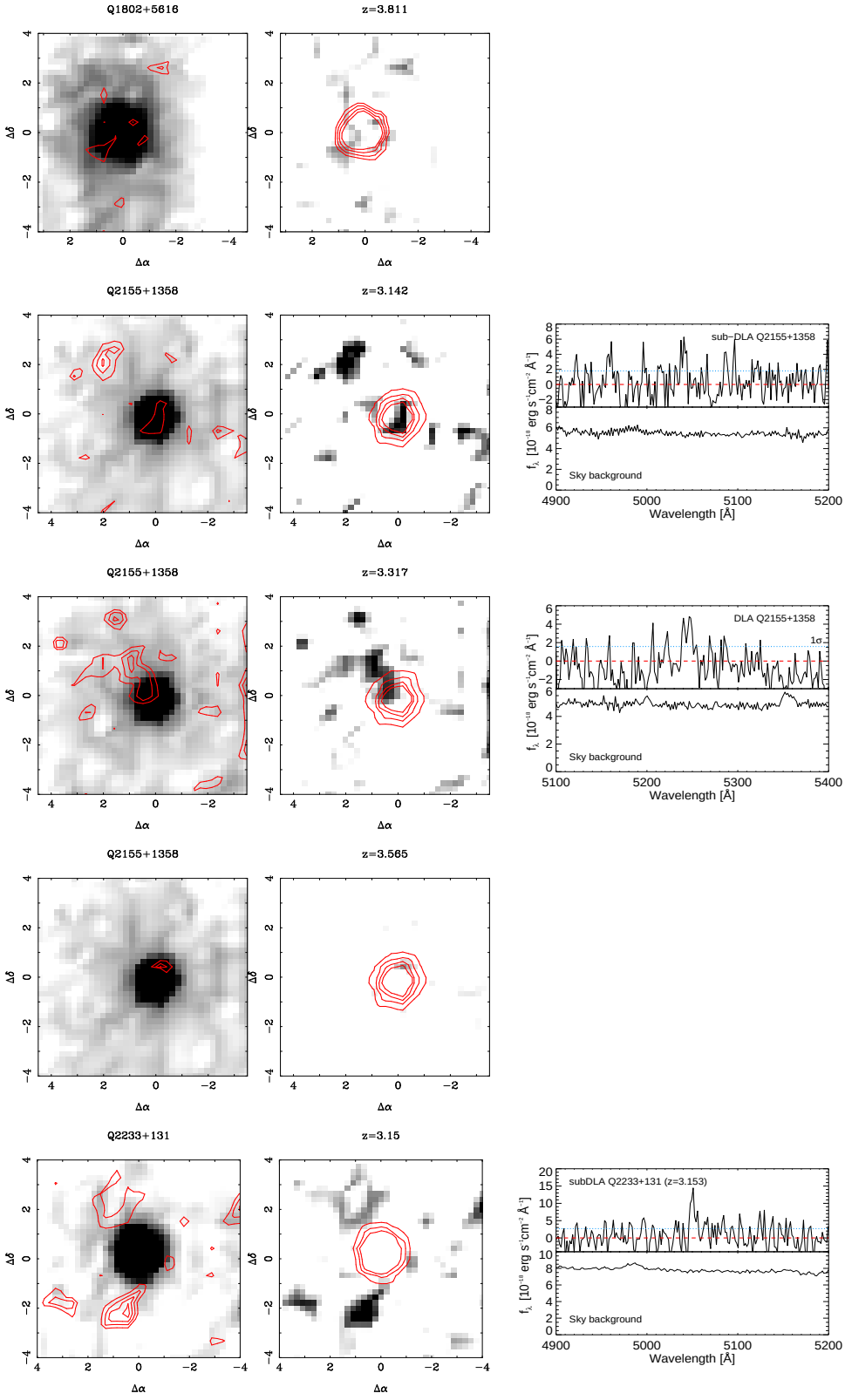

Fig. 5.3. Plots of candidates– continued.

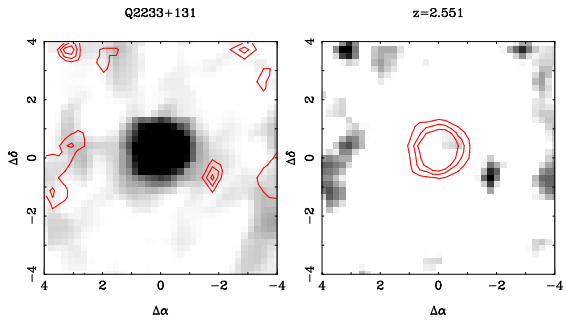

Fig. 5.3. Plots of candidates– continued.

each QSO (Schlegel et al. 1998), and the correction factors to be applied to the candidate fluxes for a Milky Way extinction curve (Fitzpatrick 1999).

5.5 Results

This section describes the classification of candidates detected and analyses data cubes for possible contaminations from unrelated emission lines. Notes on each observed object are presented as well.

5.5.1 Candidate significance

To estimate how reliable the candidate detection was various tests were applied to the data cubes. The candidates are assigned a quality number 1, 2, 3, and 4 according to how many of the following tests were passed.

1. Instead of co-adding all data-cubes, two independent subsets were created, and the emission line candidate should be visible in both sub-set combinations. Below these will be referred to as sub-combinations.

2. The emission line candidate should be visible in the simple extractions, where a Gaussian profile was not assumed. These are expected to have a lower signal-to-noise detection.

3. Emission line candidates should be visible when the QSO spectrum was subtracted from the data cube.

4. Emission line objects directly visible in individual or combined data cubes. This emission should be visible from more than one spaxel group.

Finally, the S/N ratio of the candidate Lyα emission line is also taken into account. In all cases, for a candidate to be considered further it is required to be detected above 3σ in both narrow-band images and the associated spectra. The significances of the candidates are listed in column (10) in Table 5.3, and further details for each object are described in Section 5.5.5.

5.5.2 Non detections

In the data cubes where no candidates were found, we estimated the upper limits for the emission line fluxes. To estimate upper limits, we co-added spaxels within one seeing element (e.g. 4 spaxels corresponding to a seeing of $1''$) to create a one-dimensional spectrum. Artificial emission lines

QSO	ΔRA ($''$)	ΔDEC ($''$)	b (kpc)	z	f_λ	Δ V (km s^{-1})	σ	*FWHM* (km s^{-1})	significance
(1)	(2)	(3)	(4)	(5)	(6)	(7)	(8)	(9)	(10)
Q0151+048A	2.5:0.4	-2.5: 1.7	3.3:25.4	1.9363	(150±70)	+225	7	280±220	conf.
Q0953+4749	–1.2	–0.2	9.0	3.4041	(6.6±2.9)	0	15	290±260	2
	–0.5	1.8	11.1	3.9029	(4.9±2.1)	+780	16	570±230	3
Q1347+112	–2.0	1.5	20.2	2.4835	(3.5±1.9)	+1080	8	190±370	3
	–4.1	0.4	34.3	2.0568	(4.2±3.0)	+670	7	610±210	1
Q1425+606	–4.1	0.4	32.3	2.8280	(8.5±3.1)	+80	14	590±220	3
Q1451+1223	–3.0	3.8	39.2	2.4764	(5.8±2.6)	+640	10	320±260	3
	–1.0	2.8	22.5	3.1739	(3.1±2.0)	+210	7	$<$100	3
Q1759+7539	–1.4	3.5	30.0	2.6377	(5.8±3.0)	+1050	10	290±220	2
	0.1	–1.2	9.4	2.9090	(6.0±2.9)	–80	21	240±260	1
Q1802+5616	–0.2	–2.0	14.9	3.3820	(3.5±0.9)	-610	10	180±90	4
	0.2	1.8	12.9	3.7652	(4.6±1.9)	+200	7	$<$100	2
Q2155+1358	0.7	1.2	10.2	3.3174	(9.4±3.0)	+100	9	780±210	3
	1.7	1.9	19.4	3.1461	(4.1±2.4)	+290	7	260±220	3
Q2233+131	0.6	2.3	18.0	3.1543	(9.6±2.5)	+100	9	230±110	conf.

Table 5.3. Properties of candidate Lyα emission lines. All candidates with any detection significances are included. Column 2, 3, and 4 list the offsets of the candidate in RA and DEC and in projected kpc at the Lyα emission redshifts (in col. 5), respectively. Column 6 list the integrated Lyα flux in units of 10^{-17} erg cm^{-2} s^{-1}, and column 7 the velocity offset from the DLA redshift. Column 8 lists the integrated signal-to-noise ratio of the Lyα emission line, and column 9 gives the line width of the emission lines. Fluxes have not been corrected for Galactic extinction. Column (10) lists the significance of the detections as described in the text. Conf. implies candidates which were already confirmed (Møller et al. 1998; Djorgovski et al. 1996). High significance values implies better candidates.

QSO	$E(B-V)$	$f_{\rm frac}$
Q0151+048A	0.044	1.216
Q0953+4749 (z =3.4041)	0.011	1.032
Q0953+4749 (z =3.9028)		1.028
Q1347+112 (z =2.4835)	0.035	1.145
Q1347+112 (z =2.0568)		1.163
Q1425+606 (z =2.827)	0.012	1.043
Q1451+1223 (z =2.4764)	0.031	1.128
Q1451+1223 (z =3.1739)		1.102
Q1759+7539 (z =2.6377)	0.053	1.220
Q1759+7539 (z =2.91)		1.199
Q1802+5616 (z =3.3820)	0.052	1.164
Q1802+5616 (z =3.7652)		1.145
Q2155+1358 (z =3.3174)	0.067	1.222
Q2155+1358 (z =3.1461)	0.067	1.237
Q2233+131	0.068	1.240

Table 5.4. Column 2 and 3 give values of the Galactic reddening and the corresponding correction factor to be applied to the emission line candidates.

QSO	$z_{\rm abs}$	$f_{\rm lim}(3\sigma)$
Q0953+4749	4.244	2.5
Q1451+1223	2.256	4.0
Q1802+5616	3.554	4.0
Q1802+5616	3.811	2.2
Q2155+1358	3.565	3.5
Q2233+131	2.551	4.8

Table 5.5. DLA and sub-DLA systems where no candidate emission lines were found and 3σ upper limits for the line fluxes. Fluxes are given in units of 10^{-17} erg cm^{-2} s^{-1}.

with varying line fluxes were added to this spectrum at the DLA wavelength, and Gaussian profile fits to these lines were used to estimate the detection level. Results are listed in Table 5.5. The varying limits are a result of the wavelength dependent noise in the data cubes and in particular the presence of residuals from nearby sky emission lines.

5.5.3 Experiments with artificial objects

To investigate how the efficiency of the visual inspection depended on object properties, several experiments with constructed artificial data cubes were made. Similar to artificial experiments for one- and two-dimensional data sets, an artificial emission line object was added to the data cubes. Artificial objects were described by the location in RA and DEC, central wavelength, peak emission flux, and the widths in RA, DEC and wavelength. For simplicity we assumed that an emission line object could be represented by a Gaussian profile in each direction, i.e. described by a Gaussian ellipsoid in the data cube.

We first tested completely simulated data cubes with statistical noise levels corresponding to the typical noise level in the combined data cubes. An emission line object with a flux of 5×10^{-17} erg cm^{-2} s^{-1}, a width of 800 km s^{-1}, and spatial *FWHM* of 1″ in both RA and DEC was placed at a previously known wavelength. In the stacked spectra (similar to that shown in Fig. 5.2) no objects could be seen immediately. Only after inspecting the data cube in the visualisation tool, the emission line was identified, extracted and analysed in the same way as the real data. Similar tests were made by adding an emission line to a real data cube, where the background noise included the systematic noise as well as the pure Poissonian noise. These tests produced similar results and showed that the presence of a faint emission line does not necessarily imply that the emission line object is visible in the stacked spectra.

We also tried an automatic routine where the re-detection of the artificial objects was done with no visual or manual intervention. Narrow-band images were created in wavelength regimes around the artificial line and a two-dimensional Gaussian profile was fit to the images. When an object was detected, spaxels around the centre within the corresponding seeing *FWHM* were co-added. For the detection of an emission line the location was constrained to be within $\pm$10 Å of the input central wavelengths. A series of tests showed that the recovered flux was consistent within 1σ errors, estimated from the RMS deviation of the differences between input and output flux, for fluxes as small as 5×10^{-17} erg cm^{-2} s^{-1}. In a typical data cube this was also the detection limit where 50% of the objects were re-identified, while the fraction of re-identified emission lines at this flux level from a visual inspection was larger.

Tests on the frequency of false detections in data cubes where no objects were present showed that simultaneous detections of objects in a number of narrow-band images and associated spectra with S/N > 3 occurred in less than 5% in a series of 100 experiments. Therefore false detections can not explain the large number of candidate objects. However, as explained, visual inspections do find more faint lines such that the fraction of fake signals could be larger but probably still < 10%.

All the experiments with very faint objects showed that the resulting PSF in a narrow-band image was not symmetric, and the odd shapes of the candidates in Fig. 5.3 can be explained by the experiments.

5.5.4 Field Lyα emitters

Observations of very high redshift objects have partly focused on detecting Lyα emission from galaxies to determine the global comoving star-formation rates in the Madau diagrams (e.g. Hu et al. 1998, 2004).

The density of Lyα emitters at $z \sim 3$ is estimated to be $\sim$3.5 arcmin^{-2} Δz^{-1} with line fluxes brighter than a mean of $f = 7 \times 10^{-17}$ erg cm^{-2} s^{-1} (Hu et al. 1998; Kudritzki et al. 2000). In our survey, the 9 data cubes sample a total redshift interval of $\Delta z = 21.55$ around $z \approx 3$. Statistically, it is expected that there is 1.3 field Lyα emitters in the whole sample presented here. Because these very faint lines are difficult to locate when the approximate wavelength is not known in advance, we did not look for field emission objects. The small number of expected field emitters furthermore shows that the emission candidates, if proved to be real, are very unlikely interloping field Lyα emitters.

5.5.5 Notes on individual objects

This section explains for each individual QSO the detection significance of the candidates and where no candidates were found, upper limits for detections are estimated. Comparisons of the QSO redshifts with literature values are presented. Magnitudes reported below are in the Vega system, and no correction for Galactic extinction is applied. For some of the objects imaging data were obtained from public archives to check the position of the candidates with respect to higher spatial resolution data.

Q0151+045A

This is a $z_{\rm em} \approx z_{\rm abs}$ system at $z \approx 1.93$. After flux calibration, our spectrum is a factor of 3 brighter than in Møller et al. (1998). Convolving the QSO spectrum with a broad V band filter resulted in a magnitude difference of 2 with that in the literature. Although the conditions were stable during the observations the low instrument sensitivity at 3560 Å combined with a variable extinction coefficient at Calar Alto makes the calibration uncertain.

Extended Lyα emission was observed in a region of $3 \times 6''$ around the QSO mostly to the east of the QSO (Fynbo et al. 1999). Follow up long slit spectroscopy along the longest extension reveled velocity structures of 400 km s^{-1} that could be interpreted as a rotation curve (Møller 1999).

In the IFS data extended emission is detected to some degree in Fig. 5.3, but not with the same detail as in the higher spatial resolution and larger field of view data in Fynbo et al. (1999). This is the only case in the sample where extended emission is found. However, the low signal in this spectral region prevents us to determine the exact extension and velocity components to be compared with the results in Møller (1999). In fact, our spectra indicate no velocity structure over the extended emission region. The spectrum shown in Fig. 5.3 is the total spectrum co-added from the whole nebula.

Q0953+4749

This $z_{\rm em} = 4.457$ QSO has three DLAs at $z_{\rm abs}$ = 3.404, 3.891, and 4.244. Bunker et al. (2003) report $z = 3.407$ for the the lowest redshift DLA. The signal-to-noise ratio in this region of the spectrum is too low to determine z satisfactorily for the DLA line, and because the the spectrum

redwards of the QSO is not covered, we can not determine the systemic redshift of this system from associated metal absorption lines.

A candidate from the lowest redshift DLA is visible in narrow-band image in Fig. 5.3. Independent sub-combinations and the corresponding spectrum show a faint emission line. Likewise for the simple extraction, the object is visible in narrow-band images but has a too noisy spectrum to allow identification of an emission line. These are not shown here. We note that this emission line coincides with a sky emission line (offset by –1.6 Å as indicated in the spectrum in Fig. 5.3), thus the emission feature could be due to sky subtraction errors, and we only assign this candidate significance 2. A Lyα emission line from the DLA galaxy has been reported (Bunker et al. 2005, in prep.) but its line flux is below our detection limit.

For the second DLA system at $z = 3.8901$ similar results were found i.e. the object is present in sub-combinations, however, the emission in the simple- extracted images appears to be shifted by $\sim 0\farcs5$ to the east compared to the Gaussian extraction. This candidate is assigned significance 3. The locations of the candidates were compared to WFPC2 images obtained from the HST archive (Bunker et al. 2005, in prep.), but no broad band counterpart could be identified. No candidate was found for the highest redshift DLA to a detection limit reported in Table 5.5.

Q1347+112

This $z_{\rm em} = 2.679$ QSO has a DLA at $z_{\rm abs} = 2.471$ and another possible DLA at $z_{\rm abs} = 2.05$, although this system needs confirmation. The QSO spectrum shows an absorption line system at $z = 2.621$ (Turnshek et al. 1989), but its $N(\mathrm{H\,I})$ is not reported, and we do not consider this system further here.

A DLA emission candidate for the $z = 2.471$ DLA is visible in independent data sets in both narrow-band images and the co-added one-dimensional spectrum. These are similar to the images presented in Fig. 5.3. In the simple extraction, the spectrum is too noisy to allow identification of the emission feature in the spectrum. For the lower redshift DLA system we detect a candidate emission line object, but this candidate is less certain due to an increase in the background noise short-wards of 3750 Å combined with increasing flat field errors towards blue wavelengths. In fact, the object was not seen in one of two individual sub-combinations and therefore the candidate is assigned a low significance.

A snapshot WFPC2 image from the HST archive with an exposure time of 260 s is insufficient to detect faint objects nearby the QSO.

Q1425+606

This $z_{\rm em} = 3.163$ QSO has a DLA at $z_{\rm abs} = 2.827$.

Because this QSO is very bright, strong residuals within $1''$ from the QSO centroid are present in the narrow-band image. A faint object offset by $\sim 4''$ to the west is visible in the narrow-band image in Fig. 5.3. The candidate is present in sub combinations in both narrow-band images and constructed spectra. In the simple combination the candidate is not clearly visible in the narrow-band image, but knowing the location of the associated spaxels for the object the emission line appears with a lower signal. Having passed these tests the object is assigned a significance of 3. A Gaussian line profile is a bad representation, and it appears to have a blue cut-off similar to those observed for high redshift Lyα emission objects (Hu et al. 2004).

Having found a candidate at the edge of the field of view in the data cube is a reason for some skepticism. In PMAS data cubes, spaxels in the west region are more noisy than the average, and the low signal spectra could appear as artificial emission lines. Having noted that, the object does pass the tests for being a good candidate and we keep this candidate into considerations.

Q1451+1223

This $z_{\rm em} = 3.246$ QSO has a DLA at $z_{\rm abs} = 2.469$ and two sub-DLAs at $z_{\rm abs} = 3.171$ and $z_{\rm abs} = 2.254$. Deep broad-band images of the field surrounding this QSO was obtained by Steidel et al. (1995), who found no obvious candidates to the absorbers. Using deep NICMOS images Warren et al. (2001) found one candidate offset by 3.″9 to the south-west of the QSO, but this object is outside field of view of the IFS data.

First we investigate the DLA system. Close to the QSO centre an object with an emission line appears after the QSO subtraction (see Fig. 5.3), but this is likely due to residuals. A Lyα emission line candidate to the DLA system offset by $\sim$4″ to the north west appears in the IFS data in both narrow-band imaging and constructed spectra in sub combinations of data sets. Also in the simple extracted spectra, the candidate is visible and we assign a significance of 3 to the candidate. For the $z = 3.171$ sub-DLA system an object is detected as shown in Fig. 5.3. Narrow-band images from sub combinations still show the emission line candidate, while the corresponding spectra have emission lines with very low signals. This object is also visible in the simple extracted data cube both in a narrow-band image and the associated spectrum. The candidate is also assigned a significance of 3.

A comparison of the PMAS data sets with an HST/STIS image shows that the emission line candidate lies in regions where no continuum emitting counterpart are found.

Q1759+7539

This $z_{\rm em} = 3.05$ QSO has a DLA at $z_{\rm abs} = 2.625$ and a sub-DLAs at $z_{\rm abs} = 2.91$. A NICMOS snapshot survey showed no bright candidates near the QSO sight line, but the images were too shallow to detect galaxies fainter than L^* (Colbert & Malkan 2002).

The candidate detected for the DLA system in Fig. 5.3 lies to the edge of the field of view and can be affected by flat field errors, that increase towards the edge of the field. In fact, the candidate is not visible in sub combinations, and is therefore assigned a low significance of 2, because the emission line still appears to be bright. In the spectrum with the largest signal a Gaussian line profile is a bad representation of the line profile, which appears to have a blue cut-off. This effect is not as strong as seen for the Q1425+606 candidate, however. A bright area 1.″8 south west of the QSO appears after the QSO emission is subtracted but it is likely an effect of the PSF subtraction. It has no emission lines at this wavelength and is not considered further.

The higher redshift sub-DLA system apparently has a bright candidate which is visible only after the QSO PSF has been subtracted from the final cube. However, the candidate is only visible in one out of two sub combinations and we assign this candidate a low significance of 1.

Q1802+5616

This $z_{\rm em} = 4.158$ QSO has four DLAs at $z_{\rm abs}$ = 3.391, 3.554, 3.762, and 3.811. For this QSO $V = 18.3$ is reported in the literature (Véron-Cetty & Véron 2001). A convolution with a Bessell V band transmission gives $V = 22.0$ suggesting that the flux calibration is seriously affected, but this is uncertain due to the low signal-to-noise ratio in that spectral range.

The candidate galaxy for the lowest redshift DLA system was directly visible in the reduced, combined data cube (see Fig. 5.2). Also in individual sub-combinations and in the simple extracted spectrum the candidate can be identified such that this candidate is assigned a high value of 4.

In a narrow-band image at the wavelength of Lyα at $z = 3.7652$ there is a faint emission region (see Fig. 5.3) and the corresponding spectrum shows an emission feature. However, this line is coincident with a faint sky emission line, so the candidate is less certain. At the redshifts of the other DLA systems we found no candidates.

Q2155+1358

This $z_{\rm em} = 4.256$ QSO has a DLA at $z_{\rm abs} = 3.316$ and three sub-DLAs at $z_{\rm abs} = 3.142$, 3.565, and 4.212. The observations only cover Lyα at the three lowest redshift systems, and the spectrum as seen in Fig. 5.1 is strongly affected by the Lyα forest.

The candidate Lyα emission line associated with the DLA system is visible in independent sub combinations and in the simple extraction of the data sets and was therefore assigned a high value of 3. Because of the partial spatial overlap with the QSO, the emission from the QSO was subtracted to give a cleaned emission line object and associated spectrum shown in Fig. 5.3.

A candidate was found for the $z = 3.142$ redshifts sub-DLA system as shown in Fig. 5.3. This object was visible in two separate sub-combinations, but only one associated spectrum showed an emission line, so that this object is potentially a good candidate. The simple extraction shows the same candidate with a low-signal in the associated spectrum. No candidate was found for the $z = 3.565$ sub-DLA.

Q2233+131

This $z_{\rm em} = 3.295$ QSO has two sub-DLAs at $z_{\rm abs} = 3.153$ and $z_{\rm abs} = 2.551$.

The galaxy responsible for the $z = 3.153$ DLA was found by Steidel et al. (1995), and follow-up spectroscopy confirmed this by the detection of Lyα emission (Djorgovski et al. 1996). Previous IFS of this object suggested that the Lyα emission was extended (Christensen et al. 2004). This is not confirmed by the higher resolution data, although that there appears to be some faint emission to the east of the object in Fig. 5.3. Because the Lyα emission line from the sub-DLA galaxy is a previously confirmed object, we do not treat this object similar to the candidates in the study below. No candidate was found for the $z = 2.551$ sub-DLA system.

5.6 Candidate properties

Having detected candidate Lyα emission lines from a sample of DLAs this section proceeds with a more detailed analysis of the properties. Only those candidates assigned values 3 and 4 are included in the following analyses such that the sample consists of 8 good candidates. With these 8 candidates, the detection fraction is ∼40%. The average redshift of all the DLAs in the whole sample is $\bar{z}_{\rm sample} = 3.13$ while that of the candidates is $\bar{z}_{\rm cand} = 3.06$, hence we find no preference for detection of either lower or higher redshift candidates. We emphasise that the candidates are detected at the 3–4σ level, but with this in mind we proceed with comparing their properties with those of confirmed Lyα emission lines from objects described in the literature (e.g. Møller et al. 2002).

5.6.1 Line fluxes

Fig. 5.4 shows the inferred line fluxes of the candidates as a function of redshifts. Triangles denote our candidates and the square symbols indicate already confirmed objects from the literature. This figure shows that the line fluxes for the candidates are similar to the line fluxes for the previously confirmed objects.

In a Fabry-Perot imaging survey of 8 DLA systems Lowenthal et al. (1995) inferred upper limits for Lyα emission from DLA systems of $3{\times}10^{-17}$ erg cm^{-2} s^{-1}. With that detection limit some objects should have been detected. Although their filter widths were generally larger (18 Å *FWHM*) than what used here (10 Å) such that any emission would fall within the filter, their central wavelength could be shifted from the location of the DLA Lyα emission, where the transmission is lower. Another limitation to their analysis was that no investigation of QSO-PSF subtracted images

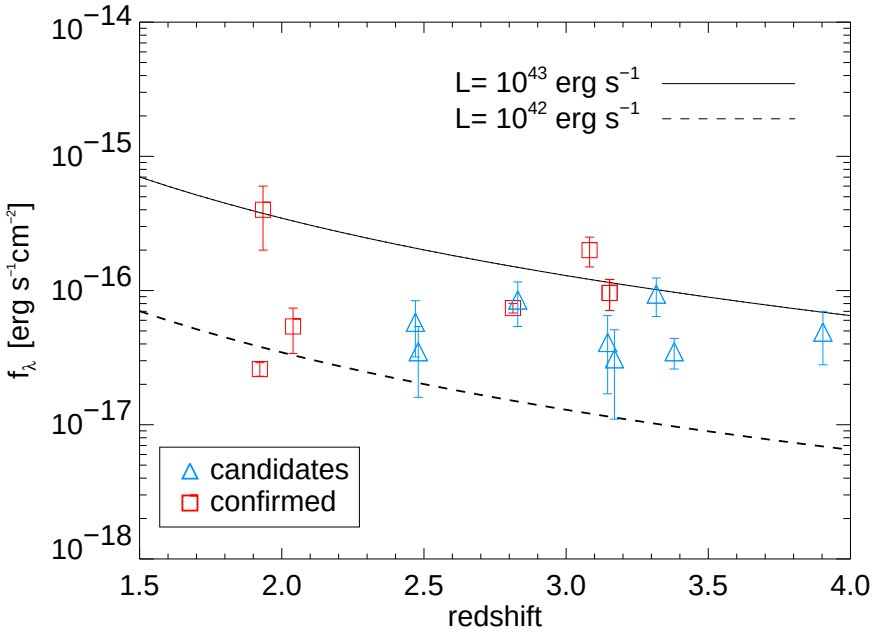

Fig. 5.4. Line fluxes of Lyα emission objects as function of redshift, where square symbols represent already confirmed objects and triangles the candidates. The solid and dashed lines correspond to luminosities of 10^{43} and 10^{43} erg s^{-1}, respectively.

was done and combined with a seeing of $\sim$2″, Lyα emission lines could be hidden in the wings of the QSO PSFs. IFS observations are more suitable for this investigation because of the possibility of tuning narrow-band filters. Furthermore, the knowledge of the variations of the QSO PSF as a function of wavelength allows a modeling and subtraction of the QSO emission (Wisotzki et al. 2003; Sánchez et al. 2004).

5.6.2 Velocity differences

It is expected that there is an anti-correlation between the Lyα luminosity and the velocity difference between the Lyα emission line and optical emission lines (Weatherley et al. 2005). The resonance nature of Lyα emission affects the line profile by absorption at the blue side of the line profile which shifts the measured redshift towards larger values. Hence, lower luminosity lines could be more shifted than brighter ones. This explanation is supported by the study of Lyα emission lines from LBGs (Shapley et al. 2003). Most Lyα emission lines from high redshift galaxies are redshifted relative to the systemic velocities, but the Lyα line from one LBG has a velocity offset of –180 km s^{-1} (Erb et al. 2003).

Fig. 5.5 shows the velocity differences between Lyα emission lines and the DLA redshifts for the candidates as a function of the Lyα luminosity. We note that the only candidate that shows a negative velocity offset is the best candidate in the sample as shown for the $z = 3.391$ DLA towards Q1802+5616 in Fig. 5.2. For the candidates we find an average velocity difference of 320$\pm$520 km s^{-1}, which is very similar to the velocity differences measured for LBGs; Pettini et al. (2001) find 560$\pm$410 km s^{-1} while a larger sample has ΔV = 510 km s^{-1} (Shapley et al. 2003). With the current velocity uncertainties for the candidates and the small number of objects available, Fig. 5.5 shows neither a clear correlation nor an anti-correlation between the two parameters.

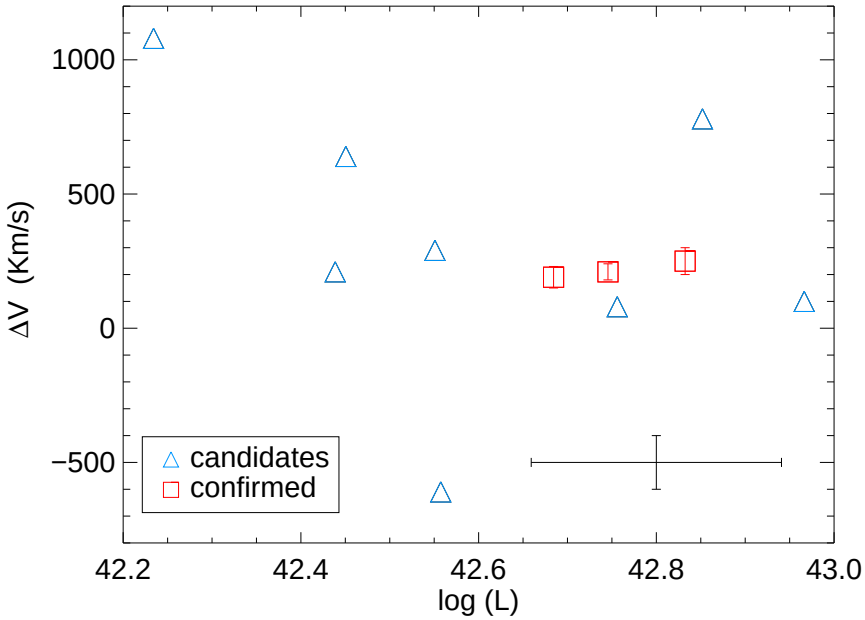

Fig. 5.5. Velocity difference between the Lyα line and DLA redshifts as a function of the Lyα luminosity. An average error bar for the Lyα emission candidates is shown in the lower right corner.

5.6.3 H I extension

The average impact parameter of $\sim$20 kpc derived for the candidates is larger that expected by numerical simulations which favor impact parameters of 3 kpc for typical DLA galaxies and only few DLA galaxies with $b > 10$ kpc at all redshifts (Okoshi & Nagashima 2005; Hou et al. 2005). One possibility for this large disagreement is, as also pointed out in Hou et al. (2005), that their simulations assume a single disc scenario, while DLA galaxies could lie in groups and the real absorbing galaxy could lie closer to the QSO sight line. This is naturally also possible for the observed DLA galaxies. Larger DLA galaxy sizes of 10–15 kpc at $2 < z < 4$ are inferred in other simulations (Gardner et al. 2001).

An anticorrelation between $N(\mathrm{H\,I})$ and the distance to the nearest galaxy was found in simulations (Gardner et al. 2001), but no analysis of this effect for observed DLA galaxies have been attempted. Only a trend for larger column density absorbers at smaller impact parameters was observed in a sample of DLA galaxies at $z < 1$ (Rao et al. 2003). At lower column densities in the Lyα forest such an anticorrelation has been shown to exist (Chen et al. 1998, 2001). Observations of the galaxies giving rise to Mg II absorption lines showed an anti-correlation between the impact parameters and column densities of both Mg II and H I (Churchill et al. 2000). Nevertheless, more recent observations of a larger sample have indicated that the correlation is not always present (Churchill et al. 2005).

We here investigate whether the candidates show a similar anticorrelation. Using the impact parameters for the candidates as a proxy for the sizes of neutral gas envelopes, we investigate average properties of DLA galaxies. This is necessarily a rough approximation because large morphological differences between individual systems are expected (Rao et al. 2003; Chen & Lanzetta 2003). Specifically, the possible presence of sub-clumps is neglected.

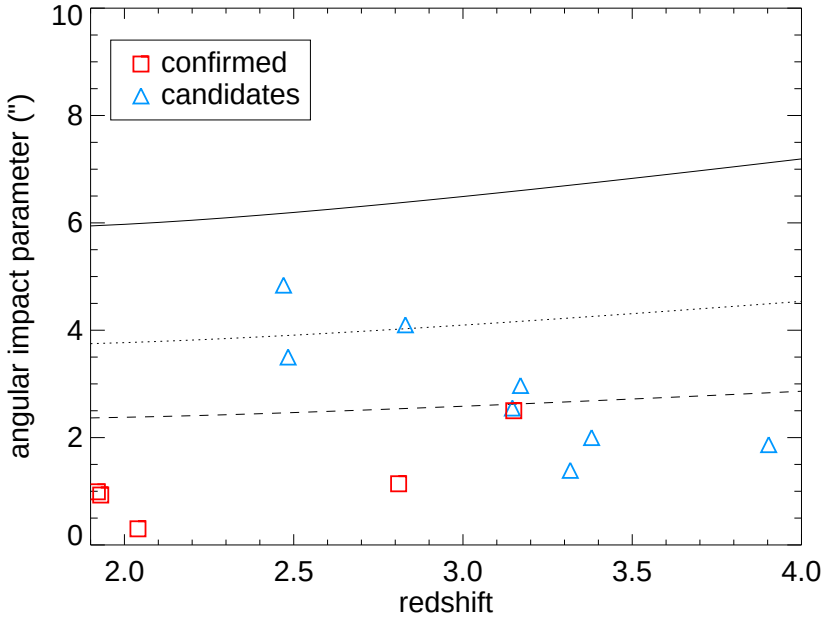

Fig. 5.6. Angular impact parameter vs. redshift. The solid line corresponds to the relation derived in Chen & Lanzetta (2003) for an L^* galaxy, while the dashed and dotted lines correspond to galaxies with luminosities $L = 10\%L^*$ and $L = 1\%L^*$, respectively. Squares are objects from the literature and triangles the candidates from this survey.

DLA galaxy sizes and luminosities

To analyse the sizes of DLA galaxies at $z < 0.65$ Chen & Lanzetta (2003) describe the extension of the neutral gas cloud associated with DLA galaxies as

$$\frac{R}{R^*} = \left(\frac{L}{L^*}\right)^t, \tag{5.1}$$

where a fit to the observed DLA galaxies gives $R^* \approx 30$ kpc, $t = 0.26^{+0.24}_{-0.06}$, and L^* corresponding to a galaxy with $M^* \approx -20.4$. From morphologies and impact parameters Chen et al. (2005) argued that dwarf galaxies only, do not represent the DLA galaxy population at $z < 1$. Because the angular distance changes little at redshifts larger than 1, we would expect in the case of no evolution with redshift, that the impact parameter of high redshift DLA systems are similar to those at lower redshifts. However, if the DLA galaxy population evolves from low luminosity objects at high redshifts to higher luminosity objects at lower redshifts, this will affect the expected impact parameters at high redshifts. In Fig. 5.6 the impact parameters of candidates and confirmed objects are shown as a function of the redshifts. Overlayed on this figure are curves for the size-luminosity relation for low redshift DLA galaxies. From this figure it is apparent that high redshift DLA galaxies are either sub-luminous, or do not follow the low redshift scaling relations.

Powerlaw profiles

Using similar arguments as above one could expect that there is a relation between the impact parameter and the column density measured for the DLA. Fig. 5.7 shows the same objects with their impact parameters in kpc as a function of the $N(\mathrm{H\,I})$ measured for the DLA system. We

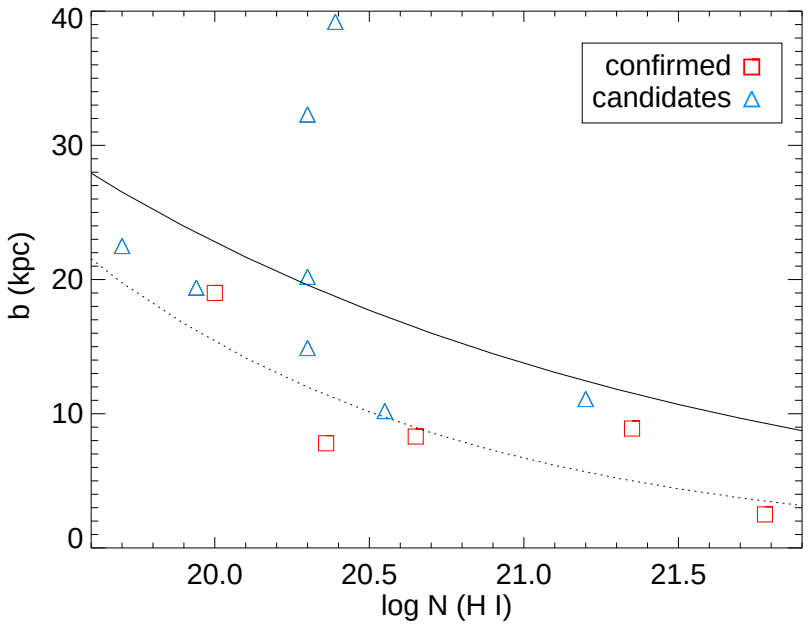

Fig. 5.7. Impact parameter as a function of the DLA column density of neutral hydrogen for the candidates and previously confirmed objects. The solid and dotted lines are fits to the relation $b/b^* = (N/N^*)^\beta$ for the candidates and confirmed objects, respectively.

assume a similar scaling relation as in Eq. (5.1) for the impact parameter and $N(\mathrm{H\,I})$, i.e.

$$\frac{b}{b^*} = \Big(\frac{N(\mathrm{H\,I})}{N(\mathrm{H\,I})^*}\Big)^\beta \tag{5.2}$$

We chose $\log N(\mathrm{H\,I})^*$ = 20.3 and an error for the impact parameter given by the fibre size 0.″5 corresponding to 3.5–4 kpc. A fit of the observed impact parameters for the candidates gives $b^* = 19.6 \pm 3.4$ kpc, and $\beta = -0.22 \pm 0.18$ as shown by the solid line, while for the confirmed objects, we find $b^* = 12.0 \pm 3.7$ kpc and $\beta = -0.36 \pm 0.14$. Disregarding the two candidate objects with largest impact parameters a fit to Eq. (5.2) yields results that are consistent with that for the confirmed objects within the errors. However, even including these two objects, the fit to the candidates is consistent with that for the confirmed objects within 1σ uncertainties.

For a randomly inclined discs the average impact parameter is related to the disc radius by $\bar{b} \approx 0.5R$. Combining this with Eq. (5.2) and the Holmberg scaling relation $R/R^* = (L/L^*)^t$, we see that

$$\frac{L}{L^*} = \frac{1}{0.5}\Big(\frac{N(\mathrm{H\,I})}{N(\mathrm{H\,I})^*}\Big)^{\beta/t}. \tag{5.3}$$

The Holmberg relation for local galaxies gives $t = 0.4$ consistent with $t = 0.26^{+0.24}_{-0.06}$ measured for low redshift DLAs (Chen & Lanzetta 2003). For $\beta \approx -0.3$ we see that $L/L^* \propto (N(\mathrm{H\,I})/N(\mathrm{H\,I})^*)^{-1}$, i.e. higher column density absorbers should belong to less luminous galaxies. Observations at $z < 1$ have indicated exactly such a trend that DLAs with larger column densities belong to lower luminosity galaxies (Rao et al. 2003). However, the number of galaxies that enter the sample is still small. Numerical simulations of DLA galaxies at $z < 1$ have shown that the column densities depend only weakly on the galaxy luminosities (Okoshi &

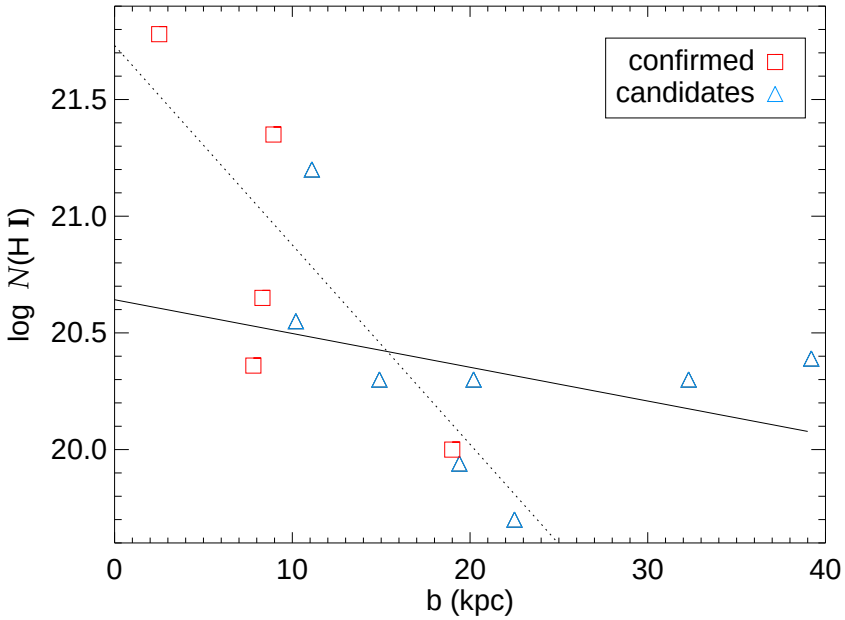

Fig. 5.8. Column density of neutral hydrogen as a function of impact parameter for the candidates and previously confirmed objects. The *solid line* shows the fit to all the candidates and the *dotted line* neglects the two candidates with the largest impact parameters.

Nagashima 2005).

Exponential profiles

21 cm observations of H I discs in the local Universe have shown that they follow exponential profiles although with some scatter. Here we fit the impact parameter distribution with the relation

$$N(\mathrm{H\,I}) = N(\mathrm{H\,I})_0 \exp(-b/h) \tag{5.4}$$

where h is a scale length and $N(\mathrm{H\,I})_0$ the central column density. The resulting fit to all the candidates is shown by the solid line in Fig. 5.8, which has $\log\ N(\mathrm{H\,I})_0 = 20.6 \pm 0.9$ cm^{-2} and $h = 30 \pm 16$ kpc. Neglecting the two candidates with the largest impact parameters gives the fit shown by the dotted line which has $\log N(\mathrm{H\,I})_0 = 21.7 \pm 1.1$ cm^{-2} and $h = 5.1^{+2.5}_{-1.3}$ kpc. This result is similar within the uncertainties to a fit to the confirmed objects only ($\log N_0 = 21.7 \pm 1.1$ cm^{-2} and $h = 4.5^{+3.6}_{-1.4}$ kpc).

Local disc galaxies have H I scale lengths ranging from ∼2 kpc to ∼6 kpc, with a tendency for early Hubble type galaxies having smaller scale lengths and later types having larger scale lengths. Radio observations of the H I profile in low surface brightness galaxies have indicated scale lengths > 10 kpc (Matthews et al. 2001). Hence, the impact parameters of the candidates are in agreement with the hypothesis that DLA galaxies are large spirals.

We note that no DLAs observed to date has log $N(\mathrm{H\,I})$>22 cm^{-2}, which in relation to the central density of log $N(\mathrm{H\,I})$= 21.7 cm^{-2} could be a curious coincidence. More likely, however, the biases that affect QSO surveys and detection of very high column density DLAs affect these results too.

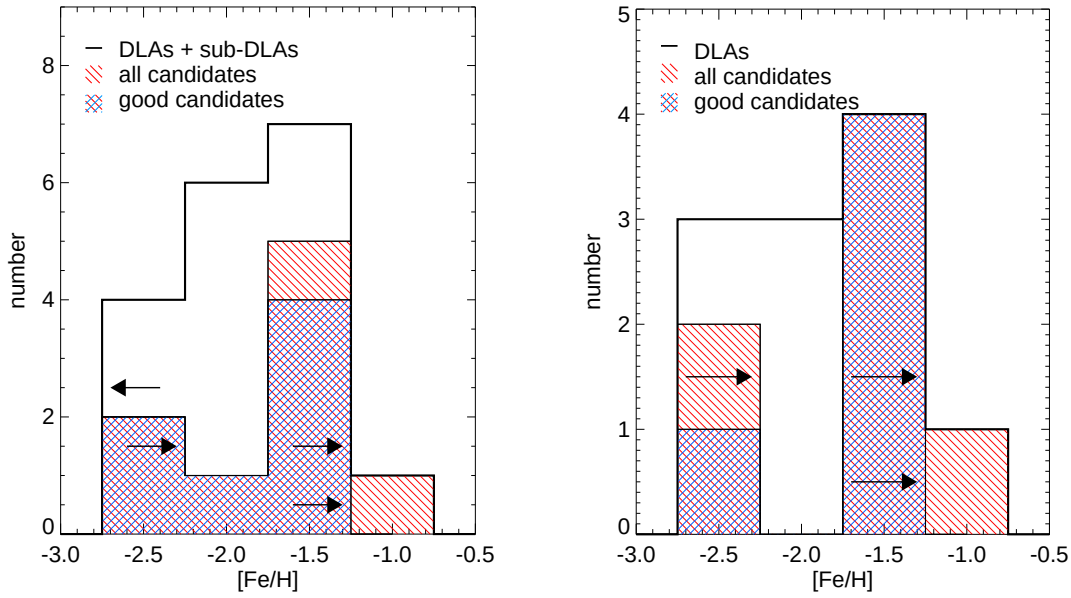

Fig. 5.9. *Left panel:* [Fe/H] metallicity distribution of all the DLA and sub-DLA systems in our sample (solid line) compared to that of all the candidates (hashed) and that of the good candidates only (cross hashed). Arrows correspond to DLAs that only have limits to their metallicity determination. In the *Right panel* the distributions of DLA systems only is shown.

5.6.4 Metallicity effects on Lyα emission

Using a space based imaging survey and follow up long-slit spectroscopic observations, Møller et al. (2004) found indications for a positive metallicity–Lyα luminosity relation, such that in their sample Lyα emission was preferentially observed for higher metallicity systems. They argued that this positive correlation could over-power the negative dust-Lyα luminosity effects which are expected to be strong in high metallicity environments (Charlot & Fall 1993). Studies of Lyα emission from nearby star-forming galaxies have not revealed any correlations between metallicity and Lyα emission strength though (Keel 2005).

In this context we investigate the distribution of metallicities for the DLA galaxies with candidates in comparison to the total sample. For the previously confirmed objects a metallicity estimate was only found for the sub-DLA towards Q2233+131. This object was not included in the analysis here, but even if it had been included, the results would not change. We also excluded from the analysis the other systems for which no metallicities are reported in the literature.

Fig. 5.9 shows the distribution of metallicities ([Fe/H]) for the 18 DLAs with known metallicities in the survey. The left panel shows the distribution of all the DLAs and sub-DLAs in our survey with metallicities found in the literature, while the right panel excludes sub-DLA systems. The red hashed histogram shows the distribution of all the candidates irrespectively of the significance, while the cross hashed histogram includes the good candidates only (i.e. candidate significance ≥ 3). In this survey we do not find a relation between a candidate selection and the DLA metallicity. For example, the DLA system with the highest metallicity in our sample has no good candidate.

In many DLAs, Fe is depleted onto dust grains which biases the metallicity towards smaller values. A better measure of the true metallicity is given by [Si/H], because Si is less depleted than Fe and has typical metallicities 0.3 dex higher than derived from Fe. A similar picture emerges when the distributions of Si is analysed as shown in Fig. 5.10. Also in this figure, no apparent difference of the distributions is visible.

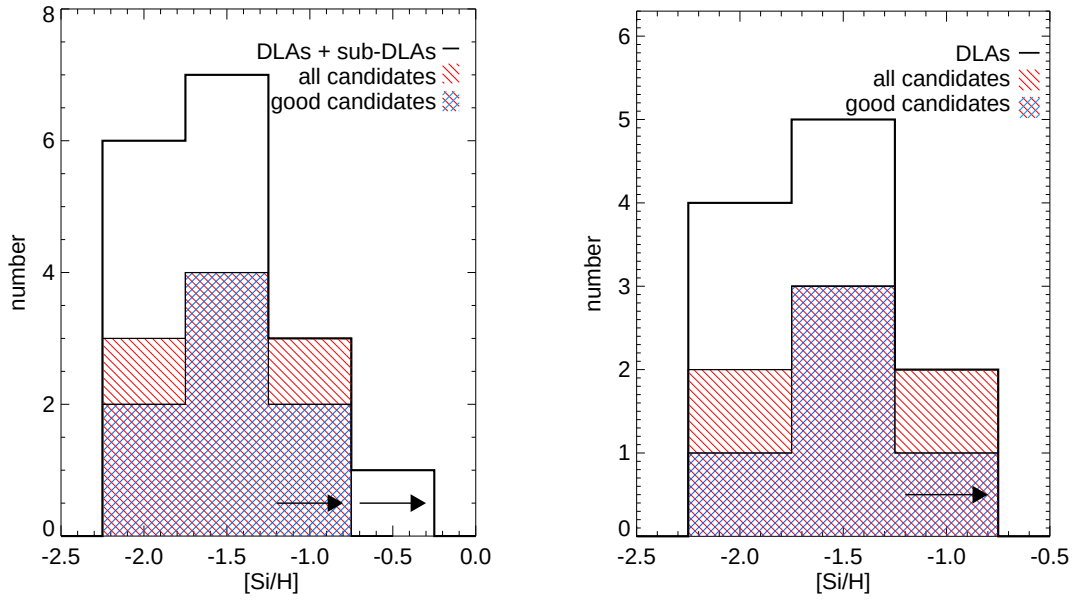

Fig. 5.10. *Left panel:* [Si/H] metallicity distribution of all the DLA and sub-DLA systems in the survey (solid line) compared to that of all the candidates (hashed) and that of the good candidates only (cross hashed). The arrows correspond to DLAs that only have limits to their metallicity determination. The *Right panel* shows the distributions of DLA systems only.

To investigate the possibility for different distributions, we compared the cumulative distributions of metallicities for the DLA candidates with those without candidates as shown in Fig. 5.11. A two sided Kolmogorov Smirnov (KS) test gives the probability of 99% that the two samples have the same underlying distributions. A similar analysis for the distributions of [Fe/H] instead of [Si/H] shows that the distributions are similar on the 67% level. Only few DLAs are included in this survey, but the KS test is statistically valid for sample sizes $N_1, N2$ where $N_1 N_2/(N_1 + N_2) > 4$, which is the case here. These comparisons show that with the current sample no differences between the metallicities of the candidates and the DLAs without candidates are supported statistically.

5.6.5 Metallicity gradients

In local galaxies the metallicities of H II regions are shown to decrease with increasing radial distance in the disc (Zaritsky et al. 1994). A comparison between absorption metallicity for 3 DLAs at $z < 0.6$ with abundances derived from strong emission line diagnostics based on the DLA galaxy spectra revealed that gradients are likely present (Chen et al. 2005, find a gradient of –0.041±0.012 dex per kpc). In their study they point our intrinsic uncertainties for measuring an exact gradient due to uncertainties in the correction for dust depletion and also the inclination of the galaxy plays an important role due to projection effects.

It is highly speculative to apply the average gradient present at lower redshifts to the candidates at $z > 2$, and furthermore any gradient that is present is likely to vary from one galaxy to the other. Also we do not have any measure to determine to real radial distance because the inclination is unknown. With this in mind, Fig. 5.12 shows an estimate of the metallicity at $b = 0$ if the metallicity gradient in high redshift DLA galaxies is similar to that at lower redshift. The average metallicity and average impact parameters are calculated where all candidates are weighted equally. The result is shown by the dashed line in Fig. 5.12, and we find that at the average redshifts for the

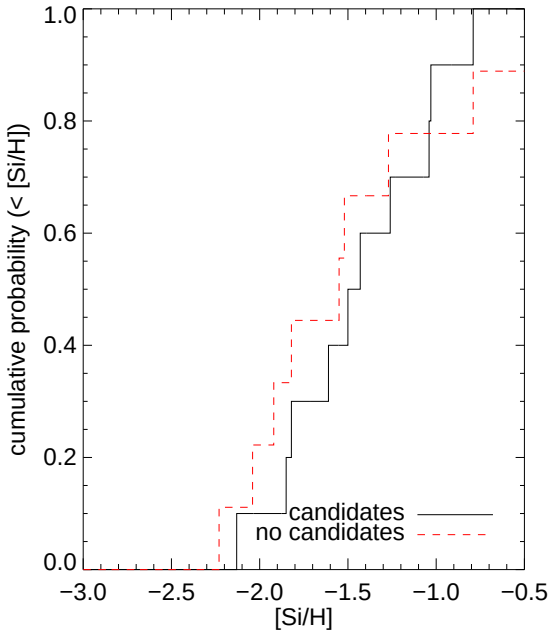

Fig. 5.11. Cumulative distribution of Si metallicities of the DLA candidates and those where no candidates were found. The probability that the two distributions are similar is 99% estimated from a Kolmogorov-Smirnov test, while a similar test of the [Fe/H] distributions gives a probability of 67%.

candidates ($z \approx 3.1$), the typical metallicity would be –0.6 dex at zero impact parameter.

If a metallicity gradient is present, we would expect to see a tendency for a higher metallicity for the candidates with smaller impact parameters. This is indicated by the dotted line in Fig. 5.12, which shows a fit to the candidates. The gradient of this line is –0.010±0.005 dex kpc^{-1}, i.e. much smaller than for lower redshift galaxies, and consistent with zero at the 2σ level.

Current numerical simulation that reproduce the metallicities of DLAs at all redshifts do not have the resolution to allow for a comparison with observations (Cen et al. 2003). Observations of nebular emission lines from seven galaxies at $2.0 < z < 2.5$ indicated an average solar metallicity (Shapley et al. 2004) which could be used to argue that DLA metallicities can actually be biased to lower values at the outskirt of galaxies.

5.7 Conclusions

We have presented an integral field spectroscopic survey of 9 high redshift QSOs, which have a total number of 14 DLA systems and 8 sub-DLA systems. The observations were obtained with PMAS on the 3.5m telescope at Calar Alto. The wavelength coverage of our spectra includes the redshifted Lyα line of all but one of the sub-DLAs. Data cubes were visually searched for Lyα emission line objects at previously known redshifts. One of the DLA galaxies Lyα emission (Q0151+048A) was previously known, as well as the sub-DLA systems towards Q2233+131. These two objects were not treated as one of the candidate emission lines detected in the survey.

Eight good candidates for Lyα emission lines from DLA and sub-DLA galaxies were found implying a detection frequency of 40%. Several tests were done to investigate the significance of the candidate detections. In just one case (Q1802+5616) an emission line object could be identified directly by visual inspection of the stacked spectra. The other candidates were only identified after

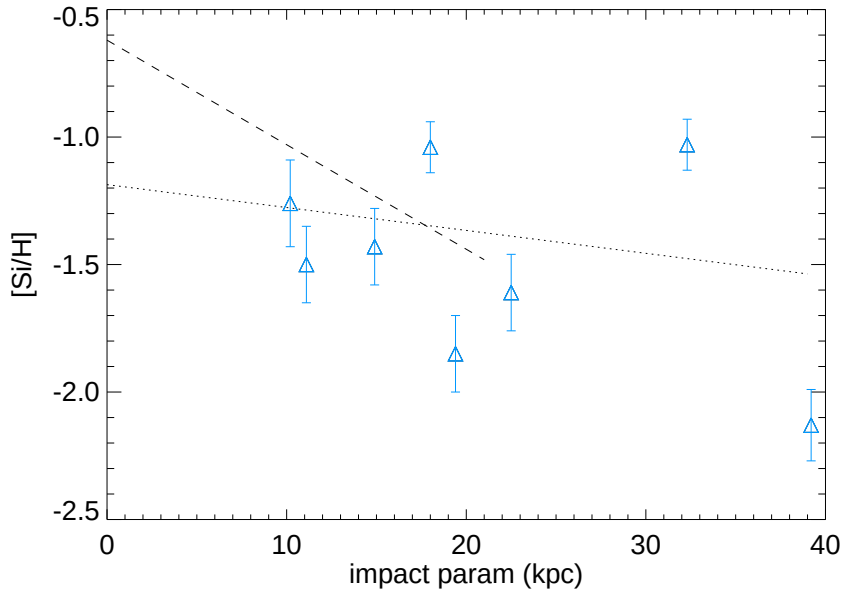

Fig. 5.12. DLA metallicities as a function of the candidate impact parameters, where symbols shapes have similar meanings as in the previous figures. The dashed line shows the average gradient (-0.041 dex kpc^{-1}) for $z < 1$ DLA galaxies, and the dotted line a fit to the candidates. This line has a gradient of -0.010 ± 0.005 dex kpc^{-1}.

combination of several spaxels using the Euro3D visualisation tool. Candidates were detected at the 3–4σ levels in constructed narrow-band images as well as in the co-added one-dimensional spectra. Until independent observations have either confirmed or rejected the candidates, a detailed analysis of the Lyα emission lines properties from the DLA galaxies can be biased. With this in mind, we compare the properties inferred from the IFS data with those for previously spectroscopically confirmed Lyα emission lines from DLA galaxies found in the literature.

We find that the total line fluxes for the candidates are comparable to the confirmed objects. Analysing the velocity offset between the DLA line and the Lyα emission lines gave no indications for systematically lower luminosities associated with larger offsets.

Metallicity distributions of the candidates in comparison to the total distribution showed that the candidates have no tendency of being detected in association with neither high metallicity DLAs ([Fe/H]>–1.5) nor low metallicity ones. The same conclusion holds for a similar comparison of metallicities of the DLAs traced by [Si/H].

The average offset for the candidates (20 kpc) is larger than for known high redshift DLA galaxies and also larger than expected from numerical simulations. We find no significant difference for the typical size of DLA galaxies compared to that for DLA galaxies at $z < 1$, which have sizes up to $R^* \approx 30$ kpc (Chen et al. 2005). Adopting the scaling relations for low redshift DLA galaxies indicates that high redshift DLA galaxies are less luminous than present day L^* galaxies. Combining the luminosity-size relation for the DLA galaxy candidates as $z < 1$ found by Chen & Lanzetta (2003) with the anticorrelation between impact parameters and DLA column density found here, indicates an anticorrelation between the DLA galaxy luminosities and the DLA column densities. Such a trend has been observed for a few DLA galaxies at $z < 1$ (Rao et al. 2003). The large impact parameters found for the candidates indicate that neutral clouds in a DLA galaxy extends significantly beyond what is expected from the visual sizes of dwarf systems.

The distribution of impact parameters for the candidate emission lines compared with the

column density of the DLA clouds indicated that the average parent galaxy can be described by an exponential disc with a characteristic scale length of 5 kpc (after rejecting two outliers). Such a scale length is similar to the H I disc scale lengths found for local spiral galaxies. Hence our results support the hypothesis that DLAs belong to large discs even at high redshifts as originally suggested by Wolfe et al. (1986). However, we can not rule out the other scenario where the Lyα emission comes from one of several smaller clumps expected to be present within $\sim$10 kpc in a hierarchical formation scenario.

It is necessary to obtain conventional slit spectra at the suggested position angle to get an independent, higher signal-to-noise ratio spectrum to confirm the existence of the emission lines. In order to confirm independently whether the emission lines are indeed Lyα at the expected wavelengths one needs to detect emission lines from other elements. These could be optical emission lines shifted to the near-IR as done for a few systems to date (Weatherley et al. 2005). Optical emission lines have the additional advantage of being less affected by dust absorption and therefore are better to estimate the star-formation rates.

The present sample of QSOs does not represent an unbiased sample such that one can specifically investigate the properties of DLA galaxies at high redshifts. Such a systematic investigation of DLA systems would benefit from the Sloan Survey Data Release 3 in which more than 500 DLAs have been identified (Prochaska 2005, in prep.). An IFS survey on an 8m class telescope should be able to go deeper than the limits presented in this paper, and therefore no need for follow-up observations should be necessary.

Acknowledgments. L. Christensen acknowledges support by the German Verbundforschung associated with the ULTROS project, grant no. 05AE2BAA/4. S.F. Sánchez acknowledges the support from the Euro3D Research Training Network, grant no. HPRN-CT2002-00305. We thank Steve Curran for maintaining the DLA list `http://www.phys.unsw.edu.au/~sjc/dla`

References

Bechtold, J. 1994, ApJS, 91, 1
Bunker, A. J., Smith, J., Spinrad, H., Stern, D., & Warren, S. 2003, Ap&SS, 284, 357
Cen, R., Ostriker, J. P., Prochaska, J. X., & Wolfe, A. M. 2003, ApJ, 598, 741
Chaffee, F. H., Stepanian, J. A., Chavushian, V. A., Foltz, C. B., & Green, R. F. 1994, Bulletin of the American Astronomical Society, 26, 1338
Charlot, S. & Fall, S. M. 1993, ApJ, 415, 580
Chen, H., Lanzetta, K. M., Webb, J. K., & Barcons, X. 1998, ApJ, 498, 77
—. 2001, ApJ, 559, 654
Chen, H.-W., Kennicutt, R. C., & Rauch, M. 2005, ApJ, 620, 703
Chen, H.-W. & Lanzetta, K. M. 2003, ApJ, 597, 706
Christensen, L., Sánchez, S. F., Jahnke, K., et al. 2004, A&A, 417, 487
Christensen, L., Sánchez, S. F., Jahnke, K., Roth, M. M., & Wisotzki, L. 2005, in Probing Galaxies through Quasar Absorption Lines, ed. P. R. Williams, C. Shu, & B. Ménard, IAU Colloquium 199
Churchill, C. W., Kacprzak, G. G., & Steidel, C. C. 2005, In Probing Galaxies through Quasar Absorption Lines (astro-ph/0504392)
Churchill, C. W., Mellon, R. R., Charlton, J. C., et al. 2000, ApJ, 543, 577
Colbert, J. W. & Malkan, M. A. 2002, ApJ, 566, 51
Dessauges-Zavadsky, M., Péroux, C., Kim, T.-S., D'Odorico, S., & McMahon, R. G. 2003, MNRAS, 345, 447
Djorgovski, S. G., Pahre, M. A., Bechtold, J., & Elston, R. 1996, Nature, 382, 234

Erb, D. K., Shapley, A. E., Steidel, C. C., et al. 2003, ApJ, 591, 101
Filippenko, A. V. 1982, PASP, 94, 715
Fitzpatrick, E. L. 1999, PASP, 111, 63
Fynbo, J. U., Burud, I., & Møller, P. 2000, A&A, 358, 88
Fynbo, J. U., Møller, P., & Warren, S. J. 1999, MNRAS, 305, 849
Gardner, J. P., Katz, N., Hernquist, L., & Weinberg, D. H. 2001, ApJ, 559, 131
Haehnelt, M. G., Steinmetz, M., & Rauch, M. 1998, ApJ, 495, 647
Hopp, U. & Fernandez, M. 2002, Calar Alto Newsletter No.4, http://www.caha.es/newsletter/news02a/hopp/paper.pdf
Hou, J. L., Shu, C. G., Shen, S. Y., et al. 2005, ApJ, 624, 561
Hu, E. M., Cowie, L. L., Capak, P., et al. 2004, AJ, 127, 563
Hu, E. M., Cowie, L. L., & McMahon, R. G. 1998, ApJL, 502, L99
Keel, W. C. 2005, AJ, 129, 1863
Kudritzki, R.-P., Méndez, R. H., Feldmeier, J. J., et al. 2000, ApJ, 536, 19
Lacy, M., Becker, R. H., Storrie-Lombardi, L. J., et al. 2003, AJ, 126, 2230
Lanzetta, K. M., Bowen, D. V., Tytler, D., & Webb, J. K. 1995, ApJ, 442, 538
Lanzetta, K. M., McMahon, R. G., Wolfe, A. M., et al. 1991, ApJS, 77, 1
Le Brun, V., Bergeron, J., Boisse, P., & Deharveng, J. M. 1997, A&A, 321, 733
Ledoux, C., Petitjean, P., Bergeron, J., Wampler, E. J., & Srianand, R. 1998a, A&A, 337, 51
Ledoux, C., Theodore, B., Petitjean, P., et al. 1998b, A&A, 339, L77
Leibundgut, B. & Robertson, J. G. 1999, MNRAS, 303, 711
Lowenthal, J. D., Hogan, C. J., Green, R. F., et al. 1995, ApJ, 451, 484
Lu, L., Sargent, W. L. W., & Barlow, T. A. 1997, ApJ, 484, 131
Lu, L., Sargent, W. L. W., Barlow, T. A., Churchill, C. W., & Vogt, S. S. 1996, ApJS, 107, 475
Lu, L., Wolfe, A. M., Turnshek, D. A., & Lanzetta, K. M. 1993, ApJS, 84, 1
Matthews, L. D., van Driel, W., & Monnier-Ragaigne, D. 2001, A&A, 365, 1
Møller, P. 1999, in Astrophysics with the NOT, 80
Møller, P., Fynbo, J. P., & Fall, S. M. 2004, A&A, 422, L33
Møller, P. & Warren, S. J. 1993, A&A, 270, 43
Møller, P., Warren, S. J., Fall, S. M., Fynbo, J. U., & Jakobsen, P. 2002, ApJ, 574, 51
Møller, P., Warren, S. J., & Fynbo, J. U. 1998, A&A, 330, 19
Okoshi, K. & Nagashima, M. 2005, ApJ, 623, 99
Outram, P. J., Chaffee, F. H., & Carswell, R. F. 1999, MNRAS, 310, 289
Péroux, C., Dessauges-Zavadsky, M., D'Odorico, S., Kim, T., & McMahon, R. G. 2003, MNRAS, 345, 480
Péroux, C., Storrie-Lombardi, L. J., McMahon, R. G., Irwin, M., & Hook, I. M. 2001, AJ, 121, 1799
Petitjean, P., Pecontal, E., Valls-Gabaud, D., & Charlot, S. 1996, Nature, 380, 411
Pettini, M., Shapley, A. E., Steidel, C. C., et al. 2001, ApJ, 554, 981
Poli, F., Giallongo, E., Fontana, A., et al. 2003, ApJL, 593, L1
Prochaska, J. X., Gawiser, E., Wolfe, A. M., Castro, S., & Djorgovski, S. G. 2003, ApJL, 595, L9
Prochaska, J. X., Henry, R. B. C., O'Meara, J. M., et al. 2002a, PASP, 114, 933
Prochaska, J. X. & Herbert-Fort, S. 2004, PASP, 116, 622
Prochaska, J. X., Howk, J. C., O'Meara, J. M., et al. 2002b, ApJ, 571, 693
Prochaska, J. X. & Wolfe, A. M. 1997, ApJ, 487, 73
Prochaska, J. X., Wolfe, A. M., Tytler, D., et al. 2001, ApJS, 137, 21
Pych, W. 2004, PASP, 116, 148
Rao, S. M., Nestor, D. B., Turnshek, D. A., et al. 2003, ApJ, 595, 94
Roth, M. M., Becker, T., Bauer, S.-M., et al. 2005, PASP, accepted

Sánchez, S. F. 2004, AN, 325, 167
Sánchez, S. F., Garcia-Lorenzo, B., Mediavilla, E., González-Serrano, J. I., & Christensen, L. 2004, ApJ, 615, 156
Schlegel, D. J., Finkbeiner, D. P., & Davis, M. 1998, ApJ, 500, 525
Schneider, D. P., Schmidt, M., & Gunn, J. E. 1991, AJ, 101, 2004
Shapley, A. E., Erb, D. K., Pettini, M., Steidel, C. C., & Adelberger, K. L. 2004, ApJ, 612, 108
Shapley, A. E., Steidel, C. C., Pettini, M., & Adelberger, K. L. 2003, ApJ, 588, 65
Smith, H. E., Cohen, R. D., & Bradley, S. E. 1986, ApJ, 310, 583
Steidel, C. C., Pettini, M., & Hamilton, D. 1995, AJ, 110, 2519
Stepanian, J. A., Chavushian, V. H., Chaffee, F. H., Foltz, C. B., & Green, R. F. 1996, A&A, 309, 702
Storrie-Lombardi, L. J. & Wolfe, A. M. 2000, ApJ, 543, 552
Turnshek, D. A., Wolfe, A. M., Lanzetta, K. M., et al. 1989, ApJ, 344, 567
Véron-Cetty, M.-P. & Véron, P. 2001, A&A, 374, 92
van Dokkum, P. G. 2001, PASP, 113, 1420
Warren, S. J., Møller, P., Fall, S. M., & Jakobsen, P. 2001, MNRAS, 326, 759
Weatherley, S. J., Warren, S. J., Møller, P., et al. 2005, MNRAS, 358, 985
Wisotzki, L., Becker, T., Christensen, L., et al. 2003, A&A, 408, 455
Wolfe, A. M., Lanzetta, K. M., Foltz, C. B., & Chaffee, F. H. 1995, ApJ, 454, 698
Wolfe, A. M., Turnshek, D. A., Smith, H. E., & Cohen, R. D. 1986, ApJS, 61, 249
Zaritsky, D., Kennicutt, R. C., & Huchra, J. P. 1994, ApJ, 420, 87

CHAPTER 6

DLA galaxy sizes, masses, and star formation rates

L. CHRISTENSEN[1]

[1] Astrophysikalisches Institut Potsdam, An der Sternwarte 16, 14482 Potsdam, Germany

Abstract

We present an analysis of the sizes and star formation rates (SFRs) of the galaxies that are responsible for damped Lyα (DLA) lines in quasar spectra. The sizes of all DLA galaxies (and candidates) traced by their $N(\mathrm{H\,I})$ extent show that DLA galaxies are consistent with being similar to local disc galaxies at both high and low redshifts. However, there is a significant scatter in the relation between the column density and the projected distances between the quasar and the absorbing galaxies, which is likely due to various absorbing galaxy types. We show that the SFRs inferred from Lyα emission lines are similar to the UV based SFRs expected for L^* galaxies at high redshifts. We furthermore show that SFRs can be reproduced assuming the validity of an average Schmidt-Kennicutt law under the assumption that DLA galaxies are exponential discs with a scale length of $\sim$5 kpc. Comoving SFRs in DLA galaxies are estimated based on the reported column density distribution. This shows that DLA host galaxies contribute significantly to, but do not dominate the comoving SFR based on luminosity selected galaxies at redshifts larger than 0.2. Although DLA galaxies at $z > 2$ are indicated to be similar in size to local large disc galaxies and hence have similar masses in H I, their total masses including stars, may well be smaller than for local disc galaxies. Likewise DLA galaxies may be sub-luminous relative to L^* galaxies at similar redshifts.

6.1 Introduction

This chapter is based on extrapolations and analyses from previous investigations. Having studied the emission lines from DLA galaxies in Chapter 5 and 3 we here proceed with an analysis of the DLA galaxies assuming that the overall properties derived for the candidates are representative for all DLA galaxies. Specifically, this chapter continues the study of properties from Lyα emission lines and star formation rates from DLA galaxies. Since Lyα photons are resonantly scattered and quenched where dust is present (Charlot & Fall 1993), deriving SFRs from Lyα emission lines gives a strict lower limit. Still, observations of Lyα emitters at $z > 2$ do try to investigate these issues. Dust is produced either by asymptotic giant branch (AGB) stars or by supernovae. At high redshifts,

low mass stars have not yet had the time to evolve to the AGB stage, so most dust production must come from Type II SNe. The inferred SFRs at $z \approx 6$ are known to be affected by absorption since the Lyα emission line profiles show distinct blue cutoffs (Hu et al. 2004). The relatively large SFRs found for high redshift Lyman break galaxies (e.g. Steidel et al. 2004) imply that dust should be present at the location of the star-forming regions. Thus, the escape of Lyα photons from high redshift Lyα emitters is governed by the same uncertainties as in DLA systems.

This chapter ignores any dust correction factor for the Lyα emission detected from DLA galaxies.

6.2 DLA galaxy sizes

We first address the question of the similarities or differences between the neutral gas in DLA galaxies and local galaxies. The latter are measured by radio observations while DLA galaxies sizes are estimated by the measured impact parameters. For this analysis we include all information about DLA galaxies at both high and low redshifts. Fig. 6.1 shows the impact parameter for spectroscopically confirmed DLA galaxies as a function of the column density $N(\mathrm{H\,I})$ measured in the neutral cloud. Data for the $z \gtrsim 2$ confirmed DLA galaxies are taken from Møller et al. (2002) and Møller et al. (2004) (*red squares*), and objects at $z < 1$ from the compilation in Chen & Lanzetta (2003). Low redshift galaxies are indicated by different symbols according to their morphological classification where the *orange spirals* are spiral type galaxies and the *green stars* indicate compact or irregular galaxies. The high redshift candidate DLA galaxies found in Chapter 5 are indicated by the *blue triangles*.

In Fig. 6.1 we also indicate typical H I profiles for nearby spiral galaxies, where the dotted line is that of an L^* Sbc galaxy, the dot-dashed line is a Scd galaxy type (Cayatte et al. 1994), and the dashed line is a low-surface brightness galaxy. It is immediately seen that the DLA galaxies show a large scatter, and do not agree exactly with one specific spiral galaxy profile. Some of the confirmed objects have higher column densities than observed for local galaxies, which is not surprising since DLA galaxies at low redshifts are shown to be of various morphological types (Le Brun et al. 1997; Rao et al. 2003; Chen & Lanzetta 2003). Furthermore, a large scatter is expected because the radio observations are not sensitive to small scale clumps in the galaxy discs.

An interesting observation is that the low redshift irregular galaxies have a tendency of having higher impact parameters for a given column density, while the galaxies with disc morphology fit well the H I profiles for different spiral classes. The impact parameters analysed here are the projected distances, whereas inclination effects will increase the real distances. However, this effect must be present in both spiral and irregular galaxy samples. It is likely that DLA galaxies have fainter companions closer to the QSO sight line, and which are too faint for detection. Irregular galaxies may be disturbed by companions, but companions are also expected nearby large disc galaxies.

6.3 Star formation rates in DLA galaxies

This section analyses the SFRs from DLA galaxies in relation to other high redshift galaxies and investigates the comoving SFR as a function of redshift.

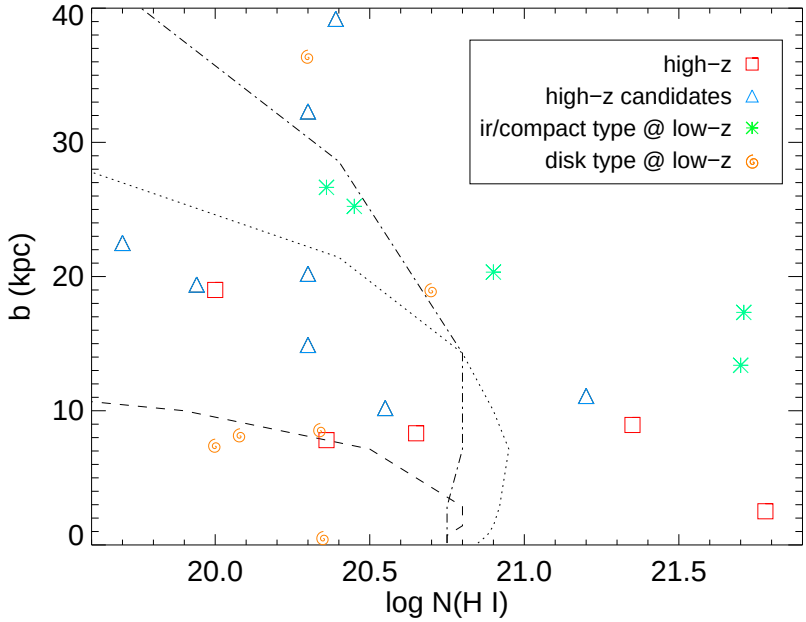

Fig. 6.1. Impact parameters as a function of the DLA $N(\mathrm{H\,I})$ measured in cm^{-2}. All spectroscopically confirmed objects to date (2005 Jun) are included. $z \gtrsim 2$ DLA galaxies are shown by *red squares*, $z < 1$ DLA galaxies with irregular or compact morphology as *green stars*, low redshift DLA galaxies with spiral morphology as *orange spirals* and the high redshift candidates from Chapter 5 as *blue triangles*. The dotted, dash-dotted, and dashed lines correspond to average H I profiles observed for Sbc, Scd, and an ultra-thin low-surface brightness galaxy (Uson & Matthews 2003), respectively.

6.3.1 Star formation rates in galaxy discs

Observations of local galaxies have shown that the SFR is linked with the surface density of their discs, Σ_{gas}, and is described by the Schmidt-Kennicutt law (Schmidt 1959; Kennicutt 1998b).

$$\Sigma_{\mathrm{SFR}} = (2.5 \pm 0.7) \times 10^{-4} \left(\frac{\Sigma_{\mathrm{gas}}}{1 \mathrm{M}_{\odot} \mathrm{pc}^{-2}} \right)^{1.4 \pm 0.15} \quad \mathrm{M}_{\odot} \mathrm{yr}^{-1} \mathrm{kpc}^{-2} \tag{6.1}$$

This equation provides at most a statistical description of the global SFR averaged over large samples of galaxies in the local Universe, and individual systems show deviations by up to a factor of 7.

For clouds with a known column density N_{20} (the column density in units of 10^{20} cm^{-2}) of neutral gas we can rewrite Eq. (6.1)

$$\Sigma_{\mathrm{SFR}} = (1.8 \pm 0.4) \times 10^{-4} N_{20}^{1.4 \pm 0.15} \quad \mathrm{M}_{\odot} \mathrm{yr}^{-1} \mathrm{kpc}^{-2} \tag{6.2}$$

which gives the rather modest SFR = $(4.8 \pm 1.1) \times 10^{-4}$ $\mathrm{M}_{\odot} \mathrm{yr}^{-1} \mathrm{kpc}^{-2}$ for a systems that just qualifies as a classical DLA. The question of the SFR in a DLA galaxy is intrinsically coupled to the size of a DLA galaxy. In the few systems where the optical emission from the galaxy has been detected, the SFR can be estimated, but a direct test of Eq. (6.2) requires that the gas distribution is known as well.

No correlation between the SFR from individual DLAs and their column densities has been found from >30 systems for which SFRs were derived based on the C II* λ1335 absorption lines

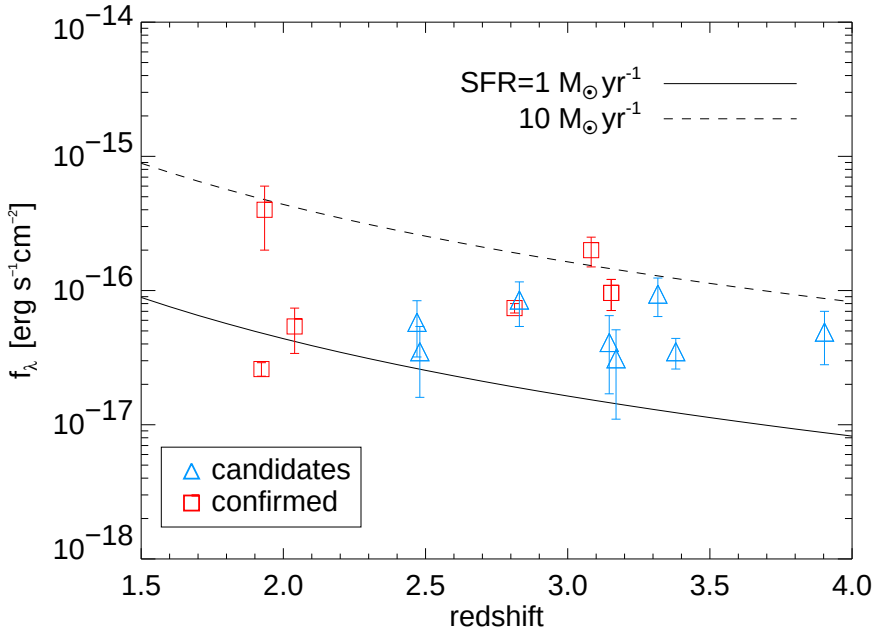

Fig. 6.2. Line fluxes of Lyα emission candidates from Chapter 5 as function of redshift (triangles), and the already confirmed objects from Møller et al. (2002) are shown by squares. The solid and dashed lines correspond to the line flux expected for an object with a star formation rate of 1 and 10 $M_\odot$ yr^{-1}, respectively, in the case of no extinction.

(Wolfe et al. 2003), but an average SFR in the sample does seem to obey the Schmidt-Kennicutt law. This conclusion is supported by the similarities between the luminosity distributions of high redshift galaxies and the DLA column density distribution (Lanzetta et al. 2002).

6.3.2 Star formation rates from line fluxes

Having found the candidate Lyα emission lines in Chapter 5 we can try to estimate the star formation rates (SFR). However, a direct conversion between the observed flux and the SFR is uncertain. It has been estimated that for a dust-to-gas ratio of 10% Galactic, Lyα photons are efficiently destroyed (Charlot & Fall 1993), but Gould & Weinberg (1996) estimate that dust absorption plays a minor role even at high column densities. When the Lyα emitting material is offset in velocity with respect to the interstellar medium Lyα photons can escape (Kunth et al. 1998). Significant quenching of Lyα photons is expected where dust is present because of the very large escape path due to resonant scattering. Dust is generally accepted to be present in DLAs because of characteristic abundance ratios calculated from metal absorption lines (Pettini et al. 1999), but the velocity structure of the emitting material is unknown. Nevertheless, with this in mind we return to these objects for a more speculative investigation of the relevance to the SFRs in the parent galaxies.

The solid and dashed lines in Fig. 6.2 correspond to the line flux expected for an object with a SFR of 1 and 10 $M_\odot$ yr^{-1}, respectively. To calculate this, a conversion between an Hα luminosity and the SFR was assumed (Kennicutt 1998a), along with a flux ratio Lyα/H$\alpha \approx 10$, i.e. $\mathrm{SFR} = L(\mathrm{Ly}\alpha)\ 7.9 \times 10^{-43}$ [erg s^{-1}] giving the SFR in units of $M_\odot$ yr^{-1}. This figure shows that the individual unextincted SFRs for the DLA galaxies are in the range between a few and $\sim$10 $M_\odot$ yr^{-1}.

We analyse the distribution of the inferred SFRs as a function of column density measured for the DLA clouds themselves to study if there could be a relation between these two parameters.

Fig. 6.3 shows the individual SFRs derived for the candidates as a function of the DLA column densities. Here candidate line fluxes listed in Table 5.3 are corrected for Galactic extinction (Schlegel et al. 1998), and values for confirmed objects from the literature are included as well (Møller et al. 2004; Weatherley et al. 2005). The solid curve shows the average SFR derived from the Schmidt-Kennicutt law assuming a DLA galaxy disc radius of 10 kpc and a constant height with a column density given on the x-axis, i.e. similar to a cylindrical disc. This is clearly a very rough simplification, but serves as a first approximation. The assumed DLA galaxy radii of 10 kpc are similar to the sizes assumed in the analysis by Wolfe et al. (2003). The derived SFRs for galaxies associated with DLA systems rely on a uniform Schmidt-Kennicutt relation even at high redshifts which is supported by numerical simulations (Nagamine et al. 2004).

The scatter of the observed points is significant, but they seem to lie within 1σ errors of the Schmidt-Kennicutt relation with a notable exception of the SFR ≈ 13 $M_\odot$ yr^{-1} point belonging to the DLA galaxy towards Q2059–360 which is a $z_{\rm abs} \approx z_{\rm em}$ system (Leibundgut & Robertson 1999). It is possible that in this systems the Lyα emission is affected by the presence of the QSO ionising flux. However, also two other confirmed DLA galaxies are $z_{\rm abs} \approx z_{\rm em}$ objects and they do not show an excess flux.

In Fig. 6.3 we also indicate the column density weighted mean SFR value for the candidates

$$\langle \mathrm{SFR} \rangle = \frac{\sum N_i \mathrm{SFR}_i}{\sum N_i}, \tag{6.3}$$

where the sum is taken over all i candidates. This gives an average SFR $= 4.1$ $M_\odot$yr^{-1}. Apparently, this average is in agreement with the predicted value, but the placement of the curve depends sensitively on the assumed DLA galaxy radius.

Instead of the assumption of a very simple disc shape, we can use the information on the average DLA galaxy neutral disc shape as described in Chapters 3.6 and 5.6.3. A fit of an exponential disc, $N = N_0 \exp(-r/h)$, to the DLA column density as a function of the measured impact parameter of the DLA galaxy candidate yielded a scale length of $h \approx 5$ kpc and log $N_0 = 21.7$ cm^{-2}. To calculate the total SFR in such a disc assuming that Eq. (6.2) holds on average, the equation

$$\begin{aligned} \mathrm{SFR} &= \int dr 2\pi r \Sigma(r) \\ &= \int dr 2\pi r (1.8 \pm 0.4) \times 10^{-4} \left(\frac{N_0}{10^{20}} \exp(-r/h) \right)^{1.4 \pm 0.15} \end{aligned} \tag{6.4}$$

gives SFR = 3.6 $M_\odot$ yr^{-1} for an average DLA galaxy. This result agrees well with both the measured average SFR, and the predicted SFR in the case of a simple cylindrical disc. Including the uncertainties for the scale length and central column density, the average SFR calculated lies in the range between 0.02 and 300 $M_\odot$ yr^{-1} within 1σ uncertainty, so the average SFR is not well constrained.

As explained in Sect. 6.2 DLA galaxies are not represented by a single morphological type. Hence these derivations must be seen as approximations which are valid only for those objects detected in emission in the integral field surveys.

6.3.3 Comoving star formation rates in DLAs

In this section we estimate the global star formation in DLAs and their contribution to the comoving SFR, i.e. their contribution in the 'Madau plot' (Madau et al. 1996). The idea is that since DLAs dominate the neutral gas mass in the Universe (e.g. Storrie-Lombardi & Wolfe 2000; Rao

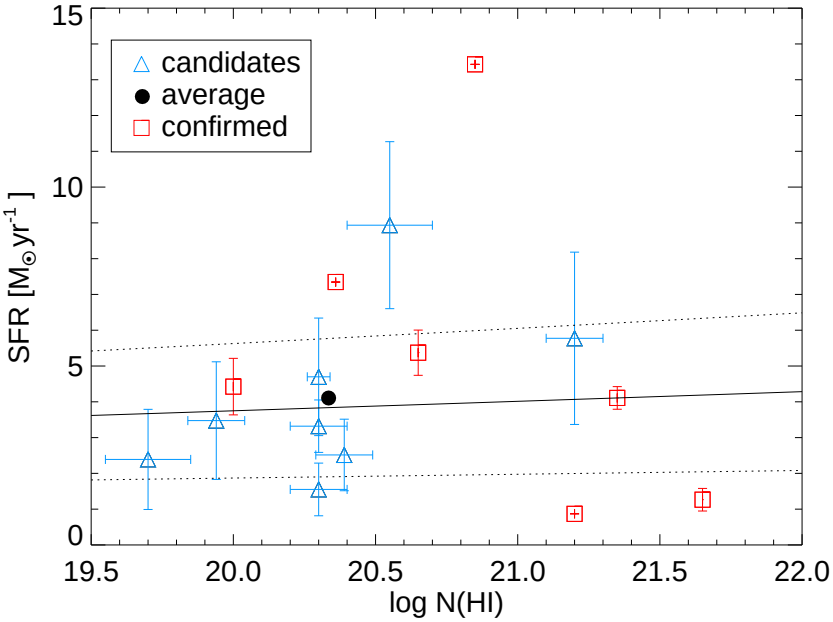

Fig. 6.3. SFRs derived from both confirmed and candidate Lyα emission line counterparts to DLAs as function of the DLA $N(\mathrm{H\,I})$ measured in cm^{-2}. Before converting to a SFR the candidate fluxes are corrected for Galactic extinction. The weighted mean value for the candidates is indicated by the black circle. The expected SFR for a galaxy with a radius of 10 kpc and assuming a Schmidt-Kennicutt law is shown by the solid line and the 1σ uncertainties are shown by the dotted lines.

& Turnshek 2000) and are believed to provide the fuel for star formation, they could to some extent trace star formation.

To determine the total contribution to the SFR in DLAs as a function of redshift $\rho(z)$, we need to know the number of DLA galaxies per redshift interval which is described by the column density distribution $f(N,z)$. Multiplying this with the SFR from each neutral cloud one can estimate the comoving SFR. Typically the observed distribution of DLAs (dN/dX) is related to the absorption distance given by

$$\frac{dX}{dz} = \frac{(1+z)^2}{\sqrt{(1+z)^2(1+\Omega_m z) - z(z+2)\Omega_\Lambda}} \tag{6.5}$$

This can be related to the SFR as a function of redshift once we know the number of DLAs per unit redshift dN/dz

$$\rho(z) = \Sigma_{\mathrm{SFR}} \frac{dN}{dX}\frac{H_0}{c} = \Sigma_{\mathrm{SFR}} \frac{H_0}{c}\left(\frac{dX}{dz}\right)^{-1}\frac{dN}{dz} \tag{6.6}$$

Often the number density of DLAs is described by a functional form $f(N)$. Storrie-Lombardi & Wolfe (2000) find $dN/dz = N_0(1+z)^\gamma$ with best fit values $N_0 = 0.055$ and $\gamma = 1.11$. Both Storrie-Lombardi & Wolfe (2000) and Péroux et al. (2003) find that the column density distribution can be described by a gamma distribution over the redshift interval $0 < z < 4$. This is given by

$$f(N,z) = \frac{f^*}{N^*}\left(\frac{N}{N^*}\right)^{-\beta}\exp(-N/N^*) \tag{6.7}$$

where the characteristic values, f^* and N^* are evaluated at different redshift intervals.

To calculate the comoving SFR in DLAs we substitute Eq. (6.2) and Eq. (6.7) into Eq. (6.6) and integrate over N

$$\rho(z) = 1.8 \times 10^{-4} \frac{H_0}{c} \left(\frac{dX}{dz} \right)^{-1} \int N_{20}^{1.4} f(N, z) dN \tag{6.8}$$

to give the SFR density in units of $M_{\odot}yr^{-1}Mpc^{-3}$.

In Fig. 6.4, ρ is derived from parameters estimated at 4 different redshift intervals shown by the *red triangles* (Péroux et al. 2003), while the *blue squares* show the two redshift intervals in Storrie-Lombardi & Wolfe (2000). Data points from these surveys are compared to the comoving star formation density derived from optical surveys as indicated by the *black stars* (Lilly et al. 1996; Steidel et al. 1999). High redshift data points are corrected for dust extinction. Comoving SFRs in DLAs derived directly from the C II* absorption line technique are indicated by the *green circles* (Wolfe et al. 2003; Wolfe 2005). Published values have been converted to the adopted cosmology with $\Omega_{\Lambda} = 0.7$ and H_0 = 70 km s^{-1} Mpc^{-1}.

At the highest redshift interval the two data points from the DLA surveys in Péroux et al. (2003) and Storrie-Lombardi & Wolfe (2000) have different values, but are nevertheless consistent with each other within 2σ. The large difference between the predictions is caused by the relatively small value of $N^* \approx 3 \times 10^{20}$ cm^{-2}, which is a factor of $\sim$5 smaller than at lower redshifts (Péroux et al. 2003). Thus, the small comoving SFR density is due to the apparent lack of very high column density systems at $z > 3.5$. A larger sample of DLAs from the SDSS does on the other hand show that half of the sample at $z > 3.5$ have log $N(\mathrm{H\,I})$> 21.5 cm^{-2} (Prochaska & Herbert-Fort 2004). Conversely, the large value at the highest redshift is caused by a large normalisation value of f^* (Storrie-Lombardi & Wolfe 2000).

The comoving SFR traced by DLAs is smaller by a factor of $\sim$10 than for the Lyman break galaxies (LBGs) apart from the highest redshift bin, but considering error bars, the comoving SFRs from the LBGs and DLAs are consistent within 2σ around z = 2–3. A slightly different method to derive ρ is presented in Hopkins et al. (2005), who use instead the exact measured DLA numbers instead of a functional form of the DLA population to derive values that are consistent with those presented here. The main difference is their extension of the study to low redshifts as well. These findings are interpreted such that DLAs do not contribute significantly to the comoving SFR, which could be dominated by sub-mm galaxies and LBGs.

6.3.4 Comparisons between Lyman break galaxies and DLA galaxy SFRs

It has been stated that DLAs and Lyman break galaxies (LBGs) are two separate populations based on metallicity arguments (Pettini et al. 2001), while their morphologies and colors indicate that DLA galaxies are just a faint end extension of the LBG population (Møller et al. 2002).

In Chapter 5 we demonstrated that Lyα emission could be present for a large fraction of DLA galaxies. In comparison, only $\sim 25\%$ of LBGs show bright Lyα emission lines with large equivalent widths (Shapley et al. 2003). Metallicities for the two samples are different, where LBG abundances at $z = 2.5$ derived from strong emission lines are approximately solar (Shapley et al. 2004), whereas high redshift DLAs have metallicities of 1–10% solar (Pettini et al. 2002). Furthermore, the unobscured rest-frame UV continuum emission from LBGs suggest SFRs ranging between 5 and 66 $M_{\odot}yr^{-1}$ (Pettini et al. 2001; Steidel et al. 2004), which is about an order of magnitude larger than the SFR derived from the average Lyα flux from LBGs (Shapley et al. 2003). Two DLA galaxies, in comparison, have SFRs of 10 and 28 $M_{\odot}yr^{-1}$ derived from their [O III] emission lines (Weatherley et al. 2005), whereas SFRs derived from their UV continuum emission are $\sim$5 $M_{\odot}yr^{-1}$. These SFRs appear to be similar to the SFRs derived from Lyα lines in Chapter 5. Hence based on the SFR estimates, dust is likely more abundant in LBGs where significant quenching of Lyα photons

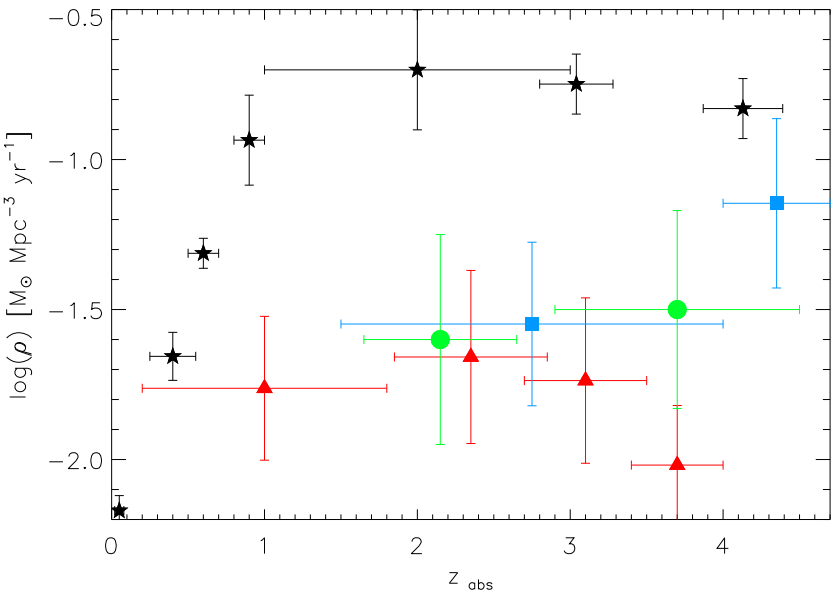

Fig. 6.4. Comoving SFR density traced by DLAs assuming validity of the Schmidt-Kennicutt law for high redshift galaxies. Studies using a gamma distribution to fit the DLA column density distribution are indicated by the *blue squares* and the *red triangles* (Péroux et al. 2003; Storrie-Lombardi & Wolfe 2000). 1σ error bars are derived by propagating errors in the Kennicutt law. Overlayed on this plot are data from flux-limited surveys (*stars*) (Lilly et al. 1996; Steidel et al. 1999), and the comoving SFR in DLAs inferred from absorption line studies (*green circles*) (Wolfe et al. 2003; Wolfe 2005). Values have been converted to the adopted flat cosmology with $H_0 = 70$ km s^{-1} Mpc^{-1} and $\Omega_\Lambda = 0.7$.

occurs. This interpretation is supported by observations of the Lyα equivalent width (EW) observed for the two samples. DLAs have on average EW$\sim$50 Å (Møller et al. 2002) while LBGs have EW = 3–20 Å (Steidel et al. 1996). In pure star-forming galaxies Lyα EW is expected to be 200 Å (Charlot & Fall 1993), suggesting that Lyα photons escape more easily from DLAs than in LBGs, but that dust absorption may still be important for the DLA galaxy Lyα emission lines. Metallicities alone can probably not account for the differences, because in local galaxies the metallicity is not the dominant factor for the Lyα emission, but rather the kinematics may have an important role (Kunth et al. 1998, 2003).

Assuming validity of the Schmidt-Kennicutt law also for LBGs, their large SFRs would indicate large column densities, log $N(\mathrm{H\,I}) > 22$ cm^{-2}, which is larger than the column density measured for any known DLA. This could imply that DLA surveys are biased against the detection of large column density clouds, and that the comoving SFR in DLA galaxies is in reality larger. The reason for this bias may be that the cross section for a very large column density clouds is small and that a large sample of DLAs needs to be observed before a very high column density DLA is found. Rao (2005) estimates than > 1000 DLAs are needed to find just one high $N(\mathrm{H\,I})$ DLA. This interpretation is supported by the observations of very small molecular hydrogen fractions in DLAs (Ledoux et al. 2003), indicating a bias against star forming regions. Thus, the DLAs detected in quasar surveys to date do not trace the strongest star formation regions in the Universe.

6.3.5 Predicting star formation rates

The distribution of SFRs derived for the candidates can be compared to the expected values for very simple models of galaxy evolution. We here assume that the SFR is traced by Lyα emission and the

conversion factor is uncertain by a factor of $\sim$2. Uncertainties of the line flux for the candidates with detection levels $<3\sigma$ in Chapter 5, imply an additional factor of $\sim$2 in the uncertainty. Therefore, when a comparison is made with model predictions we need to take this into account, rejecting only models that predict SFR much different than observed.

In the most simple case we consider a massive (spiral) galaxy similar to the Milky Way, forming all its 10^{11} stars at a constant rate between $z_{\rm form} = 10$ and $z = 0$. This redshift interval corresponds to a cosmic time of 13 Gyr, such that the mean SFR is $\sim$8 $M_{\odot}$yr^{-1}. This model can not be ruled out by the Lyα emission lines from DLA galaxies. However, such a model is clearly too simple, and it is currently believed that star formation to build up massive galaxies takes place in one or several bursts. Instead a model where $z_{\rm form} = 5$ and the star formation switches off at $z = 1$ has a cosmic time interval of 4.6 Gyr which gives an average SFR $\approx$ 22 $M_{\odot}$yr^{-1}, which is larger than the inferred SFRs. However, considering the uncertainties of converting Lyα flux to a SFR, this model can not be ruled out either. The SFR limits derived from an Hα study is in conflict with such a large SFR though (Bunker et al. 1999). Nevertheless, such a simple model can be ruled out by the low metallicities in DLAs. In a closed box model the metallicity would increase substantially in disagreement with observational data which indicate only a mild increase of the metallicity with cosmic time (Prochaska et al. 2003; Kulkarni et al. 2005). This model neglects inflows of primordial gas, which likely affect DLAs because of the apparent constant density of neutral gas in DLAs with redshift (Rao & Turnshek 2000). If the neutral gas in DLA is depleted by the formation of stars new DLAs need to be formed again at lower redshifts.

Perhaps a better way to compare SFRs from DLA galaxies with models is to consider model DLAs from numerical simulations. Hou et al. (2005) consider random sight lines through simulated data cubes and when a sight line intercepts a galaxy which has a column density in the DLA regime, the SFR in the galaxy is noted. This technique indicates a comoving SFR similar to that for LBGs. The simulations also show that DLA galaxies are on the average much fainter than LBGs, in agreement with the observations.

6.3.6 DLA and L^* galaxies

Observations have suggested that DLA galaxies can be sub-luminous compared to L^* galaxies at both high and low redshifts, which we will return to in Sect. 6.4. We here proceed by investigating their SFRs relative to these luminous galaxies.

Numerical simulations by Cen et al. (2003) have shown that a median high redshift DLA galaxy is has L = 1.1L^* where L^* is measured at $z = 3$. Fitting a Schechter luminosity function to field galaxies at $z = 0$ has indicated that $M_B^* = -20.4$ (Liske et al. 2003). Analysing the luminosity function at $z = 3.5$ Poli et al. (2003) find a strong evolution and $M_B^* = -22.3 \pm 0.3$ in agreement with the study of LBGs at $z = 3$ in Shapley et al. (2001). We can use this information to derive the SFR for a typical, massive high redshift galaxy. Using empirical template spectra for various Hubble type galaxies in Kinney et al. (1996) the SFRs of an L^* galaxy can be derived from a conversion between the flux at 2800 Å in the rest frame and the SFR (Kennicutt 1998a).

We construct spectra of a galaxy with M_B = –22.3$\pm$0.3 from the Kinney et al. (1996) templates, and find the template flux at 2800 Å which is converted to an unobscured SFR. Because it is not known what type of galaxies the DLAs reside in at $z \approx 3$ we investigate all types. The derived SFRs vary strongly with the template type: An Sa type galaxy has SFR = 2.1$\pm$0.5 $M_{\odot}$ yr^{-1}, while an Sc galaxy has SFR = 16$\pm$4 $M_{\odot}$ yr^{-1}. Starburst galaxies, on the other hand, are categorised according to their intrinsic reddening. A starburst galaxy with a very small reddening, $E(B-V) < 0.1$ has SFR = 30$\pm$8 $M_{\odot}$ yr^{-1}, and a starburst galaxy with a large internal reddening of $0.61 < E(B-V) < 0.7$ has an unobscured SFR = 9$\pm$2 $M_{\odot}$ yr^{-1} predicted by its UV continuum.

As mentioned, very high SFRs for DLA galaxies are excluded on the basis of the Hα study in Bunker et al. (1999) indicating that SFR < 20 M$_\odot$ yr^{-1}. It is therefore not likely that DLA galaxies are on the average much brighter than L^* galaxies of the unobscured starburst type. Comparing the SFRs derived for either candidates or confirmed objects with those for typical galaxies at $z \approx 3$ shows that DLA galaxies are consistent with having as large SFRs as L^* galaxies.

At $z \approx 0$, the numerical simulations in Cen et al. (2003) indicate that the median DLA galaxy has $L = 0.5L^*$, and using M_B^* = –20.4 at $z = 0$ calculations similar to that above indicate that a median DLA galaxy has a SFR ranging from 0.1 to 2.5 M$_\odot$yr^{-1} for different galaxy types. Comparing these predictions with the SFRs derived from nebular lines from DLA galaxy at $z < 1$ in Chapter 3 gives consistent results.

6.4 DLA galaxy masses

Masses for the average neutral gas disc can be calculated assuming a DLA galaxy morphology. This gives 2×10^9 M$_\odot$ for the simple cylindrical disc and 7×10^8 M$_\odot$ for an exponential disc, but including uncertainties in the calculations masses $\gtrsim10^{10}$ M$_\odot$ are allowed. Note that the scalings and hence disc masses are derived for the DLA galaxies with detected emission lines, and nothing can be stated about the remaining DLA galaxies.

In the local Universe, a 21 cm survey of galaxy discs has indicated a characteristic H I mass of 7.6×10^9 M$_\odot$ determined from a Schechter function fit to the disc mass distribution (Rosenberg & Schneider 2002). Using this survey to predict DLA galaxy properties at $z = 0$, Rosenberg & Schneider (2003) derived H I masses of 10^9 M$_\odot$ for a predicted average DLA galaxy. This is comparable to the H I mass of 1.3×10^9 M$_\odot$ measured from 21 cm emission from one DLA galaxy at $z = 0.009$ (Bowen et al. 2001), while another very low redshift DLA galaxy has a very low H I mass $<10^7$ M$_\odot$ (Kanekar & Chengalur 2005). For comparison, the Milky Way disc has a total H I mass of 3×10^9 M$_\odot$, and the mass including the stellar contribution is $\sim 10^{11}$ M$_\odot$. Thus, local galaxy neutral gas discs have masses roughly similar to the average DLA galaxy mass traced by their H I.

Simulations have shown that the ratio of mass in stars to gas mass in a DLA galaxy is $\sim$3 at $z \approx 3$ (Nagamine et al. 2004). To calculate the baryonic mass in DLA galaxies we add this contribution and predict an average DLA galaxy mass of 8×10^9 M$_\odot$ at $z \approx 3$. Comparing these indications with the simulations in Nagamine et al. (2004) would suggest that, including the stellar masses a $z = 0$ disc galaxy with a characteristic luminosity L^* is more massive by a factor of $\sim$10 compared to a high redshift DLA galaxy. Assuming a similar mass-to-light ratio with redshift would imply that the average DLA galaxy has a luminosity of $\sim$0.1 L^*, where L^* is estimated at $z = 0$. These findings are consistent with the predicted luminosities for low-redshift DLA galaxies (Rosenberg & Schneider 2003).

Other investigations have supported the suggestions that high redshift DLA galaxies are sub-luminous. Comparing the observed column density distribution of DLAs with those expected from model galaxies lead Boissier et al. (2003) to the same conclusion, i.e. that at $z = 0$ the number density of large disc galaxies is sufficient to explain the number density of DLAs. On the other hand, the models predict that at $z > 2$ disc galaxies are not numerous enough to account for the observed number of DLAs. These observations are consistent with the results indicated here that high redshift galaxies are not necessarily massive.

6.5 Conclusion

We have investigated the SFRs in DLA galaxies from various points. We first used the measured Lyα emission lines from confirmed and candidate DLA galaxies to estimate the SFRs, and showed that disc radii of 10 kpc and an average Schmidt-Kennicutt law would reproduce the measured SFRs.

Secondly, we used existing studies of the DLA column density distributions to derive the comoving SFR in DLAs. We showed that DLA galaxies contribute significantly to the global SFR density, but their contribution lies below that for luminosity-selected high redshift galaxies. The comoving SFRs from DLA galaxies are smaller than for LBGs by approximately an order of magnitude. However, as the Lyα emission lines only measure a lower limit to the intrinsic SFR, the contribution from DLA galaxies could be larger. In principle, if the largest DLA column densities are missed from the quasar surveys, the comoving SFR in DLAs will be underestimated.

Simplified demonstrations were used to indicate that the average $z \approx 3$ DLA galaxy has a mass similar to neutral discs in the local Universe, but because only the neutral gas is measured, they are not necessarily massive and luminous L^* galaxies. Nevertheless, comparing the SFRs derived from Lyα emission at $z > 2$ and nebular emission lines at $z < 1$ indicates that DLA galaxies have SFRs comparable to an L^* galaxy.

At $z \lesssim 1$ DLA galaxies span a wide range of morphologies, but the existence of some L^* galaxies could indicate that the population of DLA galaxies evolve to more massive systems with cosmic time. Such a scenario is in agreement with the hypothesis that systems that are responsible for DLAs at high redshifts will progressively merge to form more massive galaxies at low redshifts (e.g. Haehnelt et al. 1998).

Acknowledgments. L. Christensen acknowledges support by the German Verbundforschung associated with the ULTROS project, grant no. 05AE2BAA/4.

References

Boissier, S., Péroux, C., & Pettini, M. 2003, MNRAS, 338, 131
Bowen, D. V., Tripp, T. M., & Jenkins, E. B. 2001, AJ, 121, 1456
Bunker, A. J., Warren, S. J., Clements, D. L., Williger, G. M., & Hewett, P. C. 1999, MNRAS, 309, 875
Cayatte, V., Kotanyi, C., Balkowski, C., & van Gorkom, J. H. 1994, AJ, 107, 1003
Cen, R., Ostriker, J. P., Prochaska, J. X., & Wolfe, A. M. 2003, ApJ, 598, 741
Charlot, S. & Fall, S. M. 1993, ApJ, 415, 580
Chen, H.-W. & Lanzetta, K. M. 2003, ApJ, 597, 706
Gould, A. & Weinberg, D. H. 1996, ApJ, 468, 462
Haehnelt, M. G., Steinmetz, M., & Rauch, M. 1998, ApJ, 495, 647
Hopkins, A. M., Rao, S. M., & Turnshek, D. A. 2005, ApJ accepted (astro-ph/0505418)
Hou, J. L., Shu, C. G., Shen, S. Y., et al. 2005, ApJ, 624, 561
Hu, E. M., Cowie, L. L., Capak, P., et al. 2004, AJ, 127, 563
Kanekar, N. & Chengalur, J. N. 2005, A&A, 429, L51
Kennicutt, R. C. 1998a, ARA&A, 36, 189
—. 1998b, ApJ, 498, 541
Kinney, A. L., Calzetti, D., Bohlin, R. C., et al. 1996, ApJ, 467, 38
Kulkarni, V. P., Fall, S. M., Lauroesch, J., et al. 2005, ApJ, 618, 68
Kunth, D., Leitherer, C., Mas-Hesse, J. M., Östlin, G., & Petrosian, A. 2003, ApJ, 597, 263

Kunth, D., Mas-Hesse, J. M., Terlevich, E., et al. 1998, A&A, 334, 11
Lanzetta, K. M., Yahata, N., Pascarelle, S., Chen, H., & Fernández-Soto, A. 2002, ApJ, 570, 492
Le Brun, V., Bergeron, J., Boisse, P., & Deharveng, J. M. 1997, A&A, 321, 733
Ledoux, C., Petitjean, P., & Srianand, R. 2003, MNRAS, 346, 209
Leibundgut, B. & Robertson, J. G. 1999, MNRAS, 303, 711
Lilly, S. J., Le Fevre, O., Hammer, F., & Crampton, D. 1996, ApJL, 460, L1
Liske, J., Lemon, D. J., Driver, S. P., Cross, N. J. G., & Couch, W. J. 2003, MNRAS, 344, 307
Madau, P., Ferguson, H. C., Dickinson, M. E., et al. 1996, MNRAS, 283, 1388
Møller, P., Fynbo, J. P., & Fall, S. M. 2004, A&A, 422, L33
Møller, P., Warren, S. J., Fall, S. M., Fynbo, J. U., & Jakobsen, P. 2002, ApJ, 574, 51
Nagamine, K., Springel, V., & Hernquist, L. 2004, MNRAS, 348, 435
Péroux, C., McMahon, R. G., Storrie-Lombardi, L. J., & Irwin, M. J. 2003, MNRAS, 346, 1103
Pettini, M., Ellison, S. L., Bergeron, J., & Petitjean, P. 2002, A&A, 391, 21
Pettini, M., Ellison, S. L., Steidel, C. C., & Bowen, D. V. 1999, ApJ, 510, 576
Pettini, M., Shapley, A. E., Steidel, C. C., et al. 2001, ApJ, 554, 981
Poli, F., Giallongo, E., Fontana, A., et al. 2003, ApJL, 593, L1
Prochaska, J. X., Gawiser, E., Wolfe, A. M., Castro, S., & Djorgovski, S. G. 2003, ApJL, 595, L9
Prochaska, J. X. & Herbert-Fort, S. 2004, PASP, 116, 622
Rao, S. M. 2005, in Probing Galaxies through Quasar Absorption Lines, ed. P. R. Williams, C. Shu, & B. Ménard, IAU Colloquium 199
Rao, S. M., Nestor, D. B., Turnshek, D. A., et al. 2003, ApJ, 595, 94
Rao, S. M. & Turnshek, D. A. 2000, ApJS, 130, 1
Rosenberg, J. L. & Schneider, S. E. 2002, ApJ, 567, 247
—. 2003, ApJ, 585, 256
Schlegel, D. J., Finkbeiner, D. P., & Davis, M. 1998, ApJ, 500, 525
Schmidt, M. 1959, ApJ, 129, 243
Shapley, A. E., Erb, D. K., Pettini, M., Steidel, C. C., & Adelberger, K. L. 2004, ApJ, 612, 108
Shapley, A. E., Steidel, C. C., Adelberger, K. L., et al. 2001, ApJ, 562, 95
Shapley, A. E., Steidel, C. C., Pettini, M., & Adelberger, K. L. 2003, ApJ, 588, 65
Steidel, C. C., Adelberger, K. L., Giavalisco, M., Dickinson, M., & Pettini, M. 1999, ApJ, 519, 1
Steidel, C. C., Giavalisco, M., Pettini, M., Dickinson, M., & Adelberger, K. L. 1996, ApJL, 462, L17
Steidel, C. C., Shapley, A. E., Pettini, M., et al. 2004, ApJ, 604, 534
Storrie-Lombardi, L. J. & Wolfe, A. M. 2000, ApJ, 543, 552
Uson, J. M. & Matthews, L. D. 2003, AJ, 125, 2455
Weatherley, S. J., Warren, S. J., Møller, P., et al. 2005, MNRAS, 358, 985
Wolfe, A. M. 2005, in Probing Galaxies through Quasar Absorption Lines, ed. P. R. Williams, C. Shu, & B. Ménard, IAU Colloquium 199
Wolfe, A. M., Prochaska, J. X., & Gawiser, E. 2003, ApJ, 593, 215

CHAPTER 7

Extended line emission surrounding radio-loud quasars at $0.6 < z < 0.9$

L. CHRISTENSEN[1], K. JAHNKE[1], L. WISOTZKI[1,2], S. F. SÁNCHEZ[1,3], K. EXTER[4], M. M. ROTH[1]

[1] Astrophysikalisches Institut Potsdam, An der Sternwarte 16, 14482 Potsdam, Germany

[2] Potsdam University, Am Neuen Palais 10, 14469 Potsdam, Germany

[3] Centro Astronomico Hispano Aleman de Calar Alto, Spain

[4] Instituto de Astrofísica de Canarias, La Laguna, Tenerife

Abstract

We present optical integral field spectroscopy of extended emission line regions around three radio-loud quasars at redshifts $0.6 < z < 0.9$. The two lobe-dominated quasars have extended [O II] line emission aligned with the radio jet, while no extended emission is found from the one core-dominated quasar. The emission lines have widths $<$1000 km s^{-1}. Within the $8'' \times 8''$ field of view of the integral field unit emission within $\sim$30 kpc from the core can be probed. Velocity structures of $\sim$800 km s^{-1} in the brightest nebula detected around 3C 196 are inconsistent with a rotation. The nebula is aligned with the radio hot spots and shows both a redshifted and a blueshifted component. This alignment effect supports the hypothesis that the extended emission is caused by a jet-cloud interaction. A pronounced bend at the location of the hot spots is reported in the literature, which supports the jet-cloud interpretation. 3C 196 also has extended emission from [Ne III] suggesting a high ionisation 30 kpc from the QSO nucleus. The non-detection for the core-dominated quasar could be influenced by PSF subtraction residuals if line emission is also present along the line of sight.

7.1 Introduction

Extended narrow emission line nebulae have been detected around quasars at redshifts between 0 and 4 and extending to more than 100 kpc from the QSO nuclei (e.g. Heckman et al. 1991; Bremer et al. 1992). At low redshift detailed analyses of the host galaxies are enabled by observations of the stellar continuum emission. However, in several cases the line emission extends farther out than in the continuum and the question is what causes this emission. Possibilities are photoionisation from

† A version of this paper will be submitted to *Astronomy & Astrophysics*.

the central source, ionising radiation from massive stars in star-forming regions in the host galaxy, or interaction of the jets from radio-loud quasars (RLQs) with the surrounding material. The latter interpretation is indicated by observations of alignment of the radio jets with the optical continuum and extended emission line regions (McCarthy et al. 1987). Such interactions cause formation of shocks which compress and heat the gas, and subsequent recombination line emission will cool the material. Remnants from galaxy mergers (Stockton & MacKenty 1987), material falling into dark matter potentials (Haiman & Rees 2001), or cooling flows in massive galaxy clusters (e.g. Fabian & Crawford 1990) have been offered as possible explanations for the extended emission line regions.

To investigate the structure and kinematics of these nebulae, narrow- and broad-band images, and slit spectroscopy has been used traditionally. Integral field spectroscopy (IFS) presents an alternative technique that allows imaging and spectroscopy simultaneously. IFS of six RLQs at redshift $0.26 < z < 0.60$ has shown that extended emission line nebulae are common, but they are not always aligned with the radio axis (Crawford & Vanderriest 2000). At $z \approx 0.3$ no correlation was observed between the continuum and [O III] emission line regions in 47 QSOs (Stockton & MacKenty 1987). After an alignment between the radio axis and the extended emission around one lobe-dominated quasar had been reported in Bremer (1997) IFS of this object gave evidence for a jet-cloud interaction (Crawford & Vanderriest 1997). Another example of a jet-cloud interaction in one RLQ is presented in Márquez et al. (2000). At $z > 2$, detections of extended [O II] and [O III] emission lines have indicated no strong evolution with redshift and a tendency for stronger line emission spatially coincident with the stronger radio emission (Wilman et al. 2000).

The AGN unification scheme states that radio galaxies and RLQs are the same objects viewed at different angles relative to their jets (Barthel 1989). Hence, information on RLQs can be gained by studies of radio galaxies instead. Radio galaxies have extended line emission aligned to within 25° of the radio jet (McCarthy et al. 1987). Also the continuum emission from the host galaxy appears aligned with the radio emission in radio galaxies, suggesting that collimation of the nuclear ionising flux plays no role. Rather, the observations have been interpreted as star formation triggered by an outflow along the radio axis (McCarthy et al. 1987). RLQs show extended stellar continuum emission from the host galaxy, however with a smaller extension than their line emission, and the alignment is not well-determined at high redshifts (Heckman et al. 1991; Hutchings 1992).

This paper presents IFS of three RLQs at $0.6 < z < 0.9$ and an analysis of the alignment effect. The data set was obtained in connection with a project aimed at detecting emission from galaxies associated with intervening damped Lyman-α absorption lines (Christensen et al. 2004b,a). The three-dimensional data allow an analysis of the extended line emission regions at the QSO redshifts. From the original sample of seven QSOs at $z < 2$, only three RLQs have redshifted optical emission lines within the wavelength range of the observations.

Throughout this paper a flat cosmology with $H_0 = 70$ km s^{-1} Mpc^{-1}, $\Omega_m = 0.3$ and $\Omega_\Lambda = 0.7$ is adopted.

7.2 Observations and data reduction

Observations were carried out with two integral field spectrographs; INTEGRAL mounted on the 4m William Hershell Telescope, La Palma (Arribas et al. 1998), and the Potsdam Multi Aperture Spectrophotometer (PMAS) mounted on the 3.5m telescope at Calar Alto (Roth et al. 2000, 2005). Table 7.1 presents a log of the observations.

7.2.1 INTEGRAL observations

The observations were obtained with the SB2 fibre bundle, which consists of 189 object fibres plus 30 sky fibres. Each fibre has a diameter of $0\farcs9$ on the sky giving a field of view of $12'' \times 16''$ with a

Name	alias	redshift	date	instrument	exptime (s)
Q0738+313	OI 363	0.63	2003-04-27	PMAS	2×1800
			2003-04-30	PMAS	2×1800
			2004-01-16	INTEGRAL	4×1800
Q0809+4822	3C 196	0.871	2004-01-16	INTEGRAL	8×1800
Q1622+236	3C 336	0.927	2003-04-27	PMAS	6×1800
			2003-06-19	PMAS	4×1800
			2003-06-20	PMAS	8×1800

Table 7.1. Log of the observations.

non-contiguous sampling. We used a 600 lines mm^{-1} grating with a dispersion of 3 Å pixel^{-1} and a spectral resolution of 6 Å measured from the width of sky emission lines. The full wavelength coverage of all spectra is 5000–8000 Å.

Data reduction was performed with IRAF using software written specifically for the reduction of INTEGRAL data (see Garcia-Lorenzo et al. 2005). Bias frames were subtracted and the frames were cleaned for cosmic ray hits using the algorithm described in Pych (2004). All spectra were extracted using the trace of the 219 spectra on the CCD found from an exposure of a continuum lamp obtained at the beginning of the night. Wavelength calibration was done using exposures of emission line lamps also extracted for each fibre. The RMS deviation of the wavelength for sky emission lines for each spectrum was determined to be $<$0.2 Å. Differences between the individual fibre transmissions as a function of wavelength were corrected for by modeling the transmission of sky flat frames obtained at twilight. Two regions on the CCD were affected by scattered light but there only in the blue end of the spectral range and only affecting some of the spectra. Otherwise, scattered light was found to be negligible compared to the overall read noise of the CCD. Spectra from sky-fibres located in a ring around the central fibre bundle were examined, and those uncontaminated by the QSO flux were averaged and subtracted from each object spectrum. To facilitate inspection, the data were interpolated onto a cube of square pixels with sizes of $0\farcs3\times0\farcs3$.

7.2.2 PMAS observations

PMAS has 16×16 fibres coupled to a lens array and has a contiguous sampling of the sky. The instrument configuration used provided a field of view of $8''\times8''$ and using gratings with 300 and 600 lines mm^{-1} resulted in spectral resolutions of 6.6 Å and 3.3 Å, respectively.

The method for reducing PMAS data is essentially the same as for INTEGRAL data and was done with software written in IDL (Becker 2002). The main difference is the sky subtraction because PMAS does not have allocated sky fibres. Instead, an average sky spectrum was created from spectra at the edge of the field of view uncontaminated by the QSO or the nebulae. Because the spatial position of the nebulae were previously unknown, several different selections of sky spectra were examined before selecting an appropriate sky background spectrum. For the final sky background spectrum we selected spaxels where no emission lines were detected visually around the wavelength range of interest. Hence, an over-subtraction of the extended emission should be a small effect.

Both data sets were flux calibrated by comparison with observations of spectrophotometric standard stars observed at the same nights and with the same setup as used for the objects. Further visualization of the data cubes was done with the Euro3D visualization tool (Sánchez 2004).

7.3 Results

This section presents results obtained for each of the RLQ. To detect the extended line emission it was first necessary to subtract the nuclear QSO emission because this was by far the dominant contribution. First a one-dimensional spectrum of each QSO was extracted from the data cubes as shown in Fig. 7.1. To get a clean spectrum of the extended emission line nebulae uncontaminated by the QSO emission we used the approach to subtract the bright QSO emission described in Sánchez et al. (2004). Briefly, this method removes the QSO spectrum by modeling each monochromatic slice in the cube and assumes smoothly varying parameters with wavelength. For the PMAS data, we used a simpler method by subtracting a scaled version of the one-dimensional QSO spectrum from each object spectrum in the data cube and minimised the residuals.

7.3.1 Q0738+313

This is a core-dominated RLQ (Stanghellini et al. 1997). Chandra X-ray observations have revealed an X-ray jet with several knots extending to the South-East of the quasar (Siemiginowska et al. 2003). The end of the X-ray jet at 200 kpc is spatially coincident with the weaker extended radio emission. Hutchings (1992) obtained broad-band and narrow-band images centered on the [O II] emission line at the quasar redshift and found evidence for a detached region of [O II] emission approximately $2''$ in size and offset by $\sim 3''$ to the north-east.

The [O II] emission line is within the wavelength range of the observations, but subtraction of the QSO emission from the IFS data cubes revealed no extended emission in either data sets. A narrow-band image created from the INTEGRAL data cube of the wavelength region around [O II] at $z = 0.63$ is shown in Fig. 7.2. No bright emission features with associated emission lines were found. Other narrow-band images offset by up to 1000 km s^{-1} relative to the quasar redshift were also examined, but no line emission regions were found either. We also note that the nuclear [O II] emission line shown in Fig. 7.1 appears weak.

We estimate an upper detection limit for extended [O II] emission of about 3×10^{-17} erg cm^{-2} s^{-1}arcsec^{-1} in the INTEGRAL data set and 2×10^{-17} erg cm^{-2} s^{-1}arcsec^{-1} in the PMAS data set, based on experiment with artificial emission lines.

7.3.2 Q0809+4822

This is a steep-spectrum, lobe-dominated RLQ (Pooley & Henbest 1974), with a pronounced bend at location of the hot spots (Brown et al. 1986). Extended oxygen emission has previously been reported based on long-slit spectroscopic observations (Fabian et al. 1988), and the [O II] and [O III] emission ratio was interpreted as a cooling flow (Crawford & Fabian 1989). Because the night was non-photometric we do not obtain spectrophotometric results. Therefore all derived fluxes are relative.

Extended emission

The data cube of this object clearly showed extended [O II] emission; even in the frame where the QSO emission was present as shown in Fig. 7.3 which presents the spectra between 6850 Å and 7080 Å. This figure stacks all the spectra in the INTEGRAL data according to the spiral pattern arrangement of the fibre bundle. Co-adding all the spectra associated with the extended emission after the QSO emission was subtracted resulted in an emission line with a total flux of 1.2×10^{-15} erg cm^{-2} s^{-1} with a *FWHM* of 650$\pm$180 km s^{-1}.

After subtracting the QSO emission the residual spectra are shown as the stacked spectra in the right panel in Fig. 7.3. Residual emission from the QSO is still present due to uncertainties in the

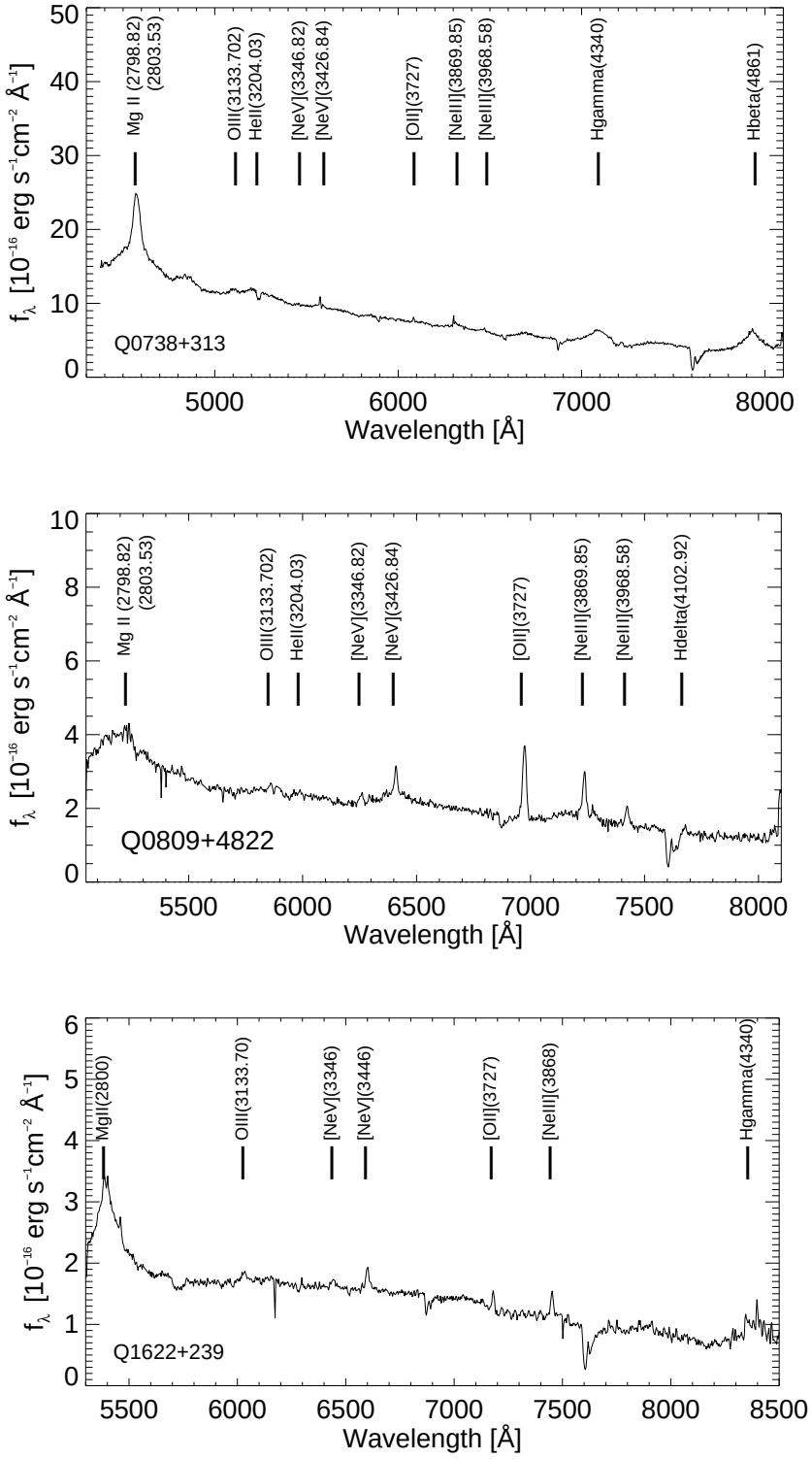

Fig. 7.1. One-dimensional spectra of the quasars extracted from the data cubes. Emission lines have been indicated.

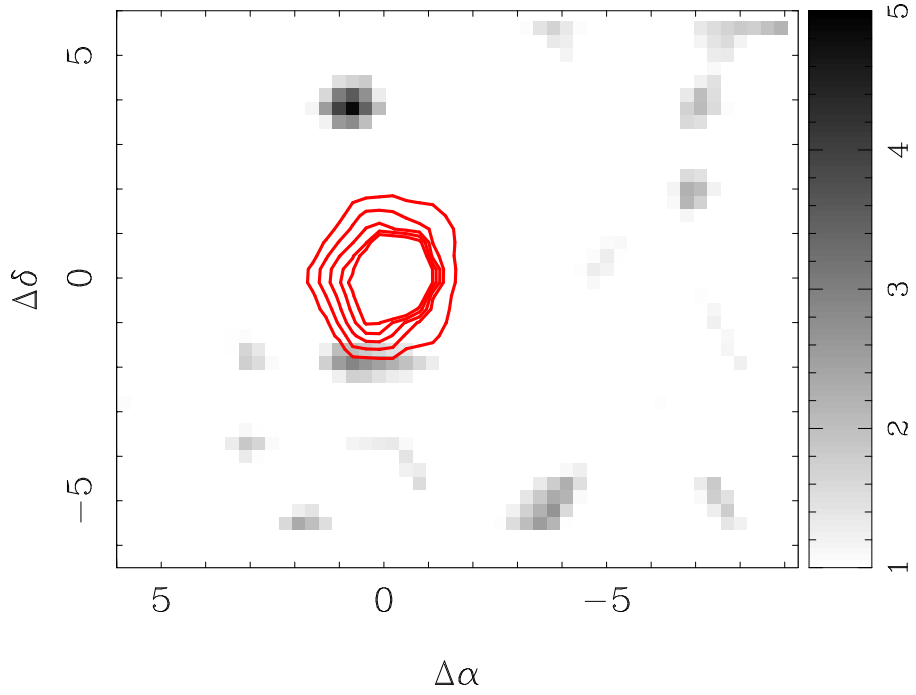

Fig. 7.2. Narrow-band image of Q0738+131 created from the INTEGRAL data at $6070 < \lambda < 6090$Å which includes [O II] at $z = 0.63$. The scaling has been chosen to show features brighter than 2σ above the background noise, and no extended emission line features surrounding the quasar are detected. The small features visible in this image are not significant. The contours show an off-band narrow-band image of the QSO centered at (0,0) where the innermost contour represent the seeing *FWHM*.

wavelength dependent PSF determination, but this effect is strong for only the central three pixels as shown in Fig. 7.4. The emission is predominantly located in two regions. North of the quasar the emission extends to 3″ (22 kpc), while a brighter region extends out to 5″ (36 kpc) to the south as can be seen in Fig. 7.4.

Besides [O II] emission we also detected extended [Ne III] λ3869 emission associated with the brightest [O II] region to the south of the QSO. Co-adding these spaxels to the south of the QSO centre gives the one-dimensional spectrum shown in Fig. 7.5. The extension of the nebula appears smaller than for the [O II] region, but the signal-to-noise level did not allow for a detailed analysis. The emission line ratio log([Ne III]/[O II]) $\approx$ –0.6$\pm$0.1 is larger than observed for H II regions in local galaxies (Oey et al. 2000), where values between –1.6 and –0.7 are found, indicating that the ionising flux is harder around the RLQ. Compared to the much lower redshift RLQ 4C 37.43, it has a similar emission line ratio in the extended nebula (Stockton et al. 2002). The signal-to-noise level in our cleaned spectrum is too low to allow detection of extended emission from other emission lines.

To check for the presence of fainter extended emission farther away than 5″ from the quasar centre, 30 spectra were co-added at several spatial locations, but with negative results. From the non-detections of emission lines, we derive an upper limit for emission in the surrounding field of $\sim 1 \times 10^{-17}$ erg cm^{-2} s^{-1} arcsec^{-2} in the INTEGRAL data. Not surprisingly, we find no continuum emission farther than 5″ from the QSO either.

Because our observing campaign was targeted towards finding emission from a $z = 0.4367$ galaxy responsible for the DLA, the wavelength coverage was not optimal compared to similar studies of other QSOs, which use the [O II] / [O III] line ratio to derive an internal gas pressure (e.g. Crawford & Vanderriest 2000). Therefore the present data cube does not allow modeling of the

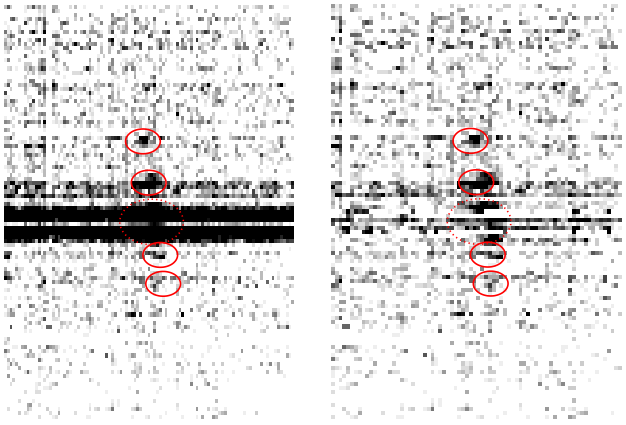

Fig. 7.3. Stacked spectra of Q0809+4822 in the wavelength region 6850–7080 Å with the dispersion axis horizontal. The 188 spectra are arranged according to the spiral pattern in the INTEGRAL fibre bundle. In the left panel, emission from the QSO is dominating but also the extended emission is clearly seen as indicated by the circles. In the right panel the QSO emission has been subtracted.

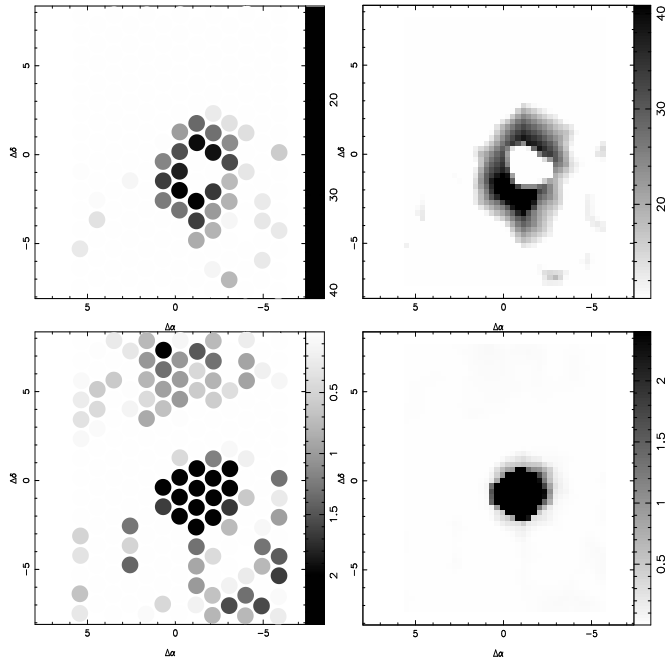

Fig. 7.4. The *upper left panel* is a narrow-band image of the [O II] emission at $z = 0.871$ from Q0809+4822. It shows the intensities in the INTEGRAL spaxels where the non-contiguous layout of the fibres is visible. In the *upper right* hand panel, the image has been interpolated to a finer grid scale of 0.″3. Residuals from the QSO subtraction are present at the central three spectra. In the *bottom left panel* an image of the QSO continuum in adjacent wavelength is shown for comparison of the PSF, and the *bottom right panel* shows the corresponding interpolated image. The QSO centre is located at (–1,–1) in all panels.

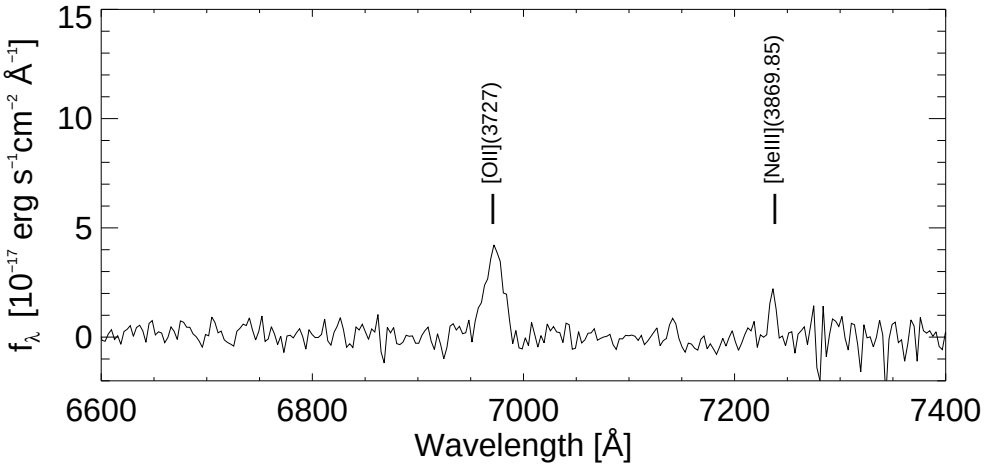

Fig. 7.5. One-dimensional spectrum of the brightest region to the south of Q0809+4822 where both [O II] and [Ne III] lines appear extended.

ionising conditions in the nebulae.

Fig. 7.3 shows that the extended emission around the QSO is shifted in wavelength in the different fibres. Fitting Gaussian profiles to the individual spectra gives evidence for systematic velocity structure over the nebula as shown in Fig. 7.6. Only spectra with [O II] detections larger than 2σ above the background are shown in colours. Compared to the systemic redshift of the QSO, the bright southern region has a relative blueshift of about -360 km s^{-1}, whereas the fainter north western region is redshifted by up to +500 km s^{-1}. Another representation in Fig. 7.7 shows a grey scale image of the intensity in the [O II] line emission region and the velocity structures of the emission are indicated by contours. Differences between contour levels are 100 km s^{-1} and blueshifted velocities are shown as dashed contours.

Two radio hot-spots found at 5 GHz with a separation of $5\farcs8$ at P.A. $\approx 120°$ (Pooley & Henbest 1974) are indicated by the letters A and B in Fig. 7.7. Whereas the position of the southern spot is close to the bright [O II] emission line region, the emission is fainter near the northern hot-spot. The southern lobe is associated with the blueshifted emission, and the northern one with the redshifted part. This presents clear evidence for an interaction with the radio jets.

We note that the northern emission line region is spatially coinciding with the Hβ emission from the DLA galaxy at $z = 0.4367$, which lies $1\farcs5$ to the north-west of the QSO (Le Brun et al. 1997; Chen et al. 2005). Hence some of the northern emission nebula could be contaminated from this intervening galaxy. The [O II] emission line flux we recover from this galaxy is consistent with that in Chen et al. (2005), while the Hβ line flux in the IFS data is about twice their value. We therefore conclude that we detect additional extended [O II] emission from the northern nebula.

7.3.3 Q1622+239

Q1622+239 is a steep-spectrum lobe-dominated RLQ with radio lobes separated by $28''$ at PA $\approx 30°$ and a jet extending to the south-east of the QSO (Pooley & Henbest 1974; Bridle et al. 1994). Both Bremer et al. (1992) and Steidel et al. (1997) report extended [O II] emission at $z = 0.927$ to the north and south of the QSO. This emission, detected $5''$ from the core, was previously interpreted as due to a cooling flow (Bremer et al. 1992). The quasar is located in a region where many galaxies are observed close to the sight line. Most of the galaxies are intervening, but seven galaxies have

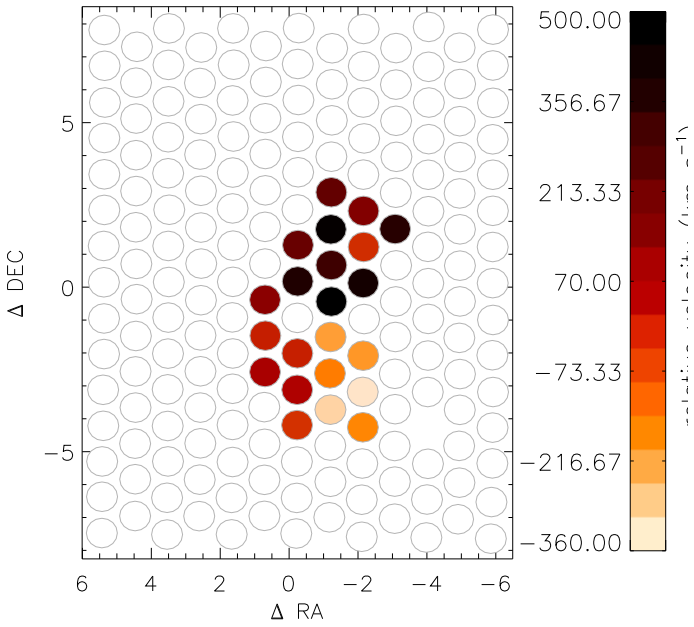

Fig. 7.6. Velocity structures of the extended [O II] emission around Q0809+4822 determined after the QSO emission was subtracted. Outlined circles indicate the spectra where no [O II] emission lines could be fit due to their low signal-to-noise levels.

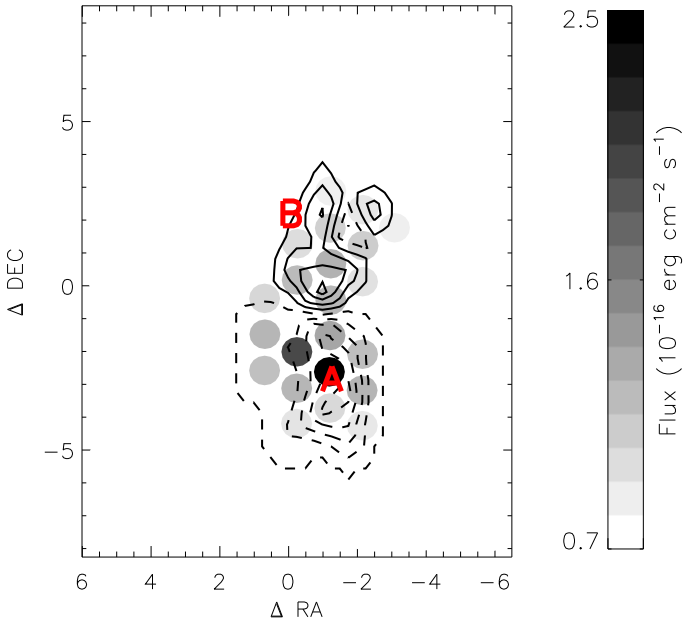

Fig. 7.7. Image of the [O II] line emission intensity around Q0809+4822 with velocity contours overlaid. Contour levels are separated by 100 km s^{-1} and negative velocities are shown by the dashed lines. The letters A and B indicate the position of the two radio hot-spots.

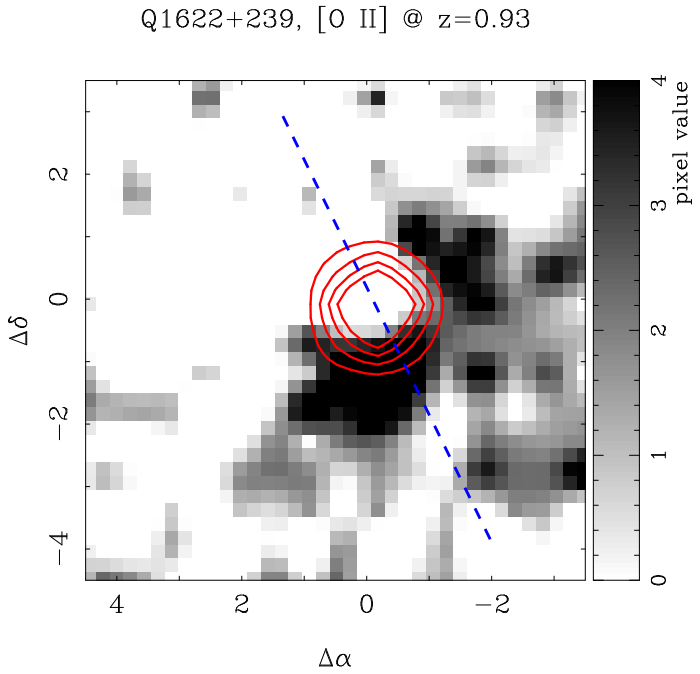

Fig. 7.8. Narrow-band interpolated image of the [O II] line emission region from Q1622+239. The field of view is $8''\times8''$, north is up and east to the left. The emission region to the north-west is equivalent to the location of the object denoted '2' in Steidel et al. (1997). A narrow-band image slightly towards redder wavelengths ([O II] at $z = 0.930$) shows emission at larger distances than in this image, which is consistent with the $2\farcs58$ offset reported in Steidel et al. (1997). Contours show an off-band narrow-band image where the innermost contour represent the seeing *FWHM*. The dashed blue line represents the orientation of the radio jet which extends beyond the field of view of the IFS data.

redshifts consistent with being associated with a cluster at $z = 0.923$, i.e. at the quasar redshift (Steidel et al. 1997).

Fig. 7.8 shows a narrow-band image of the extended emission region which appears to the south and north-west of the QSO, with the brightest region towards the south. The latter is spatially coincident with the radio-jet, whereas the north-west emission line region is not aligned. A narrow-band image offset to slightly longer wavelengths showed the emission feature extending further to the north-west, being spatially coincident with the emission feature denoted '2' detected in a continuum image in Steidel et al. (1997). A one-dimensional spectrum of that region in the data cube indicated $z = 0.9300 \pm 0.0009$ in agreement with $z = 0.931$ measured by Steidel et al. (1997). Furthermore, the data cube allowed a confirmation of their object '3' at $z = 0.892$, $3''$ to the east of the QSO.

The integral field data with PMAS only allowed detection of the emission to $\sim2''$ from the QSO, and a detailed analysis of the emission line region was not possible with the signal-to-noise level in each individual spectrum from the data cube. In the co-added one-dimensional spectrum for the whole emission line region the total line flux measured is $(3.8 \pm 1.4) \times 10^{-16}$ erg cm^{-2} s^{-1} after correction for Galactic extinction (Schlegel et al. 1998). After correcting for the instrumental resolution, the line width is 910±280 km s^{-1}.

Possibly, the emission to the north-west is unrelated to the QSO and only belongs to the galaxy '2' in Steidel et al. (1997), thus we determine the properties of the southern region only. Here the flux is $1.8 \pm 0.5 \times 10^{-16}$ erg cm^{-2} s^{-1} and the *FWHM* is 720±200 km s^{-1}. The redshift measured is $z = 0.9274 \pm 0.0005$ consistent with the redshift reported for the QSO.

7.4 Discussion and conclusions

We have presented integral field spectroscopy of three RLQs, where one is core-dominated and the other two are lobe-dominated. Extended [O II] emission is seen around the two lobe-dominated RLQs, and the emission is spatially coincident with the radio emission. All extended emission lines from the extended regions are relatively narrow with $FWHM < 1000$ km s^{-1}. The brightest object (3C 196) has velocity structures of more than 800 km s^{-1} over approximately 60 kpc. Compared to the two objects studied in Crawford & Vanderriest (2000) that show alignment of the velocity structure with the radio jet, 3C 196 presents a clearer evidence for a jet-cloud interaction. The emission line nebula has both a red- and a blueshifted component aligned with the radio hot spots, and the velocity is larger than expected for a rotation curve. The bend of the radio emission at the location of the hot spots noted in Brown et al. (1986) supports this interpretation.

Extended [Ne III] emission is detected for 3C 196 at a distance of 30 kpc from the quasar nucleus, but only in the southern region where the [O II] emission is strongest. Because the [Ne III]/[O II] line flux ratio is larger than observed in H II regions, harder ionising radiation must be present, but for a detailed modeling more emission lines are needed. Ionisation conditions can be analysed in the extended nebulae provided that the [O III] emission line is detected too. Combining the observed emission line ratios with knowledge of the quasar ionising flux allows to determine the nebulae pressure though photoionisation modeling. However, this approach is only justified when [O II] and [O III] arise in the same medium. This is sometimes neglected as pointed out in Stockton et al. (2002) who find that the [O II] emission arises in a much denser medium than [O III] in one RLQ.

The alignment of the nebular emission line regions with the radio jets indicates that some interaction could be present. To determine whether the line emission is created by the ionising quasar flux which is collimated along the radio jet, it is necessary to determine the underlying continuum flux. If a significant stellar emission component is present then one can rule out this scenario. No extended continuum emission is detected in either object analysed here, but if it were present, the bright nuclear flux complicates the detection. Deeper (imaging) data can resolve this issue. Furthermore, if the extended emission is caused by an interaction with the radio jet, larger field of view observations of Q1622+239 are necessary to analyse the effects at larger distances corresponding to the widely separated radio-lobes.

In the unification scheme, the core-dominated RLQs have their radio jet orientation closely aligned with the sight line. If radio jets cause interaction with the surrounding material and give rise to line emission, a core-dominated RLQ would have less extended emission than lobe-dominated RLQs. No extended emission line regions were detected for the one core-dominated RLQ analysed here.

An alternative scenario where the extended emission is dominated by the QSO ionising radiation directed in a cone (Haiman & Rees 2001; Weidinger et al. 2005) can not be rejected completely on the basis of this investigation. However, the velocity structure of the nebulae around Q0809+4822 would support the hypothesis that it is the interaction of the material with the radio jet which causes an outflow of the material.

Acknowledgments. L. Christensen acknowledges support by the German Verbundforschung associated with the ULTROS project, grant no. 05AE2BAA/4. S.F. Sánchez and K. Exter acknowledges the support from the Euro3D Research Training Network, grant no. HPRN-CT2002-00305. K. Jahnke acknowledged support from DLR.

References

Arribas, S., Carter, D., Cavaller, L., et al. 1998, in Proc. SPIE Vol. 3355, p. 821-827, Optical Astronomical Instrumentation, Sandro D'Odorico; Ed., 821–827
Barthel, P. D. 1989, ApJ, 336, 606
Becker, T. 2002, PhD thesis, Astrophysikalisches Institut Potsdam, Germany
Bremer, M. N. 1997, MNRAS, 284, 126
Bremer, M. N., Crawford, C. S., Fabian, A. C., & Johnstone, R. M. 1992, MNRAS, 254, 614
Bridle, A. H., Hough, D. H., Lonsdale, C. J., Burns, J. O., & Laing, R. A. 1994, AJ, 108, 766
Brown, R. L., Broderick, J. J., & Mitchell, K. J. 1986, ApJ, 306, 107
Chen, H.-W., Kennicutt, R. C., & Rauch, M. 2005, ApJ, 620, 703
Christensen, L., Hjorth, J., & Gorosabel, J. 2004a, A&A, 425, 913
Christensen, L., Sánchez, S. F., Jahnke, K., et al. 2004b, A&A, 417, 487
Crawford, C. S. & Fabian, A. C. 1989, MNRAS, 239, 219
Crawford, C. S. & Vanderriest, C. 1997, MNRAS, 285, 580
—. 2000, MNRAS, 315, 433
Fabian, A. C. & Crawford, C. S. 1990, MNRAS, 247, 439
Fabian, A. C., Crawford, C. S., Johnstone, R. M., Hewett, P. C., & Allington-Smith, J. R. 1988, MNRAS, 235, 13P
Garcia-Lorenzo, B., Sánchez, S. F., Mediavilla, E., Gonzales-Serano, J. I., & Christensen, L. 2005, ApJ, 621, 146
Haiman, Z. & Rees, M. J. 2001, ApJ, 556, 87
Heckman, T. M., Miley, G. K., Lehnert, M. D., & van Breugel, W. 1991, ApJ, 370, 78
Hutchings, J. B. 1992, AJ, 104, 1311
Le Brun, V., Bergeron, J., Boisse, P., & Deharveng, J. M. 1997, A&A, 321, 733
Márquez, I., Pécontal, E., Durret, F., & Petitjean, P. 2000, A&A, 361, 5
McCarthy, P. J., van Breugel, W., Spinrad, H., & Djorgovski, S. 1987, ApJL, 321, L29
Oey, M. S., Dopita, M. A., Shields, J. C., & Smith, R. C. 2000, ApJS, 128, 511
Pooley, G. G. & Henbest, S. N. 1974, MNRAS, 169, 477
Pych, W. 2004, PASP, 116, 148
Roth, M. M., Bauer, S., Dionies, F., et al. 2000, in Proc. SPIE, Vol. 4008, 277–288
Roth, M. M., Becker, T., Bauer, S.-M., et al. 2005, PASP, accepted
Sánchez, S. F. 2004, AN, 325, 167
Sánchez, S. F., Garcia-Lorenzo, B., Mediavilla, E., González-Serrano, J. I., & Christensen, L. 2004, ApJ, 615, 156
Schlegel, D. J., Finkbeiner, D. P., & Davis, M. 1998, ApJ, 500, 525
Siemiginowska, A., Stanghellini, C., Brunetti, G., et al. 2003, ApJ, 595, 643
Stanghellini, C., O'Dea, C. P., Baum, S. A., et al. 1997, A&A, 325, 943
Steidel, C. C., Dickinson, M., Meyer, D. M., Adelberger, K. L., & Sembach, K. R. 1997, ApJ, 480, 568
Stockton, A. & MacKenty, J. W. 1987, ApJ, 316, 584
Stockton, A., MacKenty, J. W., Hu, E. M., & Kim, T. 2002, ApJ, 572, 735
Weidinger, M., Møller, P., Fynbo, J. P. U., & Thomsen, B. 2005, A&A, 436, 825
Wilman, R. J., Johnstone, R. M., & Crawford, C. S. 2000, MNRAS, 317, 9

CHAPTER 8

Extended Lyman-α emission nebulae around bright $z \sim$3 radio-quiet quasars

L. CHRISTENSEN [1], K. JAHNKE [1], L. WISOTZKI [1,2], AND S. F. SÁNCHEZ [3]

Astrophysikalisches Institut Potsdam, An der Sternwarte 16, 14482 Potsdam, Germany

Potsdam University, Am Neuen Palais 10, 14469 Potsdam, Germany

Centro Astronomico Hispano Aleman de Calar Alto, Spain

Abstract

We present integral field spectroscopic (IFS) observations of extended nebulae emitting narrow Lyα emission lines from a sample of seven bright high redshift quasars (QSOs) at $2.7 < z_{\rm em} < 4.5$. Narrow-band images created from the data cubes centered at wavelength of Lyα emission at $z_{\rm em}$ show emission in five of the QSOs. Four are radio-quiet QSOs and one is a radio-loud, core-dominated quasar. All emission line nebula appear asymmetric and the brightest QSOs also have the brightest Lyα nebulae with surface flux densities up to 2–3$\times 10^{-16}$ erg cm^{-2} s^{-1}arcsec^{-2}. Velocity structures and surface density profiles are examined for the two brightest systems. We find velocities between $\sim$600 km s^{-1} at the QSO position to $\sim$200 km s^{-1} at a distance of $3 - 4''$ from the QSO. This corresponds to a projected distance of 15–25 kpc at the QSO redshifts and supports the theoretical predictions. None of the nebulae show emission lines from heavier elements to a 3σ detection limit of 4×10^{-17} erg cm^{-2} s^{-1}arcsec^{-2}, suggesting that the nebulae arise in low-metallicity material. The five extended nebulae have total Lyα fluxes corresponding to $\sim$1–2% that of the Lyα flux from the QSOs within a 20 Å wide narrow-band image. This fraction is an order of magnitude smaller than found for radio-loud, steep spectrum QSOs reported in the literature. Statistical tests indicate that Lyα luminosities in the extended nebulae are not correlated with the central QSO ionising flux. The extended nebulae luminosities are strongly correlated with their sizes, which suggests a difference in the surroundings. Also for the radio-loud objects reported in the literature the sizes appear to be correlated with the radio-power. Our observations hence suggest that very luminous extended Lyα nebulae seen around high redshift QSOs are intrinsically related to the radio emission.

[†] A version of this paper will be submitted to *Astronomy & Astrophysics*.

8.1 Introduction

Extended Lyα emission regions around high redshift QSOs are found for both radio-quiet QSOs (RQQs) (Bremer et al. 1992; Fried 1998; Møller et al. 2000; Bunker et al. 2003; Weidinger et al. 2004) and radio-loud quasars (RLQ) (Heckman et al. 1991a; Wilman et al. 2000). A radio-weak QSO in the Hubble Deep Field South has similar characteristics as the Lyα emission surrounding radio galaxies and RLQs (Bergeron et al. 1999). In a scenario where matter is falling into a potential well, Lyα photons are created via cooling processes. Emission from a QSO can greatly enhance the brightness of the emission. In a simple model of infalling material, Lyα emission should be detectable in a region of $\sim 3''$ around QSOs, equivalent to $\sim$20–25 kpc at $z \approx 3$, and with a typical surface flux density of $10^{-16} - 10^{-18}$ erg cm^{-2} s^{-1}arcsec^{-2} (Haiman & Rees 2001). Other investigations have reported companion Lyα emitting objects at the QSO redshifts and may be influenced by the QSO ionising radiation (Hu et al. 1996; Petitjean et al. 1996). Believed to contain obscured QSOs, radio galaxies also show very extended and quiescent Lyα emission line nebulae (Villar-Martín et al. 2003).

Strong asymmetric Lyα emission nebulae have been discovered to be common for lobe-dominated RLQs (Heckman et al. 1991b; Lehnert & Becker 1998). Specifically, these RLQs have a high frequency of extended Lyα emission aligned with the spatial orientation of the radio jets. Furthermore, these studies showed that the strongest line emission is mostly associated with the location of the stronger radio lobe. To summarise, extended Lyα emission line regions are present around different types of AGN at high redshifts, but what determines the properties has not been firmly established.

The unification scheme of AGN states that the observed characteristics depend on the orientation of the obscuring torus with respect to the sight line through the surrounding broad- and narrow-line regions (Barthel 1989). The Magorrian relation explains that the black hole mass is correlated with the bulge mass. Hence the luminosity of the AGN is related to the black hole mass when assuming that the accretion rate is a constant fraction of the Eddington accretion rate. This implies that equal luminosity AGN should harbor equal mass black holes. The fact that radio power is unrelated to either host galaxy masses or luminosities (Dunlop et al. 2003) suggests that a different mechanism is responsible for the radio loudness. Invoking a black hole spin could be the dominating factor (Blandford 2000), but this is still not know.

Studies of spatially extended Lyα emission have attempted to answer the question whether the emitting gas is infalling or outflowing. The mechanisms responsible for the emission can be radiation from massive stars in the host galaxy or scattered light from the AGN. These possibilities raise the fundamental question of QSO formation and AGN fueling. If the QSO emission is directed in a cone with some opening angle, the surface brightness profiles can be used as a proxy for the direction of the QSO emission cone (Weidinger et al. 2004, 2005).

In this paper we explore the correlation between radio power and Lyα emission nebulae around QSOs. Because of the unknown location of Lyα emission at the QSO redshift in the case of a highly asymmetric nebula integral field spectroscopy (IFS) is well suited. Previous IFS studies of extended line emission regions around RLQs have focused on optical emission lines from low redshift objects (e.g. Durret et al. 1994; Crawford & Vanderriest 2000). We investigate a sample of 7 bright QSOs at $2.7 < z < 4.5$ to look for extended narrow Lyα emission at the QSO redshifts. IFS is well suited for the purpose because of the possibility for creating narrow-band images at any suitable wavelength with an adjustable band width and to simultaneously investigate velocity profiles.

Throughout the paper, we assume a flat cosmology with $\Omega_\Lambda = 0.7$ and H_0=70 km s^{-1} Mpc^{-1}.

(1) Coordinate name	(2) Alt. name	(3) $z_{\rm em}$ (ref)	(4) $z_{\rm em}$ (cube)	(5) V (cube)	(6) seeing	(7) exptime (s)	(8) class
Q0953+4749	PC 0953+4749	4.457	–	R=20.0	1.0	16200	RQQ
Q1347+112		2.679	2.679	18.7	0.6	12600	RQQ
Q1425+606	SBS 1425+606	3.17	3.203	16.5	1.0	10800	RQQ
Q1451+1223	B1451+123	3.246	3.261	18.6	0.8	12600	RQQ
Q1759+7539	GB2 1759+7539	3.050	3.049	17.0	1.2	12600	RLQ
Q1802+5616	PSS J1802+5616	4.158	–	R=20.7	1.0	27000	RQQ
Q2233+131		3.298	–	18.3	0.7	18000	RQQ

Table 8.1. List of observed QSOs. Redshifts for the QSOs reported in the literature are compared to the redshift determined from the IFS data cube. The '–' signs in column 4 correspond to data where we could not determine the QSO redshift from the emission lines covered by the IFS. Redshifts derived from the IFS data correspond to vacuum corrected wavelengths. Column 5 gives the QSO magnitudes in the Vega system, and column 6 the seeing in arcseconds measured in the data cubes. Column 7 lists the total integration time and the last column report the class of object defined from radio observations.

8.2 Data set

Observations were done with the Potsdam Multi Aperture Spectrophotometer (PMAS) (Roth et al. 2005), mounted on the 3.5m telescope at Calar Alto during several observing runs in the period 2002–2004. The study was carried out in connection with a different programme to study emission from Damped Lyα absorbers (Christensen et al., 2005 in prep.; Chapter 5). Out of the original data set of 9 QSOs, 7 observations covered Lyα at the QSO redshifts in the spectral window. The DLA redshifts are different from the QSO redshifts and therefore emission lines at the QSO redshifts have an unambiguous origin. No attempts were made to make a systematic survey with unbiased selection effects, and therefore the sample contains one flat spectrum, core-dominate RQQ and six RQQs at $2.7 < z < 4.5$ as listed in Table 8.1. Furthermore, only observations of the 4 lowest redshift objects covered the wavelength of C IV λ1549 at the QSO redshift. Because of varying conditions, the total integration times for each objects were adjusted to give the same signal-to-noise levels in the data cubes, and sometimes the observations were even repeated.

Detailed descriptions of the data reduction and analysis are presented along with the Damped Lyα absorber study (Christensen at al, 2005, in prep.). In summary, after the data reduction each observation of the QSO is contained in a data cube of spatial dimensions of $8'' \times 8''$ arranged in 16×16 spectra. The spectral dimension has an interval in the range 1500 to 3000 Å and a spectral resolution of 3 and 6 Å was obtained for the two setups used. Wavelength calibration was done in the standard manner using exposures of emission line lamps. Errors in the wavelength calibration in the final data cubes are estimated from strong sky emission lines indicating typical uncertainties of 0.5 Å. Flux calibrations as well used standard procedures by observations of spectrophotometric standard stars at the beginning and the end of each night.

8.3 Analysis

This section describes the process used to detect extended emission line regions, and notes for each observed object. A detailed analysis of the two brightest nebulae is presented here.

8.3.1 Subtracting the QSO emission

Because the extended Lyα emission lines are narrower than the broad QSO emission lines and more extended than the nuclear continuum, subtraction of the QSO emission is necessary. Different methods for subtracting the QSO in the data cubes were investigated. The procedure that gave the smallest QSO subtraction residuals for the spectra and therefore used throughout the paper is described below. Alternatively, modeling of the QSO image PSF in each monochromatic slice was also investigated (e.g. Sánchez et al. 2004); the outcome gave similar results in terms of spectral properties.

From each reduced data cube a one-dimensional QSO spectrum was created by co-adding spectra from several fibres (equivalent to spatial pixel elements called "spaxels"), within a $2''$ radial aperture. For each spaxel we determined a scale factor between the total one-dimensional QSO spectrum and each individual spaxel in an interval bracketing the QSO Lyα emission line and subtracted it from the initial spectrum. To a first approximation this process created a data cube that retained the extended emission line region. To refine the process of finding pure emission lines, this emission line cube was subtracted from the original cube to create a cube with the QSO emission only. A new one-dimensional QSO spectrum was created, scaled to each spaxel and subtracted. The process was iterated until stable solution was found which occurred usually after 3 iterations only. In the end, the residual data cube where the QSO emission was subtracted contained narrow emission lines which did not contribute significantly to the total QSO emission.

To examine the data cubes for extended emission, narrow-band images were created choosing band widths corresponding to twice the measured *FWHM* of the emission lines and centered on the Lyα emission wavelength at the QSO redshifts. To find these widths, one-dimensional spectra associated with the emission lines were created first, and more spaxels were added if they showed up as bright points in the narrow-band images. This process was iterated interactively using the Euro3D visualisation tool (Sánchez 2004). Fig. 8.1 shows narrow-band images centered on the wavelengths where narrow Lyα emission was found. These Lyα emission images are on-band subtracted by off-band images, where the off-band images were created from adjacent wavelengths. The peak intensities were determined by fitting two-dimensional Gaussian functions in the on- and off-band images. Then the off-band image was scaled to the on-band peak and subtracted. We verified that the QSO spectrum subtraction technique gave similar results as the on-off band images for the location, extension, and morphology of the narrow Lyα emission region.

8.3.2 Notes on individual objects

A visual inspection of the data cubes before the QSO emission was subtracted gave no clear indication of whether extended emission was present or not. At $z > 3$ it is not expected to find extended continuum emission because much higher spatial resolution would be required (Jahnke et al. 2004). Because the continuum is undetected, the QSO emission subtraction method will not be affected by any underlying continuum emission. In this section the results are presented in detail for each individual object, and much of the description refers to the images and spectra in Fig. 8.1. Non-photometric conditions during the observations or intrinsic variability of the QSOs makes it difficult to determine whether spectrophotometric results were obtained, and flux uncertainties are estimated to be $\sim$20%.

Q0953+4749

Only the QSO Lyα and Lyβ emission lines are included the spectral window and both are affected heavily by absorption lines in the Lyα forest. Hence no attempt was made to estimate the QSO redshift from the data cube.

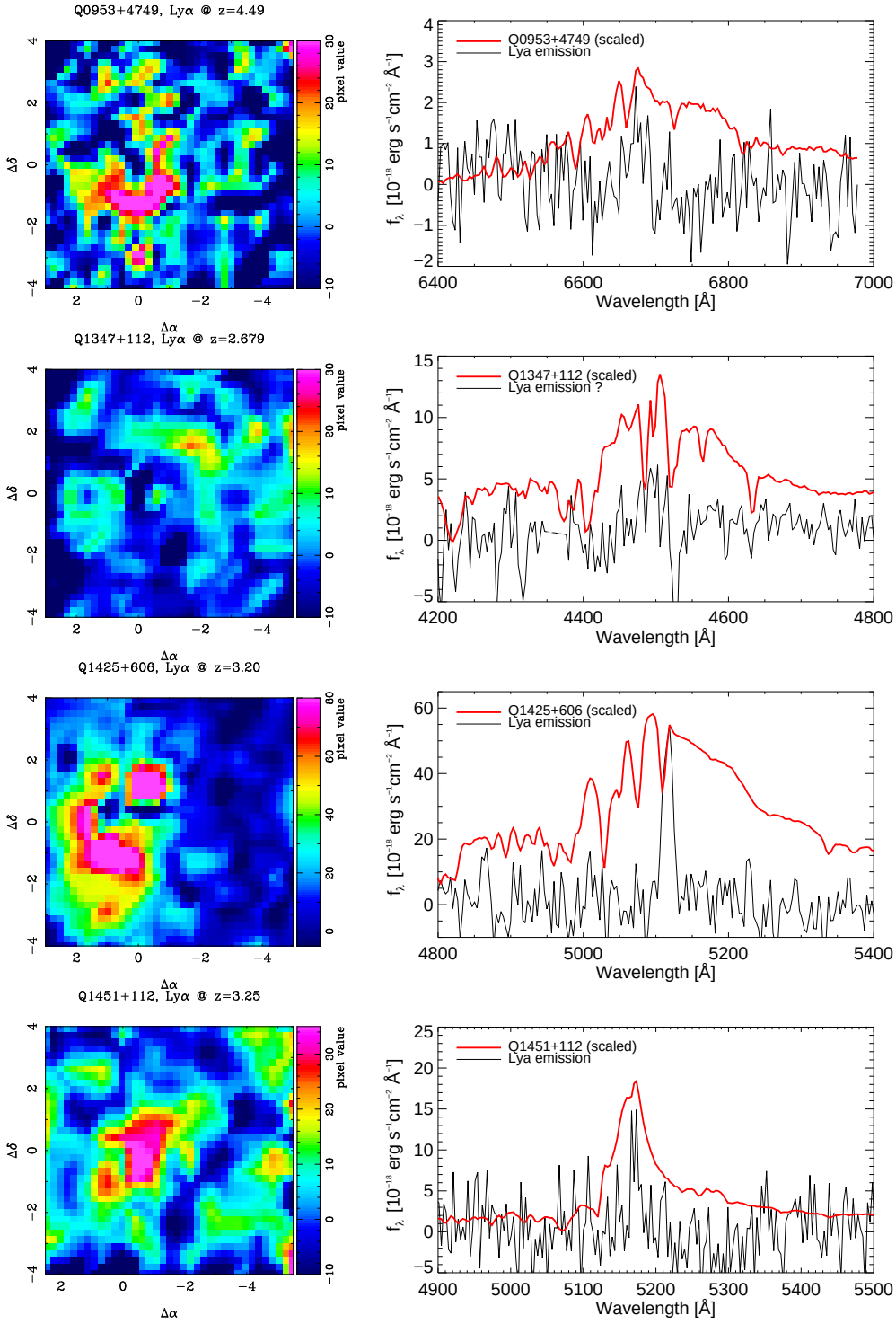

Fig. 8.1. Extended Lyα emission line regions at the QSO redshifts. *The left hand panels* show $8'' \times 8''$ narrow-band images created using a simple on-band minus off-band image technique. The centres of the QSOs are placed at the coordinates (0,0). All images are interpolated representations with pixel sizes of $0\farcs2$ with the orientation north up and east left. Bright QSOs have strong residuals within the central $1''$. The *Right hand panels* show the spectra of the extended narrow Lyα emission (thin line) compared with the QSO spectra scaled down by a factor of 40 (thick red line). The spectrum from Q1802+5616 was only scaled down by a factor of 3. No extended emission was found from Q1802+5616 and Q1347+112. Where found, the Lyα emission lines from the extended nebulae are clearly more narrow than the broad QSO lines.

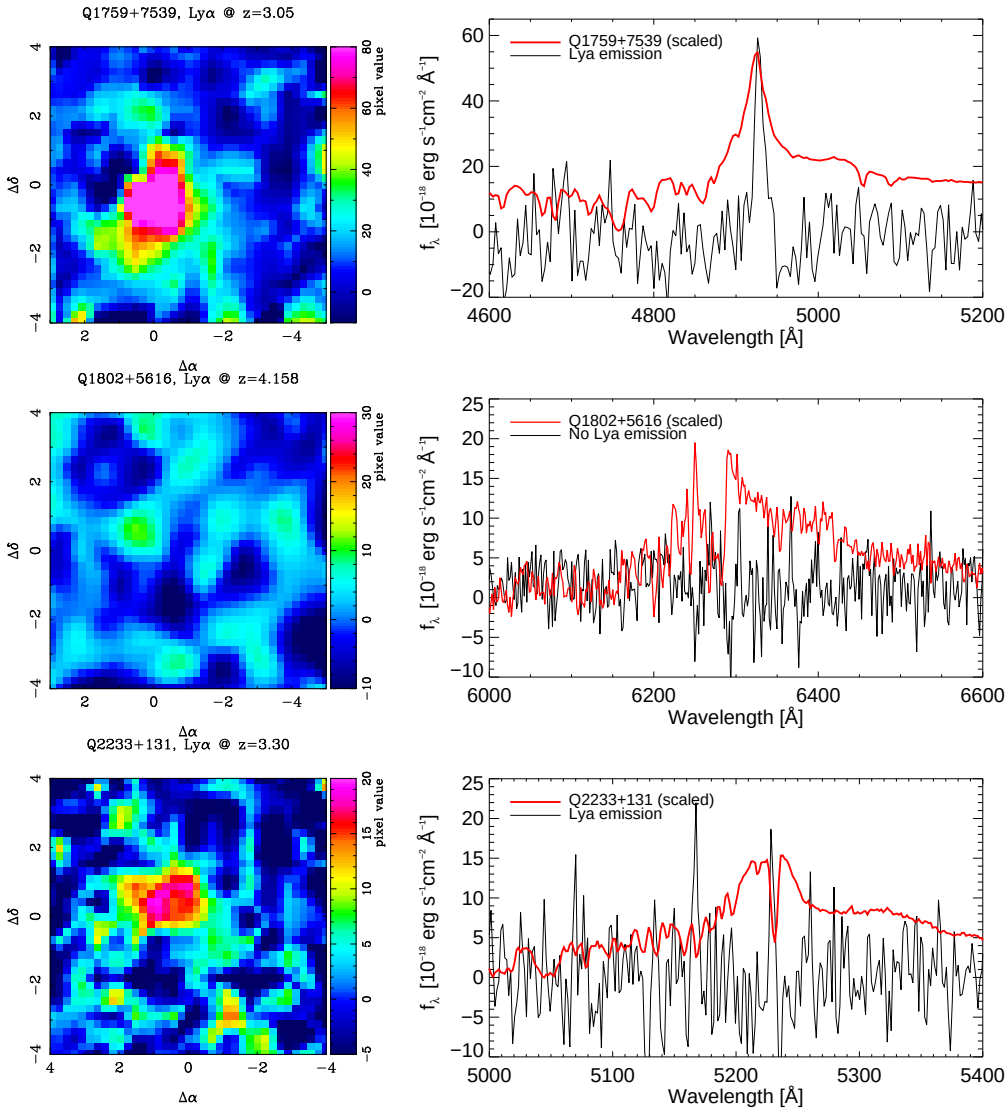

Fig. 8.1. *continued.*

Around Q0953+4749 we find extended narrow Lyα emission at 6670 Å as also reported in Bunker et al. (2003). The emission is mostly towards the south of the QSO. The signal-to-noise level in the data cube is too low to investigate the dynamics and morphology of this emission line region. Apparently the emission in Fig. 8.1 extends over 2″, but the exact extension is uncertain.

Q1347+112

Lyα emission from this QSO appears in a region of the CCD affected by a bad column, which after QSO subtraction cause a distinct structure extending over the field in a narrow-band image. This can be seen to the north-west of the QSO centre in Fig. 8.1. Furthermore, the emission line is coinciding with a faint sky emission line from which sky-subtraction residuals could be interpreted as narrow emission lines. Nonetheless, faint extended emission appears to be present, but the reality of it is questioned and any further analysis excluded.

Q1425+606

To estimate the QSO redshift a Gaussian function was fit to the O I λ1302 emission line which indicates $z_{\rm em} = 3.2030 \pm 0.008$. This is somewhat higher than $z = 3.17$ reported in the literature, which we also derive from the C II λ1335 and C IV λ1549 lines. As a reference we use $z_{\rm em} = 3.203$ because the O I line is a more reliable redshift indicator.

Q1425+606 has one of the brightest extended emission regions among the sample as shown in Fig. 8.1, and it is also the brightest QSO in the sample. It causes large QSO subtraction residuals, but these are at a level consistent with Poissonian statistics. Any narrow Lyα emission that may be present within a radius of 0.″5 from the QSO centre is heavily affected by these subtraction residuals, hence we do not recover the structure of the nebula here.

The Lyα emission is clearly asymmetric with most of the emission coming from a region to the south-east of the QSO. Co-adding spaxels in the region where the Lyα emission is brightest gives a spectrum with a Lyα emission line with a total line flux of $(7 \pm 1) \times 10^{-16}$ erg cm^{-2} s^{-1}. This emission line is much narrower than the Lyα emission from the QSO itself.

Q1451+112

The broad QSO Lyα emission line is strongly affected by absorption lines in the Lyα-forest. An estimate of the QSO redshift is difficult because the red wing of the O I λ1302 line is affected by residuals from the 5577 Å sky line. However, we adopt $z = 3.261$ estimated from this emission line. A lower redshift of $z = 3.2468$ is inferred from the C IV λ1549 line.

After QSO spectral subtraction a faint narrow emission line region is found extending to $\sim$2″ to the north-west and west of the QSO as seen in Fig. 8.1. This narrow emission line has $z = 3.2530$ implying a velocity difference of 700 km s^{-1} relative to the C IV line but a blue shift of 600 km s^{-1} relative to the O I line. Further analysis of the structure of the emission line region is not possible with the signal-to-noise level in the individual spaxels.

Q1759+7539

This object is the only RLQ in the sample with a core-dominated, flat-spectrum radio emission (Hook et al. 1996), and like Q1425+606 it is also very bright in the optical. A Gaussian fit to the QSO C IV emission line gives $z = 3.0486 \pm 0.008$, where the error includes the wavelength calibration error. The Lyα emission line gives a similar result; other emission lines are fainter or do not allow for a good determination of the redshift because absorption lines affect the line profiles.

The on–off band image in Fig. 8.1 shows the clear presence of an extended structure to the south-west of the QSO centre. Further analysis of the structure of the nebula was done using the same procedure as described for Q1425+606 and will be reported below.

Q1802+5616

No Lyα emission line nebula was found at the QSO redshift, but this is likely due to the faintness of the QSO. Its broad Lyα line is $\sim$40 times fainter than for the two bright QSOs in our sample. Thus if present, the Lyα emission line nebula should have a total flux of 3×10^{-17} erg cm^{-2} s^{-1} which below the detection limit in this data cube. This flux has been estimated applying a global scaling relation between the QSO emission and the extended narrow emission as detailed in Sect. 8.4. Because the QSO Lyα emission line falls close to the strong sky emission line at 6300 Å strong residuals are present and this object is not considered further here.

Q2233+131

Only the broad Lyα emission line from the QSO is within the spectral range and it is affected by both Lyα-forest lines and a strong Si II λ1260 absorption line associated with the DLA system. Therefore we rely on the literature value for the QSO redshift.

Referring to Fig. 8.1 again, after QSO subtraction we find an emission line object 1″ to the north-east of the QSO. To the limit of the detection this object does not appear to be very extended. Co-adding the spaxels within the nebula results in an emission line at 5227 Å, i.e. shifted by about +200 km s^{-1} relative to the QSO redshift. The strong feature in the spectrum at 5150 Å in Fig. 8.1 is caused by residuals of the blended night sky emission lines at 5149 and 5153 Å.

8.3.3 Velocity structures

For the two brightest nebulae we here proceed with a more detailed investigation of the velocity structures and morphologies.

We start with the pure emission line nebula around Q1425+606. For each spaxel we fitted a Gaussian profile to the spectrum around the expected position of the Lyα line using `ngaussfit` in IRAF. After an automatic fit to all spectra in the cube, the fit of each individual spectrum was checked interactively and corrected when obvious errors occurred. No constraints on the parameters in the fits were imposed. These fits were used to estimate for each spaxel the line flux, centroid, and *FWHM*. Results from these fits are show in Fig. 8.2 and are presented as maps that retain the individual spaxels rather than the interpolated images shown Fig. 8.1. Only spaxels that have sufficient signal to allow for a visual detection of an emission line are included. As a reference point for the velocity, shown in the upper left panel, we use the QSO redshift $z_{\rm em} = 3.203$ and find evidence for velocities of $\sim$600 km s^{-1} close to the QSO and decreasing to 100–200 km s^{-1} at a distance of 3.″5 from the QSO. In projection this corresponds to $\sim$ 25 kpc. Using instead the redshifts inferred from the C IV and C II lines implies velocity offsets of $\sim$3000 km s^{-1} at the center.

The surface brightness of the Lyα emission ranges from 2×10^{-16} erg cm^{-2} s^{-1}arcsec^{-2} close to the QSO to $\sim2\times10^{-17}$ erg cm^{-2} s^{-1} arcsec^{-2}, 3″ from the QSO. After correcting the measured *FWHM* for the instrumental resolution, we find typical line widths of 10–15 Å corresponding to a velocity dispersion of 600–900 km s^{-1}. No apparent structures are present over the face of the nebula as illustrated in the lower left panel. Some indications of smaller velocity dispersions closer to the QSO seems to be present, but the level of the uncertainty is high in this region due to QSO PSF subtraction residuals. In the upper right panel in Fig. 8.1 we show the flux in each spaxel overlayed by velocity contours.

The lower right hand panel in Fig. 8.2 shows the radial profiles of the velocity and Lyα surface brightness by points connected by solid and dashed lines, respectively. These profiles were derived at PA=135° east of north where the emission line region appears to have the largest extension. Values at each point are derived by adding values from 4 spaxels and the errors are estimated from the RMS deviations. Errors bars in the plot correspond to adding in quadrature the RMS deviations and typical errors for the velocity and line flux for a single spaxel. The surface brightness profile has an exponential scale length of $\sim$2.″5 corresponding to 20 kpc at the QSO redshift.

Subtracting the QSO PSF around the C IV emission line using a similar QSO subtraction procedure reveals no emission line in either narrow-band image or one-dimensional spectrum. We derive a 3σ upper detection limit of 4×10^{-17} erg cm^{-2} s^{-1} based on experiments with artificial emission lines in the extracted one-dimensional spectrum.

Similar maps of the velocity structures of the Lyα nebula around Q1759+7539 are presented in Fig. 8.3. The surface brightness shows clearly bright parts to the south-west of the QSO, but also to the east some fainter emission appears to be present. However, this is not clearly visible in the on–off band image in Fig. 8.1. Including the eastern part of the nebula, the total extension of the nebula

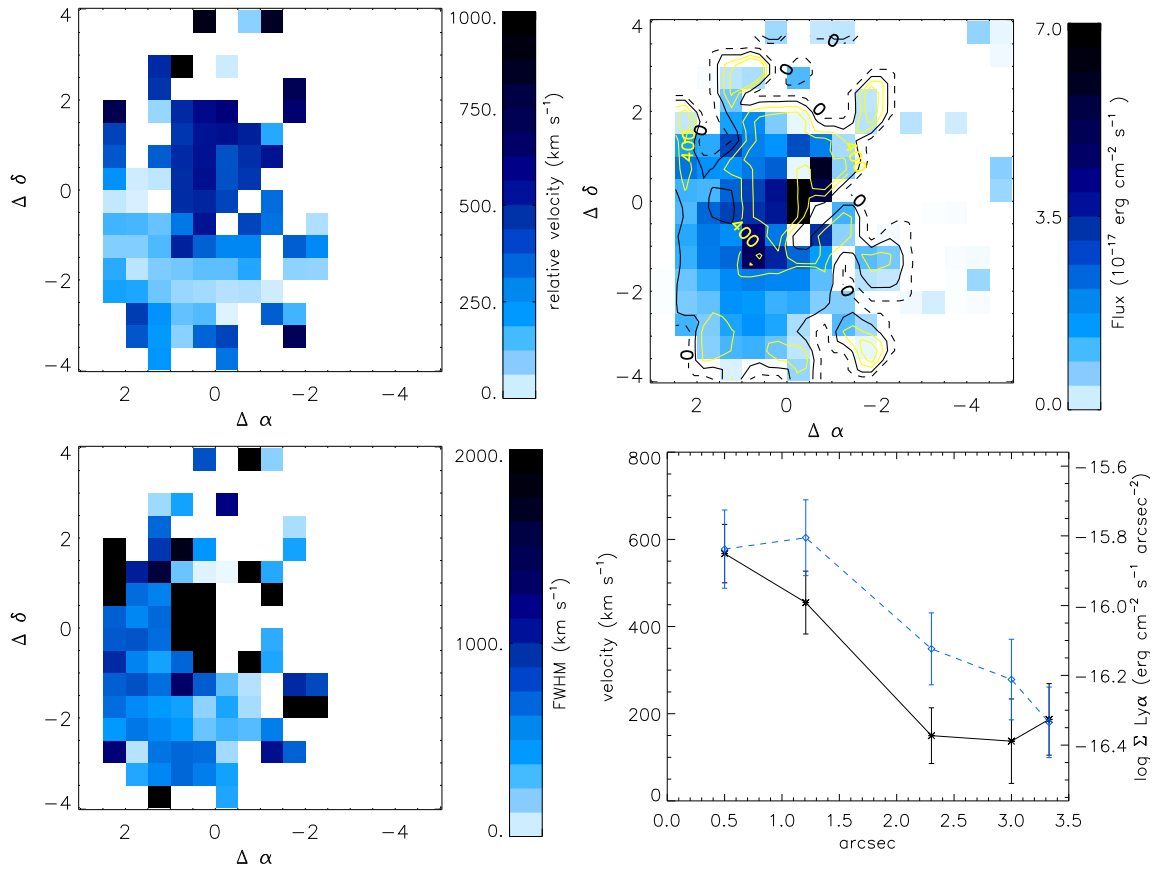

Fig. 8.2. Maps of derived properties for the Lyα emission nebula around Q1425+606. White fields correspond to spaxels where the Lyα emission line could not be recognised visually. *Upper left panel*: Map of the Lyα emission velocity relative to the QSO redshift. *Upper right panel*: Map of the integrated flux from each spaxel with smoothed velocity contours overlaid. *Lower left panel*: Map of the Lyα *FWHM* corrected for the instrument resolution. The *lower right panel* shows the radial profiles of the velocity component (solid line, left side axis) and Lyα surface flux density (dashed blue line, right axis) starting from the centre of the QSO along a direction with PA = 135° east of north. A fit of the radial surface brightness profile by an exponential function gives a scale length of $\sim 2\farcs5$ (20 kpc).

appears to be greater than $8''$ along the longest axis. Considering the bright part of the nebula along PA = 225°, the velocity increases with distance from the QSO although the uncertainties are large and the profile is consistent with a slope of zero within 1σ uncertainties. Furthermore, the analysis of the velocity structure is complicated by the complex velocity structure in the nebula as indicated by the velocity contours in the upper right panel. This is also the case for the *FWHM* in the lower left panel, where it is constant within errors at $\sim$450 km s^{-1} in the bright part of the nebula. The western part of the nebula shows similar velocities of 200$\pm$150 km s^{-1} relative to the QSO redshift but the *FWHM* is significantly larger: $>$ 1100 km s^{-1}.

The surface brightness profile has an exponential scale length of $1\farcs4$ corresponding to $\sim$10 kpc. This is smaller by a factor of two compared to the value estimated for the Q1425+606 nebula.

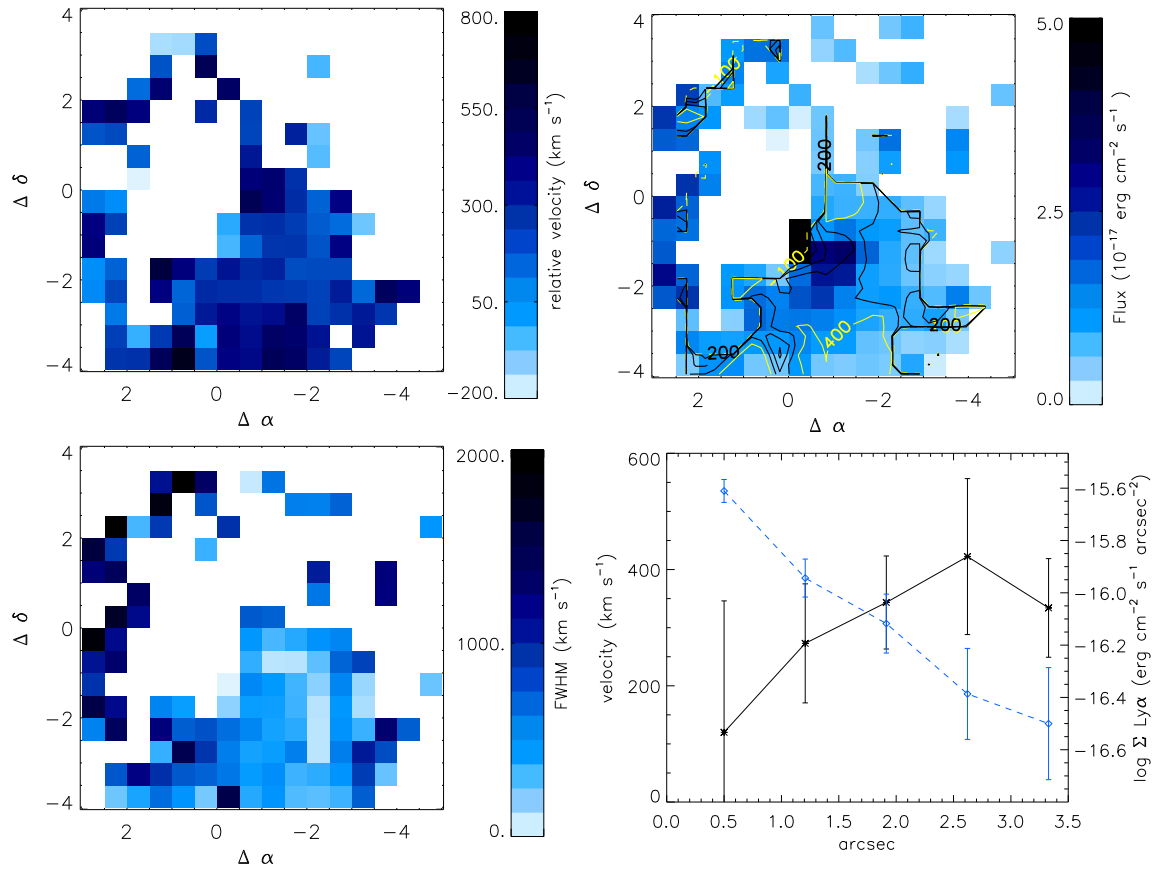

Fig. 8.3. Maps of the Lyα emission nebula surrounding Q1759+7539. The panels are similar to those described in Fig. 8.2. Profiles in the lower right panel are derived at PA = 225° east of north. A fit of an exponential function to the radial surface brightness profile gives a scale length of $\sim$1.″4 corresponding to 10 kpc at the QSO redshift.

8.4 Results

We detect extended Lyα emission for 5 of the 7 systems. It is possible that all 7 QSOs have extended emission, but one QSO is too faint, and the other is affected by a CCD defect at the wavelengths of interests. Compared to the broad Lyα emission lines from the core of the QSO, the nebulae have much narrower Lyα emission lines. The emission appears to be asymmetric and mostly one-sided, and the brightest extended Lyα emission nebulae are found around the brightest QSOs.

Table 8.2 summarises the properties for each object. Fluxes are corrected for galactic reddening using the dust-maps of Schlegel et al. (1998). Only for the two brightest objects the surface brightness could be measured. The maximum angular sizes of the nebulae are measured along the longest extension, and for the fainter Lyα emission regions the extension is estimated by the offset between the QSO centroid and the most distant emission seen in the IFS data. Errors of these values are comparable to the spaxel size, which at the QSO redshifts approximately sample 5 kpc. Velocity offset uncertainties listed in column 9 are mainly caused by uncertainties in the wavelength calibration leading to uncertainties for the derived redshifts of $\Delta z \approx 0.0005$. Velocity offsets are derived from the emission lines in the one-dimensional spectra, and therefore can differ from the velocities derived from the kinematical analyses.

(1) Name	(2) z (Lyα)	(3) V km s^{-1}	(4) Σ (Lyα) erg cm^{-2} s^{-1}($''$)$^{-2}$	(5) size kpc	(6) $f_{\rm tot}$ erg cm^{-2} s^{-1}	(7) $\log L_{\rm tot}$ erg s^{-1}	(8) *FWHM* km s^{-1}	(9) Δ V km s^{-1}
Q0953+4749	4.489			13	0.36 ± 0.17	42.9±0.3	1000	1800±200
Q1425+606	3.204	600–200	2×10^{-16}	34	9.8 ± 0.8	43.9±0.1	500	100±100
Q1451+122	3.253			15	1.8 ± 0.5	43.2±0.1	500	–600±100
Q1759+7539	3.049	200–300	3×10^{-16}	60	9.9 ± 1.6	43.9±0.1	450	0±100
Q2233+131	3.301			10	0.92 ± 0.43	43.0±0.3	<400	200±100

Table 8.2. Properties of the Lyα nebulae around the QSOs. Columns (1) list the names, (2) the redshifts derived from the narrow emission lines, (3) velocity relative to QSO redshift and its range, (4) peak surface brightness, (5) apparent extension of the Lyα nebula, (6) total Lyα flux from the nebula given in units of 10^{-16}, (7) total luminosity in the nebulae, (8) Emission line *FWHM* corrected for instrumental resolution, (9) Relative velocity offset between the narrow emission line and the QSO redshift. Fluxes have been corrected for Galactic reddening. An analysis of the surface brightness has been attempted only for the two objects with very bright nebulae.

8.4.1 Emission line flux

In a narrow-band imaging study of high redshift steep-spectrum, lobe-dominated RLQs Heckman et al. (1991b) (hereafter H91b) found that extended Lyα emission was a common feature around these objects. The extended Lyα emission flux contained ∼10–20% that of the QSOs within their filter width of 15 Å. To estimate the effect for the IFS data, we integrate the extended narrow-Lyα flux in the nebulae from Gaussian fits to the one-dimensional spectrum. To calculate the flux from the QSO in the same wavelength interval we integrate the one-dimensional QSO spectra from –10 Å to +10 Å centered on the narrow Lyα emission wavelength. The reason for choosing a filter width of 20 Å is due to the redshift difference between the two samples. All fluxes are corrected for Galactic extinction. In Fig. 8.4 we show the integrated extended nebula fluxes as a function of the constructed narrow-band QSO fluxes. We find that the flux in the extended emission represents approximately 1–2% of the QSO flux. For comparison the Lyα emission line fluxes in the H91b sample are shown by the filled squares in Fig. 8.4 which demonstrates that for a given QSO flux, more flux is found in the extended nebulae around RLQs relative to RQQs. We see that the narrow-band Lyα flux from the QSOs span the same range in the two samples, but the IFS data have extended Lyα nebulae approximately an order of magnitude below that of the H91b sample. Arrows in the figure indicate upper limits to the detection of extended Lyα emission.

Sensitivities in the two studies reach about the same levels of 1×10^{-17} erg cm^{-2} s^{-1} arcsec^{-2}, and H91b uses narrow-band filters with a width of 15 Å which corresponds to the width we use for the calculation of the fluxes. Therefore, the two studies are directly comparable. Because of the cosmological dimming of $(1+z)^4$, the redshift differences between the two samples has an effect on the extension of the nebulae emission. The H91b sample which has a median redshift of 2.2, effectively can measure emission which is a factor of $(1+3.11)^4/(1+2.2)^4 = 2.7$ fainter than in the IFS study. Even considering this fact, the median extension in the H91b sample is 11$''$ (or 90 kpc in the adopted cosmology), which is significantly larger than the extensions found here ∼4$''$ (or ∼30 kpc at $z = 3$). This seemingly consistent difference between the two samples of RLQs and RQQs could be caused by intrinsic properties. A counter-example which suggests that the picture is less simple, is the strong very extended Lyα emission seen for a radio-weak QSO but this could be an example of a transition object (Bergeron et al. 1999).

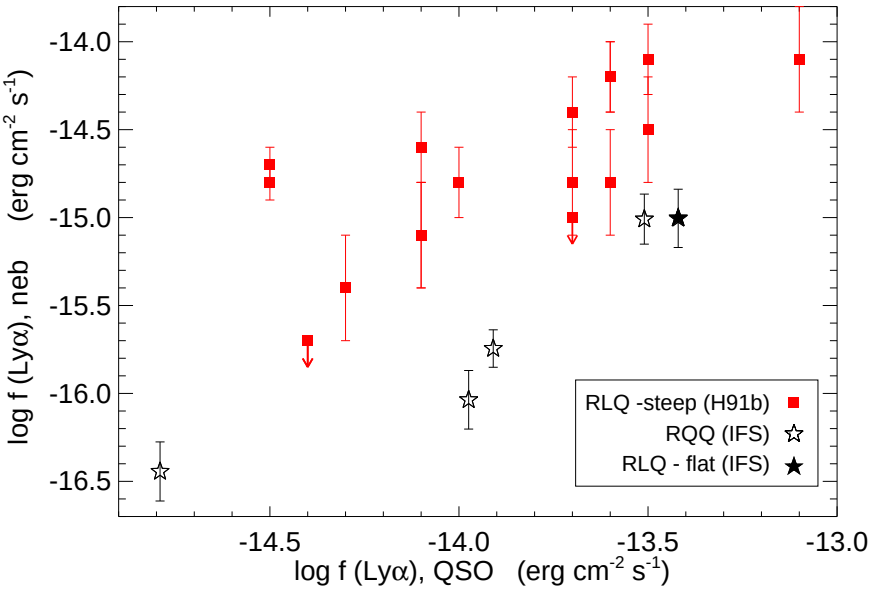

Fig. 8.4. Integrated Lyα emission line flux from the extended nebulae as a function of the flux from the QSO within a 20 Å wide band. The IFS results are indicated by stars, where the filled star represents the one core-dominated RLQ, and the outlined stars the four RQQs. Squares represent the emission line nebulae seen surrounding 18 lobe-dominated RLQs from the sample in H91b (some of the points overlap in this figure). Arrows indicate upper limits for objects where no extended Lyα emission was found. The correlation for the RLQ has a flatter slope than for the RQQs, but are consistent with having the same slope within errors.

8.4.2 Emission line luminosities

We investigate whether the redshift differences between the two samples cause any effect. Using line fluxes reported above we calculate the luminosities for the given cosmology. Similar results are obtained with the luminosities as indicated in Fig. 8.5. This figure shows that within the uncertainties for the scaling correlations, the total luminosities in the Lyα nebulae from RLQs are consistent with being 10 times brighter relative to those from RQQs.

Simple statistical tests support that there is a linear relation for the RQQs and the one RLQ from the IFS sample in Fig. 8.5. A Pearson test gives a correlation coefficient of 0.91$\pm$0.05 for a linear correlation, where the error bar is derived by boot strapping techniques by adding random values corresponding to the uncertainties for the luminosities. Here the uncertainty of the QSOs luminosities are assumed to be pure Poissonian. A corresponding analysis for the RLQs gives a moderate linear correlation coefficient of 0.63$\pm$0.06, where the non detections in H91 are excluded. For the full sample of 20 objects we find no obvious correlation, and a correlation coefficient of 0.35$\pm$0.05. The non detections can be included in a generalised Kendall test, which rejects the null hypothesis that a correlation is not present with a probability of 96%.

To test whether there is a factor of 10 in difference between the luminosities of the Lyα nebulae for the two samples, the luminosities from the IFS data were multiplied by 10. The test then gives a correlation coefficient of 0.78 and the generalized Kendall test gives a probability of 99.98% for a correlation. Hence, these simple statistical tests justify the qualitative description of the difference for the two samples given above.

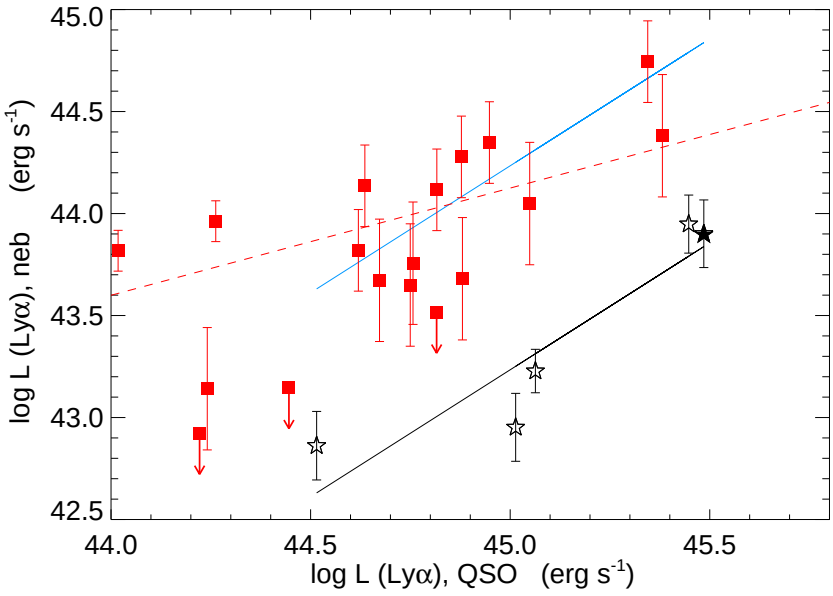

Fig. 8.5. Integrated Lyα emission line luminosities for the extended nebulae corresponding to the points in Fig. 8.4, and the symbols shapes are similar to Fig. 8.4. The solid black line gives a fit to the IFS data and the dashed red line a fit to the RLQs. Within errors, the relation is consistent with being a factor of 10 brighter than for the IFS data as indicated by the solid blue line.

8.4.3 Quasar luminosities

To investigate whether the QSO ionising radiation has an effect, we first estimate the continuum ionising flux from the QSO. We take the UB or V magnitudes reported for the QSOs in the literature, and use a QSO template spectrum to calculate a K-correction between the observed band and the rest frame flux at 912 Å to calculate the quasar luminosities. The templates spectrum used is a hybrid of the SDSS composite spectrum (Vanden Berk et al. 2001) and the composite FUSE spectrum (Scott et al. 2004). For the Q0953+4749, its reported V band magnitude is heavily affected by absorption in the Lyα forest. At $z = 4.489$ the mean transmission in the Lyα forest is 0.33 (Songaila 2004), thus we adopt a correction of 1.2 magnitudes in addition to the K-correction. Most other quasars have magnitudes measured slightly to the red of the Lyα emission lines, or the transmissions bluewards of the Lyα lines are not as strongly affected at $z \approx 2$. Figure 8.6 shows the luminosities of the extended Lyα nebulae as a function of the predicted quasar luminosities at 912 Å. Symbol shapes are similar to the previous figures.

Taken at face value irrespectively on the small number statistics, the RQQs are offset to brighter nuclear powers, but this is a selection effect, because the quasars observed here were required to be bright. The one RLQ in the IFS sample has properties similar to the RLQs in the H91b sample. One may argue that the flux in the extended emission is independent on the nuclear emission for the total sample of quasars. Similar results were reached using K-corrections to estimate the luminosities at rest-frame 1450 Å, showing that the results are independent on the specific point of reference.

Additionally we investigate how the total quasar Lyα fluxes correlate with the predicted quasar luminosities. There appears to be a correlation that quasars with brighter 912 Å continuum emission also have brighter Lyα emission (estimated within the 20 Å wide band). Considering the RLQ in the H91b sample only, a Pearson test gives a correlation coefficient of –0.73, while the total sample has a correlation coefficient –0.57$\pm$0.03. Again Poissonian uncertainties are assumed and bootstrap

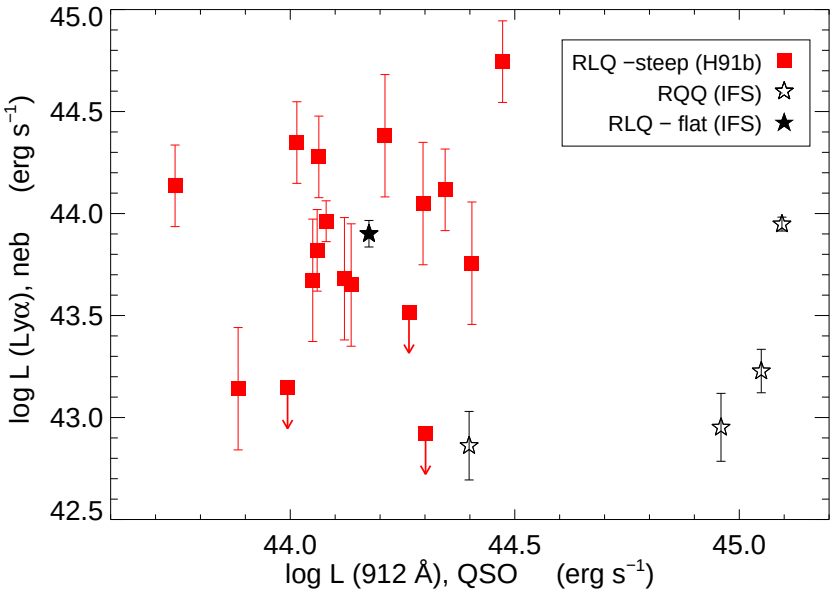

Fig. 8.6. Extended Lyα emission line luminosities as a function of the predicted quasar luminosities at the rest-frame 912 Å. There is no significant correlation between the extended emission line luminosities and the nuclear luminosities.

tests used to derive errors.

8.4.4 Lyα nebula extension

The median size in the H91b sample is ∼90 kpc which is significantly larger than the ∼30 kpc found for the less bright nebulae in the IFS data. The upper panel in Fig. 8.7 shows the total flux in the nebulae as a function of the apparent maximum projected angular size, and in the lower panel the fluxes are converted to luminosities. Smaller nebulae have smaller total fluxes whereas RLQs from H91b are larger and brighter. A Pearson test to the distribution of fluxes in the total sample gives a correlation coefficient of 0.73±0.06 (in the upper panel), whereas the luminosity-size distribution has a correlation coefficient of 0.44±0.03 (lower panel).

Morphologically there could be a difference between the RQQs and RLQs as also pointed out in Haiman & Rees (2001). For the RQQs in this IFU study we find evidence for one-sided emission only. Such a one-sided emission was also observed for another RQQ (Weidinger et al. 2005). In comparison, the Lyα nebulae around the RLQs in the H91 study are asymmetric but clearly not always one-sided. Similarly, the one core-dominated RLQ in Fig. 8.3 shows possibly emission on both sides of the QSO.

8.4.5 Correlations including errors

The treatment of the properties described above avoided the upper limits measured for three of the RLQs. Here we use a generalised Kendall tests, which allows a treatment of limits as well. Tests performed here relate to the correlations studied in the previous section, and Table 8.3 reports the probabilities for the null hypothesis that no correlation exists. Only correlations giving probabilities above 98% are considered as indications of a correlation. The purpose is to determine what could be fundamental relations that govern the observed properties of the emission line nebulae.

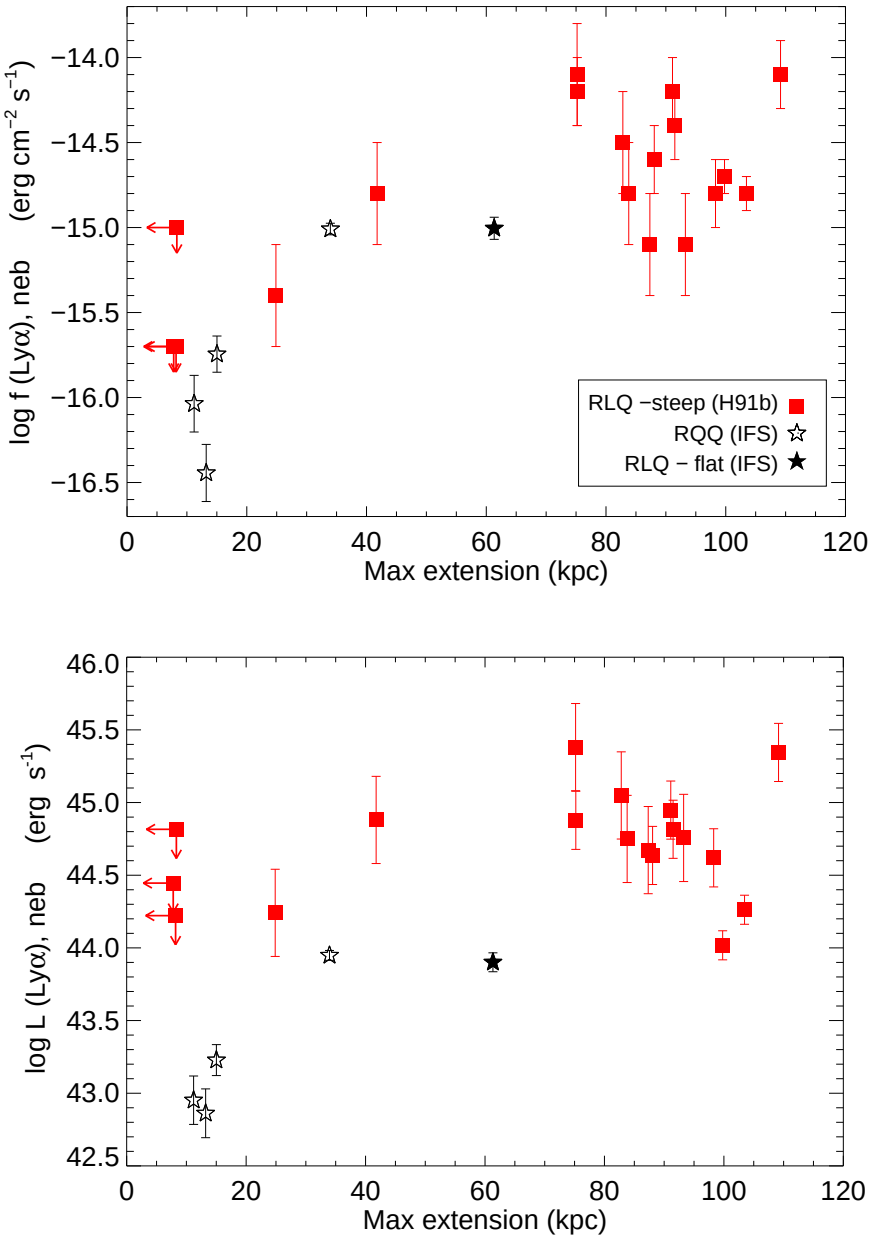

Fig. 8.7. The upper panel shows the total nebula fluxes as a function of the maximum projected sizes for the Lyα nebulae and the lower panel the same after converting the fluxes to luminosities. Symbols shapes are similar as in Fig. 8.4 and arrows indicate upper limits.

In summary, for the tests we use the total Lyα luminosity in the extended nebulae ($L_{\mathrm{Ly}\alpha,\mathrm{neb}}$), the total flux from the QSO within the 20 Å band centered on the Lyα line ($L_{\mathrm{Ly}\alpha,\mathrm{QSO}}$), the maximum extension of the extended Lyα nebulae (size), and the predicted quasar luminosities at the rest frame 912 Å ($\mathrm{L}_{\mathrm{QSO},912}$).

The indication of a correlation between the QSO Lyα luminosity and the luminosities at 912 Å could be caused by the fact that both are measuring the rest frame emission from the QSO since the luminosities at 912 Å are derived using a single QSO template. Otherwise the luminosities at 912 Å

	$L_{\mathrm{Ly}\alpha,\mathrm{neb}}$	size	$\mathrm{L}_{\mathrm{QSO},912\mathrm{\AA}}$
$L_{\mathrm{Ly}\alpha,\mathrm{QSO}}$	0.038 (0.617)	0.634 (–0.142)	0.007 (–0.814)
$L_{\mathrm{Ly}\alpha,\mathrm{neb}}$	...	0.002 (0.948)	0.790 (0.079)
size	...	...	0.290 (0.316)
P(5 GHz)	0.098 (0.490)	0.017 (0.712)	0.095 (0.498)

Table 8.3. Generalized Kendall's test probabilities for the null hypothesis that no relation exists between any two given quantities for a sample that includes the IFS objects and the RLQs in H91b. The values in brackets give the correlation coefficients. The observed properties involved here are: the total luminosity in Lyα in the extended nebulae ($L_{\mathrm{Ly}\alpha,\mathrm{neb}}$), the flux from the QSO within a 20 Å wide band ($L_{\mathrm{Ly}\alpha,\mathrm{QSO}}$), the maximum extension of the extended Lyα nebulae (size), the quasar luminosities estimated at the rest-frame 912 Å, and the total radio power at 5 GHz (for the RLQs only).

do not show strong correlations with neither nebulae sizes nor luminosities.

The nebula sizes have the strongest correlation with the nebula Lyα luminosity. This simply implies that more luminous nebulae have larger sizes, which is also shown in Fig. 8.7. A somewhat weaker correlation exists between the QSO Lyα luminosity and the nebula Lyα luminosity as also described in the previous section.

Furthermore, we briefly investigate whether there are any relations with the radio power at 5 GHz reported in the NED database for the RLQs. As indicated in Table 8.3 the only correlation that is present is with the size of the Lyα nebulae.

8.5 Discussion

We have presented evidence for differences in the extended Lyα nebulae around RQQs in the IFS sample when compared to RLQs investigated in the literature. The extended Lyα emission around RLQs was shown to be a factor of $\sim$10 fainter than the nuclear emission (H91b), whereas the nebulae around the RQQs studied with IFS are $\sim$100 times fainter than the quasar luminosities within a 20 Å wide band. This significantly fainter emission from two RQQs has been suggested to be caused by a smaller covering factor of the neutral material around the RQQs (Bremer et al. 1992). In this context it is possibly a coincidence, that the one flat-spectrum RLQ in the IFS sample appears to have a luminosity similar to the brightest RQQ, while its luminosity at 912 Å and the linear nebula size is more similar to the RLQ sample. Investigations of the linear sizes of the nebulae around the two samples provide further evidence for differences where the nebulae from RLQs are found to be larger than from the RQQs.

Which are the effects that cause these distinct properties? Firstly, the quasar ionising flux could be the main factor determining the nebula luminosity. In this case it is expected that the continuum luminosity from RLQs is brighter than from RQQs, which is in contradiction with the predicted 912 Å luminosity. The statistical tests give no evidence for a correlation of the line emission with the quasar ionising flux.

Secondly, we investigate the velocities inferred from the line widths which could suggest a disturbed medium. In the H91b sample of RLQs the measured nebular Lyα line widths are $700 - 1000$ km s^{-1}, which is slightly larger than the $\sim$500 km s^{-1} found in this IFS study. Radio galaxies show Lyα line fluxes similar to the bright objects in this sample and have similar velocity dispersions of about 1000 km s^{-1} (van Ojik et al. 1997). Nevertheless, the possible small differences should be studied in more detail to find whether there are differences in the environment.

Alternatively, external conditions could be responsible for the flux differences. One could speculate that the RQQs reside in less dense environments, but this appears to be in contradiction

with the conclusion that there are no differences between the host galaxies of the two populations at low redshifts (Dunlop et al. 2003). However, that study focused on the stellar light whereas we look at the neutral gas traced by emission lines. Higher spatial resolution images in a larger field are needed, e.g. with the HST to study potential environmental differences in detail. Differences in the environment could affect the Lyα emission we detect. We know that the Lyα flux detected is a strict lower limit because of resonance scattering and dust absorption. Indeed we find evidence for this in the brightest emission lines which show red asymmetries.

Observations have shown that lobe-dominated RLQs have Lyα emission nebulae which are aligned but not exactly correlated in location with the lobes (H91b). Also optical emission line regions do not always show obvious alignment with the radio emission (Crawford & Vanderriest 2000). This suggests that the radio emission simply traces the direction of the AGN ionising cone, but that an interaction between the radio-jet and the environment is not necessarily the cause. For RQQs, the radio emission is typically 2–3 orders of magnitude fainter than for RLQs. If an interaction with a faint radio jet would be solely responsible for the Lyα nebulae in the RQQs, the Lyα emission should be much fainter than that observed.

The AGN unification scheme states that the different radio properties of radio-loud objects are related to their viewing angle (Barthel 1989), and core-dominated RLQs have jets very close to the sight line. Assuming that external conditions are similar for the two bright emission nebulae studied here, a difference in viewing angle is supported by the observed scale lengths in the surface brightness profiles. The smaller scale-length of the nebula related to the core-dominated RLQ would be consistent with the ionising emission from the QSO having an orientation closer to the sight line than for the RQQ.

Extended C IV and He II emission has been observed in one RLQ associated with Lyα emission (Lehnert & Becker 1998), but most RLQs only have upper limits for the C IV line flux (Heckman et al. 1991a). For the two brightest objects considered here, where the tightest constraints can be made, we find upper limits of the flux ratio f(C IV)/f(Lyα)$<$0.04. This ratio is smaller than found for any radio galaxy, and could again be caused by a difference in the viewing angle (Villar-Martin et al. 1996). Another explanation is that the objects studied here have less metal enriched surroundings, i.e. again suggesting that the environment is affected.

8.6 Summary

We have investigated a sample of seven bright high redshift QSOs using integral field spectroscopy with PMAS to examine extended Lyα emission at the QSO redshifts. The sample is taken from a different study of intervening damped Lyman α systems such that the sample selection is not well defined. Primarily, the QSOs studied here are bright and have $2.7 < z < 4.5$. Five QSOs in this sample have sufficiently good signal, and show evidence for asymmetric (mainly one-sided) extended emission. The remaining two are either too faint to allow for detection of extended emission or affected by a CCD defect. Of the five objects studied, four are radio-quiet QSOs. Compared to the broad QSO Lyα emission lines, the extended emission regions clearly have smaller velocity dispersions suggesting velocities of $\sim$500 km s^{-1}. The two brightest QSOs (Q1425+606 and Q1759+7539 with $V \approx 16$ and 17, respectively) show the brightest extended emission; the first is radio quiet, the second radio-loud with a core-dominated radio morphology. The brightest emission in these nebulae is around 2–3$\times10^{-16}$ erg cm^{-2} s^{-1} arcsec^{-2} and extending to $\sim$4″, which confirms the theoretical prediction in Haiman & Rees (2001). Beyond 4″ the emission line nebulae are fainter than the detection limit in the integral field data. However, the field of view of 8″$\times$8″ of the IFS data does not allow us to study the nebulae at larger distances.

We find a correlation between the total narrow Lyα flux in the extended nebulae and the flux from the QSOs within at 20 Å wide band centered on the Lyα emission lines. The extended emission line nebulae contain 1–2% of the QSO flux, which is an order of magnitude smaller than the $10-20$% found for RLQs in the literature (H91b). On the other hand, the nebula sizes analysed here are a factor of a few smaller than detected around RLQs. These results indicate that apart from the radio flux from AGN, also the extended emission line regions differ between loud and quiet objects. The radio-loud core-dominated QSO in our sample has Lyα properties similar to the bright radio-quiet QSO. These results suggest that the extended radio lobes, or alternatively the same process that creates these, is responsible for the main fraction of Lyα line emission in steep-spectrum, lobe-dominated RLQs. For RQQs (and one core-dominated RLQ) the fainter emission could be caused by the ionising flux from the QSO alone.

Statistical tests were performed to demonstrate that there is a correlation between properties measured for the objects. We compared correlations between the nebulae Lyα luminosities, sizes, the QSO luminosities at 912 Å, a constructed QSO Lyα narrow-band luminosity, and the radio power reported in the literature. These tests indicate that the extended nebulae are not correlated with the QSO ionising flux, represented by the predicted luminosities at 912 Å. A strong correlation between the nebulae Lyα luminosity and the maximum sizes suggests that environmental differences could be an important factor. For the RLQs only, the extension is correlated with the radio power, which on the other hand suggests that the radio power emitted by the QSOs has an effect on the environment. However, then Lyα emission would be expected to always be aligned with the radio emission, which is not the case.

Integral field spectroscopy appears to be ideally suited to examine the structure of the narrow emission line regions around bright QSOs. A future investigation should examine a sample of RLQs and RQQs at similar redshifts using the same technique to study the interaction between the radio power, morphology, and the optical properties of the extended emission line nebulae.

Acknowledgments. L. Christensen acknowledges support by the German Verbundforschung associated with the ULTROS project, grant no. 05AE2BAA/4. K. Jahnke acknowledges support from the DFG.

References

Barthel, P. D. 1989, ApJ, 336, 606
Bergeron, J., Petitjean, P., Cristiani, S., et al. 1999, A&A, 343, L40
Blandford, R. D. 2000, in Astronomy, physics and chemistry of H_3^+, 811
Bremer, M. N., Fabian, A. C., Sargent, W. L. W., et al. 1992, MNRAS, 258, 23
Bunker, A. J., Smith, J., Spinrad, H., Stern, D., & Warren, S. 2003, Ap&SS, 284, 357
Crawford, C. S. & Vanderriest, C. 2000, MNRAS, 315, 433
Dunlop, J. S., McLure, R. J., Kukula, M. J., et al. 2003, MNRAS, 340, 1095
Durret, F., Pecontal, E., Petitjean, P., & Bergeron, J. 1994, A&A, 291, 392
Fried, J. W. 1998, A&A, 331, L73
Haiman, Z. & Rees, M. J. 2001, ApJ, 556, 87
Heckman, T. M., Lehnert, M. D., Miley, G. K., & van Breugel, W. 1991a, ApJ, 381, 373
Heckman, T. M., Miley, G. K., Lehnert, M. D., & van Breugel, W. 1991b, ApJ, 370, 78
Hook, I. M., McMahon, R. G., Irwin, M. J., & Hazard, C. 1996, MNRAS, 282, 1274
Hu, E. M., McMahon, R. G., & Egami, E. 1996, ApJL, 459, L53
Jahnke, K., Sánchez, S. F., Wisotzki, L., et al. 2004, ApJ, 614, 568
Lehnert, M. D. & Becker, R. H. 1998, A&A, 332, 514

Møller, P., Warren, S. J., Fall, S. M., Jakobsen, P., & Fynbo, J. U. 2000, The Messenger, 99, 33
Petitjean, P., Pecontal, E., Valls-Gabaud, D., & Charlot, S. 1996, Nature, 380, 411
Roth, M. M., Becker, T., Bauer, S.-M., et al. 2005, PASP, accepted
Sánchez, S. F. 2004, AN, 325, 167
Sánchez, S. F., Garcia-Lorenzo, B., Mediavilla, E., González-Serrano, J. I., & Christensen, L. 2004, ApJ, 615, 156
Schlegel, D. J., Finkbeiner, D. P., & Davis, M. 1998, ApJ, 500, 525
Scott, J. E., Kriss, G. A., Brotherton, M., et al. 2004, ApJ, 615, 135
Songaila, A. 2004, AJ, 127, 2598
van Ojik, R., Roettgering, H. J. A., Miley, G. K., & Hunstead, R. W. 1997, A&A, 317, 358
Vanden Berk, D. E., Richards, G. T., Bauer, A., et al. 2001, AJ, 122, 549
Villar-Martin, M., Binette, L., & Fosbury, R. A. E. 1996, A&A, 312, 751
Villar-Martín, M., Vernet, J., di Serego Alighieri, S., et al. 2003, MNRAS, 346, 273
Weidinger, M., Møller, P., Fynbo, J. P. U., & Thomsen, B. 2005, A&A, 436, 825
Weidinger, M., Møller, P., & Fynbo, J. U. 2004, Nature, 430, 999
Wilman, R. J., Johnstone, R. M., & Crawford, C. S. 2000, MNRAS, 317, 9

CHAPTER 9

Conclusions and perspectives

9.1 Summary

We here summarise the main conclusions that were found in this thesis. Conclusions from the individual studies are presented at the end of each chapter and will not be repeated here. Instead this chapter presents a broad discussion and describes future studies.

9.1.1 DLA galaxy metallicities

In a few cases studied to date, abundances for the DLA galaxies derived from strong emission line diagnostics show values significantly higher than the corresponding DLA cloud metallicities found from absorption lines. As suggested in Chapter 2 the inferred metallicity for the sub-DLA towards PHL 1226 is very likely to be smaller than the solar metallicity found for the host galaxy. Similar conclusions have been inferred for other DLA system (Ellison et al. 2005; Chen et al. 2005). One can estimate the average metallicity gradient in DLA galaxies by comparing the DLA metallicity with the impact parameter measured for the DLA galaxies. Chapter 5 investigated this for 8 candidate DLA galaxies and found only a small gradient detected at the 2σ level. Nevertheless, this study ignored depletion effects, and we conclude that this type of investigation will be improved with a larger sample of confirmed DLA galaxies.

QSO lines of sight probe randomly the distribution of neutral gas in the Universe, and hence should intercept DLAs with high metallicities as well. Because these solar metallicity absorbers are missing in current DLAs studies, this discrepancy points to a bias against high metallicity DLAs in QSO surveys. It has been shown in the literature that dust has a minor effect on the DLA surveys and that at most 50% of DLAs are missing. Nevertheless, the column density weighted metallicities are dominated by the highest column density absorbers, and if some are indeed missing the average metallicities in DLAs will be biased towards smaller values.

We also noted that the galaxies at high redshifts ($z > 2$) selected from flux-limited surveys have on the average higher star-formation rates than found for DLA galaxies. Since these galaxies have the highest star-formation rates (SFRs) they are also expected to have the highest column densities (log $N(\mathrm{H\,I})$>22 cm^{-2}) if the Schmidt-Kennicutt law can be extended to high redshift objects. Because these high column density DLAs are missing the the surveys, this is another indication that DLA surveys could be biased. However, very high column density absorbers are rare. Out of 1000 we would expect to find just one, but with the Sloan Digitized Sky Survey sample of QSO spectra, we are getting near to this number.

IFS surveys

We showed that optical emission lines from $z < 1$ galaxies can be identified, and can give redshifts consistent with those reported in the literature. None of these detections were significant, though, and most were only detected below 5σ levels. A notably exception is of course the very bright (V$\sim$ 19) sub-DLA galaxy towards PHL 1226 treated in Chapter 2.

As shown in Chapter 3 and 5, integral field spectra from the instruments PMAS and INTEGRAL, can be used to find faint emission lines from DLA galaxies. It was pointed out that a follow-up investigation is necessary to confirm the Lyα emission candidates. This goes against the idea that IFS avoids the two step procedure to confirm emission line objects, but this study was carried out at the detection limit of an integral field unit on a 4m class telescope. If the emission lines properties found here are confirmed by deeper observations, it is certain that with current integral field spectrographs on 8m class telescopes a similar project will be able to identify DLA galaxies based on IFS only.

Building upon the knowledge from the study of spectroscopically confirmed objects known previously, we identified 4 and 8 new candidate emission line objects at $z < 1$ and $z > 2$, respectively. In both Chapters 3 and 5 we analysed the candidate impact parameters as a function of the column densities of the central DLAs (and sub-DLAs). A fit of exponential profiles indicated in both cases that an average disc scale length of $\sim$5 kpc can describe the measured impact parameters. Such a result could indicate that DLA galaxies comprise a single population of large disc galaxies similar to local, late type discs. It is important to note that we are only dealing with objects detected from their *emission lines*, while other objects from the literature fall out of this relation (Turnshek et al. 2001; Chen et al. 2005). Nevertheless, there appears to be a strong anticorrelation between the two properties as was previously known to exist for lower column density absorbers (Chen et al. 2001).

We used the study of the DLA galaxy sizes to derive masses of neutral hydrogen in the discs. Because the scale length of DLA galaxies appear on the average to be similar to local galaxies, it follows naturally that they should have H I masses similar to local disc galaxies. Combining this information with results from numerical simulations we suggested that high redshift galaxies need not be luminous L^* galaxies. This conclusion is in agreement with the predicted luminosities for the DLA galaxies when adopting the scaling relation taken from the literature for low redshift DLA galaxies. These results were used for further speculations about the nature of DLA galaxies in Chapter 6. We used the candidate emission line fluxes to estimate the DLA galaxy star formation rates, and showed that these were consistent with the expectations if the Schmidt-Kennicutt law is extended to $z > 2$ and if DLA galaxies are large discs.

Using literature information of the DLA column density distribution we showed that the comoving SFRs traced by the DLA in the quasar surveys is $\sim$15% of the comoving SFR measured for high redshift galaxies in flux-limited surveys. However, in this connection, the bias against the highest column density DLAs enter these derivations as well. If very high column density absorbers are missed in the surveys, the real comoving SFR in DLAs will be larger. Larger DLA surveys will give better constraints on the column density distribution, and hence the comoving SFR traced by these objects.

A relatively small comoving SFR seems to disagree with the indications in this thesis that SFRs from individual DLA galaxies are consistent with those for L^* galaxies at all redshifts. It is possible that missing DLAs with very large column densities (and hence large SFRs) could explain this effect as well.

9.1.2 Extended emission at the QSO redshifts

Taking advantage of the full three-dimensional view towards the quasars in the IFS data set, we investigated the presence of extended emission at the quasar redshifts. As for the DLA galaxy investigation, we separated the study into which emission lines were looked for.

The low-redshift data set included three radio-loud QSOs at $z \sim 1$. For two objects we found alignment with the radio jet, while the core-dominated quasar showed no extended emission line regions. Combined with the alignment effect, the velocity structures found for one object indicate that an interaction with the radio-jet affects the emission properties. Nevertheless, the gas appears not very disturbed with velocity dispersions less than 1000 km s^{-1}. Similar velocity dispersions were found for the sample at $z > 2$ in the extended Lyα emission line regions.

Where we study the extended Lyα emission from QSOs at $z > 2$, we found properties that confirmed the predictions for the extended emission line nebulae around radio-quiet QSOs (Haiman & Rees 2001). Comparing the observed extensions and emission line luminosities with those reported for radio-loud QSOs in the literature, we found evidence some differences between the two populations. Specifically, radio-loud lobe-dominated QSOs have brighter extended emission and the nebulae have larger sizes relative to those around the radio-quiet QSOs. We investigated what could be the origin for this difference, and could rule out the scenario where the QSO ionising flux determines the properties in the nebulae. However, the sample of four radio-quiet quasars is too small to rule out that the ionising radiation plays a role for this population.

In the full sample of radio-loud and radio-quiet QSOs we then argued for other possibilities. Currently, we can not distinguish between the following scenarios for the origin of the nebulae around radio-loud and quiet QSOs: 1) Enhancement of Lyα emission from jet interaction 2) Different covering fraction of neutral hydrogen 3) Density difference in the environment 4) An evolution effect. Our investigations of the differences between the two populations indicate that the first option is the most likely. However, when an alignment effect is not always seen, this would disagree with our interpretation. Based on additional velocity structures, from the low-redshift sample we argued for the first case, but we do not have this information for the Lyα lines.

9.1.3 Integral field spectroscopy as a tool

In summary we have explored the technique of IFS to look for faint emission lines. Where other studies have provided upper limits to the detections, we here find that with an appropriate integral field unit, the detection of emission lines from DLA galaxies is feasible.

The predicted sizes of DLA galaxies are relatively small ($<$10 kpc), hence the impact parameters should be smaller than a few arcseconds. From the candidate emission line objects and the typical spiral disc galaxy sizes of DLA galaxies suggested in this thesis, it follows that the field of view of $\sim 5''$ is sufficient for this science goal. A higher spatial resolution would possibly not contribute much to the analysis of Lyα emission from DLA galaxies. Due to the faintness of the emission lines and the fact that no extended emission region was detected from any candidate, the highest signal will be obtained when the emission is collected in as few spaxels as possible. Indeed, the candidates were most easily identified when the seeing was about the size of two spaxels in the PMAS data ($1''$). For the study of emission from DLA galaxies, since they were mostly found consistent with being point sources (apart from the lowest redshift DLA and sub-DLA galaxies studied), we estimate that it is critical to have a contiguous sampling. Where INTEGRAL data was used to look for emission from DLA galaxies up to 40% of the flux was lost between fibres, and the location of the brightest emission line region is more uncertain relative to the PMAS data. This can be argued from comparing the results from the $z = 0.160$ sub-DLA galaxy in Chapter 2 with the localisation of the $z = 0.0912$ DLA galaxy in Chapter 3. For the latter object, we could point

out that the structure detected appeared similar to deeper imaging data on this object. Deeper data would be needed to study the emission region in detail.

On the other hand, the second scientific topic investigated does not require a very good spatial sampling. To study extended emission the signal collected in one spaxel improves with the spaxel size, and here a larger field of view is preferable as demonstrated with the use of INTEGRAL data. This showed that a better signal is crucial to determine the velocity structures. Furthermore, a non-contiguous sampling of the data is sufficient when it is not critical to obtain spectrophotometric results. When details are studied near the QSO sight line the better spatial sampling of PMAS is preferable.

9.2 Future outlook

Most of the studies presented in this thesis were dealing with faint objects. Using PMAS on a 4m class telescope to detect faint objects obviously requires longer integration times than needed for integral field units (IFUs) on 8m class telescopes. Hence, this section explains future studies that are planned on larger telescopes with integral field spectroscopy.

9.2.1 DLA galaxies

Selection biases from DLA samples obtained by many different surveys enter the studies presented in this thesis. Another sample with well defined selection criteria can be specified from the more than 500 known DLAs from the SDSS. From these we are able to select a sample with constraints on the redshifts and column densities of the DLAs, whereas no metallicity constraints are included.

Another investigations which is planned, is to study DLA systems which likely have internal heating from massive stars. These heating rates are determined from the C II* technique for $z \gtrsim 2$ DLAs presented in Wolfe et al. (2003). With such a study it will be possible to verify the technique to estimate SFRs in the individual DLA galaxies. A problem, however, is that Lyα is resonantly scattered and a bad tracer of the star formation rates. It would be better to search for optical emission line shifted to the near-IR. At $z = 2.3$ the strong emission lines that allow a determination of abundances are shifted into near-IR pass bands which can be observed from the ground. Hence, a comparison of abundances derived from nebular lines with metallicities from the absorption line analyses will be possible in a similar way as done for the few DLA galaxies at $z < 1$. This is nevertheless still going to be time consuming with a near-IR IFU on an 8m class telescope. Therefore a better way would be to identify DLA galaxies with particular bright Lyα emission lines for follow-up studies with conventional near-IR slit spectroscopy. Extending the studies of metallicity gradients to the high redshift galaxies will be very important in relation to the metallicities derived from absorption lines from DLAs.

This thesis also presented an estimate for the average DLA galaxy disc mass. However, this was based on statistical arguments, and included the neutral gas mass only. The estimates of DLA galaxy disc masses combined with results from numerical simulations in the literature suggested that DLA galaxies need not be as massive as the local disc galaxies. As found by numerical simulations, high redshifts DLA galaxies could as well be merging clumps (Haehnelt et al. 1998). These suggestions can be tested if one could observe the galaxy rotation curves by their optical emission lines. With current instruments, these rotation curves are probably going to be difficult to measure for galaxies at $z > 2$.

9.2.2 Extended emission around quasars

Large systematic investigations of the extended emission nebulae from bright QSOs have not been carried out to date. Most studies have focused on either a few radio-quiet or radio-loud objects, and often objects were selected because they were known in advance to have extended emission line nebulae. The problem is that the extended emission is very faint relative to the central source and long integration times are needed. The sample of QSOs investigated here are difficult to compare with those in the literature because of the different observational techniques. To investigate the differences between the extended emission from QSOs, it is necessary to have a sample of QSOs at the same redshifts and with the same luminosities, but with different radio properties. With IFS, we can try to estimate the line flux which is not spatially coincident with the radio jets to disentangle the contribution from shocks from jets to the total emission.

To determine whether there are environmental differences between the two samples, we would need to obtain higher resolution images. HST images currently provide the deepest data with the best spatial resolution which would be valuable to detect galaxies nearby the QSOs as well as allow us to study the host galaxies. Additionally, X-ray data would provide information of masses of possible clusters at the QSO redshifts to further study the effect of the environments.

References

Chen, H., Lanzetta, K. M., Webb, J. K., & Barcons, X. 2001, ApJ, 559, 654
Chen, H.-W., Kennicutt, R. C., & Rauch, M. 2005, ApJ, 620, 703
Ellison, S. L., Kewley, L. J., & Mallén-Ornelas, G. 2005, MNRAS, 357, 354
Haehnelt, M. G., Steinmetz, M., & Rauch, M. 1998, ApJ, 495, 647
Haiman, Z. & Rees, M. J. 2001, ApJ, 556, 87
Turnshek, D. A., Rao, S. M., Nestor, D., et al. 2001, ApJ, 553, 288
Wolfe, A. M., Prochaska, J. X., & Gawiser, E. 2003, ApJ, 593, 215

CHAPTER A

Data reduction

Concepts specific for integral field spectroscopy are explained in greater detail here. Since most data presented in this thesis comes from PMAS, this chapter describes the principal details for the reduction of PMAS data. The reduction of data from other instruments are related to the procedures used for PMAS data. Observations were obtained with the following three instruments

- PMAS - Calar Alto 3.5m telescope
- INTEGRAL - 4m William Herschell Telescope, La Palma
- VIMOS IFU - VLT

A.1 Reduction steps

A.1.1 Bias subtraction

A median filtered bias frame was created by combining $\sim$10 individual bias frames. Series of 10 bias frames were taken at the end of each observing night. Comparisons between combinations from several nights showed that bias level remained constant during one run. The online PMAS reduction software allowed the use of a single bias image which was smoothed before subtraction, but this option was not used.

A.1.2 Tracing the spectra

In the case of very faintly illuminated object spectra the spectra need to be located by other means than tracing each spectrum separately. During observation runs calibration spectra consisting of a continuum lamp spectrum was obtained for each object and grating position at regular time intervals. This is needed since the spectrograph flexure causes shifting of the location of the spectra on the CCD both in the dispersion and cross dispersion directions.

The tracing of PMAS spectra takes into account the structure of 16 spectra placed at a pixel separation of 14 pixels (un-binned) followed by a larger separation of 32 pixels. Whether or not the CCD was read out in binned or un-binned mode was taken into account by the tracing algorithm. Firstly a cut is made in the cross-dispersion direction and 256 peaks are located, and secondly the specific structure of the location of spectra are included. Proved as a very effective means of tracing, this procedure allowed tracing using very faintly illuminated object spectra as well. However, here we only used the continuum lamp spectra for tracing. As output, the locations for each of the 256 spectra as a function of CCD column number were recorded.

A.1.3 Cosmic ray hits

Three methods of removing cosmic ray (CR) hits from data cubes were investigated.

1. The first method investigated was COSMIC RAYS in IRAF, but this method was rejected because it did not find CRs which affected multiple pixels.

2. L.A. Cosmic (van Dokkum 2001) uses a Laplacian edge transformation to find pixels which are affected by CRs. This method is very slow, specifically on large files. We therefore chose to implement this method only for the already extracted spectra. This routine also gives an output file of the rejected spectral pixels.

3. The third method, which proved to be much faster uses simple pixel statistics for detecting CRs (Pych 2004). This method was used on the bias subtracted images before the spectra were extracted resulting in 'cleaner' output spectra. The threshold can be set to detect fainter CRs, but in this case sky emission lines were frequently identified as CRs and efficiently removed. To avoid this, a higher threshold was used, which left $\sim$10% of the original CRs in the image. Later on, after all the data reduction, CRs left in the extracted spectra were removed by method (2).

A.1.4 Spectral extraction

Using the position of each individual spectrum, which was recorded by the tracing routine the spectra were extracted. Here the different methods for extracting the spectra will be discussed.

Simple (PMAS online) extraction

In the normal observations the CCD was read out in a 2×2 binned mode. In this case the distance between consecutive spectra were 7 pixels and each spectrum had a *FWHM* of 2 pixels. The online reduction used information from the tracing and for each wavelength 7 pixels were added in the cross-dispersion direction.

Gauss extraction

The extraction described above worked perfectly for bright objects. As 7 pixels were added in the cross-dispersion direction and the *FWHM* of the spectra are much smaller a significant background signal was included in the extraction. Most of the signal from the object will fall within the spectral *FWHM* of 2 pixels, while at larger distances object fluxes are much smaller. For faint objects one can improve the signal-to-noise (S/N) ratio by choosing a weighting scheme for the extraction. Thus, taking into account the shape of the fiber in the cross dispersion direction it is possible to increase the S/N.

Assuming that the shape of the spectra can be described by a Gaussian function with a width, σ, which can change with wavelength, such a model can be incorporated while extracting the spectra by imposing weights appropriate for the Gaussian shape. The following algorithm is used to extract the spectrum along the profile given by $p_{i,w,s}$.

$$f_{i,w} = \frac{\sum_s f_{i,w,s} \times p_{i,w,s}}{\sum_s p_{i,w,s}^2} \tag{A.1}$$

where $f_{i,w,s}$ is the flux for a given fibre, i, at the wavelength w at the spatial position s.

Because the signal from the object spectra is typically very small the spectra of the continuum emission lamp were used for this analysis. For each fiber the cross dispersion shape at each wavelength was determined. As we were dealing with 256 spectra and $\sim$1024 wavelength bins,

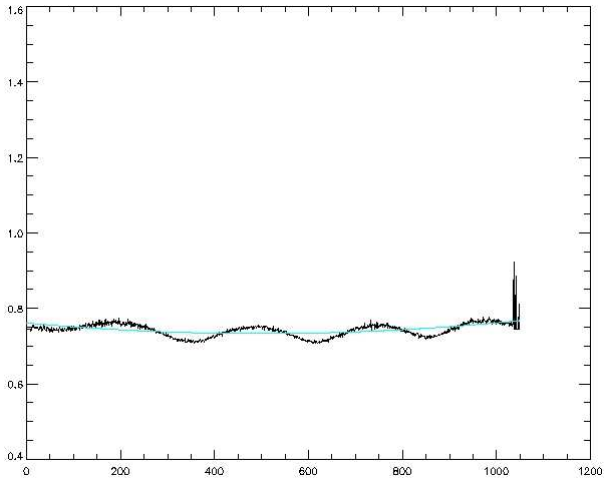

Fig. A.1. Gaussian widths (σ) from fits to a spectrum from a single fiber along dispersion direction. Pixel coordinates are given on the x-axis. The σ shown here 'wiggles' because the spectra are affected by pixelisation. The red line shows a second order polynomial fit used to create a lookup table for that particular spectrum.

$\gtrsim$260000 fits were performed for each file. It should not be strictly necessary to perform all these fits because the properties were expected to vary smoothly with wavelength. The results were saved in a lookup table. The spectra are affected by pixelisation such that the *FWHM* determined depends on the exact location of the peak flux given by the tracing routine. This gives rise to the wiggles seen in Fig. A.1. These wiggles are entirely artificial because the *FWHM* changes smoothly with wavelength. Hence for the lookup table a second order polynomial was fitted as indicated in Fig. A.1. Moreover, the wiggles seen in the figure are quite large because the spectra are actually under-sampled. A typical value obtained from fitting Gaussians is $\sigma = 0.7 - 0.8$ pixels, which gives a *FWHM* of $\sim 1.6 - 1.9$ pixels.

Optimal extraction

Instead of using an input model for the shape of the spectra the shape of an object spectrum itself can be used to determine the appropriate weights. This method was introduced in Horne (1986), who noted that the S/N of the output spectrum could be increased by $\sim$10%. The same code could not be used here because no sky spectrum was recorded in adjacent lines on the CCD as for slit spectra.

A.1.5 Wavelength calibration

Wavelength calibration was done using a graphical user interface routine written by T. Becker specifically for PMAS data. Simultaneously with the continuum spectra used for tracing, emission line lamps were turned on, making it necessary to use only one calibration frame for each second long object integration. These spectra were extracted in a similar manner as the object spectra.

The software compared lines of known wavelengths to the spectra and for each spectrum matched the offset and dispersion. Typically between 10 and 30 bright lines were used for fitting a second order polynomial to the line spectra. The standard deviation for the fits were of the order of 10% of the pixel size. E.g. the uncertainty for the wavelength calibration was found to be 0.3 Å for the V300 grating and 0.16 Å for the V600 grating, respectively. Results for the fits were saved

in a lookup table that contained information for each of the 256 spectra, and could later be used for dispersion correction of the associated object data.

A.1.6 Flat fielding

No standard pixel-to pixel variation on the CCD could be applied because it was not possible to make a conventional illumination of the entire CCD. Instead we had to rely on the overall effect of the transmission of a fibre relative to an average value. Usually, spectra of the sky at twilight were obtained and extracted as the other science spectra. Each of the individual spectra were divided by an average spectrum, created by averaging the 256 spectra. This process created a two-dimensional flat-field spectrum which was normalised and smoothed, and flat-fielding science observation was done by dividing the extracted science spectra by this two-dimensional frame.

Flat field accuracy

Since all object observations are definitely not flat due to the target QSO, the accuracy of the flat fielding was analysed by the following method.

First, the 'real' flat field was created as described above. We uses this flat field to correct other flats taken on different nights. Six different flat fields were compared. These flat field corrected sky flats were analysed by calculating the mean and standard deviation in each monochromatic slice. The result showed that the 256 pixels in each slice had consistent values to within 1.3$\pm$0.8% for flat-fields obtained on the same night and 1.7$\pm$0.9% for 3 sky-flats obtained on different nights. Hence we found that the data reduction and flat fielding procedures produced reduced spectra with less than 2–3% uncertainties for the flat-fielding.

A.1.7 Flux calibration

The spectra were corrected for atmospheric extinction and telescope plus instrument sensitivities using following method. First, the airmass header keyword was updated to account for the shift in airmass during the observations. Specifically, the header keyword points to the time when the header was written, i.e. to the beginning of the observation, and this can change significantly with long integration times.

An airmass correction was applied to each individual stacked spectrum, using the relation between the observed flux, $f_{\mathrm{obs},\lambda}$ and the corrected flux, f_{corr}.

$$f_{\mathrm{corr},\lambda} = f_{\mathrm{obs},\lambda} \times 10^{0.4XE_\lambda}, \tag{A.2}$$

where X is the airmass, and E_λ is the extinction coefficients obtained from a standard extinction curve for Calar Alto (Hopp & Fernandez 2002).

An instrumental sensitivity function was calculated from comparing the observed spectrum of a spectrophotometric standard star with table values in either IRAF or STSDAS. Such a sensitivity function, S_λ, is defined by

$$S_\lambda = 2.5(\log(C) - \log(f_\lambda)) \tag{A.3}$$

where C is the count rate of the observations, i.e. the number of counts per second and f_λ is the standard star flux. Applying this sensitivity function to the reduced data yielded the final flux calibrated spectrum by

$$f_\lambda = \frac{10^{-0.4S_\lambda}}{t \cdot \mathrm{CDELT}} \tag{A.4}$$

where t is the integration time and CDELT is the the dispersion in the reduced spectra measured in Å per pixel.

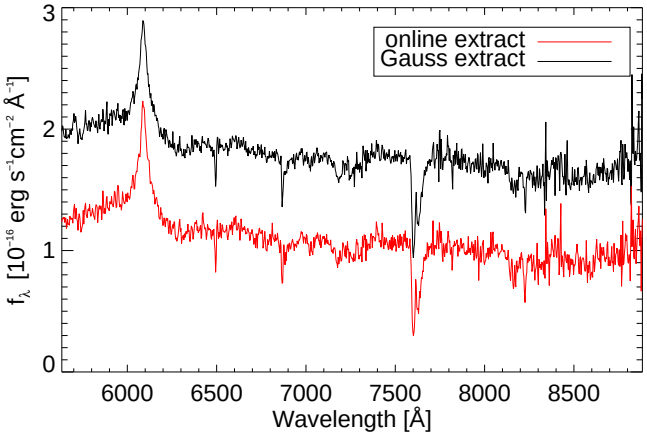

Fig. A.2. The two lines show the resulting spectra of Q1209+107 using the online extraction and the Gauss extraction methods. For visual comparison the spectra have been offset from each but their absolute calibrations are the same within 2%. Since this object is a relatively bright QSO there is no apparent difference between the S/N ratios in the two spectra.

A.1.8 Comparison between extraction methods

For bright objects e.g. the relatively bright QSOs (and standard stars) the chosen algorithm for extraction played no role and the S/N ratios of the resulting spectra were the same. A comparison of the two flux calibrated spectra in Fig. A.2 shows that the flux calibration is consistent with each other to within 2%.

An eventual increase in S/N was investigated through an inspection of an area of the spectrum where there were no contaminating emission or absorption lines, and wavelengths where skylines were strong was avoided. This left an area between pixel numbers 100 to 300 for analysis, which showed an increased S/N level of 6% from the standard extraction to the Gauss extraction.

Analysis of the signals in very faint spectra

For investigating the results in the case of very faint objects, we selected an exposure which was read noise dominated. For this purpose we used data from PSS J2155+1358, a very high redshift QSO ($z = 4.256.$), which has a LLS at the same redshift. At wavelengths shorter than 4794 Å the emission from the QSO is totally absorbed. As the spectra from IFU data were easily traced, the emission collected in the extraction gave a measure of the background noise in the extracted spectra.

The noise of the background was found by calculating the standard deviation of the spectra over a range of 200 pixels bluewards of the LLS cutoff in a region free of sky emission lines. The noise in the background from the online reduced spectra was 7.8±1.9 ADU while for the Gauss extraction it was 5.7±0.4 ADU, where the uncertainties denote the RMS values calculated from the 256 spectra. The explanation for this improvement is straight forward. Under the simple extraction 7 pixels on the CCD are added to give each spectral pixel resulting in the noise $N = \sqrt{7} \times n$, where n is the noise per (pre-extracted) pixel. Assuming instead a Gaussian spectral profile, the effective 'extraction width' is equal to the integrated Gaussian profile, when the peak intensity is 1 and the spectral width σ as measured directly. This gives $\sqrt{(2\pi)^{0.5} \times \sigma} \times n$, and the ratio between these estimates of the noise for a typical σ = 0.8 pixels is ∼0.54, i.e. the effective number of pixels extracted is almost halved.

A sourceless noise is calculated by

$$N = \sqrt{n_p b + n_p RON^2 + n_p b_{\rm dark}} \tag{A.5}$$

where n_p is the number of pixels that is extracted. Where no significant contribution from the dark current $b_{\rm dark}$ is present, which was found to be negligible in the PMAS data, the noise in the case of a 'Gauss extraction' is $N({\rm Gauss}) = \sqrt{0.54} \times N \approx 0.73 \times N$.

The extracted flux under the assumption of a Gaussian profile affects the level of the extracted signal which is naturally smaller due to the smaller background contribution. The signal to noise ratio is

$${\rm SNR} \approx \frac{S}{\sqrt{S + n_p b + n_p RON^2}} \tag{A.6}$$

where S is the total integrated flux of the source. For an object that is much brighter than the background ($S >> b$), the resulting SNR does not change with the Gaussian extraction method, while in the case the signal from the object is of the same order as the background ($S \approx b$), we expect that SNR improves. Rewriting the SNR equation

$${\rm SNR} = \frac{S}{\sqrt{S + N^2}} \tag{A.7}$$

where N is taken from Eq.(A.5), and assuming $S \approx N^2$, we find the improvement of the SNR by dividing the equations for the SNR in the two cases, i.e. SNR(Gauss) $= \sqrt{2}/\sqrt{1 + 0.73^2} \approx 1.14$ SNR, i.e. the SNR is improved by 14% with a Gaussian extraction compared to the standard extraction. For fainter sources where $S < N^2$ the SNR improves by a factor between 14 (when $S = N^2$) and 88% (when $S = 0$).

A.1.9 Sky subtraction

An optimal sky-subtraction for fibre based spectrographs is described in Wyse & Gilmore (1992). Theoretically, it should be possible to obtain sky subtraction to better than 1% accuracy, but as explained below, non optimal wavelength calibrations leads to systematic effects in the real data and the theoretical limit is not accomplished. Because of the different arrangement of the fibres in the integral field unit for the instruments each case for the subtraction of the background sky emission is explained here.

PMAS

PMAS does not have separate sky fibres. In the case where the observed objects do not fill out the whole of the field of view, one can select appropriate fibres e.g. at the edge of the field, or in between objects. Because the spectral resolution changes over the CCD with differences for the measured *FWHM* in sky lines of 15–20%, the sky subtraction will have strong residuals. However choosing background spectra that are located close on the CCD to the object spectra will give better results. In practice, this implies selecting sky spaxels to the east or west of the object of interest. When the object position is not known a priori, several different attempts were done interactively.

Another method is to model the change of spectral resolution for each fibre which is possible as long as only few skylines has to be subtracted. When many skylines are present (> 10) the number of free parameters in the fits becomes large and the sky-subtraction is less accurate again. When looking only for a single emission line from an emission line object located close to sky lines, the modeling of the lines has proved to be useful, when constraints on the sky line widths was included.

An average is calculated at each wavelength for the selected spectra, and this one-dimensional spectrum is subtracted from all of the science spectra.

INTEGRAL

INTEGRAL has 30 separate sky fibres placed in a large circle around the main field of view. On the CCD these sky fibres are mixed with the science fibres which means that crosstalk between fibres will affect the sky fibres close to any bright object on the CCD. Because in this case a QSO was placed in the centre of the frame, the affected sky fibres were easily recognized and not selected for sky subtraction. Typically, 20 spaxels were chosen, and the average spectrum was subtracted from all spectra.

In INTEGRAL frames the change of dispersion over the CCD is substantial, with Gaussian *FWHM* measured in strong sky lines varying by 20–30% over the field. This necessarily causes very strong sky subtraction residuals. Because the flux in the sky lines are constant for the spectra, modeling of the sky background will be the best solution.

VIMOS

VIMOS data was acquired for one object only, and while more data are available in public archives, these were not included here. The high resolution data consist of 1600 spectra with a spatial sampling of $0\farcs33$ per spaxel. Data reduction was done with a modified version of the PMAS reduction tool. The automatic detection and tracing algorithm takes into account the arrangement of the spectra on the CCD specifically for VIMOS frames. Background subtraction was done statistically, by selecting several spaxel surrounding the source, and the background counts were constructed for each wavelength by selecting the median of the spaxels values.

A.1.10 The AG camera as a photometer

Obtaining spectrophotometry for sources at non photometric nights can be done provided that the magnitude of a field star within the PMAS acquisition and guiding camera observations is known. As demonstrated in Christensen et al. (2003) spectrophotometry was obtained for a variable source by the monitoring of a Type Ia SN during peak brightness. This method used information of stars in the field of the acquisition images. For on source integrations lasting typically half a night, this procedure is obviously no longer accurate due to the sky variability at Calar Alto which will change extinction coefficients. In this case, one can only get an estimate of the variability of the photometry throughout the night using the archived images of the guide star.

A.2 Combinations of data cubes

Until now, the reduction of individual frames has been described. This sections explains investigations of several methods for combining individual data cubes of a given target to increase the signal.

A.2.1 Simple image combination

The most simple form for combining the images is to ignore effects of differential atmospheric refraction (DAR). This is sufficient when the data cubes were obtained at low (or non varying) airmasses. Combining the cubes one only needs information of the spatial shift. Using a standard rejection criteria within IRAF one can furthermore remove cosmic ray hits which were left over from the data reduction.

A.2.2 Differential atmospheric corrections

Photons with different wavelengths change their paths through the atmosphere due to the refraction properties of the atmospheric layers. This causes a slight shift in the apparent position of an object on the sky when observed in the red and the blue. In data cubes from optical IFS data, this effect is substantial when the airmass during the observations is high. Shifts of $2''$ are often seen when $X > 1.5$ over a wavelength interval of 3000 Å. When data cubes are combined, this effect has to be corrected for. An analytical expression exists giving the amount and the direction of the DAR correction for the ground level pressure and humidity (Filippenko 1982). However, this is an approximation assuming a plane parallel atmosphere, which is clearly not the case for the atmospheric layers above the mountains of most observatories.

Analysing optical IFU data, we have found systematic effects that change the direction of the DAR by up to 10° relative to the theoretical prediction. An explanation for this is a shift of the real zenith to a geometrical zenith, perhaps not stationary for the observatory (Thomas Becker, 2004, priv.comm.). No exact analytical expression has been found to solve this problem, so most data presented in this thesis has assumed that the theoretical expression by Filippenko (1982) can be applied. Tracing the change of the centroid of a bright point source with wavelength in a data cube that was corrected for the theoretical DAR, we have found that the residuals of up to 10%.

The science case we are interested in are mostly focused in a short wavelength interval. We have found that the theoretical DAR correction is sufficient within in an interval of 500 Å.

A.2.3 Drizzling

To avoid small shifts in the centroid that appear when using the theoretical DAR correction a different approach can be taken. In most of the data cubes analysed a QSO dominates the emission. Tracing the centroid of the QSO through the data cube this information can be used to correct for the DAR empirically. First, each monochromatic image is fit by a two dimensional Gaussian function. We then assume a smoothly varying spatial offset with wavelength, which is used to calculate a shift for any chosen reference wavelength. The fractional pixel shifts are applied to the data cubes by a modified version of the drizzle package by Fruchter & Hook (2002). Pixel sizes can be changed similarly as for the regular drizzling of undersampled data, but this option was not used here.

A.3 Handling the spectra

After all the initial data reduction steps the data needs to be corrected for several effects.

A.3.1 Telluric lines

These lines are caused by absorption in the earth's atmosphere by O_2 and H_2O molecules and are present mostly in the red end of the spectra. For example, the strong A and B bands at 6868 Å and 7595 Å are difficult to remove. As they are strongly variable, a correction for this requires observation of a spectrophotometric standard star close in time and position with the science observations. Typically, an O or B star is used for this purpose, since a featureless continuum can be used to trace the absorption line profiles. Unless otherwise described, these features in the spectra were left untouched. Chapter 2 contains an example of how a correction can be done using the spectrum from the QSO in the same field as the object which spectrum needed to be corrected for telluric lines.

A.3.2 Vacuum corrections

The observed wavelength of an emission line is shifted relative to the wavelength it had originally when emitted from, say, a distant galaxy. Emission lines are not detected in a pure vacuum, while the photons were emitted in (almost) vacuum conditions. To calculate the vacuum wavelength one uses the expression

$$\frac{\lambda_{\rm vac}}{\lambda_{\rm air}} = 1.0 + 2.735182 \times 10^{-6} + \frac{131.4182}{\lambda_{\rm vac}} + \frac{2.76249 \times 10^8}{\lambda_{\rm vac}} \tag{A.8}$$

for wavelengths $\lambda > 2000$ Å.

A.3.3 Heliocentric corrections

As the earth moves around the sun the observed wavelength emitted by a distant object receives a small change which depends on the time of the observation and the position of the object on the sky. The velocity of the earth around the sun is $\sim$30 km s^{-1} which then corresponds to the maximum shift of a line. The shift for an object with right ascension α and declination δ is

$$V = V_x \cos\alpha \cos\delta V_y \sin\alpha \cos\delta V_z \sin\delta, \tag{A.9}$$

where V is the velocity of the earth towards the target. The heliocentric wavelength is then

$$\lambda_{\rm helio} = \frac{\lambda_{\rm obs}}{1 - \frac{V}{c}}. \tag{A.10}$$

A.3.4 Aperture corrections

To collect the total flux large apertures have to be used at all wavelengths. However, this will increase the noise due to the large background flux collected. One can instead use smaller apertures, and scale this to the total flux by comparing with the total flux obtained with larger apertures, similar to the standard practice imaging analyses. Another issue which must be considered is if the correction for atmospheric refraction is properly corrected for. To account for this one can make a wavelength dependent aperture correction by dividing the spectrum with the large aperture with that from the smaller aperture, make a smooth polynomial fit to the fraction, in order to create a wavelength dependent aperture correction. In the thesis, this is often done for the standard stars, which are usually not corrected for atmospheric dispersion, and for the QSOs to increase to signal to noise ratio of the QSO spectra.

A.4 Artificial emission line experiments

Mostly through this thesis localisation of faint emission line candidates, as well as localisation of previously known objects, were done interactively using the Euro3D visualisation tool (Sánchez 2004). To analyse the efficiency of the visual detection of emission lines several experiments were done. In a similar way as artificial objects can be added to 1- or 2 dimensional data sets, a code was developed to simulate an emission line object with a Gaussian shape in a data cube. As input parameters for the fake emission line object one needs the spatial Gaussian width, σ, which is a measure of the seeing, and the third Gaussian width σ_{FWHM} giving the width of an emission line in the dispersion direction. No complex structures were simulated. The program can either add an emission line to an existing data cube, or make a complete simulation of a data cube by adding any levels of noise to the background level. Always in the tests described

below, the input flux was estimated in a noise-free data cube so that effects due to pixelisations and fitting Gaussian functions to these were avoided. The input flux was calculated using Eq. (B.9): $f_{\rm line} = (2\pi)^{1.5} I_0 \sigma^2_{\rm seeing} \sigma_{FWHM}$, where I_0 is the peak flux of the emission line object.

A.4.1 Visual re-identification

We created a data cube with 0 counts and added random Gaussian noise corresponding to the noise level in a real data cube. In real data cubes the noise level is a function of wavelength and strongly depending on sky subtraction residuals, but these effects were ignored. A faint emission line was added with typical characteristics of the detected emission lines, e.g. with a line flux 5×10^{-17} erg cm^{-2} s^{-1}, and *FWHM* = 1″in both RA and DEC, and a velocity dispersion of 5 pixels (roughly corresponding to the velocity dispersion of the candidate emission objects widths of $\sim$ 300 km s^{-1}). Following, the data cube was converted to a row stacked spectrum (i.e. equivalent to several two dimensional spectra) and inspected visually. For these faint lines the emission line object could not be identified directly above the noise level, but when the visualisation tool was used the emission object could be (re-)identified. In the visualisation tool the true spatial PSF could not be reconstructed well either, and often showed extensions in one direction as demonstrated in Fig. A.3.

A.4.2 Visual object recovering

A series of experiments were constructed to test the differences between the input and output parameters. Table A.1 lists experiments carried out. Here the noise in the data cube was simulated, i.e. it is pure Gaussian, and the input wavelength was irrelevant, only the relative shift of the recovered line was considered important. To explain the idea behind the various tests listed in Table A.1 the following items were taken into account.

- Line flux bracketing typical values taken to be between 3 and 7×10^{-17} erg cm^{-2} s^{-1}.
- Background noise bracketing values obtained in the final reduced data cubes, i.e. between 2 and 3×10^{-18} erg cm^{-2} s^{-1} Å^{-1}.
- Line widths smaller than 1000 km s^{-1} and down to the resolution limit.
- Effective seeing between 1″ and 1.″5.

Tests 1 through 5 showed that generally the emission line flux was recovered when the objects could be identified visually. Furthermore, the true velocity dispersion was not very well recovered, and always underestimated. This is potentially a very important consideration for the interpretation of real data. Apparently emission lines with small velocity dispersions for a constant flux level were more easily recovered due to the efficient localisation of the peak emission.

The PSF recovery became increasingly difficult when the (simulated) seeing increased, as was also found for intrinsically faint objects and high background noise levels. Fig. A.3 shows an example of the irregular PSF that is recovered from test no. 10. In the left hand image, the input object from a noise free data cube is shown. In the right hand image the recovered emission line object is shown where noise has been added. The contours in each panel correspond to the object in the other. These plots are similar to those of the real data in Chapter 5 and it is visually obvious that the spherically symmetric PSF can not be reproduced for faint objects when the background noise is included.

Table A.1. Artificial emission line experiments

Test no.	λ (Å)	f^{a}	*FWHM* (km s^{-1})	seeing ($''$)	Noise^{a}	λ (Å)	f^{a}	*FWHM* (km s^{-1})	seeing ($''$)	comments
1	4499.2	3.0	1000	1	0.2	4501.6±0.9	4.4±2.1	360±250	1.0	
2	4499.2	5.0	1000	1	0.2	4497.7±1.3	4.1±1.9	570±220	1.2	
3	4499.2	7.0	1000	1	0.2	4498.9±1.5	7.3±2.1	870±220	0.9	
4	4499.2	3.0	1000	1	0.3	4499.4±10	6.1±4.3	810±420	1.8	noisy spec.
5	4499.2	5.0	1000	1	0.3	4499.1±1.9	3.4±1.9	340±190	3.0	low flux
6	4499.2	7.0	1000	1	0.3	4500.7±2.0	7.0±2.3	1300±350	0.9	
7	4499.2	3.0	800	1	0.2	4497.2±4.0	2.5±1.6	730±370	1.1	noisy spec.
8	4499.2	5.0	800	1	0.2	4498.3±1.1	4.7±1.2	640±130	1.4	
9	4499.2	7.0	800	1	0.2	4498.9±0.8	6.7±1.3	660±100	1.2	
10	4499.2	3.0	800	1	0.3	4499.9±0.7	5.6±2.8	360±200	1.4	large flux
11	4499.2	5.0	800	1	0.3	4500.3±1.3	5.1±3.6	360±360	2.0	
12	4499.2	7.0	800	1	0.3	4498.4±1.5	8.5±2.9	730±230	1.2	
13	4499.2	3.0	500	1	0.2	4499.3±0.8	3.4±1.9	440±230	1.7	
14	4499.2	5.0	500	1	0.2	4499.8±0.5	5.5±1.4	400±130	1.0	
15	4499.2	7.0	500	1	0.2	4499.0±0.3	6.1±1.2	340±80	1.1	
16	4499.2	3.0	500	1	0.3	4498.4±0.3	5.1±1.7	300±60	0.9	large flux
17	4499.2	5.0	500	1	0.3	4498.7±0.5	6.4±2.5	400±100	1.4	
18	4499.2	7.0	500	1	0.3	4499.8±0.4	6.6±2.5	290±70	1.6	
19	4499.2	5.0	1000	1.5	0.2	4501.6±1.7	6.2±2.7	680±260	1.5	
20	4499.2	5.0	1000	1.5	0.3	4495.0±1.0	6.8±1.8	630±140	2.8	not recovered
21	4499.2	5.0	800	1.5	0.2	4500.3±2.3	4.6±1.8	1000±220	1.2	
22	4499.2	5.0	800	1.5	0.3	4498.6±2.4	13.3±3.7	1300±300	2.5	large flux
23	4499.2	5.0	500	1.5	0.2	4499.7±2.1	5.0±2.1	870±300	1.3	
24	4499.2	5.0	500	1.5	0.3	4498.9±1.8	4.9±1.8	420±100	1.8	

[a]Flux in units of 10^{-17} erg cm^{-2} s^{-1}.

Input and output properties of simulated emission lines. Each object was visually re-identified in a manner similar to that applied to the real data. Column 2 lists the input wavelength of the artificial line, and column 3 and 4 list the total flux, and the line *FWHM*, respectively. The effective seeing *FWHM* is given in column 5 and the artificial noise level added to the data cube in column 6. The output parameters are listed in the right part where column 7 trough 10 list the parameters for the line recovered though the visualisation tool. The last column gives general comments to the detected line.

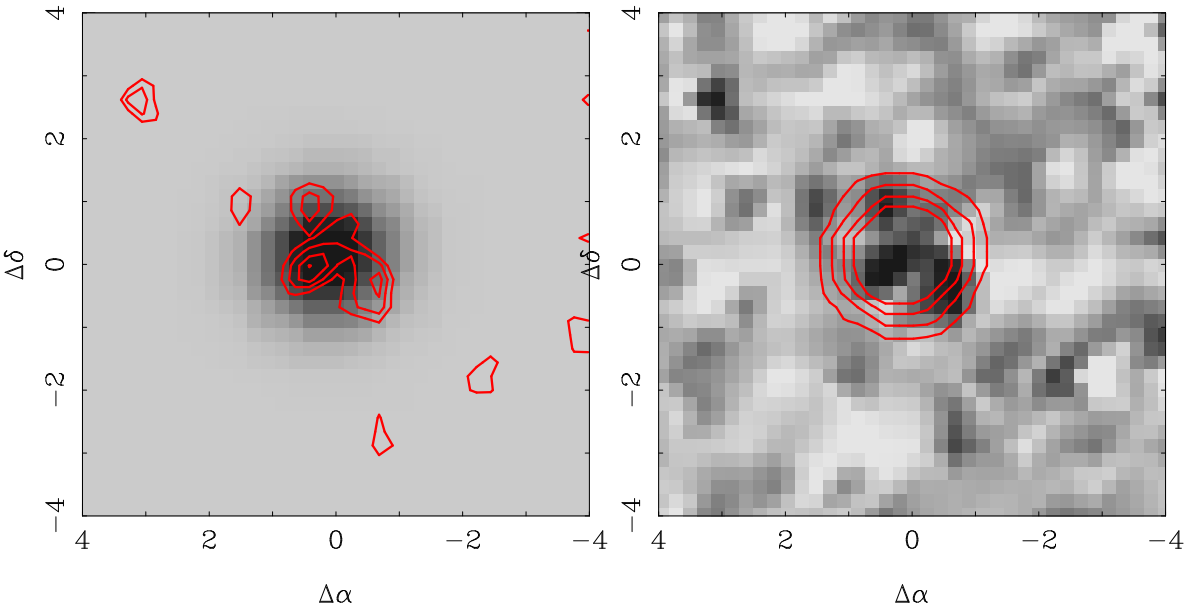

Fig. A.3. Reconstructed images from a simulated PMAS data cube. *Left panel:* Narrow- band image of a simulated emission line (test no. 10) here shown without additional noise and contours of the recovered emission line object is overlayed. Contour levels correspond to 2,3,4 σ above the background noise. In the *right panel* the image is the recovered emission line object where noise was added to the data cube, and the contours correspond to the input object, where the innermost contour correspond to the spatial *FWHM*.

A.4.3 Bootstrap tests

To get an idea of how well the parameters were recovered for faint emission lines, a code to automatically perform the analysis described above was written. The tests described here used as an input the artificial data cubes with artificial emission lines at known locations. The automated process located and co-added spectra within one times the spatial *FWHM* [1] . Only the central emission wavelength was known, while the location in RA and DEC was estimated from a Gaussian fit to a narrow-band image that was convolved with a Gaussian function with a width matching that of the seeing[2] . This procedure was necessary to reject wrongly identified objects associated with spurious large signals from single spaxels. A second pass though a two-dimensional Gaussian fit was done to recenter the emission feature. Spectra within one times the seeing radius centered on the peak found from the two-dimensional fitting was co-added to create a one-dimensional spectrum. Increasing the area of co-added spaxels also increased the statistical noise, while only adding a small fraction of flux from the emission line. The resulting signal-to-noise ratio of the emission line was largest when only spaxels within one seeing element was included for the created one-dimensional spectrum. Table A.2 lists calculations for the signal, noise and signal to noise ratio of an emission line with typical characteristics.

A Gaussian emission line was fitted to the one-dimensional spectrum, where the centroid was allowed vary at 4500±10 Å and the *FWHM* varied from 200 to 1200 km s^{-1}. Errors for the output parameters were estimated from 1σ standard deviations in a series of 1000 experiments and the results are listed in Table A.3. The last column in the table gives the fraction of correct re-

[1] The fitting procedure described here was developed in IDL and incorporates an external fitting package (MPFIT) written by Craig B. Markwardth; `http://cow.physics.wisc.edu/~craigm/idl/idl.html`

[2] A similar method is used by daofind in the IRAF/DAOPHOT package. To check that the correct centroid was found, comparisons was made with the IDL routine GCNTRD, which is distributed with the IDL astro package, and which uses the DAOPHOT find algorithm. The same centre was always found, but the simple Gaussian smoothing routine proved to be faster.

diameter	f erg cm^{-2} s^{-1}	N erg cm^{-2} s^{-1} Å^{-1}	S/N
$1''$	4.81×10^{-17}	2.5×10^{-18}	4.5
$2''$	4.99×10^{-17}	5.0×10^{-18}	2.4
$3''$	5.00×10^{-17}	7.5×10^{-18}	1.6

Table A.2. Extracted flux f, noise N, and signal-to-noise ratio for a one-dimensional, coadded spectrum, when integrated over the line width. The values are given for different extraction radii. The input object has a seeing of $1''$, a total flux of 5.0×10^{-17} erg cm^{-2} s^{-1}, and background noise level 2.5×10^{-18} erg cm^{-2} s^{-1}per pixel.

identifications for the automatic procedure. To find this number, we included only those (artificial) objects that had emission lines at the allowed wavelength range, had a minimum flux at 1×10^{-17} erg cm^{-2} s^{-1}, and emission line widths in the range specified above.

The average recovered line fluxes were consistent with the input, but the uncertainties in the outputs were large. Therefore the automatic procedure, while successful in locating the object, had a tendency to over- or underestimate the flux relative to the visual approach.

Tests with science data cubes

In a similar way as described above, artificial objects were added to real data cubes, i.e. no noise term was added to the cubes. The object was placed at random wavelengths, where the noise level in the data cube was approximately constant both in wavelength and in narrow-band images. To analyse the difference between the input and output flux, a series of 1000 tests with an object of known total flux was done. Fig. A.4 shows the result, where the straight line indicates equal input and output flux. Black dots denote the extracted flux where the spatial location of the object was previously know, while the red dots indicate the extracted flux when the spatial position was unknown. Error bars in the figure indicate the 1σ standard deviation of the recovered fluxes. For large line fluxes, the agreement between the input and output flux is good, while the relative errors increase with decreasing flux levels. The total number of emission line objects that were recovered were counted and the dashed line in the lower panel in Fig A.4 indicates the input flux where 50% of the objects were recovered successfully. This occurred at $f \approx 6 \times 10^{-17}$ erg cm^{-2} s^{-1}.

One reason why many of the faint objects were missed in the automatic detection procedure, was due to the odd PSF, that made the placement of the centroid uncertain, so that spaxels that were not related to the emission object were used for the one-dimensional spectrum. Where visual detections were done, more objects were re-identified than in the automatic detection.

A.5 Spurious detections

A 3σ detection of an emission line in a spectrum can be spurious although Gaussian statistics indicate a confidence of 99%. To detect faint emission line candidates, an additional constraint was put on the narrow-band images that they be detected by more than 3σ above the background noise. Using these constraints, tests were carried out to investigate the frequency of random occurrences of emission lines present in both spectra and narrow-band images simultaneously where both are detected by a signal $> 3\sigma$.

We took a reduced data cube, selected a random position, and co-added 4–6 spaxels to create a one-dimensional spectrum. Over the whole wavelength range we searched for emission lines with S/N$>$ 3 in intervals of 20 Å in width. When such a line was found a narrow-band image was created centered on the emission line and with a width of ±5 Å. Contour maps were created from

Table A.3. Artificial emission line experiments

Test no.	Input obj λ (Å)	f^{a}	*FWHM* (km s^{-1})	seeing ($''$)	Noise[a]	output λ (Å)	f^{a}	*FWHM* (km s^{-1})	seeing ($''$)	f_{id}
1	4499.2	3.0	1000	1.0	0.2	4498.2±4.4	2.9±1.8	670±150	1.2±0.1	0.45
2	4499.2	5.0	1000	1.0	0.2	4498.7±3.7	4.6±2.8	670±130	1.3±0.1	0.60
3	4499.2	7.0	1000	1.0	0.2	4498.9±3.0	6.9±4.0	680±100	1.0±0.1	0.75
4	4499.2	3.0	1000	1.0	0.3	4498.6±5.9	3.4±2.1	710±160	1.2±0.1	0.35
5	4499.2	5.0	1000	1.0	0.3	4498.0±4.5	4.2±2.8	690±140	1.2±0.1	0.41
6	4499.2	7.0	1000	1.0	0.3	4498.5±3.9	6.0±3.8	640±130	1.1±0.1	0.56
7	4499.2	3.0	800	1.0	0.2	4498.4±4.3	2.7±1.5	650±140	1.2±0.1	0.40
8	4499.2	5.0	800	1.0	0.2	4498.7±3.3	4.2±2.4	620±120	1.1±0.1	0.54
9	4499.2	7.0	800	1.0	0.2	4499.0±2.7	6.2±3.2	600±100	1.0±0.1	0.67
10	4499.2	3.0	800	1.0	0.3	4498.2±4.8	3.5±2.1	680±150	1.2±0.1	0.36
11	4499.2	5.0	800	1.0	0.3	4498.3±4.1	4.3±2.8	650±140	1.2±0.2	0.41
12	4499.2	7.0	800	1.0	0.3	4498.9±4.0	5.1±3.5	610±120	1.3±0.2	0.47
13	4499.2	3.0	500	1.0	0.2	4498.5±4.3	2.6±1.4	640±150	1.3±0.1	0.37
14	4499.2	5.0	500	1.0	0.2	4498.8±3.4	3.3±1.8	590±140	1.0±0.1	0.39
15	4499.2	7.0	500	1.0	0.2	4499.0±2.8	4.5±2.3	540±100	0.9±0.1	0.41
16	4499.2	3.0	500	1.0	0.3	4498.1±4.6	3.4±2.0	690±150	1.2±0.1	0.37
17	4499.2	5.0	500	1.0	0.3	4498.3±4.2	3.7±2.1	630±150	1.1±0.1	0.33
18	4499.2	7.0	500	1.0	0.3	4498.8±3.6	4.5±2.7	610±140	1.1±0.1	0.36
19	4499.2	5.0	1000	1.5	0.2	4498.7±3.9	2.3±1.1	660±130	1.2±0.1	0.56
20	4499.2	5.0	1000	1.5	0.3	4498.4±4.1	2.2±1.3	650±150	1.2±0.1	0.46
21	4499.2	5.0	800	1.5	0.2	4498.7±3.2	2.6±1.3	600±120	1.2±0.1	0.57
22	4499.2	5.0	800	1.5	0.3	4498.5±3.5	2.9±1.3	580±130	1.2±0.1	0.41
23	4499.2	5.0	500	1.5	0.2	4499.1±2.1	3.8±1.2	490±80	1.2±0.1	0.55
24	4499.2	5.0	500	1.5	0.3	4499.0±2.4	3.7±1.1	510±100	1.2±0.1	0.5

Input and output properties of simulated emission lines. Columns listed here are similar to those in Table A.1. f_{id} indicates the fraction of correct automatic re-identifications.

[a]Flux in units of 10^{-17} erg cm^{-2} s^{-1}.

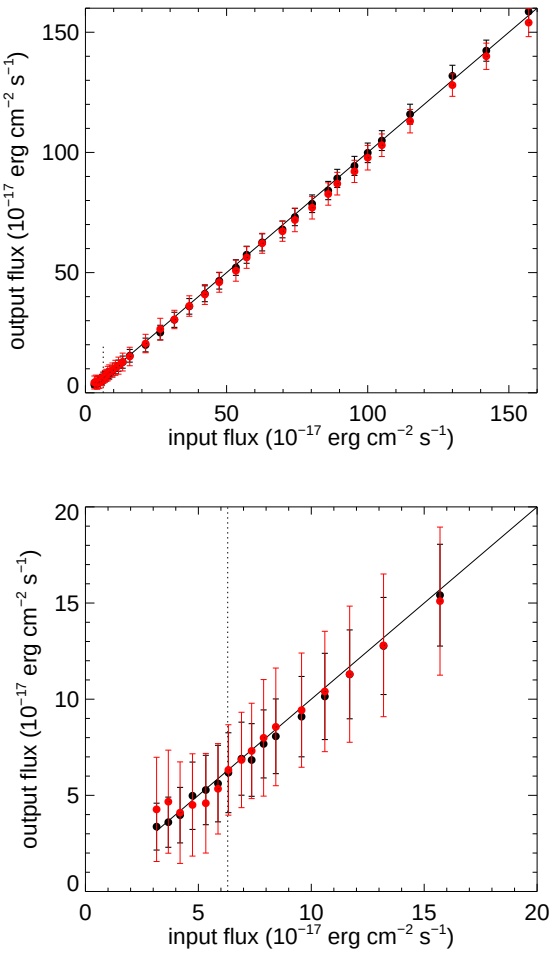

Fig. A.4. Difference between input and output (automatically recovered) flux for a series of experiments with objects of different flux levels. The black dots are derived for known positions and the red ones when the object is randomly placed and subsequently detected. The *Lower panel* is a zoom of the low flux region. The vertical dotted line corresponds to a 50% completeness detection limit, which is $f \approx 6{\times}10^{-17}$ erg cm^{-2} s^{-1}. In both panels the straight line is the one-to-one correlation.

this image where contours were taken to be 2, 3, and 4σ above the background. A visual inspection of these objects was done to determine whether an object was visible at the position of the spaxels that were selected in the first place. A large number of tests were made by selecting various spatial locations for the spaxel selection. In a series of 50 tests, simultaneous detection of emission lines and objects in the narrow-band images, occurred in 1 ± 1 cases reflecting a random contamination of 2 ± 2%. When applying the results of this test to the detections of candidates in a wavelength range of ±10 Å from the centre of a DLA line, this test indicated that the contamination from spurious detections was fairly small.

A similar analysis for a purely simulated data cube with noise levels similar to that in the real data, showed that a random contamination did not occur at all. This implies that systematic effects are present in the real data cubes, and that a quantification of the noise in each pixel in the data cube is very important for the further analysis of objects.

References

Christensen, L., Becker, T., Jahnke, K., et al. 2003, A&A, 401, 479
Filippenko, A. V. 1982, PASP, 94, 715
Fruchter, A. S. & Hook, R. N. 2002, PASP, 114, 144
Hopp, U. & Fernandez, M. 2002, Calar Alto Newsletter No.4, http://www.caha.es/newsletter/news02a/hopp/paper.pdf
Horne, K. 1986, PASP, 98, 609
Pych, W. 2004, PASP, 116, 148
Sánchez, S. F. 2004, AN, 325, 167
van Dokkum, P. G. 2001, PASP, 113, 1420
Wyse, R. F. G. & Gilmore, G. 1992, MNRAS, 257, 1

CHAPTER B

Basic concepts

This chapter gives the basic equations that are used in the thesis without the full details.

B.1 Prediction of absorber sizes

Several relations found for galaxies can be combined to predict the sizes of DLA galaxies. The Holmberg relation associates the luminosity with the size of a galaxy through

$$\frac{R}{R^*} = \Big(\frac{L}{L^*}\Big)^{\beta} \tag{B.1}$$

Following the argument in Wolfe et al. (1986) and Tytler (1987) the average absorption cross section is

$$A(L) = \pi R^2/2 = \frac{\pi}{2}(R^*)^2(L/L^*)^{2\beta}, \tag{B.2}$$

where the factor of 2 is due to the smaller impact parameter for a randomly inclined disc. Usually in the literature the absorbing distance is used:

$$\frac{dX}{dz} = \frac{(1+z)^2}{\sqrt{(1+z)^2(1+\Omega_m z) - z(z+2)\Omega_\Lambda}} \tag{B.3}$$

The number density of absorbers can be derived

$$\frac{dN}{dz} = \frac{c}{H}\frac{dX}{dz}\int_0^\infty dL\Phi(L)A(L) \tag{B.4}$$

where dr/dz is the proper distance, and Φ is the Schechter (1976) luminosity function

$$\Phi(L)dL = \Phi^*\Big(\frac{L}{L^*}\Big)^{\alpha}\exp(-L/L^*)d(L/L^*) \tag{B.5}$$

Substituting Eqs. (B.2), (B.5), and replacing with the absorbing distance dX/dz in Eq. (B.4) one finds after the integration the relation

$$\frac{dN}{dz} = \frac{\pi}{2}\frac{c}{H}\Gamma(1+2\beta+\alpha)\Phi^* R^{*2}\frac{(1+z)^2}{\sqrt{(1+z)^2(\Omega_m z+1) - \Omega_\Lambda z(z+2)}} \tag{B.6}$$

This equation can be rearranged to solve for R^*.

Observed values for the luminosity function are $\Phi = 1.6\times10^{-2}h^{-3}$ Mpc^{-3}, $\alpha = -1.38$ (Dickinson 1998), and $dN/dz = 0.3$ at $z \approx 3$ for DLA systems (Turnshek et al. 1989). For a

cosmology with $\Omega_m = 0.3$, $\Omega_\lambda = 0.7$, and $H_0 = 70$ km s^{-1} Mpc^{-1}, Eq. (B.6) yields $R^* = 42$ kpc for $\beta = 0.4$ which is typically found for the Holmberg relation. Using instead the luminosity function of field galaxies at $z = 3$ in Poli et al. (2003), and the observed $\beta = 0.26$ (Chen & Lanzetta 2003), we find $R^* = 32$ kpc when using their fixed faint end slope of $\alpha = -1.44$. Poli et al. (2003) selected LBGs to a faint magnitude limit and showed a very significant evolution in the faint end of the luminosity function affecting α and hence R^*. A very steep faint end slope of $\alpha = -1.8$ in the luminosity function (Shapley et al. 2001) suggests much smaller impact parameters (the gamma function becomes negative for these values). Hence from the large range of derived sizes it is clear, that the sizes of the DLA galaxies predicted from a theoretical basis are highly uncertain because of the uncertainties from the luminosity function and the relevant scaling in the Holmberg relation. Furthermore, it is still not proved that LBGs and DLA galaxies probe the same galaxy population and hence if the Holmberg relation can be extended to DLA galaxies.

B.2 Emission line analysis

Fits to Gaussian line profiles give as an output the intensity, I, and the width of the line, σ. The line flux derived from integrating a Gaussian function from $-\infty$ to ∞ is

$$f_{\rm line} = \sqrt{2\pi} I \sigma \tag{B.7}$$

In two dimensions the flux is found from a surface integral which gives

$$f_{\rm line} = 2\pi I \sigma_1 \sigma_2 \tag{B.8}$$

In 3 dimensions the total flux is found from an integration over 3 parameters

$$f_{\rm line} = (2\pi)^{1.5} I \sigma_1 \sigma_2 \sigma_3 \tag{B.9}$$

where σ_1, σ_2, and σ_3 are the Gaussian standard deviations in the 1.st, 2.nd, and 3.rd dimensions, respectively.

B.3 Abundances from emission lines

This section describes the basic equations which function as a basis for the derivation of abundances from strong emission lines in Chapter 2.

Oxygen abundance

The R_{23} intensity ratio defined as

$$R_{23} \equiv \frac{[\mathrm{O\,II}]\lambda 3727 + [\mathrm{O\,III}]\lambda 4959 + [\mathrm{O\,III}]\lambda 5007}{\mathrm{H}\beta} \tag{B.10}$$

introduced by Pagel et al. (1979) has often been used to estimate oxygen abundances using emission lines from extragalactic sources. However, the R_{23} vs. (O/H) relation is double valued for high metallicities making it difficult to determine oxygen abundances using this diagnostic.

The R_{23} relation can be combined with the calibrations in Kobulnicky et al. (1999) to yield oxygen abundances

$$12 + \log(\mathrm{O/H}) \;=\; 9.265 - 0.33 \log R_{23}$$

$$-0.202(\log R_{23})^2 - 0.207(\log R_{23})^3 \\ -0.33(\log R_{23})^4 \quad \text{(B.11)}$$

Pilyugin (2001) gives a different calibration of the R_{23} ratio by introducing the ionization parameter, P.

$$P = \frac{f_{[\mathrm{O\,III}]\lambda 4959+\lambda 5007}}{f_{[\mathrm{O\,II}]\lambda 3727} + f_{[\mathrm{O\,III}]\lambda 4959+\lambda 5007}} \quad \text{(B.12)}$$

$$12 + \log(\mathrm{O/H}) = \frac{R_{23} + 54.2 + 59.45P + 7.31P^2}{6.07 + 6.71P + 0.371P^2 + 0.243R_{23}} \quad \text{(B.13)}$$

For lines with uncertain fluxes, propagation of errors though Eq. (B.13) results in larger error bars than for the other calibrations. Therefore, this diagnostics was not used.

Another strong emission line diagnostic is the relation

$$O3N2 \equiv \log \frac{[\mathrm{O\,III}]\lambda 5007/\mathrm{H}\beta}{[\mathrm{N\,II}]\lambda 6583/\mathrm{H}\alpha} \quad \text{(B.14)}$$

calibrated by Pettini & Pagel (2004). For a sample of 137 extragalactic H II regions they derive the relation

$$12 + \log(\mathrm{O/H}) = 8.73 - 0.32 \times O3N2 \quad \text{(B.15)}$$

The $O3N2$ ratio benefits from the fact that the involved lines in the ratios are separated by short wavelength ranges and the quantity is largely unaffected by dust obscuration.

Oxygen abundances using line diagnostics have been calibrated by other authors. For example, the oxygen abundance can be estimated from the ratio $N2 \equiv \log([\mathrm{N\,II}]/\mathrm{H}\alpha)$ (Denicoló et al. 2002)

$$12 + \log(\mathrm{O/H}) = (9.12 \pm 0.05) + (0.72 \pm 0.10)N2, \quad \text{(B.16)}$$

and a slightly different calibration of the $N2$ ratio is given in Pettini & Pagel (2004)

$$12\log(\mathrm{O/H}) = 9.37 + 2.03N2 + 1.26N2^2 + 0.32N2^3 \quad \text{(B.17)}$$

Nitrogen

In addition to the oxygen abundance one can use emission lines to derive a nitrogen to oxygen abundance ratio. Applying the relation between R_{23} and the [N II] temperature in Thurston et al. (1996)

$$t_{[\mathrm{N\,II}]} = 6065 + 1600\log(R_{23}) \\ +1878\log(R_{23})^2 + 2803\log(R_{23})^3, \quad \text{(B.18)}$$

the abundances of ionised nitrogen can be derived using the relation between temperature and nitrogen to oxygen ratio (Pagel et al. 1992)

$$\log \frac{\mathrm{N^+}}{\mathrm{O^+}} = \log \frac{[\mathrm{N\,II}]\lambda\lambda 6548, 6583}{[\mathrm{O\,II}]\lambda\lambda 3727, 3729} + 0.307 \\ -0.02\log t_{[\mathrm{N\,II}]} - \frac{0.726}{t_{[\mathrm{N\,II}]}} \quad \text{(B.19)}$$

where $t_{[\mathrm{N\,II}]}$ is expressed in units of 10^4 K. Disregarding ionization corrections the nitrogen abundance can be derived assuming (N/O) = ($\mathrm{N^+/O^+}$). As shown by the models in Thurston et al.

(1996) this approximation is accurate within 5%.

B.4 Error propagation

The definition of error propagation for a quantity $f(x_i)$ is

$$\sigma_f^2 = \sum_i \left(\frac{df}{dx_i}\right)^2 \sigma(x_i)^2 \tag{B.20}$$

Flux error
For the one-dimensional Gaussian profile, the error is

$$\sigma(f)^2 = [(\Delta I/I)^2 + (\Delta\sigma/\sigma)^2]2\pi(I\sigma)^2 \tag{B.21}$$

where Δ represent the measured uncertainties. Including the error of the continuum placement the equation becomes

$$\sigma(f)^2 = [((\Delta I + \Delta\mathrm{cont})/I)^2 + (\Delta\sigma/\sigma)^2]2\pi(I\sigma)^2 \tag{B.22}$$

As another example we examine the errors in flux ratios as used in the derivation of abundances. We take the definition $N2 = \log(\mathrm{N\,II}/\mathrm{H}\alpha)$, and to derive the error of $N2$ Eq. (B.20) gives

$$\Delta N2 = \frac{1}{\mathrm{N\,II}/\mathrm{H}\alpha\log(10)}\Delta(\mathrm{N\,II}/\mathrm{N\,II})^2 + (\Delta_{\mathrm{H}\alpha}/\mathrm{H}\alpha)^2\frac{\mathrm{N\,II}}{\mathrm{H}\alpha} \tag{B.23}$$

References

Chen, H.-W. & Lanzetta, K. M. 2003, ApJ, 597, 706
Denicoló, G., Terlevich, R., & Terlevich, E. 2002, MNRAS, 330, 69
Dickinson, M. 1998, in The Hubble Deep Field, 219
Kobulnicky, H. A., Kennicutt, R. C., & Pizagno, J. L. 1999, ApJ, 514, 544
Pagel, B. E. J., Edmunds, M. G., Blackwell, D. E., Chun, M. S., & Smith, G. 1979, MNRAS, 189, 95
Pagel, B. E. J., Simonson, E. A., Terlevich, R. J., & Edmunds, M. G. 1992, MNRAS, 255, 325
Pettini, M. & Pagel, B. E. J. 2004, MNRAS, 348, L59
Pilyugin, L. S. 2001, A&A, 369, 594
Poli, F., Giallongo, E., Fontana, A., et al. 2003, ApJL, 593, L1
Schechter, P. 1976, ApJ, 203, 297
Shapley, A. E., Steidel, C. C., Adelberger, K. L., et al. 2001, ApJ, 562, 95
Thurston, T. R., Edmunds, M. G., & Henry, R. B. C. 1996, MNRAS, 283, 990
Turnshek, D. A., Wolfe, A. M., Lanzetta, K. M., et al. 1989, ApJ, 344, 567
Tytler, D. 1987, ApJ, 321, 49
Wolfe, A. M., Turnshek, D. A., Smith, H. E., & Cohen, R. D. 1986, ApJS, 61, 249

Acknowledgements

This project has been supported by German Verbundforschung associated with the ULTROS project, grant no. 05AE2BAA/4. The project description was primarily to use the AIP built Potsdam Multi Aperture Spectrophotometer to pursue deep spectroscopy of faint targets within the ULTROS collaboration. Additionally, being associated with the European Training Network in 3D spectroscopy, Euro3D, has given me a great opportunity to have contacts with other people who use integral field spectroscopy in their various branches of science. Many thanks to Martin Roth for encouraging me to participate in many of these meetings.

During the 3 years Ph.D. work I have benefited from input from many people. Thanks to Sebastian F. Sánchez for improving software upon request, and typically having an updated bug-free/bug-changing version of the Euro3D visualisation tool even before my asking. Likewise Thomas Becker was an invaluable help in writing software for the analysis of the data and introduced me to the art of reducing 3D data. Thanks to Knud Jahnke for reading and commenting innumerable drafts and always being able to discuss problems and to suggest interpretations.

Thanks to the Calar Alto staff, especially Nicolas Cardiel for the service observations that provided data of very good quality. The times I visited the observatory at Calar Alto, all the staff made it a very agreeable place to stay by creating a familiar atmosphere, and even made nights of bad weather enjoyable and sometimes outright fun. A terribly rare sensation for an observer. Other people who were not at all obliged to help me were invaluable for the outcome. Special thanks go to Andy Bunker (Exeter) who agreed to participate in a number of small projects although the success of getting the data has not yet been great. Katrina Exeter (IAC, Tenerife) who made me realise that the analysis of bright objects with IFS is not much easier than having to deal with faint ones. Regina Schulte-Ladbeck (Pittsburgh) for much inspiration to do metallicity studies, and Palle Møller (ESO) and Johan Fynbo (NBI-AO) for discussions and suggestions on several occasions. Finally, I would like to thank my supervisor Lutz Wisotzki for many ideas and suggestions.

Sometimes the difficulties of investigating the data presented here appeared overwhelming and highly confusing. Nevertheless, carrying on the struggle to improve the signals resulted in several surprises along the way. Very often it was discussions with other people that led to a better understanding, and in that respect I hope that my current collaborators will also be motivated to carry on with these studies in the future.

In searching out the truth be ready for the unexpected,
for it is difficult to find and puzzling when you find it.

Heraclitus